

REVIEW

of the
ELECTRICAL COMMUNICATION LABORATORY

NIPPON TELEGRAPH AND TELEPHONE PUBLIC CORPORATION

Former, Reports of the Electrical Communication Laboratory
Nippon Telegraph and Telephone Public Corporation
from Vol.1, No.1, Sept. 1953 to Vol.7, No.12, Dec. 1959

VOLUME 9
NUMBERS 3-4

Published Bimonthly by

ELECTRICAL COMMUNICATION LABORATORY
NIPPON TELEGRAPH AND TELEPHONE PUBLIC CORPORATION
1551, Kitizyôzi, Musasino-si, Tôkyô, Japan

March - April
1961

Review of the Electrical Communication Laboratory

EDITORIAL COMMITTEE

Susumu OKAMURA *Chairman*

Tadasu FUKAMI

Giichi ITO

Hideo KAWASAKI

Yukio NAKAMURA

Tatsuya SHIMBORI

Takuzo SHINDO

Toyotaro SHIRAMATSU

Takakichi UZAWA

Ginsaku YASAKI

Nobukazu NIIZEKI

EDITORIAL STAFF

Takaaki MIWA *Editor*

Tutomu SAITO *Assistant Editor*

Masao HIROSE //

The Review of the Electrical Communication Laboratory is published six times a year (bi-monthly) by the Electrical Communication Laboratory, Nippon Telegraph and Telephone Public Corporation, 1551, Kitizyôzi, Musasino-si, Tôkyô, Japan. Telephone: Tôkyô (391) 2261 and 2271.

All rights of republication, including translation into foreign languages, are reserved by the Electrical Communication Laboratory, NTT.

Subscriptions are accepted at ¥1,200 per year. Single copy ¥300 each. Foreign postage is ¥400 per year or ¥65 per copy. Remittance should be made in check payable to the Electrical Communication Laboratory and sent to the Director.

REVIEW

of the
ELECTRICAL COMMUNICATION LABORATORY

NIPPON TELEGRAPH AND TELEPHONE PUBLIC CORPORATION

Volume 9, Numbers 3-4

March-April, 1961

U.D.C. 621.318.56.066.6.001.2:[621-272:531.66

Chatter Vibration of Switching Relay*

Masao TAKAMURA,† Yuiti SHIMIZU and Yuji OTUKA

This study was made for the purpose of establishing a method of designing relays which do not chatter. The chatter occurring between various vibratory systems and a rigid body was studied, and the relationships between chatter and vibratory constants were clarified.

Moreover, the condition for which contact chatter ceases was investigated. Using this result, we developed a new type of contact spring which is suitable for use in high speed relays without chatter. The conclusion obtained here are very useful when designing relays free from contact chatter.

1. Introduction

Most relay vibrations caused by impact during relay operation or release, that is chatter, directly affect the performance of the relay as they result in faulty contact behavior. Chatter is liable to cause noise in communications circuits and the incorrect operation of telephone exchange apparatus. Also, chatter causes a marked decrease in relay life. Chatter has been investigated by many engineers who sought to understand it and eliminate its undesirable effects, but chatter is so extremely complicated that many problems are still unsolved.

There are many papers dealing with the vibrations caused by the collision between two bodies. These papers include: analyses of the vibration of an elastic body after collision with a mass⁽¹⁾⁽²⁾ or collision with a

spring,⁽⁷⁾⁽⁸⁾ those dealing with the collision of simple vibratory systems which are spring supported masses,⁽³⁾⁽⁴⁾⁽⁵⁾⁽⁶⁾ those dealing with the longitudinal impact of bars,⁽⁹⁾ etc. But the number of papers which treat repeated collisions and restitutions between two bodies such as the collisions experienced by the moving parts of relays are extremely small, and no paper contains an exposition adequate for the analysis of the chatter of relays.

This study has been performed to clarify the physical quantities involved in chatter, to analyze the dynamic characteristics of the moving parts of relays, and to obtain the design criteria necessary to prevent the chatter of relay contacts. For this purpose a general theory of the vibrations caused by collisions between two elastic bodies was developed. Then this theory was applied to the response of a vibratory system with a single degree of freedom or an elastic body which collides with a rigid body and these theoretical results compared with the experimental results.

Hertz's contact theory⁽²⁾⁽⁶⁾ is widely applied to the local deformation of contacts in

* MS in Japanese received by the Electrical Communication Laboratory, July. 6, 1960. Originally published in the *Kenkyū Zituyōka Hōkoku* (Electrical Communication Laboratory Technical Journal), N.T.T., Vol. 9, No. 12, pp. 1355-1420, 1960.

† Switching Apparatus Research Section.

impact. If we consider this local deformation of the contacts the analysis of chatter becomes much too complicated and furthermore it is not an easy matter to measure local deformation in actual relays. In order to simplify the problem the fundamental equation was derived with the simplifying assumptions that the local deformation to the contacts during impact can be neglected and that the period of the vibrations excited by the impact are extremely long compared with the duration of the contact closure during impact.

The vibration, caused by collision, of a vibratory system of nearly a single degree of freedom is quite simple; therefore knowledge of its characteristics is very useful in gaining an understanding of the physical quantities involved in chatter. Comparison of the observed values and the values calculated for this case enabled us to clarify quantitatively the vibratory constants relating to chatter and also to obtain the conditions for which contact chatter ceases. It is therefore possible to estimate the time from the commencement of operation of the vibratory system to the cessation of contact chatter and also the number of times the contacts open or close during the duration of contact chatter. Therefore, we constructed simple vibratory systems whose damping force is variable at will and investigated their chatter.

The contact spring construction most widely used in present relays is the cantilever, a beam or bar clamped at one end. The resonance of a cantilever colliding with a rigid body was calculated on a digital electronic computer in accordance with our theory, and the results obtained were compared with the results of our experiments. In this manner the fundamental concepts of relay chatter were clarified and rules for selecting the constants of the moving parts when designing relays were obtained. These rules give the conditions necessary for simplifying the chatter phenomena and those necessary for the elimination of contact chatter. Experimental vibratory systems based on these rules have been constructed and experimental and theoretical investigations of the conditions

necessary for the simplification and the elimination of contact chatter have been carried out.

2. Fundamental Equation for Chatter

It is necessary to know the dynamic behavior of the moving parts of relays if we wish to clarify the chatter of relay contacts. A general description of the response of two elastic bodies colliding with each other will be given in this section.

When two elastic bodies collide, their points of contact deform locally during impact. After the collision the points of contact separate and the two bodies vibrate independently of each other with many complex flexural modes.

According to Hertz's theory of contact,⁽⁶⁾ the local deformation of the points of contact when two bodies are in static contact is proportional to the two-thirds power of the force acting on the bodies. If Hertz's theory is also applicable in the case of collision between two bodies, the equation which describes the motion of colliding elastic bodies will be nonlinear and computations involving it will be very difficult. However there are many cases in which the local deformation of the contacts and the duration of the contact closures can be neglected when the mating parts of relays collide with each other. Therefore in our derivation of the general equation of chatter we consider a simplified model of this impact phenomenon having the following characteristics:

- (1) The local deformations of the contacts are negligibly small
- (2) The contact force resulting from impact is impulsive
- (3) The duration of the contact closures is much shorter than the period of the vibrations excited by the impact.

But since a definite period of contact closure exists in practice, the higher modes of vibrations which satisfy these assumptions do not exist indefinitely and the degree of the higher modes of vibrations that are being studied here is definite.

The response of such elastic bodies after

impact may be shown to be their free vibrations determined by the conditions immediately before impact superimposed on their forced vibrations caused by the unknown impulsive force. We determine the unknown parameter, impulsive force, in the previous representation by using the condition that the kinetic energy before and after impact is conserved. Moreover, in order to study the energy loss during impact, the coefficient of restitution which is usually used for the collision of masses is developed here for the collision of elastic bodies, and the fundamental equation of vibration caused by impact is derived.

In general, the free vibration velocities of an elastic body without damping, $\dot{\xi}_{if}$, are, as is well-known,

$$\dot{\xi}_{if} = \sum_m (A_{im} \cos \omega_{im} t + B_{im} \sin \omega_{im} t) \Xi_{im}. \quad (1)$$

Here $i=1$ or 2 corresponds to elastic body (1) or (2), where Ξ_{im} is the m -th normal function of body (i), ω_{im} is the m -th natural circular frequency of body (i), A_{im} , B_{im} are constants determined by the conditions immediately before impact, and M_i is the total mass of body (i). When impulsive force I acts on point X_i on the surface of body i , the velocity $\dot{\xi}_{iI}$ is given by⁽¹³⁾

$$\dot{\xi}_{iI} = \frac{I}{M_i} \sum_m \Xi_{imX_i} \cdot \Xi_{im} \cdot \cos \omega_{im} t. \quad (2)$$

where Ξ_{imX_i} is the value of Ξ_{im} evaluated at X_i in the direction of the impulsive force.

If elastic body (1) collides with body (2) at point X_i at time $t=0$, from (1) and (2), the velocity $\dot{\xi}_i$ of body (i) after impact is given by an expression of the form:

$$\begin{aligned} \dot{\xi}_i = & \sum_m (A_{im} \cos \omega_{im} t + B_{im} \sin \omega_{im} t) \Xi_{im} \\ & + (-1)^i \frac{I}{M_i} \sum_m \Xi_{imX_i} \cdot \Xi_{im} \cdot \cos \omega_{im} t. \end{aligned} \quad (3)$$

If the impulsive force I can be evaluated from (3), the velocity of the body after impact may be obtained.

2.1. Perfect Elastic Impact*

The kinetic energy immediately before impact at $t=-0$ and that immediately after impact at $t=+0$ will be considered making use of Eq. (3). At $t=-0$ I is equal to zero; therefore the velocity of body (i) immediately before impact, $[\dot{\xi}_i]_{t=-0}$, is

$$[\dot{\xi}_i]_{t=-0} = \sum_m A_{im} \cdot \Xi_{im}$$

Hence, the kinetic energy of body (i) immediately before impact $[T_i]_{t=-0}$ is

$$[T_i]_{t=-0} = \frac{M_i}{2} \sum_m A_{im}^2 \quad (4)$$

The velocity of body (i) immediately after impact, $[\dot{\xi}_i]_{t=+0}$, is

$$[\dot{\xi}_i]_{t=+0} = \sum_m \left\{ A_{im} + (-1)^i \frac{I}{M_i} \Xi_{imX_i} \right\} \Xi_{im}$$

Hence, the kinetic energy of body (i) immediately after impact, $[T_i]_{t=+0}$, is

$$[T_i]_{t=+0} = \frac{M_i}{2} \sum_m \left\{ A_{im} + (-1)^i \frac{I}{M_i} \Xi_{imX_i} \right\}^2 \quad (5)$$

If the assumption is made that the kinetic energy before impact is equal to that after impact, from (4) and (5), the resulting expression for the impulsive force I is

$$I = \frac{2 \cdot \sum_{i,m} (-1)^{i+1} \cdot A_{im} \cdot \Xi_{imX_i}}{\sum_{i,m} \frac{\Xi_{imX_i}^2}{M_i}}. \quad (6)$$

2.2. Coefficient of Restitution

Eq. (6) is satisfied for the case in which the duration of the contact closure during impact is extremely short compared with the period of the vibrations of the body excited

* The case in which the kinetic energy immediately before and after impact is conserved is called here: perfectly elastic impact.

by the impact. For the higher modes of vibration, however, the duration of the contact closures cannot be neglected. If step-type impulsive force acts on the body, the velocities of the higher modes after impact are decreased in proportion to the frequency of their modes.⁽¹³⁾ Therefore, the duration of the contact closures is extremely long compared with the period of the higher modes, the larger the degree m of the higher modes, the more the amplitude of higher mode decreases, and the higher modes are immediately damped out in an actual vibratory system. Hence, the highest degree m of the higher modes in (6) is finite, and the energy of the higher degree vibrations may be dealt with as energy lost during the impact. The energy lost during the impact depends upon the materials of the contacts as will be described in Section 4. From the above considerations, the conception of the coefficient of restitution used for the collision of spheres is extended to the collision of elastic bodies.

When a sphere (1) having mass M_1 and velocity v_1 collides with a material point (2) with mass M_2 and velocity v_2 , the impulsive force I_0 acting on each is given, as is well-known, by

$$I_0 = \frac{1+\alpha}{1/M_1 + 1/M_2} (v_1 - v_2) \quad (7)$$

where α is the coefficient of restitution. In (6), $\sum_m A_{im} \Xi_{imX_i}$ is the velocity of the point X_i on the elastic bodies which will collide immediately before impact; so that if $\sum_{i,m} M_i / \Xi_{imX_i}^2$ corresponds to the effective mass of the elastic bodies, Eq. (6) and (7) have the same form. If we assume that the coefficient of restitution in impacts of elastic bodies satisfies the relation $0 \leq \alpha \leq 1$ such as in case of spheres, the resulting impulsive force in impact of elastic bodies may be written in the form:

$$I = \frac{(1+\alpha) \sum_{i,m} (-1)^{i+1} \cdot A_{im} \cdot \Xi_{imX_i}}{\sum_{i,m} \Xi_{imX_i}^2 / M_i} \quad (8)$$

$0 \leq \alpha \leq 1$

The velocity of elastic bodies after impact is given by Eqs. (3) and (8) and the response of bodies after impact can be calculated from the vibratory condition of the bodies before impact.

2.3. Vibrations Involving Repeated Collision

The vibrations of the moving parts of relays usually involve repeated collisions with their mating parts. These repeated collisions, usually called chatter, may be expressed by Eqs. (3) and (8). If the n -th impact between two elastic bodies without damping occurs at $t=0$, the velocity of body (i) after the n -th impact is represented in the form:

$$\begin{aligned} \dot{\xi}_i^{(n)} = \sum_m \left[\left\{ A_{im}^{(n)} + (-1)^i \frac{I^{(n)}}{M_i} \cdot \Xi_{imX_i} \right\} \cos \omega_{im} t \right. \\ \left. + B_{im}^{(n)} \cdot \sin \omega_{im} t \right] \Xi_{im} \end{aligned} \quad (9)$$

where n is the number of the impact occurring at $t=0$.

Hence, the displacement of body (i) after the n -th impact is given by

$$\begin{aligned} \xi_i^{(n)} = \sum_m \left[\left\{ A_{im}^{(n)} + (-1)^i \frac{I^{(n)}}{M_i} \cdot \Xi_{imX_i} \right\} \sin \omega_{im} t \right. \\ \left. - B_{im} \cos \omega_{im} t \right] \frac{\Xi_{im}}{\omega_{im}}. \end{aligned} \quad (10)$$

Let t_{n-1} be the time interval from the $(n-1)$ th impact to the n -th impact, then the velocity and the displacement immediately before n -th impact are given by

$$\begin{aligned} [\dot{\xi}_i^{(n)}]_{t=0} &= [\dot{\xi}_i^{(n-1)}]_{t=t_{n-1}} \\ [\xi_i^{(n)}]_{t=0} &= [\xi_i^{(n-1)}]_{t=t_{n-1}} \end{aligned}$$

Hence, the relations between the coefficients in (9) and (10) are easily derived in the form:

$$\begin{aligned} -B_{im}^{(n)} &= \left\{ A_{im}^{(n-1)} + (-1)^i \frac{I^{(n-1)}}{M_i} \cdot \Xi_{imX_i} \right\} \\ &\times \sin \omega_{im} t_{n-1} - B_{im}^{(n-1)} \cdot \cos \omega_{im} t_{n-1} \end{aligned} \quad (11)$$

$$A_{im}^{(n)} = \left\{ A_{im}^{(n-1)} + (-1)^i \frac{I^{(n-1)}}{M_i} \cdot \Xi_{imX_i} \right\} \\ \times \cos \omega_{im} t_{n-1} + B_{im}^{(n-1)} \cdot \sin \omega_{im} t_{n-1}. \quad (12)$$

At $t=t_{n-1}$, the displacement of the contact of body (1) is equal to that of body (2), so that t_{n-1} in (11) and (12) is determined from the equation which is, from (10), given by

$$\sum_m \frac{B_{1m}^{(n)}}{\omega_{1m}} \Xi_{1mx_1} = \sum_m \frac{B_{2m}^{(n)}}{\omega_{2m}} \Xi_{2mx_2}. \quad (13)$$

The chatter in relays can be calculated successively by using the preceding equations (9)~(13) if the initial conditions are given.

2.4. Chatter of an Elastic Body with Damping

We shall consider here a cantilever with damping whose free vibration is represented as follows:

$$E_i S_i R_i^2 \frac{\partial^4 \xi_{if}}{\partial x_i^4} + r_i \frac{\partial \xi_{if}}{\partial t} + S_i \rho_i \frac{\partial^2 \xi_{if}}{\partial t^2} = 0 \quad (14)$$

Boundary conditions:

$$\begin{aligned} \text{at } x_i=0 \quad & \frac{\partial \xi_{if}}{\partial x_i} = 0, \quad \xi_{if} = 0 \\ \text{at } x_i=l_i \quad & \frac{\partial^2 \xi_{if}}{\partial x_i^2} = 0, \quad \frac{\partial^3 \xi_{if}}{\partial x_i^3} = 0 \end{aligned}$$

where E_i is Young's modulus of beam (i), S_i is the cross-sectional area of beam (i), R_i is the cross-sectional radius of gyration, x_i is measured along the centroidal axis of beam (i), l_i is the length of beam (i), and ξ_{if} is the transverse displacement of free vibration of beam (i). From (14), the velocity of free vibration $\dot{\xi}_{if}$ is given by

$$\dot{\xi}_{if} = \sum_m e^{-\delta_{im} \omega_{im} t} [A_{im} \cos \sqrt{1-\delta_{im}^2} \omega_{im} t \\ + B_{im} \sin \sqrt{1-\delta_{im}^2} \omega_{im} t] \Xi_{im} \quad (15)$$

where

$$\omega_{im} = \frac{k_m^2}{l_i^2} R_i \sqrt{\frac{E_i}{\rho_i}} \quad (16)$$

$$\delta_{im} = \frac{r_i}{2 S_i \rho_i \omega_{im}} \quad (17)$$

$$1 + \cos k_m \cdot \cosh k_m = 0 \quad (18)$$

$$\Xi_{im} = \left(\cos k_m \frac{x_i}{l_i} - \cosh k_m \frac{x_i}{l_i} \right) \\ + \frac{\cos k_m + \cosh k_m}{\sin k_m + \sinh k_m} \left(\sin k_m \frac{x_i}{l_i} - \sinh k_m \frac{x_i}{l_i} \right) \quad (19)$$

When impulsive force I acts on point X_i on the surface of this cantilever at $t=0$, the velocity $\dot{\xi}_{iI}$ is given by

$$\dot{\xi}_{iI} = \frac{I}{M_i} \sum_m e^{-\delta_{im} \omega_{im} t} \left\{ \cos \sqrt{1-\delta_{im}^2} \omega_{im} t \right. \\ \left. - \frac{\delta_{im}}{\sqrt{1-\delta_{im}^2}} \sin \sqrt{1-\delta_{im}^2} \omega_{im} t \right\} \Xi_{imX_i} \Xi_{im} \quad (20)$$

Accordingly, the response of two elastic bodies with damping colliding with each other repeatedly can be represented by the following equations which are derived in the same way as described in Section 2.3.

$$\dot{\xi}_i^{(n)} = \sum_m e^{-\delta_{im} \omega_{im} t} \left[\left\{ A_{im}^{(n)} \sqrt{1-\delta_{im}^2} - B_{im}^{(n)} \cdot \delta_{im} \right. \right. \\ \left. \left. + (-1)^i \frac{I^{(n)}}{M_i} \frac{\Xi_{imX_i}}{\sqrt{1-\delta_{im}^2}} \right\} \sin \sqrt{1-\delta_{im}^2} \omega_{im} t \right. \\ \left. - \{ A_{im}^{(n)} \cdot \delta_{im} + B_{im}^{(n)} \sqrt{1-\delta_{im}^2} \} \right. \\ \left. \times \cos \sqrt{1-\delta_{im}^2} \omega_{im} t \right] \frac{\Xi_{im}}{\omega_{im}} \quad (21)$$

$$\dot{\xi}_i^{(n)} = \sum_m e^{-\delta_{im} \omega_{im} t} \left[A_{im}^{(n)} + (-1)^i \frac{I^{(n)}}{M_i} \Xi_{imX_i} \right] \\ \times \cos \sqrt{1-\delta_{im}^2} \omega_{im} t + \left\{ B_{im}^{(n)} - (-1)^i \frac{I^{(n)}}{M_i} \right. \\ \left. \times \frac{\delta_{im} \cdot \Xi_{imX_i}}{\sqrt{1-\delta_{im}^2}} \right\} \sin \sqrt{1-\delta_{im}^2} \omega_{im} t \Xi_{im} \quad (22)$$

$$I^{(n)} = \frac{(1+\alpha) \sum_{i,m} (-1)^{i+1} \cdot A_{im}^{(n)} \cdot \Xi_{imX_i}}{\sum_{i,m} \frac{\Xi_{imX_i}^2}{M_i}} \quad (23)$$

$$\begin{aligned} A_{im}^{(n)} = & e^{-\delta_{im}\omega_{im}t_{n-1}} \left[\left\{ A_{im}^{(n-1)} + (-1)^i \frac{I^{(n-1)}}{M_i} \right. \right. \\ & \times \Xi_{imX_i} \left. \right\} \cos \sqrt{1-\delta_{im}^2} \omega_{im}t_{n-1} + \left\{ B_{im}^{(n-1)} \right. \\ & - (-1)^i \frac{I^{(n-1)}}{M_i} \frac{\delta_{im} \cdot \Xi_{imX_i}}{\sqrt{1-\delta_{im}^2}} \left. \right\} \\ & \times \sin \sqrt{1-\delta_{im}^2} \omega_{im}t_{n-1} \left. \right] \quad (24) \end{aligned}$$

$$\begin{aligned} -B_{im}^{(n)} = & e^{-\delta_{im}\omega_{im}t_{n-1}} \left[\left\{ A_{im}^{(n-1)} + (-1)^i \right. \right. \\ & \times \frac{I^{(n-1)}}{M_i} \Xi_{imX_i} \left. \right\} \sin \sqrt{1-\delta_{im}^2} \omega_{im}t_{n-1} \\ & - \left\{ B_{im}^{(n-1)} - (-1)^i \frac{I^{(n-1)}}{M_i} \frac{\delta_{im} \cdot \Xi_{imX_i}}{\sqrt{1-\delta_{im}^2}} \right\} \\ & \times \cos \sqrt{1-\delta_{im}^2} \omega_{im}t_{n-1} \left. \right] \quad (25) \end{aligned}$$

$$\begin{aligned} \sum_m \{ A_{1m}^{(n)} \cdot \delta_{1m} + B_{1m}^{(n)} \sqrt{1-\delta_{1m}^2} \} \frac{\Xi_{1mX_1}}{\omega_{1m}} \\ = \sum_m \{ A_{2m}^{(n)} \cdot \delta_{2m} + B_{2m}^{(n)} \sqrt{1-\delta_{2m}^2} \} \frac{\Xi_{2mX_2}}{\omega_{2m}}. \quad (26) \end{aligned}$$

2.5. Chatter of Two Bodies having the Same Vibratory Constants

We will investigate the case where two elastic bodies having the same vibratory constants occur the n -th impact at the contact point X_i having the same conditions. From Eq. (8), the impulsive force I in this case can be easily derived in the form:

$$I^{(n)} = \frac{(1+\alpha) \sum_m (A_{1m}^{(n)} - A_{2m}^{(n)}) \Xi_{1mX_1}}{2 \sum_m \frac{\Xi_{1mX_1}^2}{M_1}}$$

$$= \frac{(1+\alpha) \sum_m (A_{1m}^{(n)} - A_{2m}^{(n)}) \Xi_{2mX_2}}{2 \sum_m \frac{\Xi_{2mX_2}^2}{M_2}}. \quad (27)$$

Hence, from (9) and (27), the velocity at the contact of body (i) immediately before impact, $[\dot{\xi}_{iX_i}]_{t=-0}$, and after impact, $[\dot{\xi}_{iX_i}]_{t=+0}$, is respectively given by

$$\left. \begin{aligned} [\dot{\xi}_{1X_1}]_{t=+0} &= \frac{1-\alpha}{2} [\dot{\xi}_{1X_1}]_{t=-0} + \frac{1+\alpha}{2} [\dot{\xi}_{2X_2}]_{t=-0} \\ [\dot{\xi}_{2X_2}]_{t=+0} &= \frac{1+\alpha}{2} [\dot{\xi}_{1X_1}]_{t=-0} + \frac{1-\alpha}{2} [\dot{\xi}_{2X_2}]_{t=-0} \end{aligned} \right\} \quad (28)$$

If $\alpha=1$ in (28)

$$\left. \begin{aligned} [\dot{\xi}_{1X_1}]_{t=+0} &= [\dot{\xi}_{2X_2}]_{t=-0} \\ [\dot{\xi}_{1X_1}]_{t=+0} &= [\dot{\xi}_{2X_2}]_{t=+0} \end{aligned} \right\} \quad (29)$$

That is, in the case of perfectly elastic impact ($\alpha=1$), if two elastic bodies having the same vibratory constants collide with each other at the contact having the same conditions, the velocity at the contact before and after impact should be exchanged. For example, if elastic body (2) is at rest immediately before impact, the velocity at a contact of body (1) immediately after impact is zero.

2.6. Chatter of an Elastic Body Colliding with a Rigid Body

In this section we shall assume that a collision occurs between a rigid body and an elastic body. The physical nature of a rigid body is that its mass is infinite and that it vibrates neither before nor after impact. Therefore, if body $i=2$ is the rigid body in this case, the response of elastic body (1) colliding with body (2) is obtained from equation (9)~(13) by making the following substitutions.

$$\left. \begin{aligned} M_2 &\rightarrow \infty \\ A_{2m}^{(n)} &= B_{m2}^{(n)} = 0 \\ I^{(n)} &= \frac{(1+\alpha) \sum_m A_{1m}^{(n)} \cdot \bar{\varepsilon}_{1mX_1}}{\sum_m \frac{\bar{\varepsilon}_{1mX_1}^2}{M_1}} \end{aligned} \right\} \quad (30)$$

From (10) and (30), the amplitude of the higher modes resulting from impact in this case are independent of the absolute value of the mass of the elastic body, but determined by $\bar{\varepsilon}_{imX}$.

3. Method of Calculating Chatter

It is necessary to calculate chatter when designing relays. Furthermore, comparison of the calculated and observed values enable us to clarify the physical quantities involved in chatter and also to obtain the similarity laws of chatter. Here will be given a method of calculating the chatter when a vibratory system of a single degree of freedom or an elastic body, acted upon by a damping force proportional to its velocity, collides with a rigid body.

In the case of a vibratory system of a single degree of freedom, its response is comparatively simple; therefore the calculation can be easily carried out by graphical methods. In the case of an elastic body, the calculation is complicated and fairly troublesome as shown in Section 2, 3. Therefore, here will be considered a method of calculation using an electronic computer.

3.1. Vibratory System of a Single Degree of Freedom acted upon by a Damping Force Proportional to its Velocity

As shown in Fig. 1, we will consider here a vibratory system whose free vibration is governed by the differential equation:

$$m\ddot{\xi} + r\dot{\xi} + s\xi = 0 \quad (31)$$

Where $s\xi$ is the restoring force, the product of the displacement and the stiffness s ;

$r\dot{\xi}$ is the dissipative force, the product of the velocity $\dot{\xi}$ and resistance r ; and $m\ddot{\xi}$ is the inertia reaction, the product of the acceleration $\ddot{\xi}$ and the mass m .

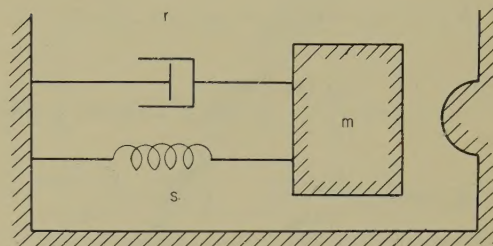


Fig. 1—Model of vibration system.

When this system collides with a rigid body at the position ξ_0 , if n -th impact occurs at time $t=0$, the displacement $\xi^{(n)}$ and the velocity $\dot{\xi}^{(n)}$ after n -th impact are as well-known, of the form:

$$\xi^{(n)} = e^{-\delta\omega t} \left\{ \xi_0 \cos \sqrt{1-\delta^2} \omega t + \frac{\dot{\xi}_{+0}^{(n)} + \delta\omega\xi_0}{\sqrt{1-\delta^2} \omega} \sin \sqrt{1-\delta^2} \omega t \right\} \quad (32)$$

$$\dot{\xi}^{(n)} = e^{-\delta\omega t} \left\{ \dot{\xi}_{+0}^{(n)} \cos \sqrt{1-\delta^2} \omega t - \frac{\dot{\xi}_{+0}^{(n)}\delta + \omega\xi_0}{\sqrt{1-\delta^2}} \sin \sqrt{1-\delta^2} \omega t \right\} \quad (33)$$

$$\delta = \frac{r}{2m\omega} < 1$$

$$\omega^2 = \frac{s}{m}$$

where δ is the damping constant, ω is the natural angular frequency, $\dot{\xi}_{+0}^{(n)}$ is the velocity immediately after the n -th impact, and ξ_0 is the position of the rigid body measured from the natural of the system, called here the predeflection.

If the $(n+1)$ impact between the system

and the rigid body occurs again at time $t = t_n$, on substituting $t = t_n$, and $\dot{\xi}^{(n)} = \dot{\xi}_0$ in (32) and (33), the velocity immediately before the $(n+1)$ th impact, $[\dot{\xi}_{-0}^{(n+1)}]$, can be easily derived in the form:

$$k_{-0}^{(n+1)} = e^{-\delta \omega t_n} \left[k_{+0}^{(n)} \cos \sqrt{1-\delta^2} \omega t_n - \frac{\delta \cdot k_{+0}^{(n)} + 1}{\sqrt{1-\delta^2}} \sin \sqrt{1-\delta^2} \omega t_n \right] \quad (34)$$

$$K_{-0}^{(n+1)} = \frac{\dot{\xi}_{-0}^{(n+1)}}{\omega \dot{\xi}_0}, \quad K_{+0}^{(n)} = \frac{\dot{\xi}_{+0}^{(n)}}{\omega \dot{\xi}_0}$$

We call $K_{-0}^{(n)}$ the coefficient of closing velocity of the n -th impact, and $K_{+0}^{(n)}$ the coefficient of restituting velocity of n -th impact. In (34), time t_n is the root of the equation.

$$1 = e^{-\delta \omega t_n} \left[\cos \sqrt{1-\delta^2} \omega t_n + \frac{K_{+0}^{(n)} + \delta}{\sqrt{1-\delta^2}} \sin \sqrt{1-\delta^2} \omega t_n \right] \quad (35)$$

Similarly, for $\delta = 1$, $K_{-0}^{(n+1)}$ is

$$K_{-0}^{(n+1)} = [K_{+0}^{(n)} - (K_{+0}^{(n)} + 1) \omega t_n] e^{-\omega t_n} \quad (36)$$

$$1 = [1 + (K_{+0}^{(n)} + 1) \omega t_n] e^{-\omega t_n} \quad (37)$$

For $\delta > 1$

$$K_{-0}^{(n+1)} = \frac{1}{2\sqrt{1-\delta^2}} \left[\left\{ (\delta + \sqrt{\delta^2-1}) K_{+0}^{(n)} + 1 \right\} e^{-(\delta + \sqrt{\delta^2-1}) \omega t_n} - \left\{ (\delta - \sqrt{\delta^2-1}) K_{+0}^{(n)} + 1 \right\} e^{-(\delta - \sqrt{\delta^2-1}) \omega t_n} \right] \quad (38)$$

$$1 = \frac{1}{2\sqrt{\delta^2-1}} \left[(K_{+0}^{(n)} + \delta + \sqrt{\delta^2-1}) e^{-(\delta - \sqrt{\delta^2-1}) \omega t_n} - (K_{+0}^{(n)} + \delta - \sqrt{\delta^2-1}) e^{-(\delta + \sqrt{\delta^2-1}) \omega t_n} \right] \quad (39)$$

Let α be the coefficient of restitution. Then the relation between the velocity immediately before and after the n -th impact is represented in the form:

$$\dot{\xi}_{+0}^{(n)} = -\alpha \dot{\xi}_{-0}^{(n)} \quad (40)$$

From (34)~(39), the velocity immediately before the $(n+1)$ th impact, $\dot{\xi}_{-0}^{(n+1)}$, and the

time interval between the n -th and the $(n+1)$ -th impact, t_n , as a function of the velocity immediately after the n -th impact, $\dot{\xi}_{+0}^{(n)}$, can be calculated and these results are shown in Figs. 2 and 3.

If the velocity of the vibratory system after the n -th impact is zero at time $t = t_n$, the displacement of the system at this time becomes maximum. For $\delta < 1$, therefore, the maximum displacement $\dot{\xi}_{max}^{(n)}$ of the vibratory system after the n -th impact is, from (32) and (33), given by

$$\frac{\dot{\xi}_{max}^{(n)}}{\dot{\xi}_0} = e^{-\delta \omega t_n} \left[\cos \sqrt{1-\delta^2} \omega \tau_n + \frac{K_{+0}^{(n)} + \delta}{\sqrt{1-\delta^2}} \sin \sqrt{1-\delta^2} \omega \tau_n \right] \quad (41)$$

$$\tan \sqrt{1-\delta^2} \omega \tau_n = \frac{\sqrt{1-\delta^2}}{\delta + 1/K_{+0}^{(n)}}$$

The relation between the restituting velocity $\dot{\xi}_{+0}^{(n)}$ and the maximum displacement $\dot{\xi}_{max}^{(n)}$ was calculated from (41) and is shown in Fig. 4.

If a vibratory system has been given the static displacement $\dot{\xi}_{st}$ and is initially at rest begins to move at $t=0$ and collides with a rigid body at $t=t_0$, the velocity $\dot{\xi}_{-0}^{(1)}$ im-

mediately before the first impact and the time t_0 can be easily derived, and these results are shown in Figs. 5 and 6.

From the above, if the coefficient of restitution is given, the chatter between a vibratory system of a single degree of freedom and a rigid body can be calculated. The velocity transition of the system immediately before or after impact is obtained from Figs. 2,

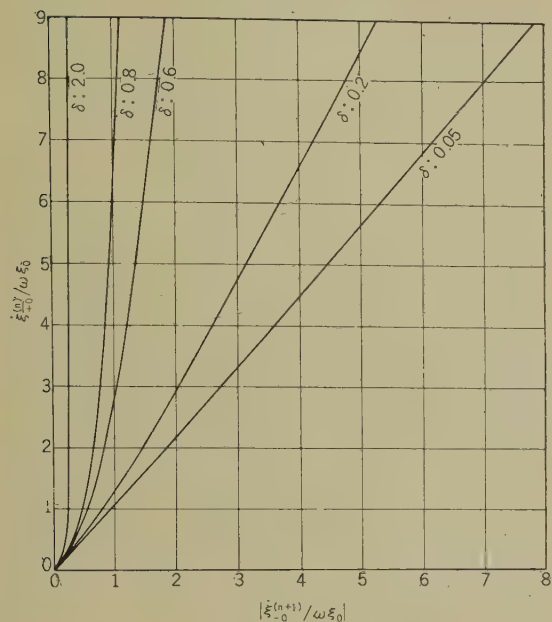


Fig. 2—Velocity relation in immediately after n th impact and before $(n+1)$ th impact.

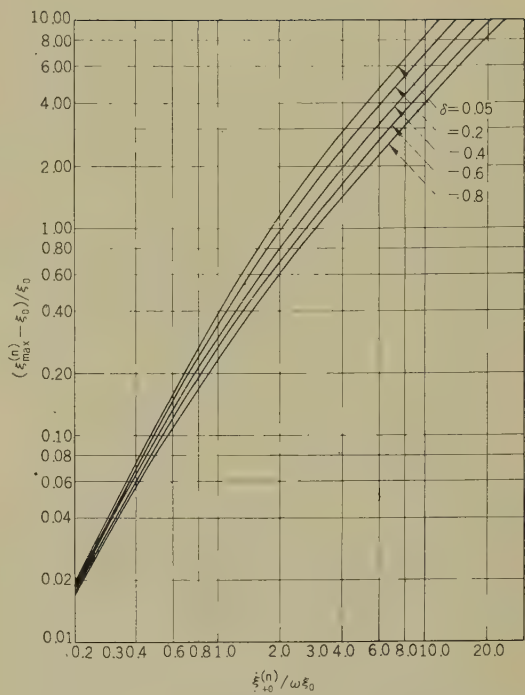


Fig. 4—Relation between velocity immediately after n th impact and maximum displacement.

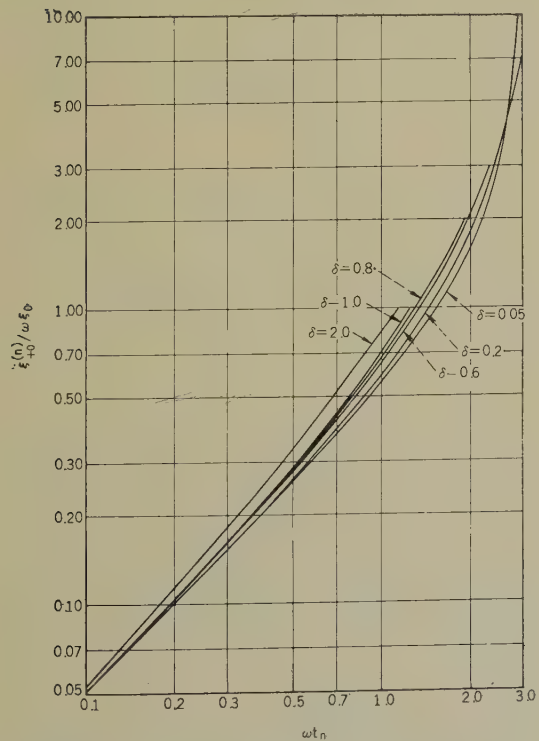


Fig. 3—Relation between velocity immediately after n th impact time interval from n th impact to $(n+1)$ th impact.

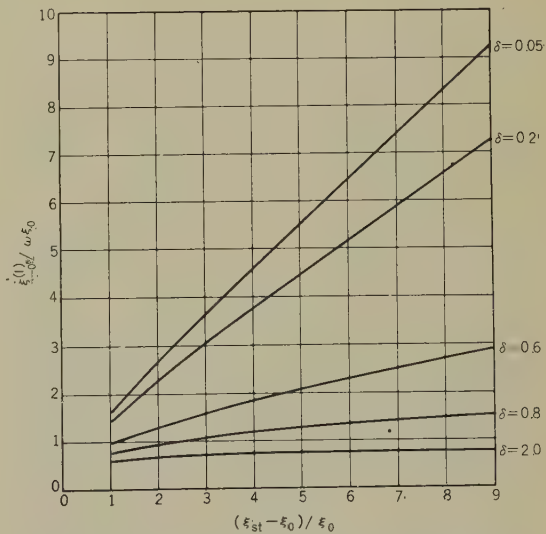


Fig. 5—Relation between initial displacement and velocity immediately before first impact.

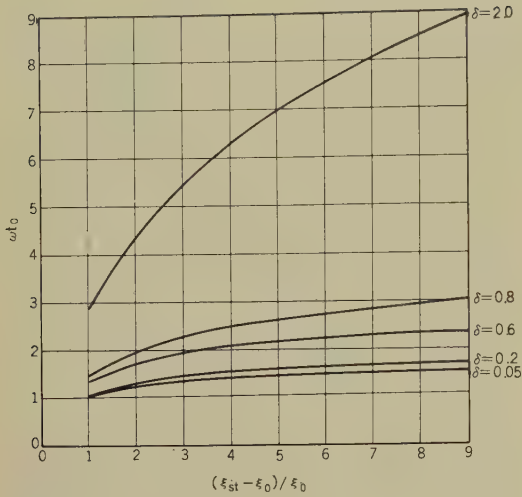


Fig. 6—Relation between initial displacement and time from beginning to move to immediately before first impact.

3, 5 and 6, and the maximum displacement transition is also calculated from Fig. 4. Determination of the velocity transition on impact and the maximum displacement transition after impact, it may be sufficient for the study of the chatter of relays.

3.3. Initial Conditions for Elastic Body

The initial conditions of the elastic body are required to compute the chatter as described in Section 2.3. We will consider here the following initial conditions for use in our study.

The elastic body is initially displaced by the elastic body by applying concentrated static force on its surface, and is kept at rest. Then, the concentrated static force is suddenly taken away, the elastic body begin to move, and then collides with its mating body. This condition is the ideal case of the contact spring in lift-off type relays. A general description of this condition is as follows.

When the concentrated static force p_0 acts on point Y on an elastic body, use of the normal function of body Ξ_m allows the distributed displacement of body ξ_{st} to be represented in form:

$$\xi_{st} = \sum_m \phi_m \Xi_m \quad (42)$$

From (42), the initial conditions in (9)~(13) can be written in the form:

$$\left. \begin{aligned} A_m^{(0)} &= I^{(0)} = 0 \\ -B_m^{(0)} &= \omega_m \phi_m. \end{aligned} \right\} \quad (43)$$

If ϕ_m in (43) is evaluated, the initial conditions of the elastic body can be obtained.

When an alternating force $p_0 e^{j\omega_c t}$ acts on an elastic body, in general the displacement of body, ξ_c , can be written in the form⁽¹³⁾:

$$\left. \begin{aligned} \xi_c &= \sum_m \frac{A_m}{\omega_m^2 - \omega_c^2} \cdot \Xi_m \cdot e^{j\omega_c t} \\ A_m &= \frac{1}{M} \iiint p_0 \cdot \Xi_m \cdot dV \end{aligned} \right\} \quad (44)$$

where V is the volume of the elastic body. When the concentrated static force p_0 acts on point Y on an elastic body, the static displacement of the body, ξ_{st} , is readily obtained in the following equation by making $\omega_c \rightarrow 0$ in (44).

$$\xi_{st} = \sum_m \frac{p_0 \Xi_{mY}}{M \omega_m^2} \cdot \Xi_m \quad (45)$$

where Ξ_{mY} is the value of Ξ_m at Y . Accordingly, from (42) and (45), ϕ_m is given by

$$\phi_m = \frac{p_0 \Xi_{mY}}{M \omega_m^2} \quad (46)$$

In many cases it is more convenient to represent the initial conditions of the contact spring of relays by the displacement of a point acted on by a static force. Let s_Y be the static stiffness of an elastic body at Y . $\xi_{st}(Y)$ be the initial displacement at Y . Then ϕ_m can also be represented by the following equation.

$$\phi_m = \frac{s_Y \cdot \xi_{st}(Y)}{M \omega_m^2} \Xi_{mY} \quad (47)$$

From the above, if ρ_0 or $\xi_{st}(Y)$ is given,

ϕ_m can be readily obtained and the chatter of the elastic body can be computed.

3.4. Determination of the Vibrating Constants of an Elastic Body

The ratios of the values of normal function $\Xi_{0mX} = \Xi_{mX} / \Xi_{1X}$, and the ratios of the natural angular frequencies $\Omega_m = \omega_m / \omega_1$ are necessary to compute the chatter of an elastic body as described in Section 2.3. We will consider here a method of determination of Ξ_{0mX} and Ω_m .

When the alternating force $Fe^{j\omega_c t}$ acts on point X on an elastic body which has no damping, the amplitude of the displacement of the body at Y , $|\xi_X(\omega_c)|$, is given by⁽¹³⁾

$$|\xi_X(\omega_c)| = \frac{F}{M} \left| \sum_m \frac{\Xi_{mX}^2}{\omega_m^2 - \omega_c^2} \right|. \quad (48)$$

In (48), the displacement for $\omega_c = 0$, that is, the static displacement $\xi_{st}(X)$ is approximately given by

$$\xi_{st}(X) \doteq \frac{F \cdot \Xi_{1X}^2}{M \cdot \omega_1^2}. \quad (49)$$

Hence, the ratio of displacement $|\xi_X(\omega_c) / \xi_{st}(X)|$ is

$$\left| \frac{\xi_X(\omega_c)}{\xi_{st}(X)} \right| \doteq \left| \sum_m \frac{\Xi_{0mX}^2}{\Omega_m^2 - \Omega_c^2} \right| \quad (50)$$

where

$$\Xi_{0mX} = \frac{\Xi_{mX}}{\Xi_{1X}} \quad (51)$$

$$\Omega_m = \frac{\omega_m}{\omega_1} \quad (52)$$

$$\Omega_c = \frac{\omega_c}{\omega_1}. \quad (53)$$

The ratios of the value of the normal function of an elastic body at a point acted on by the driving force, Ξ_{0mX} , and the ratios of the natural angular frequency Ω_m are evaluated by observation of the displacement-

frequency characteristics of the body from (50).

An actual elastic body is acted on by some damping force. The vibrating theory will be different according to the kind of damping. To simplify the theory, the damping force is assumed here to be proportional to the velocity of the body as described in (14). In this case the ratio of displacement is described, as in the case where no damping force acts, in the form:

$$\left| \frac{\xi_X(\omega_c)}{\xi_{st}(X)} \right| = \left| \sum_m \frac{\Xi_{0mX}^2}{\Omega_m^2 - \Omega_c^2 + 2j\delta_m \Omega_m \Omega_c} \right| \quad (54)$$

Accordingly, the ratio of the normal function Ξ_{0mX} , the ratio of the natural angular frequency, and the damping coefficient δ_m are determined from comparisons of the observed of displacement-frequency characteristics of the body and Eq. (54).

3.5. Calculation by Electronic Analog Computer

In this research, an electronic analog computer was used for the calculation of the chatter as described in Section 2. We will discuss here the method of calculation using the analog electronic computer. Where an elastic body acted on by damping force proportional to the velocity of the body as described in Section 2.4., collides with a rigid body, the displacement at X after the n -th impact, $\xi_X^{(n)}$, may also be represented in the form:

$$\xi_X^{(n)} = \sum_m \xi_{mX}^{(n)}. \quad (55)$$

where X is the coordinate of the contact of the elastic body, and $\xi_{mX}^{(n)}$ is the displacement component of m -th mode of vibration at X .

In (55), $\xi_X^{(n)}$ is the solution of the equation

$$\ddot{\xi}_{mX}^{(n)} + 2\omega_m \delta_m \dot{\xi}_{mX}^{(n)} + \omega_m^2 \xi_{mX}^{(n)} = 0. \quad (56)$$

The initial conditions in (56), that is, the conditions at the time the collision occurs

are given by

$$[\xi_{mX}^{(n)}]_{t=+0} = [\xi_{mX}^{(n-1)}]_{t=t_{n-1}} \quad (57)$$

$$[\dot{\xi}_{mX}^{(n)}]_{t=+0} = [\dot{\xi}_{mX}^{(n-1)}]_{t=t_{n-1}} - \frac{I^{(n)}}{M} \Xi_{mX}^2 \quad (58)$$

$$\frac{I^{(n)}}{M} = \frac{(1+\alpha)[\dot{\xi}_X^{(n-1)}]_{t=t_{n-1}}}{\sum_m \Xi_{mX}^2} \quad (59)$$

If the rigid body is displaced from the natural equilibrium point of the vibrating body in the direction that will cause it to push against the vibrating body, the time of the subsequent collision can be evaluated from the following equation:

$$[\xi_X^{(n-1)}]_{t=t_{n-1}} - \xi_0 = 0 \quad (60)$$

Eqs. (55)~(60) are given in forms that can be calculated on an electronic analog computer, but they may easily be shown to be identical to Eqs. (21)~(26).

The analog computer circuit which is used for studying vibration modes 1-4 by the equations given above, is shown in Fig. 7. The equivalent circuit of the circuit consisting of integrators (1)-(8), adders (5)-(8), and potentiometers (5)-(12) corresponds to Eq. (56) for $m \leq 4$. The output of adder (9) and the output of adder (11) correspond to the displacement and the velocity respectively of the vibrating body.

Adder (10) and the on-off device form a circuit to detect the time of the subsequent collision. Adder (10) is supplied with the output of adder (9), $\xi_X^{(n-1)}$, and the normal voltage corresponding to ξ_0 by potentiometer (13). The time when the output of adder (10) is zero corresponds to the time of the collision of the vibrating body, and at this time the on-off device operates to automatically stop the computation. The operation of adder (10) at this time corresponds to Eq. (58).

Since adders (1)-(4) compute Eq. (58),

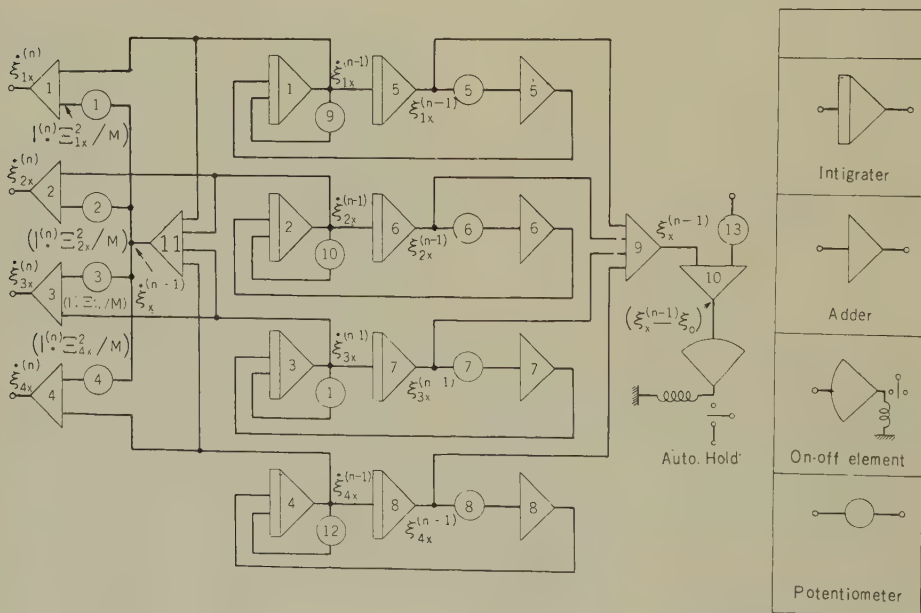


Fig. 7—Block diagram of the analog computer circuit used to calculate vibrations caused by collisions.

when the computer automatically stops, the outputs of the various adders correspond $[\dot{\xi}_{m,x}^{(n)}]_{t=+0}$.

If the outputs of integrators (5)–(8) and those of the adders (1)–(4) when the computation automatically stops are used as the initial conditions for the succeeding computation, and the outputs of adders (9) and (11) are registered, displacements and velocities of the collisions are obtained one after another.

4. Chatter of Vibratory Systems

As shown Section 2, collision between two elastic bodies produces higher-mode vibrations. Vibration with collisions shows a very complicated response, making it very difficult to know the true nature of chatter.

If it is possible to simplify vibration with collision and make it approach the response of a system with a single degree of freedom, the treatment is simple as it is sufficient to consider only the fundamental vibration components of the vibrating conditions before and after collision.

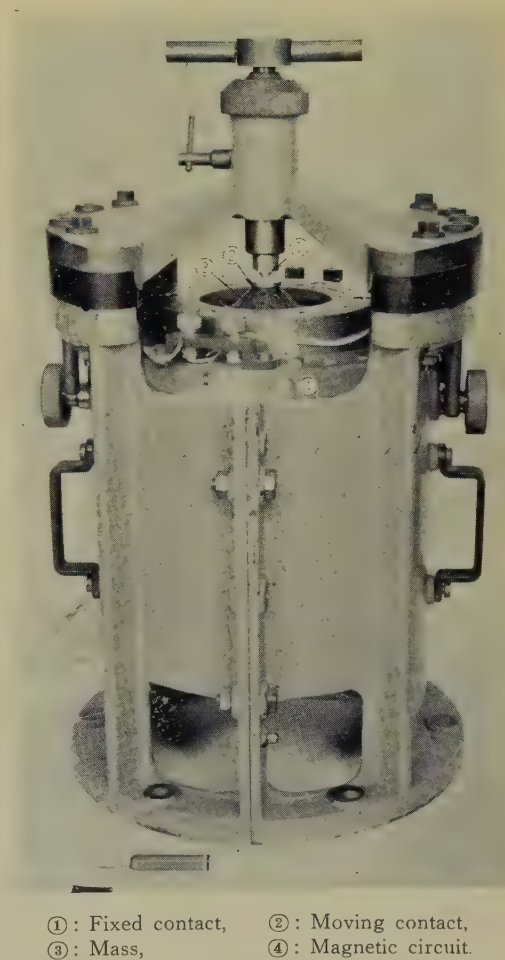
For such systems it becomes easy to study the effect of the vibration constants on chatter, the nature of the coefficients of restitution, and the conditions which lead to the cessation of chatter.

Furthermore, the rapid termination of the chatter which occurs when a relay operates causes a marked improvement in the operation of the relay. It is necessary to effectively dissipated the kinetic energy of the moving part to obtain this rapid termination of the chatter. An understanding of how the dissipation of the kinetic energy affects the chatter of a relay seems to be an effective means of studying the true nature of relay chatter. Therefore, a vibratory system having nearly a single degree of freedom which had provisions for varying the damping was experimentally constructed and the response of the system when it collided with a rigid body was measured. The physical quantities which control chatter and the conditions for the cessation of chatter was clarified by comparing the experimental and theoretical value.

4.1. Experimental Apparatus

4.1.1. General Description of the Experimental Apparatus

An overall photograph of the experimental apparatus for measuring the chatter of a vibratory system of a single degree of freedom is shown in Fig. 8, views of the vibratory portions of the apparatus are shown in Fig. 9, and a schematic diagram of this apparatus is shown in Fig. 10. The vibratory system is constructed of a massive body supported by two round, thin titanium diaphragms having



①: Fixed contact, ②: Moving contact,
③: Mass, ④: Magnetic circuit.

Fig. 8—Photograph of the experimental apparatus.

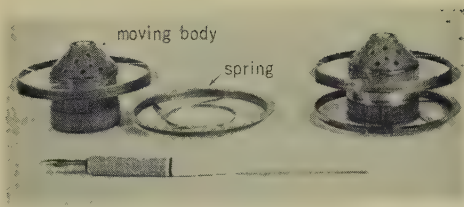


Fig. 9—Vibrating mass and diaphragms.

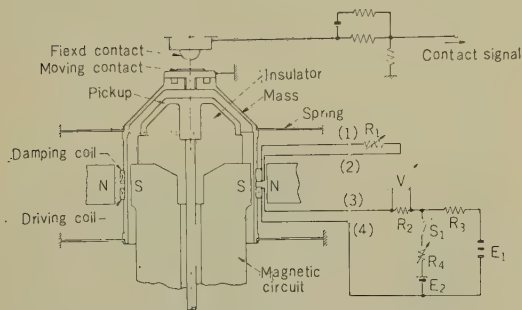


Fig. 10—Schematic diagram of the experimental apparatus.

the shape shown in Fig. 9. The massive body is made of phenolic resin, whose resistivity is very high, to reduce as much as possible the joule loss which would be present in a low resistivity body vibrating in a strong magnetic field. Damping and driving coils, which are located in the magnetic field, are also provided as shown in Figs. 8 and 10. The open circuit terminal voltage of the coils due to the vibratory system is proportional to the vibration velocity. When a variable resistor R_1 of known value is connected across the damping coil, the current flowing through the coil produces joule loss which damps the vibrations of the vibrating mass. By adjusting the value of resistor R_1 the damping constant of the vibratory system may easily be changed over a wide range. The damping coil is also used for measuring both the vibration velocity and the coefficients of restitution as well as for applying a variable damping force to the vibratory system.

The driving coil is used for giving the

ratio between the initial displacement and predeflection, ξ_{st}/ξ_0 . In this paper, the distance from the neutral of vibratory body to the fixed contact is called predeflection.

Small values of displacement are measured by coating the inner side of the conical part of the vibrating body in the region of the contact with conducting paint and then by amplifying and measuring the change in capacitance between this coating and a sensing plate. This pickup, which is shown in Fig. 10, is also used for measuring the displacement-frequency characteristics and the vibratory constants. Comparatively large values of displacement due to vibrations caused by collision were measured by focusing a parallel beam of light on the upper part of the vibrating part and then by measuring the amplified output signal of the photoelectric tubes which intercept the transmitted light.

To reduce the affects of the damping force of the air on the vibrating body, many small holes were drilled in the upper part of the body as shown in Fig. 9, and the damping coefficient of the vibrating body is very nearly that determined by the resistance in the damping coil circuit.

4.1.2. Experimental Procedure

The studies of the chatter of the vibratory system of a single degree of freedom was carried out in the following manner.

The fixed contact is adjusted to the desired point in contact with the moving contact. Then switch S_1 is closed, the contact point opens and the vibratory system comes to rest. Now, if switch S_1 is opened, the vibratory system begins to move, closing the contact points in a manner similar to those of a "lift-off" relay.

In this way, chatter was observed by varying the resistance in damping coil circuit, R_2 thus changing damping coefficient of the vibratory system.

When switch S_1 is opened, an electrical transient arises in the driving and damping coils. Actual measurements showed that it quickly damped out and disappeared within 1 msec even when the resistance in the

damping coil circuit was at its minium. The electrical transient phenomena immediately after opening switch S_1 may be neglected, as the measured value of the free vibration displacement conforms well with the calculated value. A 1 cm diameter hemispherical fixed contact and a flat moving contact were used in this section.

4.1.3. Vibration-System Constants

Five kinds of vibratory systems were experimentally manufactured to measure chatter. The measure values of the constants of these vibrations are as follows.

(a) Displacement frequency characteristics of vibratory system

The observed value of displacement frequency characteristics, when the damping coil is opened are shown in Fig. 11. As may be clearly seen from the figure, the natural frequency of the higher mode of these vibratory system is much higher than that of fundamental mode for all of the vibratory systems.

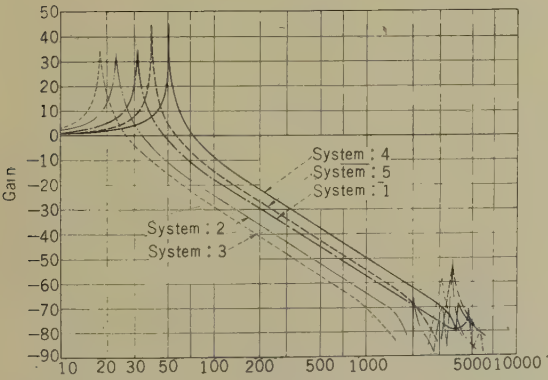


Fig. 11—Displacement frequency characteristics of vibration.

The ratio of how often higher modes occur is found to be very small in vibratory systems (1) and (4) and large in vibratory systems (2), (3), and (5). This affects the coefficient

of restitution very much, as will be later described.

(b) Damping constant

If the resistance R_s in the damping coil circuit is changed, the coefficient of restitution varies. The actually measured value of relation between the resistance R_s and damping constant δ in damping circuit of the vibratory systems is plotted in Fig. 12. The actually measured values, if R_s and δ are plotted on a logarithmic scale, can be approximated by a straight line having nearly 45° slope in the range $2 \geq \delta \geq 0.05$.

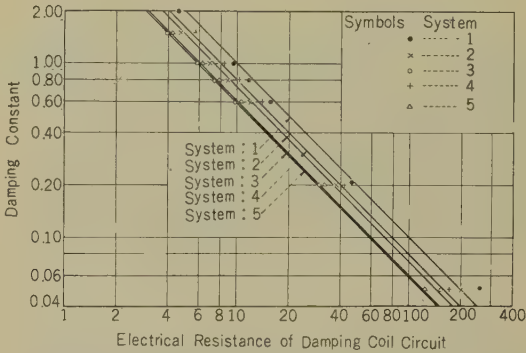


Fig. 12—Relation between the resistance in the damping coil circuit and the damping constant.

(c) Miscellaneous

Table 1 shows the resonance frequency, effective mass, and stiffness, of the vibratory system used in the experiment; and the force factor of the driving and damping coil. The velocity of vibratory system was obtained by measuring open voltage of the damping coil.

If the fixed contact shown in Fig. 10 is backed off, a current applied to the driving coil, and then switch S_1 is opened, the vibrating system will vibrate freely. If the damping coil circuit is open circuited, then the relation between the maximum voltage

Table 1
CONSTANTS OF THE VIBRATORY SYSTEM

| Vibratory system | Mass (gram) | Stiffness (dyne/cm) | Resonance frequency (c/s) | Force factor of damping coil (dyne/ab amp.) | Force factor of driving coil (dyne/ab amp.) |
|------------------|-------------|---------------------|---------------------------|---|---|
| 1 | 31.0 | 1.22×10^6 | 31.6 | 1.11×10^7 | 0.99×10^7 |
| 2 | 57.9 | 1.22×10^6 | 23.1 | 1.11×10^7 | 0.99×10^7 |
| 3 | 88.2 | 1.22×10^6 | 18.7 | 1.11×10^7 | 0.99×10^7 |
| 4 | 37.3 | 3.87×10^6 | 51.3 | 1.38×10^7 | 1.93×10^7 |
| 5 | 64.2 | 3.87×10^6 | 39.1 | 1.38×10^7 | 1.93×10^7 |

induced in the damping coil and the maximum velocity of the vibratory system, $\dot{\xi}_{f \max}$, is

$$\dot{\xi}_{f \max} = \frac{E_{\delta \max}}{A_{\delta}}$$

where A_{δ} is the force factor of the damping coil.

The maximum velocity $\dot{\xi}_{c \max}$, when the initial ξ_{st} , is given to the vibratory system, is*

$$\dot{\xi}_{c \max} = \omega \xi_{st}.$$

ξ_{st} and E_{δ} were actually measured and converted by using the force factor and resonance frequency shown in Table 1 into the maximum velocity, which is shown in Fig. 13. In the figure the solid curve shows $\dot{\xi}_{c \max}$ and the points the actually measured values, and it may be seen that they show good agreement with each other.

4.2. Coefficient of Restitution

As described in the previous section, the

* Strictly speaking; it is necessary to consider the effect of damping coefficient of vibratory system, but the damping coefficient, with damping coil open, may be neglected as it is extremely small, as shown in Fig. 11.

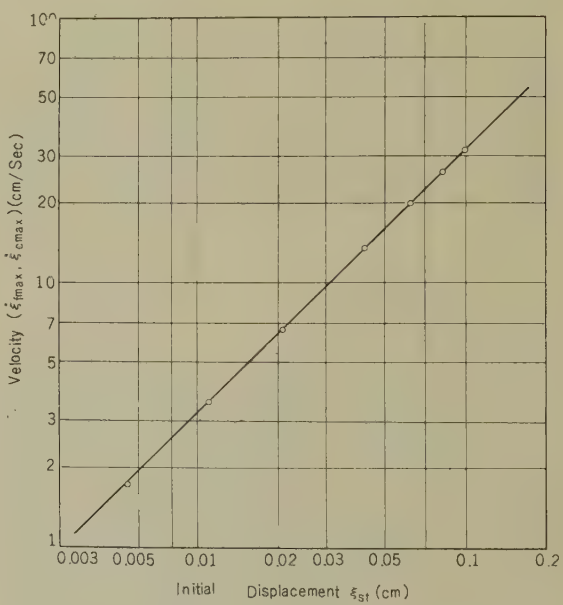


Fig. 13—Relation of $\dot{\xi}_{f \max}$ and $\dot{\xi}_{c \max}$ to ξ_{st} .
(points: $\dot{\xi}_{f \max}$, solid curves: $\dot{\xi}_{c \max}$)

constants of the vibratory system were evaluated from the measurements. If the coefficient of restitution is known, vibrations with collision will also be characterized. The following is the results of measurements of the coefficient of restitution actually measured when the vibratory system experimentally

manufactured collided with a fixed contact.

When a vibratory system with a single degree of freedom collides with a fixed contact, and the fixed contact is at a natural equilibrium point of system, the following equation can be derived from Eqs. (33) and (40).

When $\delta < 1$

$$\frac{\xi_{+0}^{(n)}}{\xi_{+0}^{(n-1)}} = \frac{\xi_{-0}^{(n+1)}}{\xi_{-0}^{(n)}} = \frac{\xi_{max}^{(n)}}{\xi_{max}^{(n-1)}} = \alpha e^{-\pi\delta/\sqrt{1-\delta^2}}, \quad (61)$$

Though the coefficient of restitution α was given by the ratio of the velocities immediately before and after collision, it is not easy to actually measure the velocity immediately after collision, as higher-mode vibrations are superimposed. If, however, the ratio of velocity immediately before the $(n+1)$ th and n -th collisions when the fixed contact is at the natural equilibrium point of the vibratory system, or the ratio of the maximum displacement after the n -th and $(n-1)$ th collisions is measured, it is possible to obtain an apparent coefficient of restitution for the n -th collision. The actually measured values of coefficient of restitution as described below were obtained by this method.

4.2.1. Effect of Higher Mode Vibration

Fig. 14 shows the observed values of coefficient of restitution when vibratory systems (1)–(5) having the constants shown in Table 1 collided with a fixed contact. As shown by the figure, the greater the velocity of a vibratory system immediately before collision,

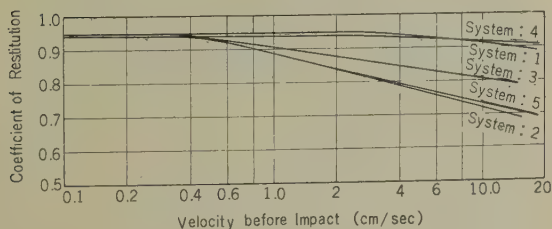


Fig. 14—Collision velocity and coefficient of restitution (observed).

the smaller the coefficient of restitution becomes.

The open circuit voltage-velocity curves of damping coil on the first collision of vibratory systems (1)–(3) is shown in Figs. 15~17. Fig. 15, (a) and (b) is for collisions of vibratory system (1) when the velocities before the collision are 0.21 and 4.2 cm/sec., respectively. If we compare them, the ratio, $\xi_{+0}(h)/\xi_{-0}$, between the higher mode vibration amplitude, $\xi_{+0}(h)$, and velocity immediately before collision, ξ_{-0} , is larger when the collision velocity is larger than when it is small, as may be seen by a comparison of Fig. 15 (a) and (b). And the higher mode vibration frequency of both is approximately 5.0 kc/s.

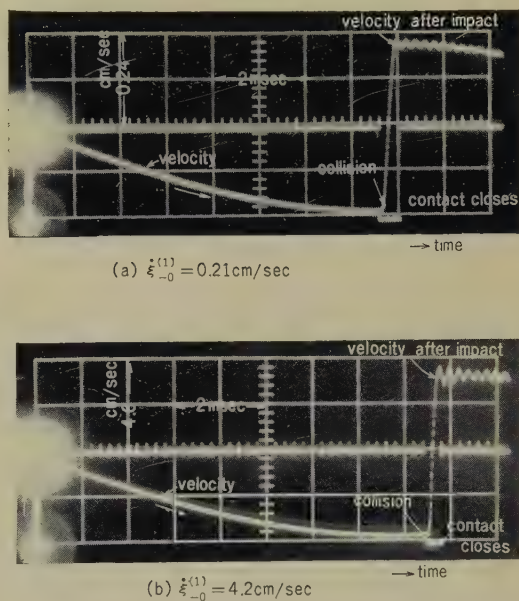


Fig. 15—Observed velocity of vibratory system-1 on its first collision.

Figs. 16 and 17 are for vibratory systems (2) and (3) where velocities immediately before collision are 6.9 and 7.3 cm/sec., respectively. $\xi_{+0}(h)/\xi_{-0}$ is larger than for vibratory system (1) and higher mode vibration frequencies are about 3.7 and 3.2 kc/sec. respectively.

If $\xi_{+0}(h)/\xi_{-0}$ is larger, the coefficient of

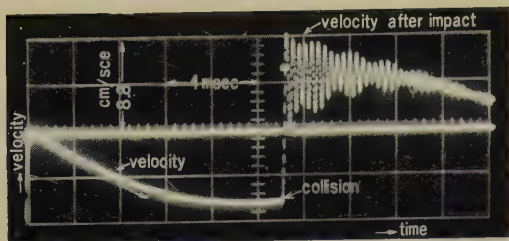


Fig. 16—Observed velocity vibratory system-2 on its first collision.
 $(\dot{\xi}_{-0}^{(1)} = 6.9 \text{ cm/sec.})$

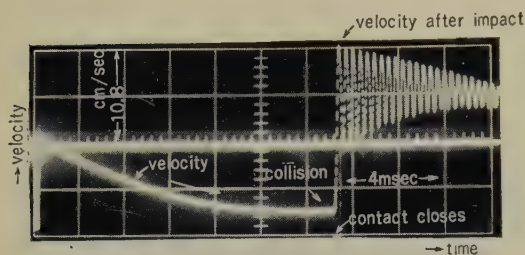


Fig. 17—Observed velocity vibratory system-3 on its first collision.
 $(\dot{\xi}_{-0}^{(1)} = 7.3 \text{ cm/sec.})$

restitution in Fig. 14 shows a small value. The higher mode vibration frequency, induced after collision, nearly conforms to that found in the displacement frequency characteristics of vibratory systems (1), (2), and (3) in Fig. 11.

In vibratory systems (2), (3), and (5), which are judged from the displacement-frequency characteristics shown in Fig. 11, to be much affected by higher mode vibrations, $\dot{\xi}_{+0}(h)/\dot{\xi}_{-0}$ becomes larger and the ratio of coefficient of restitution decreases remarkably as the velocity immediately before collision becomes larger as shown in Fig. 14.

In vibratory systems (1) and (4) which are judged, from the displacement-frequency characteristics, to be little affected by higher mode vibration, $\dot{\xi}_{+0}(h)/\dot{\xi}_{-0}$ does not increase so much as in the above systems even when collision velocity increases and the ratio of decrease in coefficient of restitution is small. Furthermore, in spite of the fact that the vibratory system is made of phenol resin in

this case, it shows an extremely high value of coefficient of restitution $\alpha \geq 0.9$ when the velocity immediately before collision is below 20 cm/sec.

From the foregoing, it will follow that the coefficients of restitution are extremely affected by higher mode vibration induced after collision. This naturally means that the vibrations after collision are assumed to have a single degree of freedom and the higher mode vibration components are considered as included in the coefficient of restitution, which is evaluated from Eq. (40).

As the higher mode vibrations nearly disappear until the following collision in the vibratory system used in this study, high vibration energy may be regarded as apparent loss energy and chatter may be studied by regarding the higher vibration energy in the coefficient of restitution as lost at the moment of collision. Accordingly, the equation indicating response given in with paragraph 3.1 for a vibratory system of a single degree of freedom repeated collisions is valid only when the higher vibration energy acts as loss energy as explained above.

Hemispherical gold-plated brass contacts with a radius of 0.5 cm and flat gold-plated brass contacts were used in this study.

4.2.2. Effect of Contact Material

To know how the coefficients restitution are affected by the contact materials, experiments were conducted using brass, copper, aluminium, and lead moving contacts.

The observed values of coefficients of restitution, when moving contacts of different materials but of the same mass, 5.3 grams, are fitted to the vibratory system (4) and made to collide with the fixed contact are shown in Fig. 18.

If flat moving contacts are made to collide with fixed contacts for the first time, the coefficients of restitution shows an extremely low value in the case of such soft materials as lead and the contacts suffer plastic deformation. As vibration energy is clearly used in plastic deformation in this case, the coefficient of restitution shows a low value.

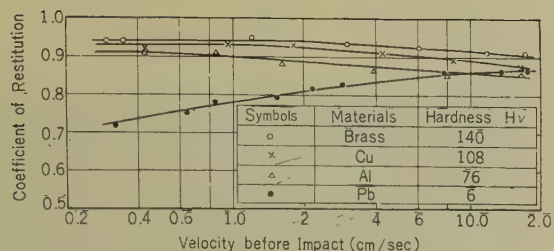


Fig. 18—Restitution coefficients and collision velocities of different metals (actually measured values).

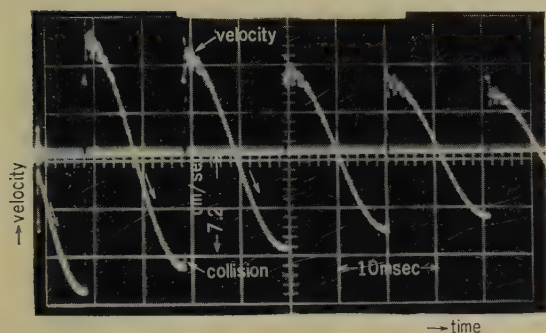


Fig. 19—Collision velocity curve of vibratory system when moving contacts are of Al (observed).
($\xi_{-0}^{(1)} = 10.3 \text{ cm/sec.}$)

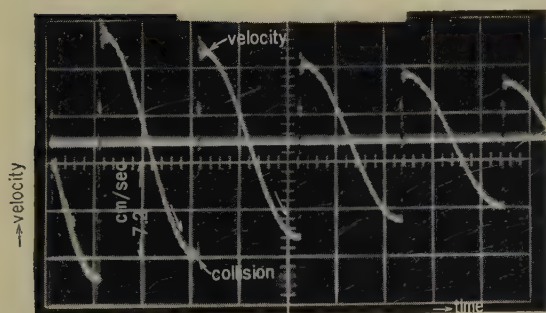


Fig. 20—Collision velocity curve of vibratory system when moving contacts are of lead (observed).
($\xi_{-0}^{(1)} = 10.3 \text{ cm/sec.}$)

If, however, they are repeatedly made to collide, the amount of plastic deformation decreases and the restitution coefficient gradually shows higher value, finally nearing a fixed value.

The coefficients of restitution shown in Fig. 18 are the values actually measured after over fifty repeated collisions at a collision velocity 25 cm/sec.

As seen from Fig. 18, the coefficients of restitution vary with the contact materials. With the brass, aluminium and lead used in the experiment, the higher the hardness of the materials, the higher the coefficients of restitution become.

The effect of the collision velocity upon the coefficients of restitution is shown in Fig. 18. The restitution coefficients of brass, copper, and aluminium decrease monotonically with increasing velocity; but on the contrary, that of lead decreases.

The observed velocities of the repeated collisions, when the moving contacts are made of aluminium or lead and the velocity immediately before the first collision is 10.3 cm/sec, are shown in Figs. 19 and 20, from which it will follow that a slight amount of higher mode vibration induced after collision is observed in each case. The amplitude of the higher mode vibration is a little larger with aluminium than with lead, but not conspicuous. Although higher mode vibration induced after collision does not vary much, an extremely low value of coefficient of restitution is shown, particularly with lead. There exists energy loss other than higher mode vibration on collision.

The hardness values shown in Fig. 18 for the contact materials is the value of hardness measured with a Vicker's hardness tester, using a load of 25 grams, after the restitution coefficients had been measured. In this experiment fixed contacts identical to those described in the preceding paragraph and flat gold-plated moving contacts were used.

4.3. Operating Time and Number of Contact Closures

While contact chatter is in progress, the

normal characteristics of a relay fail. Therefore the time from the beginning of a relay operation until the cessation of chatter; that is, the operating time, is an important factor in the determination of the operating speed of the relay. In this paper the operating time is multiplied by the natural angular frequency of the vibratory system and given as a dimensionless number. Also, the number of times the contacts open and close during operation, that is, the number of contact closures is an important factor upon which contact life depends.

Therefore, the above two factors, which are typical of the degradation of the characteristics of a relay due to chatter, will be considered hereafter.

Vibration with collision of a vibratory system of a single degree of freedom acted upon by damping force proportional to velocity is, as shown in paragraph 3.1, determined by the initial condition, ξ_{st} ; predeflection, ξ_0 ; damping coefficient, δ ; natural angular frequency, ω ; and coefficient of restitution α . Thus if the conditions for the cessation of chatter are evaluated, the operation time and the number of times the relay chatters can be estimated.

Here the conditions to end chatter are evaluated by comparing the values of operation time and the number of contact closures calculated by the method shown in paragraph 3.1 and the value actually measured.

There may be many ways of detecting the cessation of chatter, but it may be regarded as ended when the current flowing between the contacts reaches a steady state. Here, as shown in Fig. 10, the contact pulse is produced by the closure of a fixed and a moving contact which are at different potentials and recorded on an oscilloscope. The chatter is said to have caused when the signal from the contacts reaches a completely steady state.

In this experiment, the voltage between the contacts, when open, was 0.22 volts and current flowing in contact circuit, when closed, was 1.2×10^{-4} amperes.

The observed displacement curves and contact pulses for vibratory system (1) are shown

in Fig. 21, (a) and (b) respectively; $\xi_{st}/\xi_0=6$ (constant) and $\delta=0.05$ and 1.0.

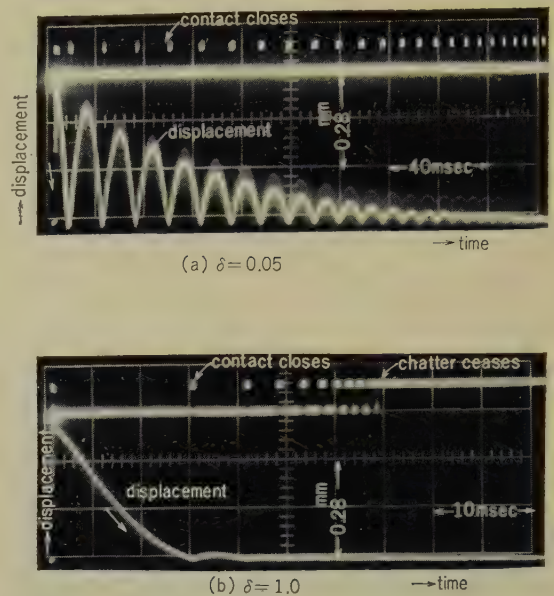


Fig. 21—Collision vibration displacement and contact pulse of vibratory system-1 (observed).
($\xi_{st}/\xi_0=6$)

As clearly seen from the displacement curve in Fig. 21 (a), the vibration with collision of the vibratory system can be regarded as being of a single degree of freedom. The interval between contact pulses becomes smaller with lapse of time. Particularly in Fig. 21 (b), nine contact pulses were observed but vibration ceased with the tenth pulse, at which time chatter is clearly found to have ended.

4.3.1. Results of Experiment

Typical examples of the operation time and the number of times chatter occurred actually measured within the experimental range shown in Table 2 using the five kinds of vibratory systems described in paragraph 4 are given in Fig. 22 and Fig. 23. In these figures, the points show the experimental values while the solid curves show the values

Table 2
RANGE OF EXPERIMENT

| Systems | 1 | 2 | 3 | 4 | 5 | Unit |
|---------------------------------|---|--------------------|--------------------|--------------------|--------------------|---------|
| Mass M | 31.0 | 57.5 | 88.2 | 37.3 | 64.2 | g |
| Stiffness s | 1.22×10^6 | 1.22×10^6 | 1.22×10^6 | 3.87×10^6 | 3.87×10^6 | dyne/cm |
| Natural Freq. | 31.6 | 2.31 | 18.7 | 51.3 | 39.1 | c/s |
| Damping Const. δ | 0.05~2 | 0.05~2 | 0.05~2 | 0.05~2 | 0.05~2 | — |
| Predeflection ξ_0 | 0.08~0.32 | 0.08~0.32 | 0.08~0.28 | 0.08~0.28 | 0.1 ~0.4 | mm |
| Initial Displacement ξ_{st} | 0.49~0.65 | 0.49~0.65 | 0.49~0.55 | 0.49~0.55 | 0.6 ~0.8 | mm |
| Moving Contact | Shape : Flat ; Material : Brass (except No. 4 of lead) | | | | | |
| Fixed Contact | Shape : Hemi-sphere of 1 cm diameter ; Material : Brass | | | | | |

calculated from $K_{-0}^{(n)} = \ddot{\xi}_{-0}^{(n)} / \omega \xi_0 \geq 0.05$ by the method shown in paragraph 3.1 using the measured values of coefficient of restitution from Fig. 14. These values show good agreement with each other. The upper part of each figure show the relation between the dimensionless operating time and the defined above damping coefficient while the lower part shows the relation between the number of contact closures and the damping coefficient. Both are represented with the value of ξ_{st} / ξ_0 as parameter.

The observed values of operating time and a number of contact closures are conspicuously affected by the coefficient of restitution when the damping coefficient is small, but the effect of coefficient of restitution becomes smaller as the damping coefficient becomes larger. That is, when the damping coefficient is small, operation time and the number of contact closures of vibratory system (5), which has a small coefficient of restitution as shown in Fig. 23, are distinctly smaller than those values in vibratory system (1) which has a larger coefficient of restitution

as shown in Fig. 22.

However, as the damping coefficient becomes larger, there is hardly any difference between the measured values of these vibratory systems.

This is because of the following facts. The coefficient of restitution, as stated above, represents the loss energy inclusive of higher mode vibration energy, and the damping coefficient represents the controlling force proportional to velocity. Both, however, belong to the same category in that they represent the dissipation of the collision vibration energy. When the damping coefficient is small, the vibration energy loss related to the coefficient of restitution predominates; but when the damping coefficient is large, the vibration energy loss related to the damping coefficient becomes predominant, and the effects of the coefficient of restitution are less likely to appear.

The relation between the damping coefficient and the operation time is that as the damping coefficient increases the operation time decreases, reaches its minimum value

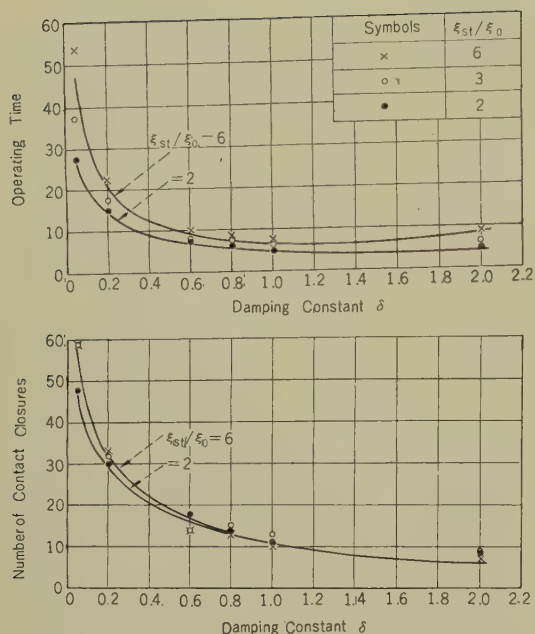


Fig. 22—Relation between operation time and number of contact closures to the damping coefficient, initial displacement, predeflection, and damping coefficient of vibratory system-1 (solid curves: calculated values; points: observed values)

at $\delta > 1.0$, and then increases.

The smaller the coefficient of restitution; that is, the larger the collision vibration energy loss, the more monotonically the number of contact closures decreases.

The contacts used in the experiment of Figs. 22 and 23 are the same as those in described in paragraph 4.2.1.

In paragraph 4.2.1 it is shown that the coefficient of restitution varies with the contact materials. Particularly with moving contacts of lead whose coefficient of restitution has a unique variation with change in collision velocity, the operation time and the number of contact closures were measured and are shown in Fig. 24.

In the figure, the points show the results actually measured, when vibratory system (4) was fitted with moving contacts of lead hav-

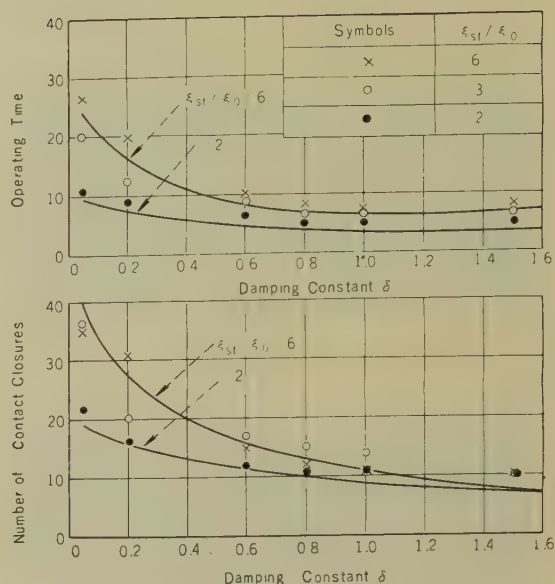


Fig. 23—Relation between operation time and number of contact closures to the damping coefficient, initial displacement, predeflection and damping coefficient of vibratory system-5 (solid curves: calculated values; points: observed values).

ing the same dimensions and shape as those described in 4.2.2, and the solid curves show the values calculated for the observed values of coefficient of restitution shown in Fig. 18 for the case of $K_{-0}^{(n)} \geq 0.05$. The calculated values and observed values of operation time and number of contact closures agree well with each other as in the case of brass contacts.

Judging from the fact that the experiments in which mass, stiffness, damping coefficients, initial displacement, predeflection, and contact materials were changed result in good agreement between calculated values and observed values, the following equation may generally be used the condition for the cessation of chatter when a vibratory system of nearly a single degree of freedom collides with fixed contacts,

$$K_{cr} = \frac{[\xi_{-0}]_{cr.}}{\omega \xi_0} \approx 0.05 \tag{62}$$

provided

- $[\xi_{-0}]_{cr.}$: Critical velocity immediately before collision
- $K_{cr.}$: Coefficient of critical closing velocity

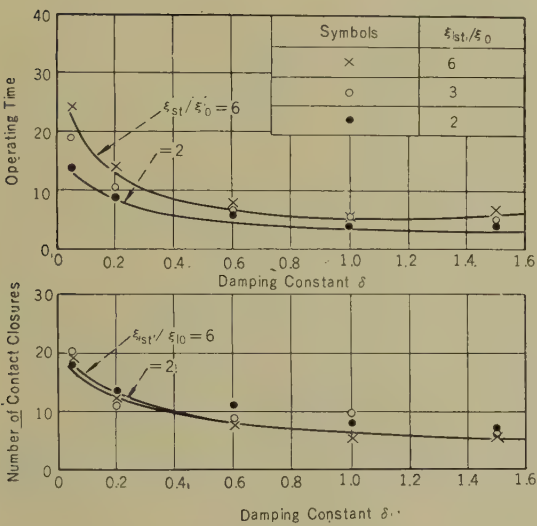


Fig. 24—Relation between operation time and number of contact closures to the damping coefficient, initial displacement, predeflection, and damping constant of vibratory system-1 (solid curves: calculated values, points: observed values).

When the collision velocity is very small, ($K_{-0}^{(n)} < 0.15$) the ratio of the time the contacts are closed to the time they are open becomes too big to be neglected, and the calculated operating time differs from the measured time. The duration of contact closures, however, will be extremely short. Therefore, the observed values of operating time shown in Figs. 22~24 will only be a little larger than the calculated values.

5. Chatter of Cantilever Spring

The response of the contact spring, that

is, the chatter caused in the operation of relays now in practical use, is very complicated. In the case of displacement of the contact spring after impact, so many higher modes of vibrations are superimposed that the maximum displacement after the n -th impact often becomes smaller than that after the $(n+1)$ th impact.

Accordingly, as shown in section 4, when the restitution of the n -th impact is obtained from the ratio of displacement after the $(n-1)$ th impact to that after the n -th impact, an irrational relation such as α (the restitution coefficient) > 1 is sometimes found. This irrationality comes from the ignorance of the fact that another impact takes place before the cessation of the higher modes of vibrations caused after impact. Therefore it can be avoided by taking the vibrations during the occurrence of impact into account.

For the purpose of analytical study on the vibration caused by contact spring impact, the "lift-off type" relay now in common use was chosen, and studies were made upon the vibration of a uniform cantilever caused by impact, because this was considered to be vibration of the most ideal form.

At first, the duration of contact closures of a uniform cantilever when it collides against a fixed contact, and the impact vibrations of two cantilevers of the same size and form, were measured. Then it was detected whether the fundamental formula for the impact vibration of an elastic body (shown in the Section 2) is reasonable or not.

Next, the response of a cantilever in the case of its impact against a fixed contact was calculated on an electronic analog computer, the calculated values were compared with the measured values, and the vibratory constant upon which the chatter of cantilever contact spring depends was obtained.

For the purpose of research on vibration due to impact, the response of the contact in direct relation to chatter was examined, and experiments were carried out on it by giving initial displacement $\xi_{st}(l)$ to the cantilever free end hung on the hook, under the initial conditions shown in the paragraph 3.3.

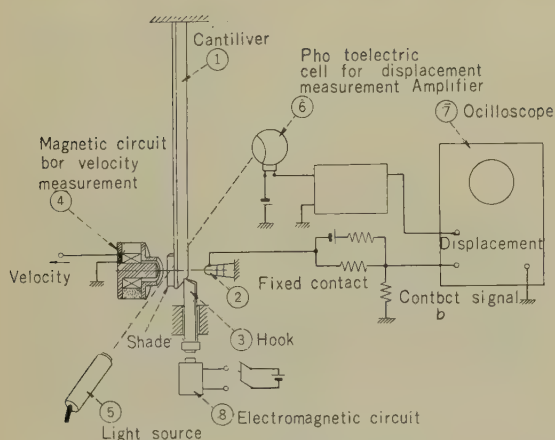
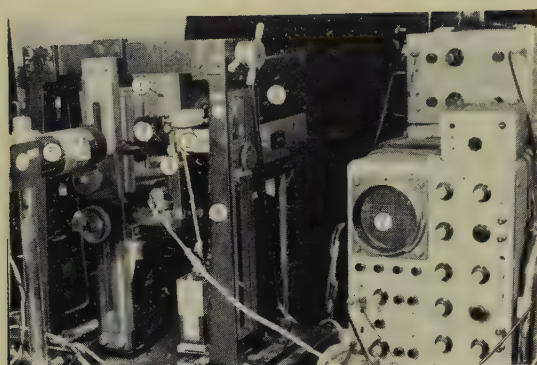


Fig. 25—Experimental equipment.

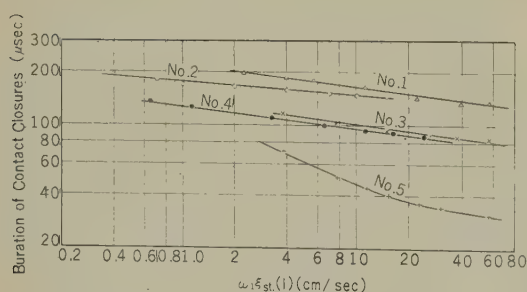


Fig. 26—Duration of contact closure and the initial displacement of the 1st impact of a uniform cantilever.

5.1. Duration of Contact Closure

The basic formula in Section 2 was derived on the assumption that the duration of contact closure at impact was much shorter than the vibration period. In order to find the upper limit of the modes of vibration of the uniform cantilever satisfying the condition shown above, the duration of contact closure at the first impact against a fixed contact of several types of uniform cantilevers were measured the duration of contact closure at the first of uniform cantilevers impact against a fixed contact were measured.

In this experiment, the impact point of the cantilever was 0.5 cm away from the free end, the fixed contact was located at the neutral of the cantilever, the initial conditions were those shown in paragraph 3.3, and the initial deflection $\xi_{st}(l)$ at the free end was changed to adjust the speed of the contact just before impact. In this way, the duration of contact was obtained.

In this case, 0.6 V was applied between the contacts, and the amplitude of the pulse caused by the contact closure at impact was observed with an oscilloscope. In this manner, the relation between the duration of contact closure and $\omega_1 \cdot \xi_{st}(l)$, where ω is the 1st natural angular frequency of the cantilever, was measured. The results are shown in Fig. 26. From the figure, within the range of this experiment, the vibratory period of a cantilever below the 3rd or 4th mode of vibration is found to be very much shorter than the duration of contact closure, which proves that the assumption from which the basic formula in Section 2 was derived is correct.

The fixed contact used in this experiment was a hemispherical brass contact with a radius of 0.3 cm whose contact part was plated with gold.

The dimensions, 1st natural frequencies, and materials of the cantilevers used to measure the duration of contact closure are shown in Table 3.

Table 3

DIMENSIONS OF CANTILEVERS USED FOR MEASURING THE DURATION CONTACT CLOSURE

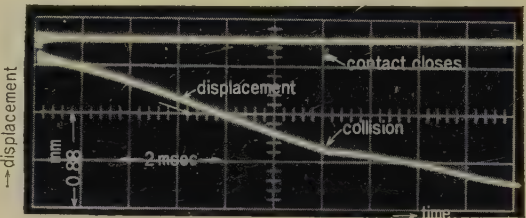
| Cantilever | Length (cm) | Width (cm) | Thickness (cm) | 1st natural frequency(c/s) | Material |
|------------|-------------|------------|----------------|----------------------------|----------|
| 1 | 5.5 | 2.0 | 0.05 | 90.3 | Brass |
| 2 | 13.0 | 2.0 | 0.05 | 16.1 | " |
| 3 | 9.5 | 2.0 | 0.10 | 60.2 | " |
| 4 | 14.5 | 2.0 | 0.10 | 25.9 | " |
| 5 | 9.5 | 0.8 | 0.10 | 61.0 | " |

5.2. Impact between Two Cantilevers with the Same Vibratory Constant

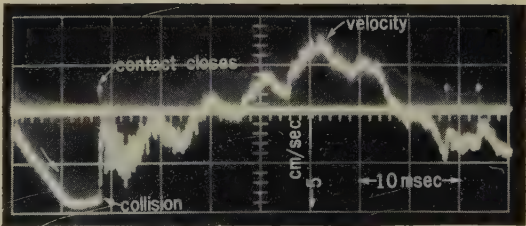
Suppose that two elastic bodies with the same vibratory constant collide against each other for the n -th time at the point of contacts X_i under the same conditions, and that elastic body (1) collides with the stationary elastic body (2) at any arbitrary velocity. Then, if the collision is perfect their velocity are exchanged as shown in the paragraph 2.5. and as a result, the vibration velocity of the point contact of elastic body (1) becomes zero immediately after the impact. In order to detect whether this relation is applicable to a real elastic body or not, measurement was carried out by using a uniform cantilever.

Two cantilevers of nearly the same dimensions, shape, and material faced each other; the free end of the cantilever (1) was given initial displacement, and it struck against cantilever (2) at rest. Then the vibratory displacement and the velocity of the point of contact of cantilever (1) were measured; some of these results are illustrated in Figs. 27 (a) and (b).

Fig. 27 (a) shows the displacement curves for the first impact of cantilever (1) together with the contact signals. As shown in this figure, the curve for the displacement at the impact is bent, while the tangential line for



(a) displacement of contact



(b) velocity of contact

Fig. 27—Contact response (measured value) at the impact of two cantilevers with the same vibratory constant (1st natural frequency: 23.8 c/s):

the displacement immediately after the impact is nearly horizontal. In other words, the velocity of the point of contact of cantilever (1) proves to be nearly zero immediately after the impact.

Fig. 27 (b) illustrates the vibratory velocity of cantilever (1) at its point of contact. As shown in this figure, the velocity is suddenly changed at impact and many higher modes of vibration are caused. In the case of the first impact, the velocity dropped nearly to zero. This seems suggestive of the coefficient of restitution appearing in Eq. (2.41).

Therefore, it has been clarified that when two elastic bodies with the same vibratory constant collide against each other they exchange velocity during impact, and as a result the basic formula in paragraph 2.5 is proved to be right.

Cantilevers (1) and (2) used in this experiment were made of brass and measured 16.2 cm in length, 1.2 cm in width, and 0.1 cm in thickness; their first natural frequencies are 23.8 c/s and 22.6 c/s respectively.

5.3. Chatter of Contact Spring

The contact response caused when the contact spring of a relay collides against a fixed contact was calculated on an electronic digital computer with the help of the basic formula shown in section 2. The results will be treated in this paragraph.

Young's modulus E , the cross-sectional area S , the cross-sectional radius of gyration R , and the density ρ of the contact spring being considered are uniform.

Besides, it is controlled by the following relations:

$$ESR^2 \frac{\partial^4 \xi_f}{\partial x^4} + S\rho \frac{\partial^2 \xi_f}{\partial t^2} = 0 \quad (63)$$

Boundary conditions:

$$\begin{aligned} \text{when } x=0 \quad & (\partial \xi_f) / (\partial x) = 0, \quad \xi_f = 0 \\ x=l \quad & (\partial^2 \xi_f) / (\partial x^2) = 0, \\ & (\partial^3 \xi_f) / (\partial x^3) = 0 \end{aligned}$$

where l = length of contact spring along the axis

x = direction of the axis

ξ_f = Free vibration displacement

If the contact spring collides against a fixed contact which is situated at its neutral position, then it is sufficient to apply the condition of Eq. (30) to the basic formula for the vibration caused by impact to make $i=1$ in Eqs. (9)–(12) correspond to the contact spring and to change Eq. (13) into

$$\sum \frac{B_{1m}^{(n)}}{\omega_{1m}} \mathcal{E}_{1mX1} = 0. \quad (64)$$

Hereafter, i will be omitted.

5.3.1. Initial Condition

The initial condition when the free end of the contact spring is loaded with a concentrated static load and the free end displacement $\xi_{st}(l)$ is given is obtained directly from Eq. (47).

As is well-known, the static stiffness s_l observed from the free end of the contact spring becomes

$$s_l = \frac{3ESR^2}{l^3}, \quad (65)$$

and the total mass M of the spring is

$$M = \rho Sl. \quad (66)$$

If Eq. (47) is rearranged after the substitution of Eqs. (65) and (66) into it, we obtain

$$\phi_m = V_{st} \cdot \frac{\omega_1}{\omega_m^2} \mathcal{E}_{ml}, \quad (67)$$

where

$$\omega_m = \frac{k_m^2 R}{l^2} \sqrt{\frac{E}{\rho}}$$

$$1 + \cos k_m \cdot \cosh k_m = 0$$

$$V_{st} = \frac{3\omega_1 \xi_{st}(l)}{k_1^4}$$

where Ξ_{ml} express the value of the m -th normal function at the free end of the contact spring.

In the following, Eqs.(43) and (67) are substituted into Eqs.(9) and (10), and the calculation is carried out under the condition $\phi_1=-1.0$.

5.3.2. Results of Calculation

The displacement and velocity of the contact were calculated for the cases when the free end of contact spring ($y_c=x/l=1$), the node of 2nd mode of vibration ($y_c=0.8$), and that of 3rd mode of vibration ($y_c=0.5$) were made to collide against a fixed contact. The calculation result is shown in Figs.28 through 30 inclusive.

In the case of these calculations, the time increase Δt was assumed to be $\Delta t=0.01/\omega_1$, taking into account the calculation time; the normal function Ξ_m was assumed to be $m\leq 3$, considering the memory capacity of the computer. Ξ_{mX} , $\Omega_m^*=f_m/f_1$, α , and $y_c=x/l$ are represented in Table 4; Ξ_{mX} showing the normal function at the contact used for this calculation, Ω_m the ratio of the first natural frequency to the m -th one, α the coefficient of restitution, and y_c the situation of the point of contact.

In Figs. 28 through 30, the upper columns, whose ordinates represent $\omega_1 \xi / V_{st}$ and abscissas $\omega_1 \Delta t$, show the relation between displacement and time length, the lower columns, whose ordinates similar. The lower columns show the relation between velocity and time length, where the ordinates represent $\dot{\xi} / V_{st}$ and the abscissa $\omega_1 \Delta t$. Each are represented without dimension. Accordingly, if ω_1 , the 1st natural angular frequency of the contact spring, and $\xi_{st}(l)$; the initial deflection at the free end; are given, the absolute values of the displacement and velocity developed with passage of time are obtained with ease.

Fig.28 shows the response caused by the impact of the free end of the contact spring. It is a very complicated response because the 1st-3rd vibration modes are super imposed.

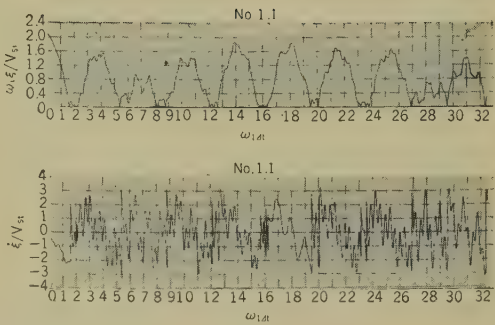


Fig. 28—Displacement and velocity (calculated values) of the free end of a cantilever spring at its impact against a fixed contact.

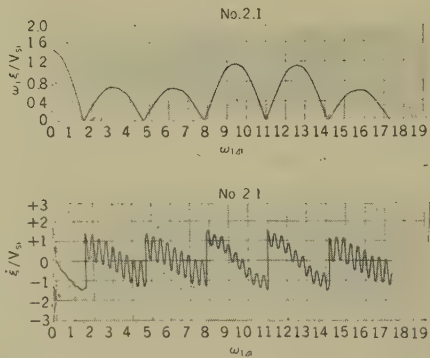


Fig. 29—Displacement and velocity (calculated values) of the node of the 2nd mode of vibration at the impact of a cantilever against a fixed contact.

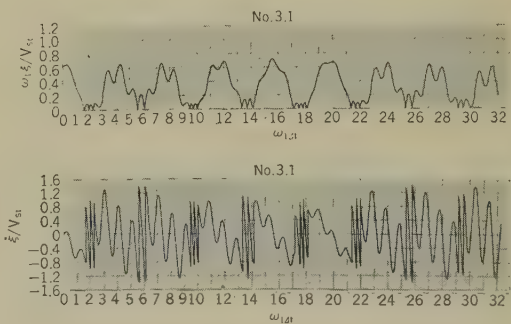


Fig. 30—Displacement and velocity (calculated values) of the node of the 3rd mode of vibration at the impact of a cantilever against a fixed contact.

* Ξ_{mX} , Ω_m , and y_c are quoted from reference (13).

Table 4

VIBRATORY CONSTANTS OF CONTACT SPRINGS USED IN THE CALCULATION

| Calculation example | ε_{1X} | ε_{2X} | ε_{3X} | Ω_1 | Ω_2 | Ω_3 | α | y_c |
|---------------------|--------------------|--------------------|--------------------|------------|------------|------------|----------|-------|
| No. 11 | -2.000 | 2.000 | -2.000 | 1.000 | 6.267 | 17.548 | 1.0 | 1.0 |
| No. 21 | -1.449 | 0.135 | 0.793 | 1.000 | 6.267 | 17.548 | 1.0 | 0.8 |
| No. 31 | -0.678 | -1.376 | -0.039 | 1.000 | 6.267 | 17.548 | 1.0 | 0.5 |

Fig. 29 illustrates response near the node of the 2nd mode of vibration ($y_c=0.8$). It is a response composed mainly of the 1st and 3rd vibration modes. In this case, the 2nd mode of vibration is scarcely caused, and so the ratio of the 1st natural angular frequency to the higher natural angular frequency nearest to it becomes $\Omega_3=17.547$.

It is higher than $\Omega_2=6.267$ at the free end. On the other hand, $|\varepsilon_{0mX}|$ at the free end is $|\varepsilon_{02X}|=|\varepsilon_{03X}|=1.0$, while that around the node of the 2nd mode of vibration is $|\varepsilon_{02X}|=0.093$, $|\varepsilon_{03X}|=0.547$. The latter is smaller than the former.

In other words, when Ω_m becomes larger and $|\varepsilon_{0mX}|$ smaller, the displacement curve should become simpler and becomes more like the curve for vibration caused by the impact of a vibratory system with a single degree of freedom.

The vibration caused by the impact around the node of the 2nd mode of vibration shows a fairly simple response, but the maximum displacement after impact does not always decrease, because higher modes of vibrations caused by previous impacts have completely ceased before a new impact occurs. This is represented by the calculated examples shown in Fig. 29.

Fig. 30 shows the calculated values for impact near the node of the 3rd mode of vibration $y_c=0.5$, when $\alpha=1$. Roughly speaking, in this case the response is composed of the 1st and 2nd modes of vibration, and the 3rd

mode of vibration does not appear.

This time, the normal function ratio $|\varepsilon_{02X}|=2.03$ is large compared with the ratio $|\varepsilon_{02X}|=1.0$ in the case of the free end of the cantilever. For this reason, even though little 3rd mode vibration appears, the displacement curves become complicated and show that the 2nd mode of vibration appears remarkably, repeats short impact vibration several times, and then has a strong repulsion.

In this calculated example, the vibration energy of the vibratory system during impact is fixed, but the maximum displacement or maximum speed after impact is larger than that before it, and the response is much varied by the condition of the impact point of the contact spring due to the difference of the normal function at the contact. This fact shows how much the chatter of a contacts spring is affected by the change of distribution of the energy of higher mode vibrations caused by impact.

5.4. Actual Chatter of Uniform Cantilever

As shown in the preceding paragraph, the chatter of the contact spring varies remarkably with the higher modes of vibrations occurring after impact, and quite a different response of displacement or velocity is often caused after impact, because of a small difference in the vibration condition before impact.

The higher modes of displacements are not so necessary to obtain an approximate solution scientifically good for the forced vibration of a common elastic body, because as shown by Eq. (44), it converges according to the order of ω_m^{-2} . For vibration caused by impact, however, the displacement of the higher mode of vibrations occurring after impact is nearly in reverse proportion to ω_m , and so even fairly high modes of vibrations must be considered as compared with the case of forced vibration.

Therefore, for the purpose of study of vibration caused by impact, it is necessary to obtain the vibratory constants of elastic body to a reasonably high mode.

Here in this paragraph, the vibratory constant is obtained by the method shown in paragraph 3.4; by using the constant, the vibration caused by collision of the contact of a uniform cantilever is calculated with an analog-type computer under the initial conditions given in paragraph 3.3, and the results are compared with the measured values.

The real characteristics of the damping force which acts on a uniform cantilever in practical use have not yet been brought to light. But by measurement, it has been found that the vibration mode of a cantilever near the natural frequency corresponds well to the natural function given in paragraph 2.4.

Here, on the assumption that a real cantilever is approximately represented by Eq. (14) and that its frequency-displacement characteristic is shown by Eq. (54), the vibratory constant to be used for the calculation of the

chatter to be discussed later is obtained by comparison between the measured values and Eq. (54).

When the driving points of cantilevers are shown by

$y_c=0.65, 0.78 \text{ and } 0.5,$

then the frequency-displacement characteristics at the driving points of the 1st to 4th modes of vibrations become as shown by Fig. 31. In addition, the normal function ratio Ξ_{0mX} obtained from the measured value of frequency-displacement characteristic shown in Fig. 31, the natural angular frequency ratio

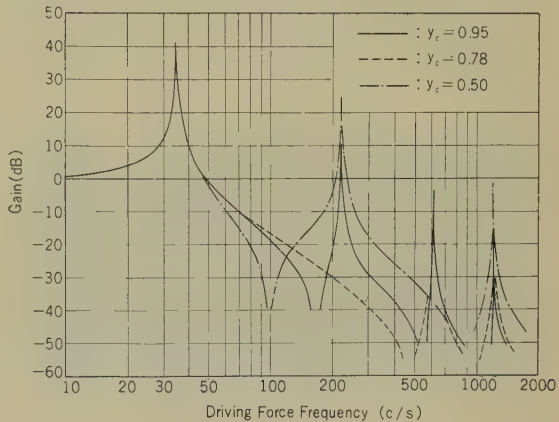


Fig. 31—Frequency-displacement characteristic of a uniform cantilever (measured values).

Table 5

VIBRATORY CONSTANTS (MEASURED VALUES) OF A UNIFORM CANTILEVER

| y_c | Ξ_{02X} | Ξ_{03X} | Ξ_{04X} | Ω_2 | Ω_3 | Ω_4 | δ_1 | δ_2 | δ_3 | δ_4 |
|-------|-------------|-------------|-------------|------------|------------|------------|------------|------------|------------|------------|
| 0.95 | -0.89 | 0.78 | -0.75 | 6.37 | 17.80 | 35.04 | 0.0041 | 0.0025 | 0.0015 | 0.0017 |
| 0.78 | 0.00 | -0.15 | 1.05 | — | 17.76 | 35.01 | 0.0042 | — | 0.0012 | 0.0019 |
| 0.50 | 2.15 | 0.00 | -2.20 | 6.35 | — | 35.04 | 0.0045 | 0.0027 | — | 0.0021 |

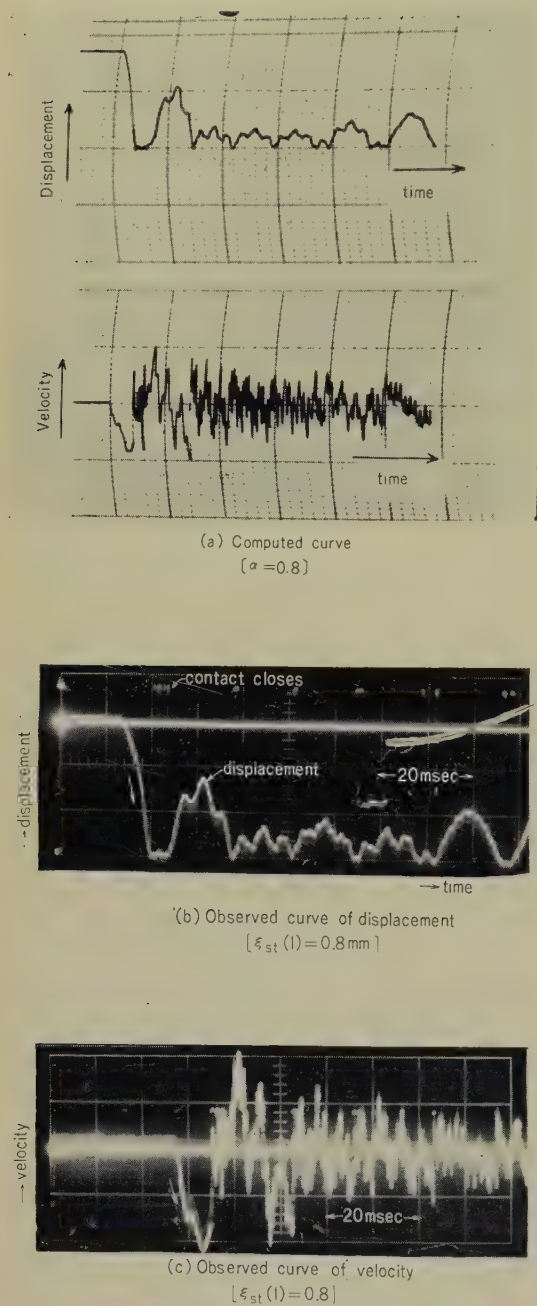


Fig. 32—Response of the free end of a uniform cantilever at the impact of a cantilever against a fixed contact ($y_c=0.95$, $\xi_0=0$).

Ω_m , and the damping constant δ_m^{ω} are shown in Table 5.

The calculated and measured values of the response for the case of the collision of a cantilever with the vibratory constant shown in Table 5, against a fixed contact are represented in Figs. 32–36.

Figs. 32–34 show the response when the point of contact of the cantilever is near the free end, $y_c=0.95$. In these figures, only the position of fixed points of contact are different

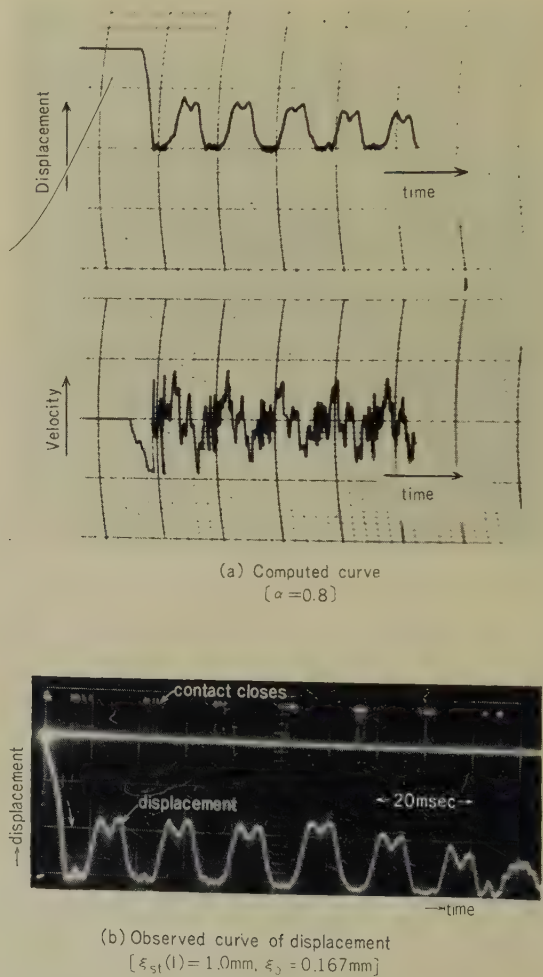
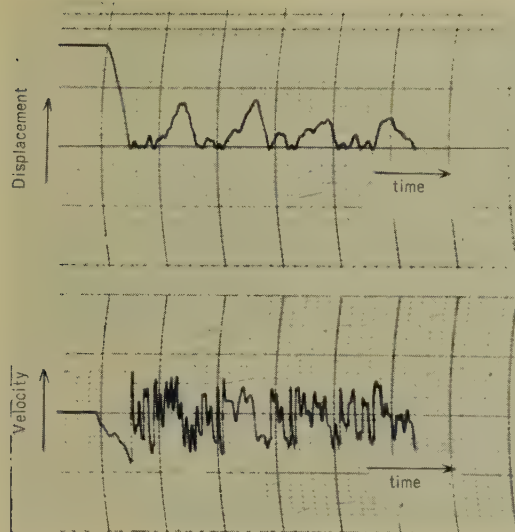
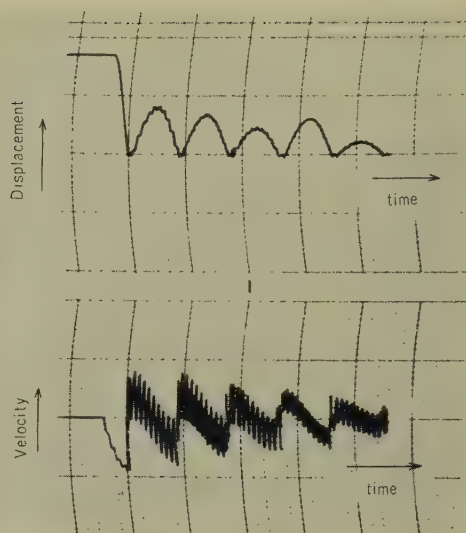


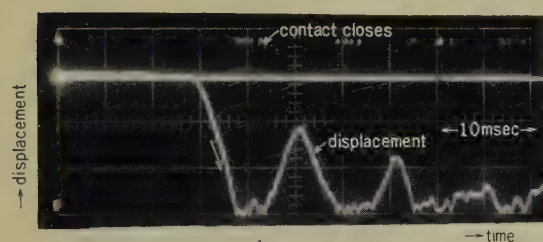
Fig. 33—Response of the free end of a uniform cantilever at the impact of a cantilever against a fixed contact ($y_c=0.95$, $\xi_{st}/\xi_0=6$).



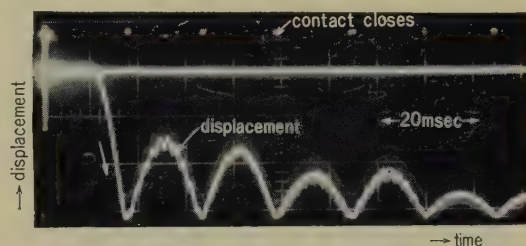
(a) Computed curve
[$\alpha = 0.85$]



(a) Computed curve
[$\alpha = 0.8$]



(b) Observed curve of displacement
[$\xi_{st}(l) = 1\text{ mm}$, $\xi_0 = 0.5\text{ mm}$]

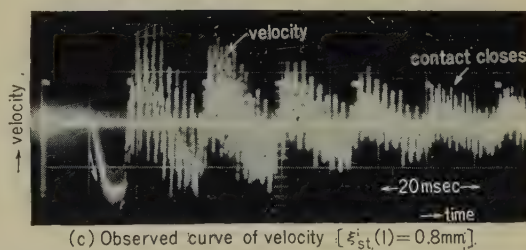


(b) Observed curve of displacement
[$\xi_{st}(l) = 0.8\text{ mm}$]

Fig. 34—Response of the free end of a uniform cantilever at the impact of a cantilever against a fixed contact ($y_c = 0.95$, $\xi_{st}/\xi_0 = 2$).

from each other, but the response are remarkably varied. This fact is essential for the consideration of the chatter of a relay. In research on the chatter of relays, consideration has long been made of contact pressure $s_X \cdot \xi_0$ (s_X : the static stiffness of elastic body observed from the contact),^{7), 25)} but actually, the chatter is controlled by ξ_0 .

Fig. 35 shows the response when the contact of a cantilever is at the node of 2nd mode of vibration, $y_c = 0.78$, and the natural contact is at the neutral position of the cantilever. The 3rd mode of vibration of the



(c) Observed curve of velocity [$\xi_{st}(l) = 0.8\text{ mm}$].

Fig. 35—Response of the node of the 2nd mode of vibration of a uniform cantilever at the impact of a cantilever against a fixed contact ($y_c = 0.78$, $\xi_0 = 0$).

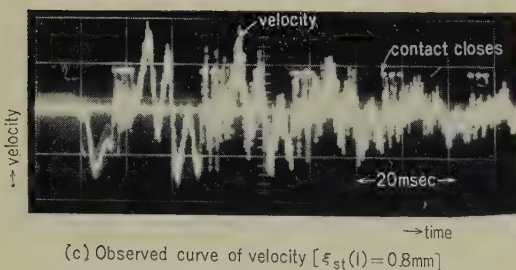
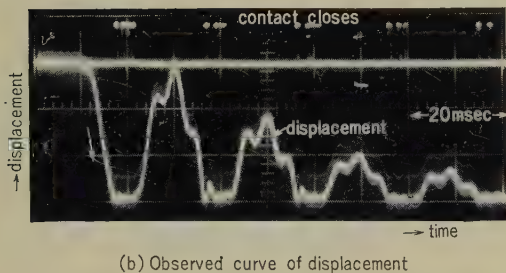
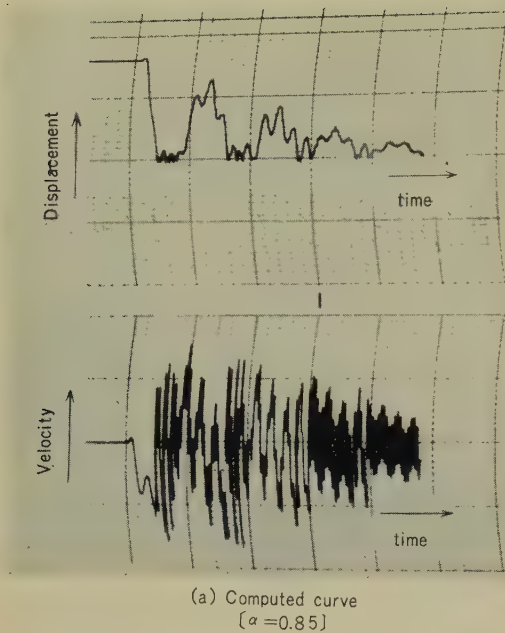


Fig. 36—Response of the node of the 3rd mode of vibration of a uniform cantilever at the impact of a cantilever against a fixed contact ($y_c=0.5$, $\xi_0=0$).

vibratory displacement in this case appears a little more remarkably than in example No. 2 of the calculated values given in the paragraph 5.3, but the response is simpler than at the free end, and resembles the vibration of a vibratory system with a single degree of freedom caused by impact.

Fig. 36 shows the response when the cantilever contact is at the node of the 3rd mode of vibration, $y_c=0.5$, and the fixed contact is at the neutral position of the cantilever. In this case, the difference between the calculated values here and the values of calculation example No. 3 in paragraph 5.3 is mainly due to the difference of coefficient of restitution.

The calculated values given above have been obtained by considering the vibrations to the 4th mode. Through comparison between the calculated and measured values, it has been found that the measured values of vibratory velocity show the occurrence of vibration of higher modes than the 4th, but that the calculated and measured values are in good correspondence. In the case of a cantilever, therefore, it is not necessary to consider the vibration of higher modes than the 4th, and it is permissible to discuss the chatter by considering these vibrations as included in the coefficient of restitution.

The coefficient of restitution used for the calculation is

$$0.8 \leq \alpha \leq 0.85.$$

As shown by the examples of measured values above, the maximum displacement or the maximum impact velocity of the contact after collision often becomes larger than before the collision, and so many higher modes of vibrations are superimposed that the coefficient of restitution is difficult to actually measure.

The coefficient of restitution in this case is varied by the higher mode vibration energy caused at collision (vibrations of modes higher than the 4th), as in the case of the single degree of freedom vibratory system shown in paragraph 4.2. And with the increase of the mode number of a given vibration, the coefficient of restitution naturally shows a higher value.

As a result of the above consideration, it has become clarified that the chatter of an elastic body can be expressed by the basic formula shown in the Section 2. Accordingly, the physical quantities which control the response of an elastic body when it collides with a fixed contact are Ξ_{0mX} , the normal function ratio at the contact; ξ_0 , the natural angular frequency ratio; ξ_{st}/ξ_0 , the ratio of the initial displacement to the predeflection; δ_m , the damping constant; and α , the coefficient of restitution.

The cantilever used in this experiment was a brass plate of: 18.0 cm length, 1.2 cm width, and 0.2 cm thickness with rectangular cross-section; the fixed contact used was a gold plated hemispherical brass contact with a radius 0.3 cm, and all the contacts of the cantilever used were gold plated.

6. Simplification of Chatter⁽²²⁾

As already mentioned, the vibration of a uniform cantilever caused by impact is so

movable contacts were flat. Their displacement and speed were measured in the same way shown in Section 5.

6.1. Chatter of Cantilever with Mass at Free End

The transverse vibration of a typical cantilever with mass at its free end is often represented by a differential equation such (63), and the boundary condition is shown by the following equations:

Boundary:

$$x=0, \quad \xi_f=0, \quad \frac{\partial \xi_f}{\partial x}=0, \quad x=l, \quad \frac{\partial^2 \xi_f}{\partial x^2}=0$$

$$ESR^2 \frac{\partial^3 \xi_f}{\partial x^3} = M_a \frac{\partial^2 \xi_f}{\partial t^2}$$

where M_a : Attached mass.

In this case, the normal function Ξ_m is as shown by

$$\Xi_m = \frac{u_m}{\sqrt{1 - \frac{2\beta}{1+\beta} \frac{\sin k_m \cdot \sinh k_m (1 + \cos k_m \cdot \cosh k_m)}{(\sin k_m + \sinh k_m)^2}}} \quad (68)$$

complicated that it cannot be treated with ease. But as is suggested in the collision of the node of 2nd mode vibration of uniform cantilever, if the normal function ratio Ξ_{0mX} at the contact is made smaller and the natural angular frequency ratio Ω_m is increased, then the response of these elastic bodies is expected to approach the single degree of freedom vibration. Besides, if the higher mode of vibration caused after impact is promptly stopped by a damping force, the chatter can probably be considered as in Section 4. To verify the assumptions mentioned above, cantilevers which simplify the vibration caused by impact were experimentally, and experimental and theoretical researches were made on their vibration caused at the collision against fixed contacts at their neutral position. The fixed contacts used in the experiments were hemispherical brass contacts 6 mm in diameter, and the

where

$$u_m = \left(\cos k_m \frac{x}{l} - \cosh k_m \frac{x}{l} - \frac{\cos k_m + \cosh k_m}{\sin k_m + \sinh k_m} \left(\sin k_m \frac{x}{l} - \sinh k_m \frac{x}{l} \right) \right)$$

In the above equation, the eigenvalue k_m is the root of the following equation.

$$\cos k_m \cdot \cosh k_m + 1 + \beta \cdot k_m (\cos k_m \cdot \sinh k_m - \sin k_m \cdot \cosh k_m) = 0 \quad (69)$$

where

$$\beta = \frac{M_a}{S \rho l}$$

Table 6
VIBRATORY CONSTANTS (MEASURED VALUES) OF A CANTILEVER
WITH MASS AT THE FREE END

| β | Ξ_{02X} | Ξ_{03X} | Ξ_{04X} | Ω_1 | Ω_2 | Ω_3 | δ_1 | δ_2 | δ_3 | δ_4 |
|---------|-------------|-------------|-------------|------------|------------|------------|------------|------------|------------|------------|
| 0.16 | -0.57 | 0.40 | -0.30 | 7.09 | 20.79 | 41.59 | 0.0026 | 0.0011 | 0.0011 | 0.0008 |
| 1.92 | -0.09 | 0.04 | — | 12.94 | 36.16 | — | 0.0041 | 0.0009 | 0.0007 | — |
| 8.32 | — | — | — | — | — | — | 0.0040 | — | — | — |

As shown by Eqs.(68) and (69) for a cantilever with mass at the free end, with increase of the mass ratio the normal function ratio Ξ_{0mi} becomes smaller and the natural angular frequency ratio Ω_m grows larger. Accordingly, when β becomes larger, the chatter should approach that for the case of a single degree of freedom vibratory system.

Subsequently, the response caused when the free end of the cantilever with mass collides with the fixed contact at the neutral position will be considered, under the initial conditions shown in paragraph 3.3.

The initial condition in this case is expressed in the same form as in the case of a uniform cantilever by substituting the following equation into Eq. (67).

$$V_{st} = \frac{3\omega_1 \xi_{st}(l)}{k_1^4(1+\beta)}. \tag{70}$$

From the values of the displacement-frequency character at the free end of the cantilever, measured under the conditions $\beta=0.13, 1.92,$ or $8.32,$ vibratory constants were obtained as shown in paragraph 6.4, and are shown in Table 6.

By using the vibratory constants in Table 6, the vibration of a cantilever caused by impact was calculated and the results are shown in Figs.37 through 39 together with the measured values.

As shown in Fig. 37, when $\beta=0.16,$ the response is very different from that caused

at the impact of the free end of the uniform cantilever ($\beta=0$) which is shown Figs. 48 and 32. When $\beta=0,$ the impact is repeated several times at short intervals after the first collision, and then a remarkable restitution occurs when $\beta=0.16,$ a remarkable 2nd mode of vibration appears after the first impact, and then the second collision occurs after the lapse of half a period of the fundamental mode of vibration.

Fig. 38 illustrates the response when $\beta=1.92.$ In this case, the velocity curves show 2nd mode of vibration slightly, but it can be regarded as a single degree of freedom vibration.

The calculated and measured shown values above are in good correspondence. In this case, the coefficient of restitution obtained by comparison between the calculated and measured values is as follows:

$$0.8 \leq \alpha \leq 0.9.$$

It has been experimentally verified for a cantilever with mass at the free end, that as the mass ratio β increases, the chatter in this case approaches the chatter in the case of single degree of freedom vibration, and that when $\beta \geq 2,$ the chatter can be treated as the chatter of the single degree of freedom vibratory system shown in the section. Most of the motions of armatures in relays now in use are considered to be those for the case of $\beta > 2.$ And so, when their restitution is discussed, the theory in Section 4 is

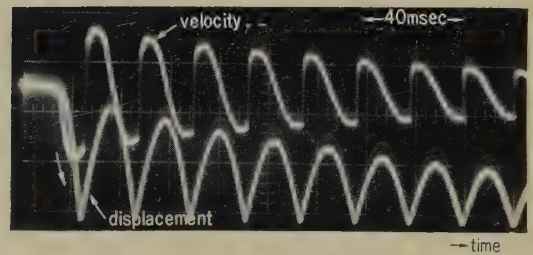
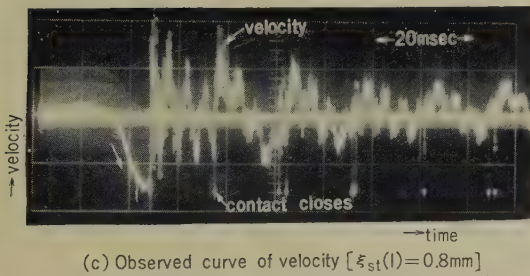
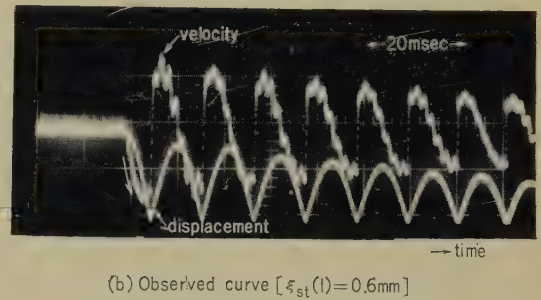
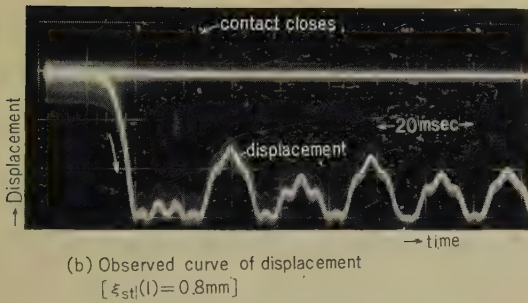
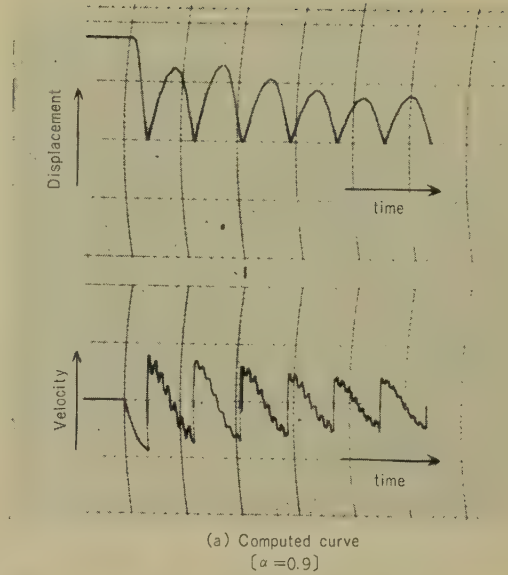
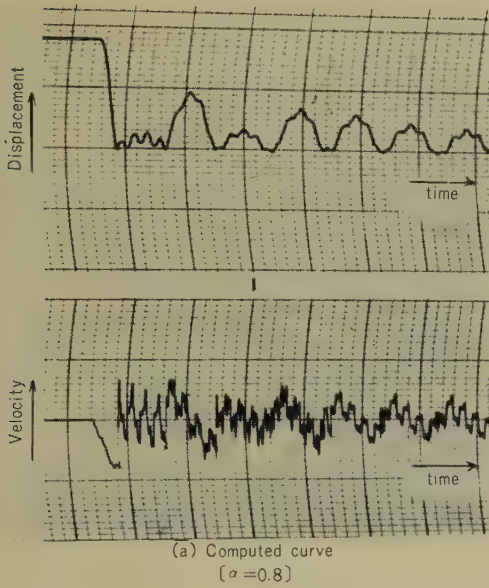


Fig. 37—Response of the free end of a uniform cantilever with mass at the free end in case of its impact against a fixed contact ($y_c=1$, $\beta=0.92$, $\xi_0=0$).

Fig. 39—Response (measured value) of the free end of a uniform cantilever with mass at the free end in the case of impact of a cantilever against a fixed contact ($y_c=1$, $\beta=8.32$, $\xi_{st}=0.6\text{ mm}$, $\xi_0=0$).

applied for convenience.

The vibratory systems used in the experiment treated in this paragraph, are as follows.

When $\beta=0.16$, aluminum bars of 16.3 cm length, 2.0 cm width, and 0.15 cm thickness with brass weights of 2.05 grams attached to the ends were used.

When $\beta=1.92$ and 8.32, aluminum bars of 9.75 cm length, 0.8 cm width, and 0.15 cm thickness with brass weights of 6.07 grams and 26.32 grams respectively attached to the ends were used similarly respectively. The contacts of their cantilever were the attached masses finished to be flat.

6.2. Chatter of Reinforced Cantilever

If the clamped end of cantilever is permitted to have angular displacement the frequency ratio of the cantilever, Ω_m is enlarged.⁽²⁴⁾

As a simple example, suppose that the transverse vibration is shown by the differential Eq. (63), and that the boundary condition is represented by the following equations.

Boundary condition:

$$\text{when } x=0, \quad \xi_f=0, \quad \frac{\partial \xi_f}{\partial x} = \gamma l \frac{\partial^2 \xi_f}{\partial x^2}$$

$$\text{when } x=l, \quad \frac{\partial^2 \xi_f}{\partial x^2}=0, \quad \frac{\partial^3 \xi_f}{\partial x^3}=0.$$

In this case, the normal function Ξ_m is

$$\Xi_m = \frac{u_m'''}{\sqrt{\frac{(\sin k_m + \sinh k_m)^2}{(\cos k_m \cdot \sinh k_m - \sin k_m \cdot \cosh k_m)^2} + \gamma}} \quad (71)$$

where

$$u_m'' = \left(\cos k_m \frac{x}{l} - \cosh k_m \frac{x}{l} \right) - \frac{\cos k_m + \cosh k_m}{\sin k_m + \sinh k_m} \left(\sin k_m \frac{x}{l} - \sinh k_m \frac{x}{l} \right)$$

$$- \frac{2\gamma k_m}{\sin k_m + \sinh k_m} \left(\sinh k_m \cdot \sin k_m \frac{x}{l} + \sin k_m \cdot \sinh k_m \frac{x}{l} \right).$$

The value of the eigenvalue k_m in the above equation is the root of the following equation.

$$\cos k_m \cdot \cosh k_m + 1 + \gamma k_m (\cos k_m \cdot \sinh k_m - \sin k_m \cdot \cosh k_m) = 0 \quad (72)$$

where γ shows the softness coefficient which represents the binding condition at the clamped end.

Eq. (72) is the same in form as the transcendental equation for a cantilever with mass at the free end. The initial condition in this case can be obtained by substituting the following into Eq. (67):

$$V_{st} = \frac{3\omega_1 \xi_{st}(l)}{k_1^4 (1+3\gamma)}. \quad (73)$$

The vibrating systems shown in Figs. 40 and 41, which are cantilevers satisfying the above conditions, were experimentally made. Most parts of these cantilevers are reinforced, being strong enough in bending endurance, and only the part near the clamped end, is not reinforced; therefore it is weak enough in bending endurance as compared with the reinforced parts. Accordingly, γ is large, and so Ω_m also becomes large. In the following, the response caused when the reinforced cantilever collides with a fixed contact at its neutral position will be considered.

The vibratory constants near the free end ($y_c=0.96$) and at the node of 2nd mode ($y_c=0.71$) of cantilever No. 1, and the vibratory constants near the free end ($y_c=0.95$) of cantilever No. 2 are shown in Table 7.

If the above measured values are compared with those for the uniform cantilever shown in Table 5, it is found that Ξ_{0mX} of the reinforced cantilever does not differ too much, but that its Ω_m is very large.

By using the vibratory constants shown in Table 7, the response of the cantilever collid-

Table 7

VIBRATORY CONSTANTS OF REINFORCED CANTILEVERS (MEASURED VALUES)

| Cantilever | y_c | ε_{02X} | ε_{03X} | Ω_2 | Ω_3 | δ_1 | δ_2 | δ_3 |
|------------|-------|---------------------|---------------------|------------|------------|------------|------------|------------|
| No. 1 | 0.96 | -0.95 | 0.78 | 23.07 | 61.47 | 0.0037 | 0.0029 | 0.0020 |
| No. 1 | 0.71 | 0.00 | 0.80 | — | 61.47 | 0.0040 | — | 0.0015 |
| No. 2 | 0.95 | -0.95 | 0.78 | 13.97 | 40.68 | 0.0031 | 0.0019 | 0.0024 |

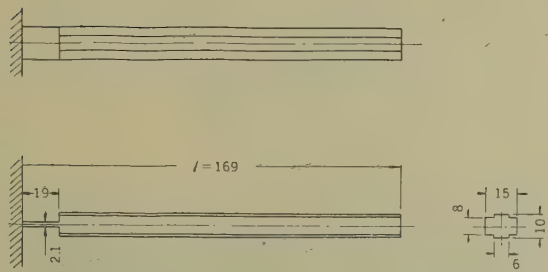


Fig. 40—Dimensions and shape of the reinforced cantilever No. 1 (unit: mm).

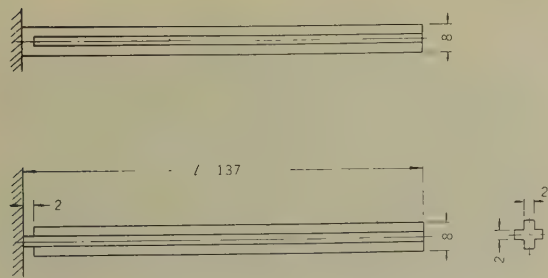
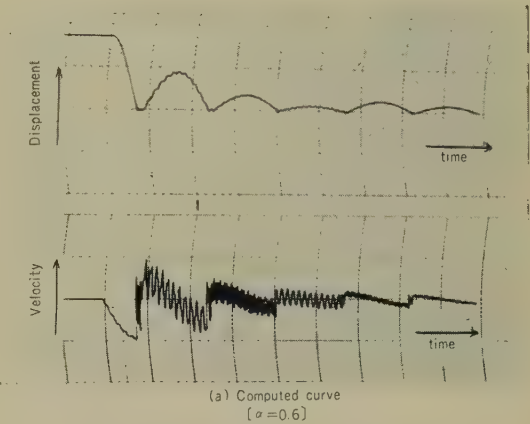
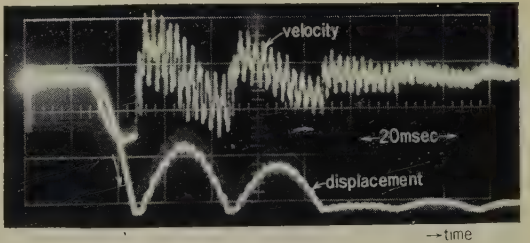


Fig. 41—Dimensions and shape of the reinforced cantilever No. 2 (unit: mm).



(a) Computed curve
[$\sigma = 0.6$]

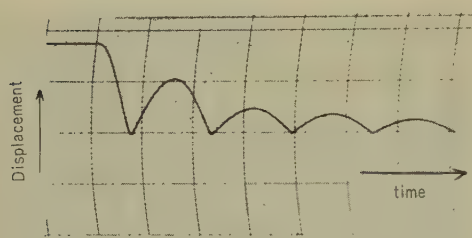


(b) Observed curve [$\xi_{st}(l) = 0.7$ mm]

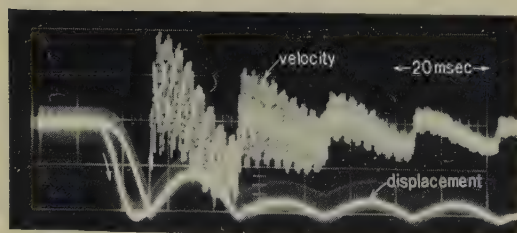
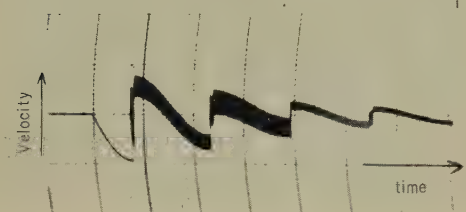
Fig. 42—Response of the free end of a reinforced cantilever at the impact of a cantilever against a fixed contact ($y_c = 0.96$, $\xi_0 = 0$).

ing with fixed contact was calculated, and the results are shown in Figs. 42~44 together with the measured ones.

Fig. 42 shows the values obtained near the free end of cantilever No. 1. At this time, the velocity curves show the combination of 1st and 2nd modes of vibration; while the displacement curves show that the degree of freedom of the response is about 1, although 2nd mode vibration of small amplitude is found. These responses are different from those in Section 4, in that they make remarkable restitution after repeating impact

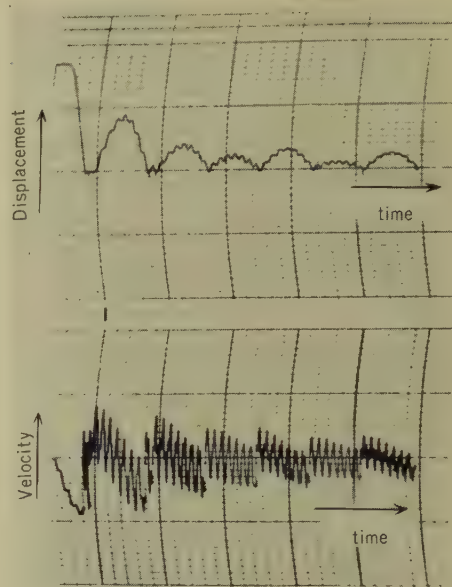


(a) Computed curve
[$\alpha = 0.6$]

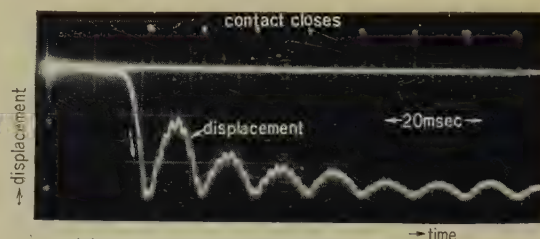


(b) Observed curve [$\xi_{st}(l) = 0.7\text{mm}$]

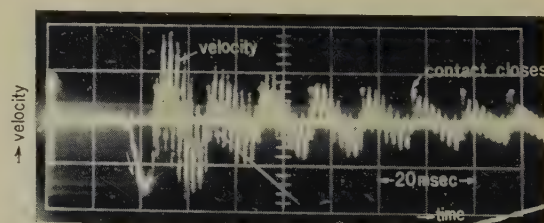
Fig. 43—Response of the node of the 2nd mode vibration of reinforced cantilever No. 1 at the impact of a cantilever against a fixed contact ($y_c = 0.71$, $\xi_0 = 0$).



(a) Computed curve
[$\alpha = 0.6$]



(b) Observed curve of displacement
[$\xi_{st}(l) = 0.8\text{mm}$]



(c) Observed curve of velocity

[$\xi_{st}(l) = 0.8\text{mm}$]

Fig. 44—Response of the free end of reinforced cantilever No. 2 at the impact of a cantilever against a fixed contact ($y_c = 0.95$, $\xi_0 = 0$).

Table 8

VIBRATORY CONSTANTS OF A COMPOUND CANTILEVER (MEASURED VALUES)

| y_c | E_{02X} | E_{03X} | E_{04X} | Ω_2 | Ω_3 | Ω_4 | δ_1 | δ_2 | δ_3 | δ_4 |
|-------|-----------|-----------|-----------|------------|------------|------------|------------|------------|------------|------------|
| 0.95 | -0.93 | 0.80 | -0.75 | 5.33 | 14.38 | 28.76 | 0.086 | 0.046 | 0.027 | 0.021 |
| 0.78 | 0.00 | -0.75 | 1.00 | — | 14.38 | 28.76 | 0.089 | — | 0.029 | 0.021 |

vibration a few times at very short intervals.

Fig. 43 shows the response obtained at the node of the 2nd mode of vibration of cantilever No. 1. In this case, the velocity curves show the combination mainly of 1st and 3rd mode vibrations, and the displacement curves show that the degree of freedom of the response is 1. As a result of comparison between the calculated values and measured values, it is found that the latter for the higher modes of vibrations caused after collision are somewhat larger.

Fig. 44 shows the response obtained near the free end of cantilever No. 2 ($y_c=0.95$). This response is nearly the same as that obtained at the node of the 2nd vibration mode shown in Fig. 35, because their frequency-displacement characteristics resemble each other. From this fact, it is found that if only the vibratory constants at the contacts are the same, cantilevers show the same response even if they have different dimensions and shapes.

6.3. Chatter of a Compound Cantilever

The rapid damping of the higher modes of vibrations by applying a damping force to the vibratory system is a good method to simplify the vibration caused by impact and to stop chatter rapidly.

Here in this paragraph, the chatter of a compound cantilever²⁶⁾ to which visco-elastic material is applied will be discussed.

As shown in Fig. 45, the cantilever used in this experiment is made of visco-elastic thermal-pressed polyisobutylene whose dimensions are: 17.5 cm length×2.0 cm width

×0.09 cm thickness; it is held between 2 sheets of brass whose dimension are 17.5 cm length×2.0 cm width×0.1 cm thickness.

In Table 8, are shown the vibratory constants near the free end ($y_c=0.95$) and at the node of 2nd mode vibration ($y_c=0.78$).

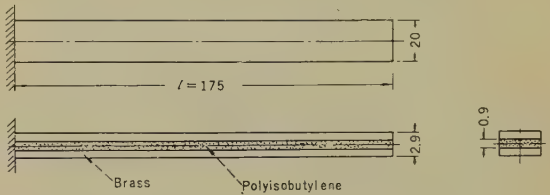


Fig. 45—Dimension and shape of a compound cantilever (unit: mm).

The frequency-displacement characteristics calculated from Eq. (54) for the vibratory constants in Table 8 have proved to correspond well to the measured values with an accuracy better than ± 1.5 dB within the measurement range. The damping force²²⁾ in this case is complicated, but it is permissible to represent the normal vibration of the compound cantilever approximately as shown in Eq. (54).

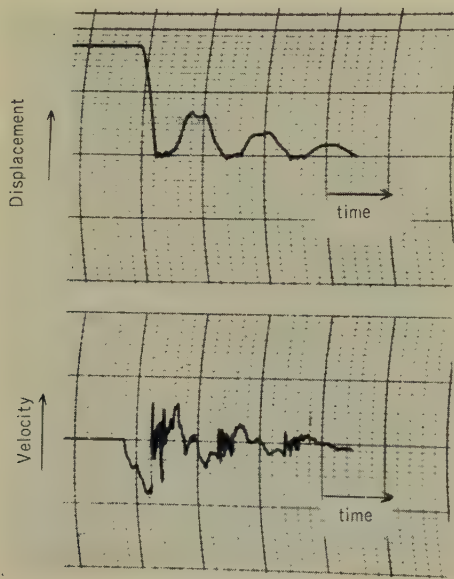
The vibratory constants of the compound cantilever given in Table 8 are a little smaller than those of the uniform cantilever given in Table 8, but E_{0mX} shows nearly the same value in either case. This is why the difference between the compound and the uniform cantilever is considered to be mainly due to damping force.

In Figs. 46 and 47 are shown the calculated and measured values of the response caused when the vicinity of the free end ($y_c=0.95$) and the node of 2nd mode vibration of the compound cantilever collide with a fixed contact at the neutral position of the cantilever.

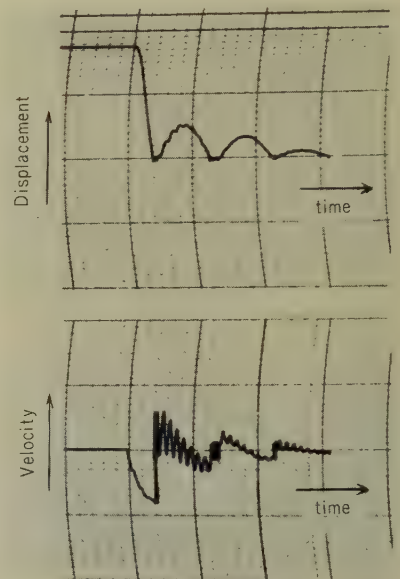
As seen from the measured values, in the case of chatter of the compound cantilever, less higher mode vibration is caused than in

the case of the chatter of a uniform cantilever, so it is sufficient to consider the 1st~4th mode vibration.

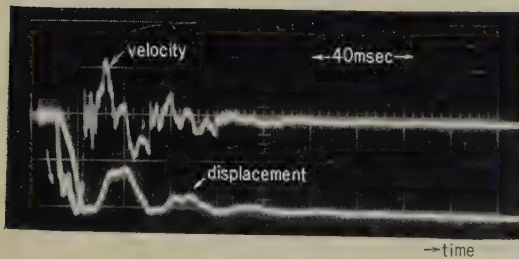
Concerning the compound cantilever, when another impact occurs after a remarkable restitution which follows an impact, the influence of the higher modes of vibrations is smaller and both the displacement curve and velocity curve are simpler than in the case of a uniform cantilever, because vibrations of



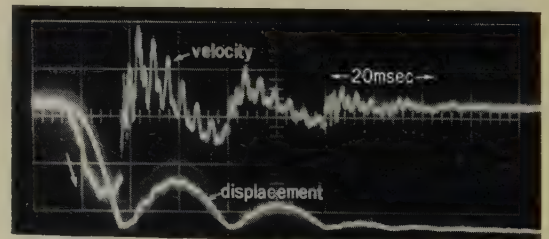
(a) Computed curve
[$\alpha=0.8$]



(a) Computed curve
[$\alpha=0.8$]



(b) Observed curve [$\xi_{st}(l)=0.8\text{mm}$]



(b) Observed curve [$\xi_{st}(l)=0.9\text{mm}$]

Fig. 46—Response of the free end of a compound cantilever at the impact of a cantilever against a fixed contact ($y_c=0.95$, $\xi_0=0$).

Fig. 47—Response of the node of the 2nd mode vibration of a compound cantilever at the impact against a fixed contact ($y_c=0.78$, $\xi_0=0$).

modes higher than the 2nd have been extinguished.

7. Prevention of Contact Chatter

In the lift-off type wire-spring relay now in practical use, as a make contact closes, the moving contact spring is moving with the actuating card or armature. Therefore, the velocity of the spring is fixed by the operating speed desired. Here, for the purpose of obtaining design data for the contact spring which is used to prevent contact chatter, the relation between the closing velocity of contact spring and contact chatter will be measured, and the conditions required of the contact spring will be considered.

In Section 4, it has been shown that the condition for which contact chatter ceases when a simple vibratory system collides with a fixed contact is $K_{cr} = 0.05$.

For the cantilever contact spring now in practical use in the wire spring relay, the existence of closing velocity of contact sufficient to prevent contact chatter has been confirmed experimentally and the critical closing velocity at which such a contact spring can be realized has been obtained. As a result, however, it has proved still insufficient for improving the speed of the relay.

In the following, a new type of contact spring good enough to improve the rapidity of relay and to prevent contact chatter will be discussed; and furthermore, design methods will be given.

7.1. Method of Experiment

Fig. 48 shows the outline of the experimental apparatus which was used to measure the number of contact closures (n) and chattering time (T)* by changing the dimension of contact spring and the contact velocity $\xi_{-0}^{(1)}$ immediately before the 1st impact.

* This means the time length from the 1st impact until the end of contact chatter. It is represented by the measured value multiplied by the 1st natural frequency ω_1 , which results in a dimensionless quantity.

As shown in this figure, vibratory system 4 in Section 4 is equipped with a hook upon which a contact spring is hung. Next, the driving coil is supplied with current by closing the switch S , and the contact spring is displaced downward together with the hook to open the contact. Subsequently, if S is opened, the current provided is turned off, and the moving contact approaches the fixed contact together with the hook. When the contact is closed, the contact spring is separated from the hook, and operates the lift-off type movement. The hook and the vibratory system serve nearly the same purpose as the relay card and armature.

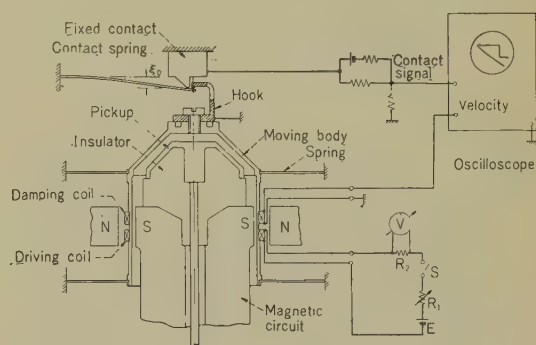


Fig. 48—Semischematic diagram of the experimental set up of experimental equipment.

In this case, if the open circuit voltage of the damping coil is observed on an oscilloscope when the contact is closed, $\xi_{-0}^{(1)}$ is obtained, while the number of contact closures and the chattering time† can be measured simultaneously from the contact signal in a manner similar to that described in Section 4.

The velocity immediately before impact was adjusted by changing the current flowing through the driving coil.

When the current supplied to the driving coil is turned off, voltage is induced in the

† "Chattering time" means the length of the period of time from the 1st impact until the end of chatter.

damping coil, as described in Section 4, but this electrical transient vanishes within 400μ sec. Within the range of experiments reported in this paper, the make of the contact occurs more than 2–3 msec after the current is turned off, and so the error in the measurement of the velocity due to this transient can be ignored.

About 10 msec after the contact is closed and the contact spring is separated from the hook, the hook comes back, it touches the contact spring again, and the contact opens. But the interval between contact signals is so short that chattering time up to 5–6 msec can be measured with ease. The condition of contact signal circuit is the same as that described in Section 4.

7.2. Critical Closing Velocity of a Cantilever Spring

As mentioned above, the chattering time T_b and the number of contact closures n_b were measured by changing the velocity of the contact spring immediately before impact ξ_{-0} , and some results are given in Fig. 49. In this figure, $K_b = \xi_{-0} / \omega_{b1} \xi_0$ (where ω_{b1} : the 1st natural angular frequency of cantilever) is abscissa, while T_b or n_b to the ordinate; the dots show measured values and the solid curves roughly represent their mean values. From the figure, it is found that when K_b is below $K_{b, cr.}$, contact chatter never occurs but when above $K_{b, cr.}$, n_b and T_b increase together. Even when the dimensions of the contact spring or the position of the contact was changed, nearly the same tendency was shown, and the value of $K_{b, cr.}$ was almost the same. Then, the dimensions of contact spring was changed as shown in Table 9 and by the method described above, the critical closing velocity $[\xi_{-0}]_{b, cr.}$ below which contact chatter never occurs, was measured, and from the measured value, $K_{b, cr.} = [\xi_{-0}]_{b, cr.} / \omega_{b1} \xi_0$ was calculated. This $K_{b, cr.}$ plotted against predeflection ξ_0 is illustrated in Fig. 50. In the figure, the measured values are somewhat different, but as shown in Fig. 50, n_b does not increase by over 2 or 3, even when K_b

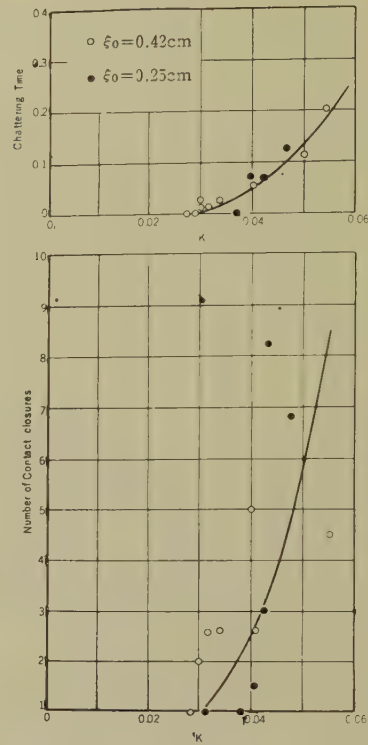


Fig. 49—Number of chatter closures, chattering time and closing velocity (measured values) ($d=0.05$ cm, $y_c=0.97$, material: german silver).

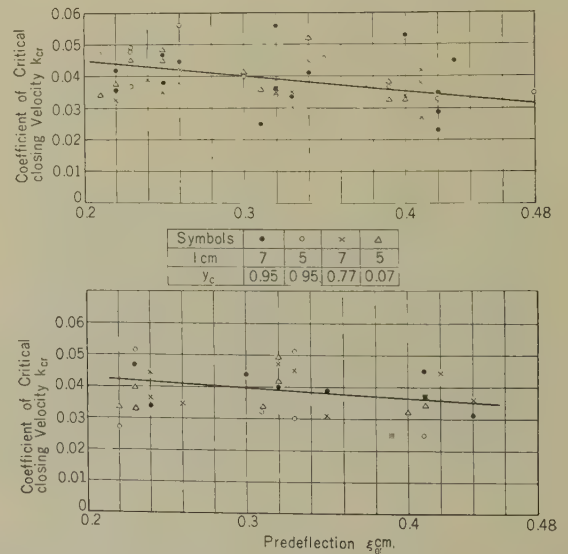


Fig. 50—Coefficient of critical closing velocity of cantilever spring.

becomes larger than $K_{b, cr.}$ by 0.01. Even when the dimensions or the material of the cantilever contact spring is changed, the following relation is permissible:

$$K_{b, cr.} \approx 0.04 \quad (74)$$

This value is about the same as the coefficient of critical closing velocity $K_{cr.}$ of simple vibratory systems.

In this manner, the condition $K_{b, cr.}$ under which contact chatter of the cantilever spring is never caused has been obtained, and so it is permissible to estimate the realizable upper limit of the velocity below which contact chatter never occurs.

For a uniform circular cantilever contact spring, when the contact is at a distance x_c from the clamped end of the spring, the realizable upper limit $[\dot{\xi}_0]_{max}$ of the predeflection is as follows:

$$[\dot{\xi}_0]_{max} = \frac{2l^2 \sigma_a y_c^2}{3Ed} \quad (75)$$

Accordingly, the realizable upper limit of closing velocity $[\dot{\xi}_{-0}]_{b, cr, max}$ below which the chatter never occurs, is shown by

$$[\dot{\xi}_{-0}]_{b, cr, max} = \frac{\sigma_a K_{b1}^2 K_{b, cr.} y_c^2}{6 \sqrt{E\rho}} \quad (76)$$

where $k_{b1}=1.8751$: 1st eigenvalue of cantilever

σ_a : Allowable stress of spring
 $y_c = x_c/l$

As seen from Eq. (76), $[\dot{\xi}_{-0}]_{b, cr, max}$ is obtainable if the material constant is given. For instance, for German silver, the material of contact springs now in practical use, if $E=1.5 \times 10^4 \text{ kg/mm}^2$, $\rho=8.48 \text{ kg/cm}^3$, $\sigma_a=30 \text{ kg/mm}^2$, $K_{b, cr.}=0.04$ and $y_c=1$ (the contact being at the free end of contact spring),

$$[\dot{\xi}_{-0}]_{b, cr, max} = 20.6 \text{ cm/sec} \quad (77)$$

7.3. Torsional Contact Spring

For the speed-up of a relay, it is necessary to increase the speed of the armature. There-

fore it is desirable to design a contact spring without contact chatter in spite of the large value of $\dot{\xi}_{-0}$. The speed of armatures of relays now in actual use is 30–40 cm/sec. As described in the preceding paragraph, improving the spring material is the only method of improving the critical closing speed $[\dot{\xi}_{-0}]_{cr, max}$. As shown by Eq. (77), so long as the spring material now in use is adopted, contact chatter cannot be completely prevented.

Next we shall discuss the torsional contact spring, a new type contact spring, to which spring material now in use is applied and whose $[\dot{\xi}_{-0}]_{cr, max}$ becomes larger.

This type of contact spring, as shown in Fig. 51, has one end fixed, while the other end is bent at a right angles. The rotating portion is supported with a bearing; l_1 is the section with torsional vibration and l_2 is the section with transverse vibration.

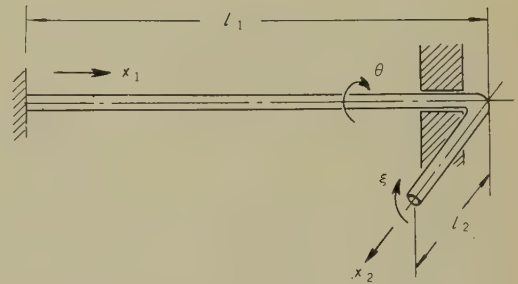


Fig. 51—Model of a torsional contact spring.

In this case, the torsional vibration of section l_1 is shown as

$$\frac{\partial^2 \theta}{\partial x_1^2} - \frac{\rho}{G} \frac{\partial^2 \theta}{\partial t^2} = 0 \quad (78)$$

The transverse vibration of section l_2 is

$$\frac{\partial^4 \xi}{\partial x_2^4} + \frac{\rho}{ER^2} \frac{\partial^2 \xi}{\partial t^2} = 0 \quad (79)$$

The shape of the cross-sectional area is the same as that of a uniform pole.

The boundary conditions are:

$$\text{at } x_1=0, \quad \theta=0$$

$$\text{at } x_1=l_1 \text{ or } x_2=0,$$

$$[\xi]_{x_2=0}=0, \quad [\theta]_{x_1=l_1}=\left(\frac{\partial \xi}{\partial x_2}\right)_{x_2=0}$$

$$\left(GI_p \frac{\partial \theta}{\partial x_1}\right)_{x_1=l_1}=\left(ESR^2 \frac{\partial^2 \xi}{\partial x_2^2}\right)_{x_2=0}$$

$$\text{when } x_2=l_2$$

$$\left(\frac{\partial^2 \xi}{\partial x_2^2}\right)_{x_2=l_2}=0, \quad \left(\frac{\partial^3 \xi}{\partial x_2^3}\right)_{x_2=l_2}=0$$

where G : Shear elasticity coefficient
 I_p : Polar moment of inertia of cross section

The normal function at section l_2 in this case is

$$\xi_{lm} = \frac{u_{lm}}{\sqrt{\frac{(\sin k_{lm} + \sinh k_{lm})^2}{(\cos k_{lm} \sinh k_{lm} - \sin k_{lm} \cosh k_{lm})^2} + \frac{\gamma}{\cos^2 \nu k_{lm}^2}}}} \quad (80)$$

where

$$\begin{aligned} u_{lm} = & (\cos k_{lm} \frac{x_2}{l_2} - \cosh k_{lm} \frac{x_2}{l_2}) \\ & - \frac{\cos k_{lm} + \cosh k_{lm}}{\sin k_{lm} + \sinh k_{lm}} (\sin k_{lm} \frac{x_2}{l_2} - \sinh k_{lm} \frac{x_2}{l_2}) \\ & - 2\gamma k_{lm} \frac{\tan \nu k_{lm}^2}{\nu k_{lm}^2} \\ & (\sinh k_{lm} \sin k_{lm} \frac{x_2}{l_2} + \sin k_{lm} \sinh k_{lm} \frac{x_2}{l_2}) \end{aligned}$$

where

$$\gamma = \frac{El_1}{2Gl_2}, \quad \nu = \sqrt{\frac{E}{G}} R \frac{l_1}{l_2^2}$$

The m -th eigenvalue k_{lm} in the above equation is the root of the following equation.

$$1 + \cos k_{lm} \cosh k_{lm} + \gamma k_{lm} \frac{\tan \nu k_{lm}^2}{\nu k_{lm}^2}$$

$$(\cos k_{lm} \sinh k_{lm} - \sin k_{lm} \cosh k_{lm}) = 0$$

(81)

Moreover, the m -th natural angular frequency of this contact ω_{lm} is shown by

$$\omega_{lm} = \frac{k_{lm}^2}{l_2^2} R \sqrt{\frac{E}{\rho}} = \frac{\nu k_{lm}^2}{l_1} \sqrt{\frac{G}{\rho}} \quad (82)$$

In Eqs. (80) and (81), when ν is extremely small, the clamped end shown in paragraph 6.2 is permitted angular displacement, and the other end is free, both being equivalent to those of a cantilever whose l_2 has been reinforced.

Fig. 52 shows the normal functions k_{lm}

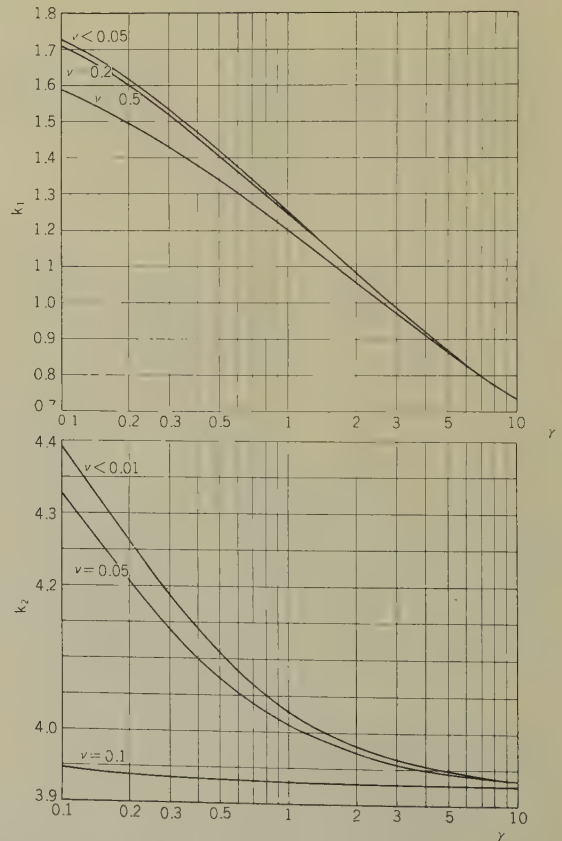


Fig. 52—Eigenvalue of a torsion contact spring.

Table 9

CALCULATED AND MEASURED VALUES OF THE NATURAL FREQUENCY
OF A TORSIONS CONTACT SPRING
(Material: stainless steel, $\sqrt{E/\rho}=4.58\times10^5$ cm/sec.)

| Wire diameter (cm) | l_1 (cm) | l_2 (cm) | r | ν | 1st nature frequency | | 2nd natural frequency | |
|-----------------------|------------|------------|------|--------|----------------------|--------------------|-----------------------|--------------------|
| | | | | | Calculated values | Measured values | Calculated values | Measured values |
| 0.045 | 5.0 | 5.0 | 1.29 | 0.0036 | 45.1 | 47.5 | 518.0 | 511.0 |
| | | 4.0 | 1.63 | 0.0057 | 65.7 | 67.3 | 828.0 | 838.0 |
| | | 3.0 | 2.21 | 0.0104 | 105.2 | 108.8 | — | — |
| | | 2.0 | 3.25 | 0.0227 | 192.6 | 197.2 | — | — |
| 0.055 | 10.0 | 10.0 | 1.30 | 0.0022 | 14.2 | 13.7 | 163.2 | 171.4 |
| | | 5.0 | 2.60 | 0.0089 | 42.0 | 46.8 | 636.0 | 638.5 |
| | | 3.0 | 4.33 | 0.0247 | 90.9 | 102.2 | — | — |
| | | 2.0 | 6.50 | 0.0555 | 168.0 | 183.5 | — | — |
| 0.080 | 8.0 | 8.0 | 1.30 | 0.0040 | 32.1 | 31.2 | 370.0 | 366.2 |
| | | 6.1 | 1.73 | 0.0070 | 48.8 | 45.5 | 628.0 | 628.0 |
| | | 4.0 | 2.60 | 0.0161 | 94.3 | 93.0 | — | — |
| | | 2.0 | 5.20 | 0.0647 | 272.4 | 277.0 | — | — |

obtained from Eq.(81), and Table 9 represents the calculated and measured values of natural frequency of actual test samples.

As seen from Table 9, the calculated values are in good correspondence with the measured ones. From Fig. 52, it is found that when ν is small, eigenvalues are the same as those shown paragraph in 6.2 and that when r becomes large, Ω_m also grows large. Accordingly, the vibration of the torsional contact spring caused by impact shows the response of a single degree of freedom similar to that described in paragraph 6.2.

7.4. Critical Velocity of Torsional Contact Spring

When the torsional contact spring closes against the fixed contact, the critical closing velocity of the contact below which contact chatter is not caused $\cdot\cdot[\xi_{-0}]_{t,cr}\cdot\cdot$ was measured in the same way as described paragraph in 7.2, and the measured values are shown in Table 11 together with the dimensions of the contact spring. From Table 10, the critical closing velocity coefficient $K_{t,cr}$ in this case is shown by

$$K_{t,cr.} = \frac{[\dot{\xi}_{-0}]_{t,cr.}}{\omega_{t1} \xi_0} = 0.025 \quad (83)$$

$K_{t,cr.}$ of the torsional contact spring is somewhat lower than $K_{b,cr.}$ of the cantilever contact spring shown by Eq. (74). However, $\omega_{t1} \xi_0$ of the torsional contact spring can be increased as described later, and so even when $K_{t,cr.}$ is small, $[\dot{\xi}_{-0}]_{t,cr.}$ can be greatly increased. For example, the measured values of contact signal under the condition that $d =$

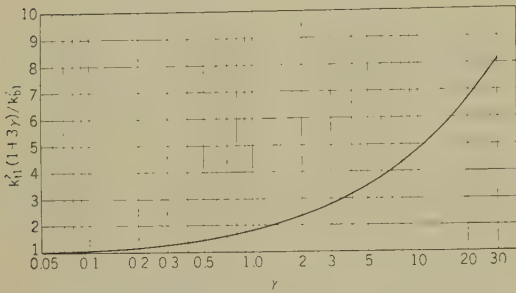
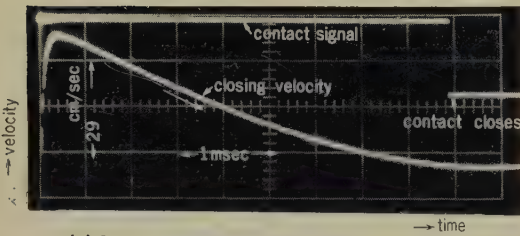
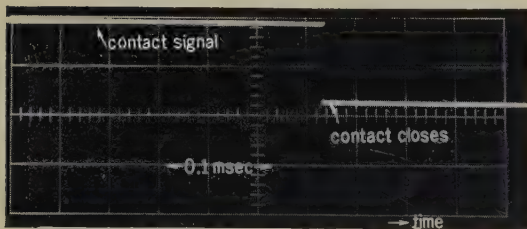


Fig. 53—Relation between μ and γ .

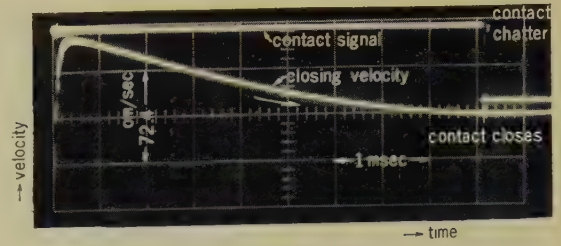


(a) Contact signal and closing velocity
 $[\dot{\xi}_{-0}] = 45.0 \text{ cm/sec}$

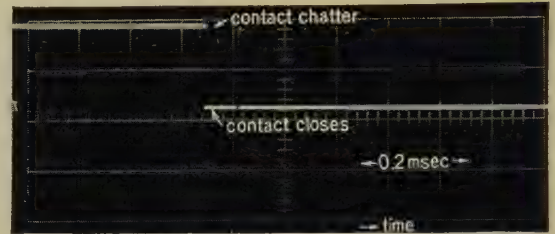


(b) Contact signal (time scale expanded)

Fig. 54—Closing velocity and contact signal of a torsional contact spring at its free end (measured values).



(a) Contact signal and closing velocity
 $[\dot{\xi}_{-0}] = 69.0 \text{ cm/sec}$



(b) Contact signal (time scale expanded).

Fig. 55—Closing velocity and contact signal of a torsional contact spring at its free end (measured values).

0.052 cm, $l_1 = 6.0$ cm, $l_2 = 1.0$ cm, $\xi_0 = 1.0$ cm and the material is German silver, are shown in Figs. 54 and 55. Fig. 54 shows examples when the critical closing velocity $[\dot{\xi}_{-0}]_{t,cr.} = 45.0 \text{ cm/sec}$. Fig. 55 shows examples when $[\dot{\xi}_{-0}] = 69 \text{ cm/sec}$, higher than in the above case, and three contact chatter are found. Therefore, if several contact chatter are permitted, the closing velocity of the contact spring can be much increased.

Subsequently, the realizable critical closing velocity of torsional contact spring will be discussed. In this case, if the contact is located at a distance of x_{2c} from the bent part of contact spring, the static stiffness s_t observed at the contact is

$$s_t = \frac{3E\pi d^4}{64l_2^3(1+3\gamma/y_{2c})y_{2c}^3} \quad (84)$$

As a result, if section l_2 is failed by simple bending when the predeflection $[\xi_0]_{\gamma max}$ is given to the contact, the upper limit $[\dot{\xi}_{-0}]_{t,cr,max}$

Table. 10
CRITICAL CLOSING VELOCITY OF A TORSIONAL CONTACT SPRING AT ITS FREE END
(MEASURED VALUES, MATERIAL: GERMAN SILVER).

| Wire dia- meter d (cm) | Length l_1 (cm) | Length l_2 (cm) | *1st natural angular frequency ω_1 | Situation of contact $y_c = x_2/l_2$ | *Stiffness ob- served from the free end s_2 (gr/cm) | Torsional angle θ_0 (°C) | Predeflection ξ_0 (cm) | *Load on the free end p_0 (gr) | Critical clos- ing velocity $[\dot{\xi}_{-0}^{(1)}]$ (cm/sec) | Critical clos- ing velocity coefficient K_{cr} . |
|--------------------------------|----------------------|----------------------|--|--|--|---------------------------------------|-------------------------------|--|--|---|
| 0.032 | 6.00 | 1.834 | 750 | 0.95 | 2.3 | 30.5 | 0.918 | 2.3 | 15.25 | 0.022 |
| | | | | | | 55.95 | 1.707 | 4.2 | 28.55 | 0.022 |
| | | | | | | 73.1 | 22.5 | 5.4 | 46.0 | 0.027 |
| 0.040 | 6.10 | 1.855 | 938 | 0.95 | 5.6 | 108.0 | 3.30 | 8.0 | 59.0 | 0.024 |
| | | | | | | 26.35 | 0.801 | 4.8 | 17.57 | 0.024 |
| | | | | | | 53.35 | 1.625 | 9.7 | 40.5 | 0.027 |
| 0.050 | 6.05 | 1.868 | 1172 | 0.95 | 13.9 | 26.65 | 0.813 | 12.0 | 30.75 | 0.032 |
| | | | | | | 56.7 | 1.721 | 25.4 | 52.5 | 0.026 |
| | | | | | | 26.1 | 0.793 | 76.2 | 53.0 | 0.035 |
| 0.080 | 6.00 | 1.873 | 1870 | 0.95 | 90.4 | 37.14 | 0.565 | 5.4 | 22.5 | 0.021 |
| | | | | | | 66.72 | 1.004 | 9.6 | 45.0 | 0.024 |
| | | | | | | 8.3 | 0.480 | 10.8 | 31.25 | 0.027 |
| 0.040 | 6.00 | 1.027 | 2372 | 0.868 | 20.1 | 56.83 | 0.884 | 19.9 | 54.32 | 0.026 |
| | | | | | | 36.83 | 0.579 | 31.6 | 60.3 | 0.034 |
| | | | | | | 49.1 | | | | |

* shows presumed values by calculation. P_0 shows the load on the free end to give θ_0 .

of the critical closing velocity of this contact spring is obtained from Eqs. (82) and (84) as follows:

$$[\dot{\xi}_{-0}]_{l, cr, max} = \frac{\sigma_a k_{t1}^2 y_{2c}^2}{6 \sqrt{E \rho}} \left(1 + 3 \frac{\gamma}{y_{2c}} \right) \quad (85)$$

where σ_a : The allowable tensile stress of the spring

k_{t1} : The 1st eigenvalue of the contact spring

$y_{2c} = x_{2c}/l_2$: The position of the contact

Furthermore, if section l_1 is failed by the maximum torsional stress,

$$[\dot{\xi}_{-0}]_{l, cr, max} = \frac{\tau_a k_{t1}^2 y_{2c}^2}{3 \sqrt{E \rho}} \left(1 + 3 \frac{\gamma}{y_{2c}} \right) \quad (86)$$

where τ_a is the allowable shear stress of the spring. So if, $\sigma_a \leq 2\tau_a$, $[\dot{\xi}_{-0}]_{l, cr, max}$ is given by Eq. (85). For instance, for a torsional contact spring of German silver, if $l_1 = 6.0$ cm, $l_2 = 1.0$ cm, $d = 0.032$ cm, $y_c = 0.86$, $E = 1.35 \times 10^4$ kg/mm², $\rho = 8.48$ gr/cm³, $\sigma_a = 30$ kg/mm², $G = 5 \times 10^3$ kg/mm², $K_{t, cr.} = 0.025$, therefore, as $\gamma = 8.1$ and $\nu = 0.08$, $k_t = 0.77$ from Fig. 52. And from Eq. (85), the following relation is found:

$$[\dot{\xi}_{-0}]_{l, cr, max} = 47 \text{ cm/sec} \quad (87)$$

This critical closing velocity is over twice as large as that of the cantilever spring described by Eq. (77).

When the contact is at the free end, if the critical closing velocity of cantilever contact spring and that of torsional contact spring are compared under the condition that the ratio of Eq. (76) to Eq. (85) is μ , then, as $y_{2c} = y_c = 1$, the following equation is obtained.

$$\mu = \frac{[\dot{\xi}_{-0}]_{l, cr, max}}{[\dot{\xi}_{-0}]_{b, cr, max}} = \frac{K_{t, cr.}}{K_{b, cr.}} \frac{k_{t1}^2 (1 + 3\gamma)}{k_{b1}^2} \quad (88)$$

$K_{t, cr.}/K_{b, cr.}$ is fixed, and so if the relation between γ and $k_{t1}^2 (1 + 3\gamma)/k_{b1}^2$ for the case of $\nu < 0.1$ is calculated, the results become as shown in Fig. 53. From Fig. 53, when γ becomes large, the critical closing velocity of

the torsional contact spring grows much larger than that of the cantilever contact spring.

In order to learn to what extent the above result is applicable to relays now in practical use, relays with torsional contact springs as shown in Fig. 56 were made for trial, and their characteristics of were compared with those of the W-A type relays now in use.



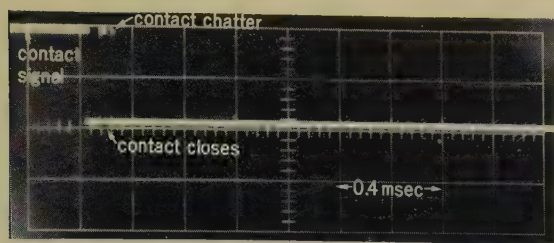
Fig. 56—Appearances of W-A relay and the trial relay.

A pure iron magnetic circuit of the same shape as those of the relays now in practical use was adopted in the experimental relays, and a torsional contact spring made of German silver with the following dimensions was used.

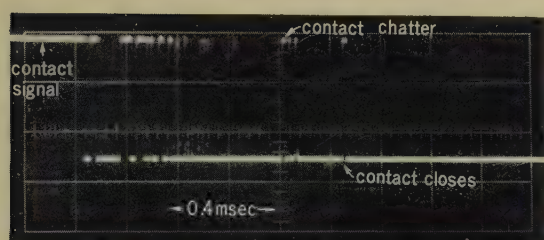
$$d = 0.032 \text{ cm}, \quad l_1 = 6 \text{ cm}, \quad l_2 = 1 \text{ cm}, \quad \xi_0 = 1 \text{ cm}.$$

The contacts were arranged for 8 pairs.

The contact chatter of the make contact and of the break contact were measured, in operating and releasing. The results at the make contact are illustrated in Figs. 57, and at the break contact the results are similar. These figures show that there is scarcely any chatter of the contacts of the experimental relay. Here, "traveling time of contact" means the timelength from the beginning of operation of the armature until closure of the contact.



(a) make-contact closes
traveling time : 3.8msec, contact travel : 0.73mm



(b) W-A Relay
traveling time : 3.6msec, contact travel : 0.77mm

Fig. 57—Contact signal of the trial relay and W-A relay at the make contact.

8. Conclusion

The physical quantity at the make contact to represent relay chatter had not been previously determined and so there were scarcely any clues to the study of the chatter in the case of the design of a relay.

As a result of researches mainly on the chatter caused when an elastic body collides with a fixed contact, the relation between chatter and vibratory constant has been clarified. Moreover, not only has a basis on which the chatter is quantitatively understood when the movable parts of a relay are designed been given, but also a guide of design for the contact spring with no contact chatter has been obtained.

The chatter caused in the case of impact of two bodies, is decided by E_{omx} (normal function ratio at the colliding point), Ω_m

(natural angular frequency ratio), δ_m (damping coefficient), ξ_{st} (initial deflection) ξ_o (predeflection), α (restitution coefficient) and the mass ratio observed from the colliding point of the two bodies. All the above-shown constants but the restitution coefficient are obtainable by considering the normal vibration of bodies at their colliding point, and can be controlled freely.

Concerning general mechanical elastic bodies, the components of higher mode vibrations of normal vibration displacement shrink by the order of ω_m^{-2} , but the components caused after impact by the order of ω_m^{-1} . Accordingly, in the case of chatter, it is necessary to consider vibrations of much higher modes than in the case of normal vibration. Hence, the complexity of chatter.

The restitution coefficient shows a higher value when the contact is harder or the vibration mode around impact is higher. When the chatter of a relay is considered, if the higher modes of vibrations caused after impact have vanished before the next impact, then it is permissible to consider that the restitution coefficient includes the energy loss of the higher mode vibrations. In the case of a uniform cantilever, as a result of research on the restitution coefficient considered to include the vibrations of modes higher than 4th, the calculated values have proved to correspond very well to the measured ones.

Formerly, the contact pressure $s_x \xi_o$ was thought of as an important factor to control the chatter of contact springs.^{7) 25)} Indeed, it is an important factor when the load on the armature is considered, but what actually has a direct influence on the chatter is predeflection ξ_o . So only in the case of comparison between the chatters of the same vibratory systems, consideration is possible by contact pressure.

According to the higher modes of vibrations caused at impact, chatter is much varied. But if natural angular frequency ratio Ω_m with most remarkable influence on chatter is enlarged, the normal function ratio E_{omx} at the colliding point is made smaller, and the higher modes of vibrations are stopped sooner, then the chatter becomes simpler, and shows the

response with single degree of freedom. The design and manufacture of such movable parts can easily be realized as shown in the Section 6.

When the contact closes, the critical closing velocity of a contact without contact chatter exists. The relation of a single degree of freedom vibratory system to a cantilever contact spring and to a torsional contact spring, the value of K_{cr} , (the critical closing velocity with no contact chatter) is nearly the same. K_{cr} , therefore, gives the design basis of a contact spring designed to prevent contact chatter.

In the body of this paper, the motion of the "lift-off type" relay was discussed as the model. This concept is applicable to the motion of a relay with two moving contacts or of a "flexure type" relay. The analytical method used in this study seems applicable not only to the chatter of relays but to the design for printing telegraphic instruments and other apparatus where impact vibration occurs.

Acknowledgement

This research was carried out at the Electrical Communication Laboratory of the Nippon Telegraph and Telephone Public Corporation. The authors owe a dept of gratitude to Dr. Hayasaka, the Assistant-Director of the Laboratory, and to Dr. Ito, the Chief of the Equipment Parts Research Section, for their kind and sincere guidance. They are also very grateful members of the Corporation.

The authors were helped with the calculations by members of the computer research group in the Electronics Section.

During the construction of the experimental apparatus they received cooperation from the members of the Model Shop Section in the Laboratory, the members of the Fuji branch of the Tokyo Shibaura Electric Company, and the members of the Iwasaki Communication Company.

Besides, they owe much to Prof. Matsudaira of Tohoku University and to Prof. Takei of the Electrical Communication College for their profitable discussions.

References

- (1) W.H. Hoppman: "Impact of a Mass on a Column," *J.A.M.*, **21**, 3, (1954).
- (2) S. Timoshenko: "Vibration Problem in Engineering," V. Nostrand, (1937).
- (3) E. E. Summer: "Relay Armature Rebound Analysis," *B.S.T.J.*, **31**, (1952).
- (4) Tsuda: On the Vibration of a Power-Transmission System Having Angular Clearances" *Trans. Jap. Soc. Mech. Eng.* **24**, 147, (1958).
- (5) Takei: "Study of Vibration Caused by Impact," Reports of Studies Contracted by the Electrical Communication Laboratory, (1959).
- (6) A. E. Love: "Mathematical Theory of Elasticity," Cambridge, (1959).
- (7) R. L. Peek Jr. & H. N. Wager: "Switching Relay Design," V. Nostrand, (1955).
- (8) T. Suzuki: "A Method of Solving the Problems of Mechanical Impact," *Technology Reports of Tohoku Univ.*, **14**, (1960)
- (9) S. Timoshenko: "Theory of Elasticity," *E. S.M.*, (1934).
- (10) Hayasaka: "Acoustic Engineering," Nikkan Kogyo Press, (Jap.) (1957).
- (11) Ito & Yamazaki: "Dynamic Electricity Drive-Static Electricity Measurement Type Vibrometer," *J. Inst. Electr. Commun. Eng. Jap.* **34**, 134, (1959).
- (12) Takamura: "Chatter Vibration of the Switching Relays" *J. Inst. Electr. Commun. Eng. Jap.* **42**, 9, p. 822, (1959).
- (13) Hayasaka: "Theory of Acoustic Vibration," Corona (Jap.), (1947).
- (14) Takamura & Otuka: "Chatter Vibration of Cantilever under Damping" *Trans. Jap. Soc. mech. Eng.* **25**, 151, p. 247, (1959).
- (15) Hidaka: "Theory of Integral Equations," Kawade, (Jap.) (1944).
- (16) Okawa: "Design for Mechanical Acoustic Vibratory Systems of Acoustic Instruments," *Electr. Commun. Labor. Techn. J.N.T.T., Jap.* (1954).
- (17) Takei & Takasi: "Method of Drawing the Phase of Side Impact of a Cantilever Taking Higher Modes of Vibrations into Account," Data of Relay Conference, 81-4, (1960).
- (18) Tuboi: "Theory of Vibration," Kawade, (Jap.) (1942).
- (19) Takamura, Yurino, & Otuka: "Damping Chatter of Single Freedom Degree Vibratory System," *J. Inst. Electr. Commun. Eng. Jap.* **43**, 12, (1960).
- (20) Nisiguti: "Method of Measuring Impact Vibration of a Relay," Hitachi Hyoron, **37**, 5,

- p. 807, (1955).
- (21) Nukiyama: "Study of Electrical Acoustic Apparatus," Maruzen, (Jap.) (1948).
- (22) Takamura, Yurino, & Otuka: "Study of the Chatter of a Relay," *Electr. Commun. Labor. Techn. Jour. N.T.T., Jap.* **9**, 12, (1960).
- (23) Ikegaya: "Study of Molded Vibrating Plate," Data of the Electrical Communication Laboratory, (1960).
- (24) Okumura & Ikeda: "Effect Elastic Settlement on the Transversal Vibration of a Pole," *Trans. Jap. Soc. Mech. Eng.* **14**, 46, p. 22, (1948).
- (25) Sinohara: "Study of an Electro-Magnetic Relay," *Electr. Commun. Labor. Techn. Jour. N.T.T., Jap.* **8**, 1, (1959).
- (26) Sugimoto: "Transversal Vibration of a Sandwich Beam," *Proc. Cong. Electr. Commun. Eng. Jap.* (1956).

* * * *

Feedback Type Distributed Amplifier Tube*

Takuya KOJIMA†

A wide-band distributed-amplifier tube in which the anode and grid form a double helix has been studied. Part of the amplified signal on the anode line is fed back to the grid line for compensation of the grid line loss in the high frequency. The bandwidth of amplification obtained with the experimental tube was from zero to 300 Mc/s. The theory of the design of the tube is described in this paper.

Introduction

In a previous report⁽¹⁾ the author discussed a distributed amplifier tube with a bandwidth of 150 Mc/s and concluded that it is necessary to make a positive-feedback-type distributed-amplifier tube for extension of the amplification bandwidth. Recently he constructed a feedback-type distributed-amplifier tube in which part of the amplified signal on the anode line is fed back to the grid line for compensation of the grid line loss. Amplification over a band from zero to 300 Mc/s was obtained with an experimental tube. In this paper, the results of experiments using experimental tubes as well as the theory of the feedback-type distributed-amplifier tube and the procedure for its design are described.

1. Characteristics of Feedback-Type Distributed-Amplifier Tube

1.1. Principle and Mechanical Construction of Feedback-Type Distributed-Amplifier Tube

In Fig. 1 the principle of the feed-back-type

distributed-amplifier tube is shown. A signal applied to the input of the grid line travels on the line and the cathode current modulated by this signal flows to the anode producing an amplified signal on the anode line which travels on the line in the same manner as in the previously described distributed-amplifier tube. In this tube, however, part of the amplified signal is fed back to the grid line through the capacitance C and the mutual inductance M between the anode and the grid lines. Thus the loss in the grid line which amounts to a considerable value in the high frequency region can be compensated. In Fig. 2 the construction of the feedback-type distributed-amplifier tube is shown. The tube is a coaxial-type triode with the cathode in the center and with the grid and anode helices coupled together and placed around it.

The physical dimensions of the electrodes

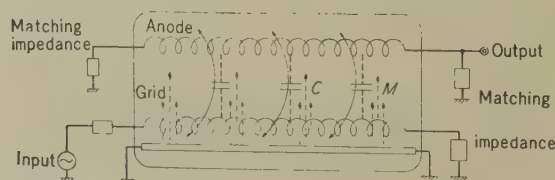


Fig. 1—Principle of feedback-type distributed-amplifier tube.

* MS in Japanese received by the Electrical Communication Laboratory, April 18, 1960. Originally published in the *Kenkyū Zituyōka Hōkoku* (Electrical Communication Laboratory Technical Journal), N.T.T., Vol. 9, No. 6, pp. 639-648, 1960.

† Electronic Components Research Section.

Table 1
DIMENSIONS OF ELECTRODES

| | | |
|-------------|----------------|----------|
| Cathode | coxide coated | |
| | length | 40 mm |
| | width | 3 mm |
| Grid Helix | triple winding | |
| | length | 40 mm |
| | wire diameter | 0.02 mm |
| | pitch | 0.3 mm |
| Anode Helix | single winding | |
| | length | 40 mm |
| | ribbon width | 0.3 mm |
| | pitch | 0.492 mm |

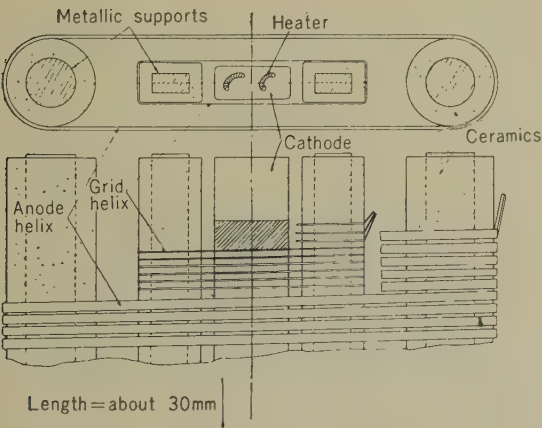


Fig. 2—Construction of feedback-type distributed-amplifier tube.

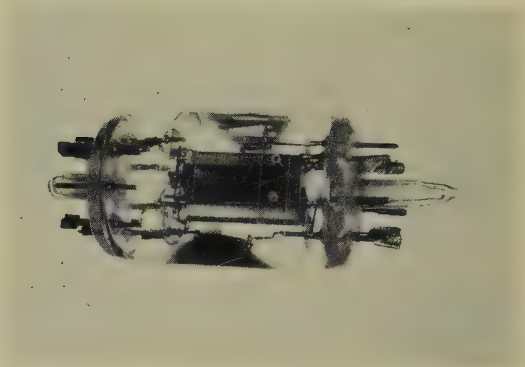


Fig. 3—Distributed amplifier tube.

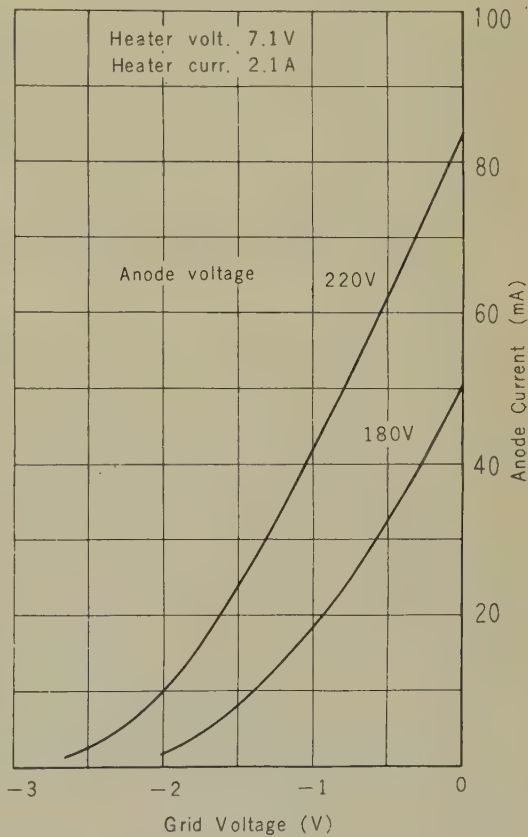


Fig. 4—Static characteristics of experimental tube.

are shown in Table 1. In Fig. 3 a photograph of a sample tube is shown.

1.2. Static Characteristics

In Fig. 4 curves of the static characteristics are shown.

1.3. Amplifications

The amplifier circuit for this tube is shown in Fig. 5. For the purpose of canceling the effects of the stray capacitances of the tube output, leads a low-pass filter circuit is connected at each line terminal. In this way matching of lines is accomplished. However the cutoff frequency of these low-pass filters limits the bandwidth of the amplifier.

The measured amplification versus frequency is plotted in Fig. 6. The gain N is generally flat in the amplification band and drops abruptly above 300 Mc/s. The voltage at the input and output is measured by crystal detectors connected to these terminals.

2. Theory of Feedback-Type Distributed-Amplifier Tube

An analysis of an amplifier tube which consists of a long straight cylindrical cathode surrounded concentrically by a helical grid and an outer helical anode was carried out by Lewis⁽²⁾ from circuit theory. We can apply his theoretical results to our experimental tubes, but first we must find method of calculating the equivalent transmission circuit of our tubes.

The general theory of amplification of the feedback amplifier, which is a simplified version of Lewis' theory, will be described first. Then the method of computing the equivalent transmission constants from the physical dimensions of the helical electrodes of the experimental tubes will be treated.

2.1. Amplification Theory of Feedback-Type Distributed-Amplifier Tube

Fig. 7 shows the equivalent transmission line of this tube whose circuit constants will

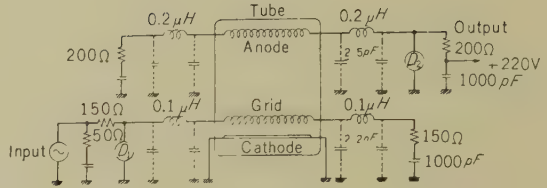


Fig. 5—Amplifier circuit.

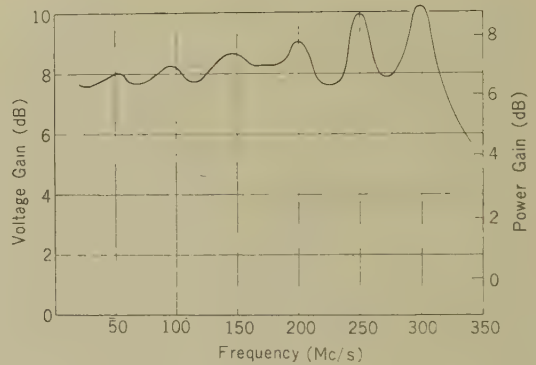


Fig. 6—Gain of experimental tube.

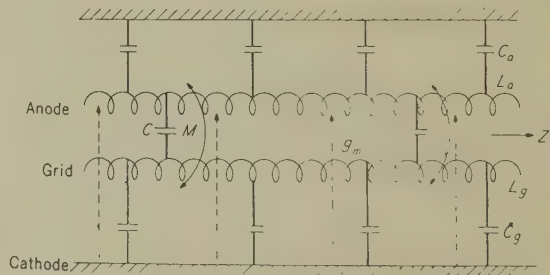


Fig. 7—Equivalent transmission line.

be determined in the following paragraphs.

The constants are as follows:

L_a : Series self-inductance per unit axial length of anode line

C_a : Shunt capacitance per unit axial length of anode line

L_g : Series self-inductance per unit axial length of grid line

C_g : Shunt capacitance per unit axial length of grid line

M : Series mutual inductance between the two helical lines

C : Shunt mutual capacitance between the two helical lines

g_m : Mutual conductance per unit axial length

z : Distance along axial.

The voltage-current equations of this transmission line are given by:

$$\left. \begin{aligned} -\frac{dE_a}{dz} &= j\omega L_a I_a + j\omega M \bar{I}_g \\ -\frac{dE_g}{dz} &= j\omega L_g I_g + j\omega M I_a \\ -\frac{dI_a}{dz} &= j\omega C_a E_a + j\omega C(E_a - E_g) - g_m E_g \\ -\frac{dI_g}{dz} &= j\omega C_g E_g + j\omega C(E_g - E_a) \end{aligned} \right\} \quad (1)$$

where

E_a : anode line voltage

I_a : anode line current

E_g : grid line voltage

I_g : grid line current.

From Eqs. (1) we obtain the equation:

$$\begin{aligned} \frac{d^4 E_a}{dz^4} &+ \{\omega^2 L_g(C_g + C) + \omega^2 L_a(C_a + C) \\ &- 2\omega^2 MC + j\omega M g_m\} \frac{d^2 E_a}{dz^2} + (L_a L_g - M^2) \\ &\times \{\omega^4 C(C_a + C_g) + \omega^4 C_a C_g + j\omega^3 C g_m\} E_a = 0. \end{aligned} \quad (2)$$

The equations for E_g , I_a , and I_g take forms similar to Eq. (2).

The solution of Eq. (2) is given by

$$E_a = C_1 e^{\Gamma_1 z} + C_2 e^{-\Gamma_1 z} + C_3 e^{\Gamma_2 z} + C_4 e^{-\Gamma_2 z} \quad (3)$$

where

$$\Gamma_{1,2} = \sqrt{\frac{-A \pm \sqrt{A^2 - 4B}}{2}} \quad (4)$$

$$\left. \begin{aligned} A &= \omega^2 L_g(C_g + C) + \omega^2 L_a(C_a + C) \\ &- 2\omega^2 MC + j\omega M g_m \\ B &= (L_a L_g - M^2) \{\omega^4 C(C_a + C_g) \\ &+ \omega^4 C_a C_g + j\omega^3 C g_m\} \end{aligned} \right\}$$

The four propagation constants give the values of forward amplification wave, backward amplification wave, forward attenuation wave and backward attenuation wave respectively.

2.2. Equivalent Transmission Line of the Feedback-Type Distributed-Amplifier Tube

2.2.1. Method of Computing Equivalent Circuit Constants

We shall use here the same method of computing the equivalent circuit constants that we used in the preceding paper for the non-feedback-type distributed amplifier tube.⁽¹⁾ However, since the present tube has a double-wound helix which was not employed in the tube described in the preceding paper, we must find a method suitable for such a double helix.

First we shall review the method applied in the preceding paper. In Fig. 8(a) an example of the grid helix is shown. Fig. 8(b) shows its equivalent circuit. The grid is transformed into the circular cylindrical form shown in Fig. 8(c). In this transformation the contour length and the distances between the helix and the internal conductor are unchanged. The gap between the helix and the inner conductor is so small that the

characteristics of the helix will not be greatly changed by the above transformation. The currents on the helix travel on the short lines through the vacuum and the short lines along the ceramics in turn. Therefore, the equivalent circuit of the helix in Fig. 8(c) will take the form shown in Fig. 8(e). Here L_v and C_v here are the series inductance and the shunt capacitance of the line through the vacuum, while L_c and C_c are the series inductance and the shunt capacitance of the line along the ceramics. These constants are computed from the results of calculations of the electromagnetic fields of the cylindrical helix in Fig. 8(d).

The composite inductance and capacitance of the equivalent line shown in Fig. 8(b) are computed by proportional addition of the

inductance and capacitance of the two lines above according to the ratio of their lengths measured along the contour.

Therefore,

$$\left. \begin{aligned} L &= \frac{l_v}{l_v + l_c} L_v + \frac{l_c}{l_v + l_c} L_c \\ C &= \frac{l_v}{l_v + l_c} C_v + \frac{l_c}{l_v + l_c} C_c \end{aligned} \right\} \quad (5)$$

In the preceding paper the experiments on the non-feedback-type distributed amplifier tube demonstrated that the method of computing the equivalent circuit of the helix grid was valid.

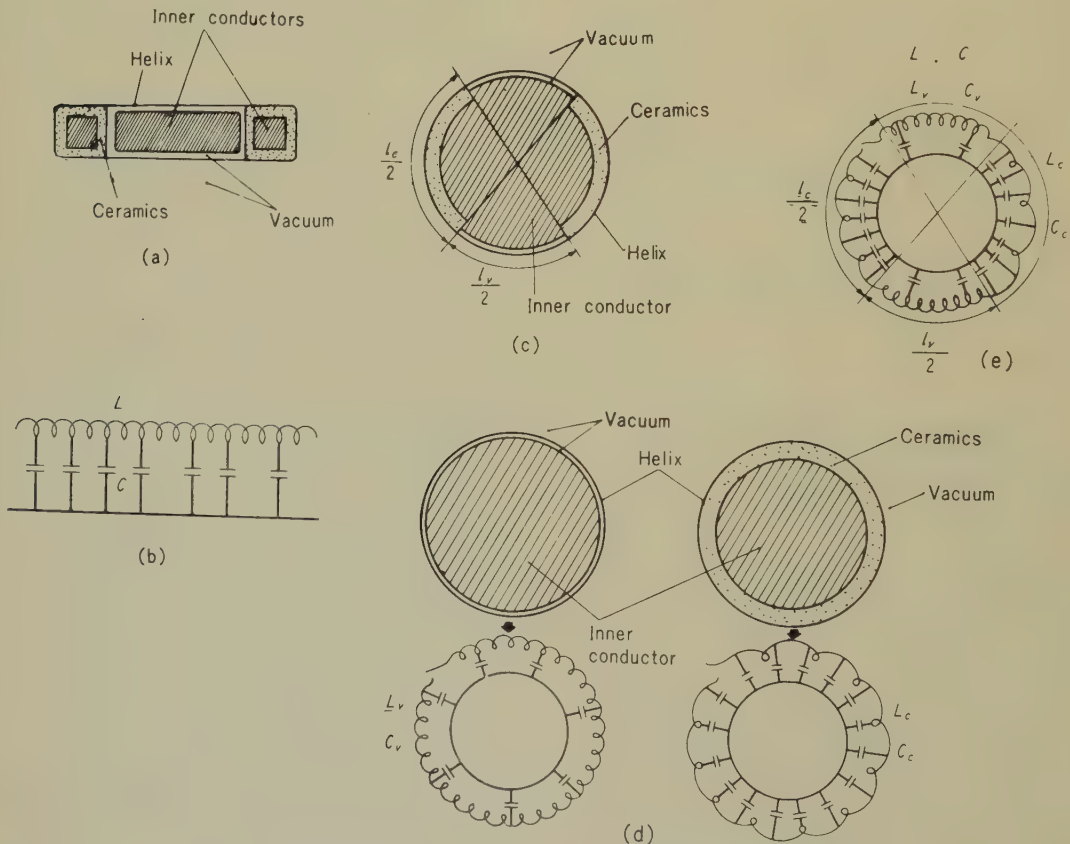


Fig. 8—Method of computing equivalent line.

2.2.2. Equivalent Line of the Double Helix

Now we shall compute the constants of the line applying the same computing method described in the preceding paragraph to the double helix of the present tubes. First the double helix shown in Fig. 9 (a) is transformed into the simplified form in Fig. 9 (b).

The lengths l_{av} , l_{ac} , l_{gc} , and l_{gc} in Fig. 9 (b) are defined as follows:

- l_{ac} : Partial length of the anode helix along ceramics
- l_{av} : Partial length of the anode helix in vacuum
- l_{gc} : Partial length of the grid helix along ceramics

Table 2
DIMENSIONS OF HELIXES

| | Helix 1 | Helix 2 | Helix 3 |
|--|--|--|--|
| Contours | Same as anode helix $l_{av}+l_{ac}$ | Same as anode helix, $l_{av}+l_{ac}$ | Same as grid helix, $l_{av}+l_{gc}$ |
| Distance between two helixes | Same as distance measured through vacuum between anode and grid. | | |
| Distance between helix and inner conductor | Distance between inner helix and inner conductor is same as the distance measured through vacuum between grid helix and inner conductor. | Same as distance measured through ceramics between anode helix and inner conductor | Same as distance measured through ceramic between grid helix and inner conductor |

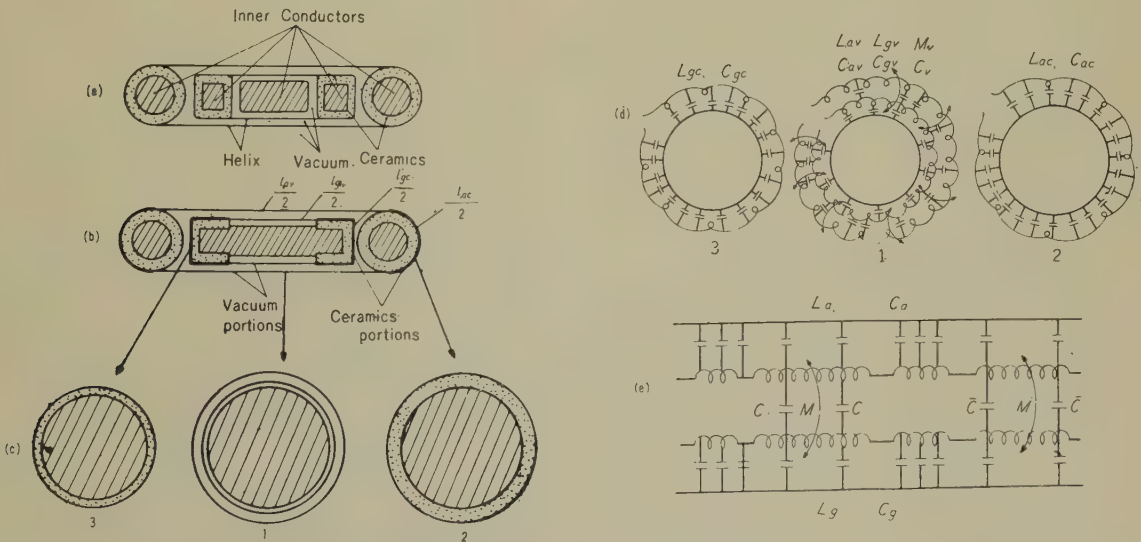


Fig. 9—Equivalent line of experimental tube.

l_{gv} : Partial length of the grid helix in vacuum.

Here we make the assumption that the inductive and capacitive coupling of the two helices occurs in the portions of the helices in vacuum and no coupling occurs in the portions of the helices along the ceramics.

Next we transform the double helix shown in Fig. 9 (b) into the three cylindrical helices as shown in Fig. 9 (c). In this transformation only the center helix becomes a double helix, and the other two helices are single Fig. 9 (b) shows that the center helix corresponds to the portions of the helices in vacuum while the right and left single helices correspond to the portions of the grid and anode helices along the ceramics. The contours and the distances between the two helices or between the helices and the inner conductors are determined by comparing them with those of the original helix of Fig. 9 (b) according to Table 2.

The electromagnetic fields of the single or double cylindrical helix in Fig. 9 (c) can be solved and will be discussed in the succeeding paragraphs. Therefore we can compute the series inductances, the shunt capacitances, the mutual inductances, and the mutual capacitances of the equivalent transmission line shown in Fig. 9 (b) for each of the helices in Fig. 9 (c). The inductance and the capacitance of the final composite equivalent line of the tubes shown in Fig. 9 (e) are calculated by proportional addition of the inductance and the capacitance obtained above according to the following relation:

$$\left. \begin{aligned} L_g &= \frac{l_{gv}}{l_{gv} + l_{gc}} L_{gv} + \frac{l_{gc}}{l_{gv} + l_{gc}} L_{gc} \\ C_g &= \frac{l_{gv}}{l_{gv} + l_{gc}} C_{gv} + \frac{l_{gc}}{l_{gv} + l_{gc}} C_{gc} \\ M &= \frac{l_{av}}{l_{av} + l_{ac}} M_v \\ C &= \frac{l_{gv}}{l_{av} + l_{ac}} C_v \end{aligned} \right\} \quad (6)$$

where $L_{gc} \sim C_{ac}$ have the meanings shown in Fig. 9 (d).

2.2.3. Electromagnetic Field of the Double Helix

In the preceding paragraph we deduced the method of computing the final equivalent line of our tube from the equivalent line constants of the three cylindrical helices shown in Fig. 9 (c). Now we have to find the equivalent lines of the three cylindrical helices. In the preceding paper we obtained the method of computing the equivalent line of the single helix, so we need not discuss it in this paper. In this paper we shall only discuss the method of computing the equivalent of the double helix.

The construction of the double helix is shown in Fig. 10. In our analysis we employ Pierce's special thin cylinder⁽³⁾ on which the current flows only in the direction of ϕ or ψ pitch angle.

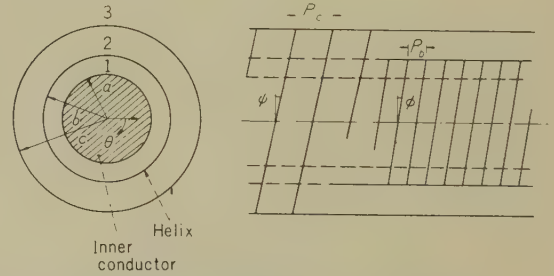


Fig. 10—Construction of double helix.

The electric and magnetic field in mediums 1, 2, and 3 shown in Fig. 10 are given as follows:

$$\left. \begin{aligned} F_r^{(1)} &= j \frac{\beta}{\gamma} \{A^1 I_1(\gamma r) - B^1 K_1(\gamma r)\} \\ F_\theta^{(1)} &= -j \frac{\omega \mu_0}{\gamma} \{C^1 I_1(\gamma r) - D^1 K_1(\gamma r)\} \\ F_z^{(1)} &= A^1 I_0(\gamma r) + B^1 K_0(\gamma r) \end{aligned} \right\}$$

$$H_r^{(1)} = j \frac{\beta}{\gamma} \{C^1 I_1(\gamma r) - D^1 K_1(\gamma r)\}$$

$$H_\theta^{(1)} = j \frac{\omega \epsilon_0}{\gamma} \{A^1 I_1(\gamma r) - B^1 K_1(\gamma r)\}$$

$$H_z^{(1)} = C^1 I_0(\gamma r) + D^1 K_0(\gamma r)$$

$$F_r^{(2)} = j \frac{\beta}{\gamma} \{A^2 I_1(\gamma r) - B^2 K_1(\gamma r)\}$$

$$F_\theta^{(2)} = -j \frac{\omega \mu_0}{\gamma} \{C^2 I_1(\gamma r) - D^2 K_1(\gamma r)\}$$

$$F_z^{(2)} = A^2 I_0(\gamma r) + B^2 K_0(\gamma r)$$

$$H_r^{(2)} = j \frac{\beta}{\gamma} \{C^2 I_1(\gamma r) - D^2 K_1(\gamma r)\}$$

$$H_\theta^{(2)} = j \frac{\omega \epsilon_0}{\gamma} \{A^2 I_1(\gamma r) - B^2 K_1(\gamma r)\}$$

$$H_z^{(2)} = C^2 I_0(\gamma r) + D^2 K_0(\gamma r)$$

$$F_r^{(3)} = -j \frac{\beta}{\gamma} B^3 K_1(\gamma r)$$

$$F_\theta^{(3)} = j \frac{\omega \mu_0}{\gamma} D^3 K_1(\gamma r)$$

$$F_z^{(3)} = B^3 K_0(\gamma r)$$

$$H_r^{(3)} = -j \frac{\beta}{\gamma} D^3 K_1(\gamma r)$$

$$H_\theta^{(3)} = -j \frac{\omega \epsilon_0}{\gamma} B^3 K_1(\gamma r)$$

$$H_z^{(3)} = D^3 K_0(\gamma r)$$

(7)

μ_0 : permeability of vacuum
 A^1, \dots, B^3 : constants.

Here mediums 1, 2, and 3 are assumed to vacuum. The boundary conditions which must be satisfied are as follows:

$$\left. \begin{aligned} \text{at } r=a \quad E_z^{(1)} &= E_\theta^{(1)} = 0 \\ \text{at } r=b \quad E_\theta^{(1)} \cos \phi + E_z^{(1)} \sin \phi &= 0 \\ E_\theta^{(1)} &= E_\theta^{(2)} \\ E_z^{(1)} &= E_z^{(2)} \\ H_\theta^{(1)} \cos \phi + H_z^{(1)} \sin \phi &= H_\theta^{(2)} \cos \phi + H_z^{(2)} \sin \phi \\ \text{at } r=c \quad E_\theta^{(2)} \cos \phi + E_z^{(2)} \sin \phi &= 0 \\ E_\theta^{(2)} &= E_\theta^{(3)} \\ E_z^{(2)} &= E_z^{(3)} \end{aligned} \right\} \quad (8)$$

$$H_\theta^{(2)} \cos \phi + H_z^{(2)} \sin \phi = H_\theta^{(3)} \cos \phi + H_z^{(3)} \sin \phi. \quad (8')$$

Substituting Eqs. (7) into Eqs. (8), we have the following relations between the constants.

$$\left. \begin{aligned} B^1 &= -\frac{I_0(\gamma a)}{K_0(\gamma a)} A^1 \\ C^1 &= \frac{\gamma \tan \phi}{j \omega \mu_0} \cdot \frac{I_0(\gamma b) K_0(\gamma a) - I_0(\gamma a) K_0(\gamma b)}{I_1(\gamma b) K_1(\gamma a) - I_1(\gamma a) K_1(\gamma b)} \\ &\quad \times \frac{K_1(\gamma a)}{K_0(\gamma a)} A^1 \\ D^1 &= \frac{\gamma \tan \phi}{j \omega \mu_0} \cdot \frac{I_0(\gamma b) K_0(\gamma a) - I_0(\gamma a) K_0(\gamma b)}{I_1(\gamma b) K_1(\gamma a) - I_1(\gamma a) K_1(\gamma b)} \\ &\quad \times \frac{I_1(\gamma a)}{K_0(\gamma a)} A^1 \\ A^2 &= \frac{1}{I_0(\gamma b)} \cdot \{I_0(\gamma b) A^1 + K_0(\gamma b) B^1 \\ &\quad - K_0(\gamma b) B^2\} \end{aligned} \right\}$$

where

suffixes r , θ , and z : radial, angular, and longitudinal coordinates

$$\beta^2 = \gamma^2 + \beta_0^2$$

$$\beta_0^2 = \omega^2 \epsilon_0 \mu_0$$

ϵ_0 : dielectric constant of vacuum

$$B^2 = \gamma^2 \tan \phi \tan \phi I_0(\gamma b) \frac{p_2}{p_1} A^1$$

$$p_1 = \gamma^2 \tan \phi \tan \phi \{I_0(\gamma b) K_0(\gamma c) - I_0(\gamma c) K_0(\gamma b)\} - \beta_0^2 \{I_1(\gamma b) K_1(\gamma c) - I_1(\gamma c) K_1(\gamma b)\}$$

$$p_2 = \frac{1}{\tan \phi \tan \phi} \{I_1(\gamma c) K_1(\gamma b) - I_1(\gamma b) K_1(\gamma c)\} \cdot \left\{ \tan^2 \phi \times \frac{I_0(\gamma b) K_0(\gamma a) - I_0(\gamma a) K_0(\gamma b)}{I_1(\gamma b) K_1(\gamma a) - I_1(\gamma a) K_1(\gamma b)} \times \frac{I_1(\gamma a)}{I_1(\gamma b) K_0(\gamma a)} - \beta_0^2 \frac{b}{\gamma} \cdot \frac{I_0(\gamma a)}{K_0(\gamma a)} \times \{K_0(\gamma b) + K_1(\gamma b)\} \right\} + \{I_0(\gamma b) K_0(\gamma a) - I_0(\gamma a) K_0(\gamma b)\} \cdot \frac{\tan \phi}{\tan \phi} \cdot \frac{I_1(\gamma c)}{I_1(\gamma b) K_0(\gamma a)} - \frac{I_0(\gamma c)}{I_0(\gamma b) K_0(\gamma a)} \}$$

$$C^2 = \frac{1}{I_1(\gamma b)} \{I_1(\gamma b) C^1 - K_1(\gamma b) D^1 + K_1(\gamma b) D^2\}$$

$$D^2 = \frac{j\omega \varepsilon_0 \gamma b I_1(\gamma b)}{\tan \phi} \left\{ \frac{1}{\gamma^2 b I_0(\gamma b)} B^2 + \frac{I_0(\gamma a)}{\gamma K_0(\gamma a)} \times \{K_0(\gamma b) + K_1(\gamma b)\} A^1 - \frac{\tan^2 \phi}{\beta_0^2 b} \times \frac{I_0(\gamma b) K_0(\gamma a) - I_0(\gamma a) K_0(\gamma b)}{I_1(\gamma b) K_1(\gamma a) - I_1(\gamma a) K_1(\gamma b)} \times \frac{I_1(\gamma a)}{I_1(\gamma b) K_0(\gamma a)} A^1 \right\}$$

$$B^3 = \frac{1}{K_0(\gamma c)} \{I_0(\gamma c) A^2 + K_0(\gamma c) B^2\}$$

$$D^3 = \frac{1}{K_1(\gamma c)} \{K_1(\gamma c) D^2 - I_1(\gamma c) C^2\}.$$

(9)

By putting Eqs. (9) into Eqs. (7) and employing the condition in Eq. (8'), we can compute the phase constant β .

Thus the electromagnetic fields of the double helix will be completely solved. However as Eqs. (9) are too complicated, we simplify them by adopting the following approximations.

For large x , we have

$$\left. \begin{aligned} I_0(x) &\approx I_1(x) \approx \sqrt{\frac{1}{2\pi x}} e^{-x} \\ K_0(x) &\approx K_1(x) \approx \sqrt{\frac{\pi}{2x}} e^{-x}. \end{aligned} \right\} \quad (10)$$

Using these formulas, we can rewrite Eqs. (9) as follows:

$$\left. \begin{aligned} B^1 &= -\frac{1}{\pi} \varepsilon^{2\xi} A^1 \\ C^1 &= \frac{\gamma \tan \phi}{j\omega \mu_0} A^1 \\ D^1 &= \frac{\gamma \tan \phi}{\pi j\omega \mu_0} \varepsilon^{2\xi} A^1 \\ A^2 &= A^1 \\ B^2 &= -\frac{1}{\pi} \varepsilon^{2\xi} A^1 \\ C^2 &= \frac{\gamma \tan \phi}{j\omega \mu_0} A^1 \\ D^2 &= \frac{\gamma \tan \phi}{\pi j\omega \mu_0} \varepsilon^{2\xi} A^1 \\ B^3 &= \frac{1}{\pi} (\varepsilon^{2\xi} - \varepsilon^{2\zeta}) A^1 \\ D^3 &= \frac{\gamma \tan \phi}{\pi j\omega \mu_0} (\varepsilon^{2\xi} - \varepsilon^{2\zeta}) A^1 \end{aligned} \right\} \quad (11)$$

where we assumed that

$$\left. \begin{aligned} \tan \phi &= \tan \phi \\ \xi &= \gamma a, \quad \eta = \gamma b, \quad \zeta = \gamma c. \end{aligned} \right\} \quad (12)$$

From the last relation of the boundary conditions (8'), we have γ , which degenerate in this case into

$$\gamma = \frac{\beta_0}{\tan \phi}. \quad (13)$$

In the general case when $\tan \phi \neq \tan \phi$, we shall have two solutions for γ .

2.2.4. Constants of the Equivalent Transmission Line of the Double Helix

The equivalent voltage of the double helix is defined by the following equations:
for inner helix

$$E_1 = \int_{r=a}^{r=b} F_r^{(1)} dr \quad (14)$$

for outer helix

$$E_2 = E_1 + \int_{r=b}^{r=c} F_r^{(2)} dr \quad (15)$$

The equivalent currents are determined as follows:

for inner helix

$$I_1 = p_b (H_z^{(1)} - H_z^{(2)})_{r=b} \quad (16)$$

for outer helix

$$I_2 = p_c (H_z^{(2)} - H_z^{(3)})_{r=c}. \quad (17)$$

From Eqs. (7) and (11) we have the following values of voltage and current:

$$E_1 = -j \frac{\beta \tan^2 \phi}{\beta_0^2} \cdot \frac{\varepsilon^\eta}{\sqrt{2\pi\eta}} (1 - \varepsilon^{2\xi - 2\eta}) A^1 \quad (18)$$

$$E_2 = -j \frac{\beta \tan^2 \phi}{\beta_0^2} \cdot \frac{\varepsilon^\zeta}{\sqrt{2\pi\zeta}} (1 - \varepsilon^{2\xi - 2\zeta}) A^1 \quad (19)$$

$$I_1 = 0 \quad (20)$$

$$I_2 = \frac{2\zeta \tan^2 \phi}{j\omega\mu_0} \cdot \frac{\varepsilon^\zeta}{\sqrt{2\pi\zeta}} A^1. \quad (21)$$

For our experimental tubes, $\tan \phi$ is small and we obtained the following relations.

$$\left. \begin{aligned} \beta^2 &= \gamma^2 + \beta_0^2 = \left(\frac{\beta_0}{\tan \phi} \right)^2 + \beta_0^2 \\ \beta &\approx \gamma = \frac{\beta_0}{\tan \phi} \end{aligned} \right\} \quad (22)$$

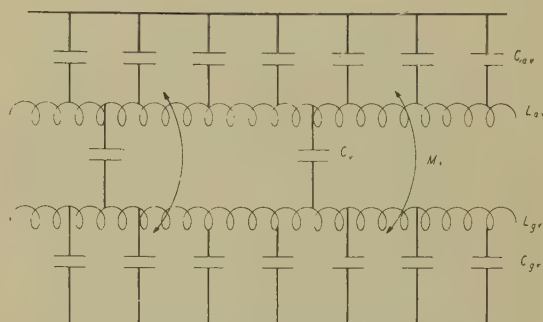


Fig. 11—Equivalent line of double helix.

Now, we can synthesize an equivalent line on which the voltage, the current, and the propagation constant are the same as those of the double helix presented in Eqs. (18)–(22). If the equivalent line is of the type presented in Fig. 11, then the voltage and current of the line may be expressed by the following equations.

$$\left. \begin{aligned} -\frac{dE_{gv}}{dz} &= j\omega L_{av} I_{av} + j\omega M_v I_{gv} \\ -\frac{dE_{gv}}{dz} &= j\omega L_{gv} I_{gv} + j\omega M_v I_{av} \\ -\frac{dI_{av}}{dz} &= j\omega C_{av} E_{av} + j\omega C_v (E_{av} - E_{gv}) \\ -\frac{dI_{gv}}{dz} &= j\omega C_{gv} E_{gv} + j\omega C_v (E_{gv} - E_{av}) \end{aligned} \right\} \quad (23)$$

where

E_{av} : voltage of the anode line
 E_{gv} : voltage of the grid line

I_{av} : current of the anode line
 I_{gv} : current of the grid line.

The phase constant of this equivalent line is calculated as follows:

$$\left. \begin{aligned} \Gamma_v &= \sqrt{-A_v \pm \frac{\sqrt{A_v^2 - 4B_v}}{2}} \\ \text{where} \\ A_v &= \omega^2 L_{gv}(C_{gv} + C_v) \\ &\quad + \omega^2 L_{av}(C_{av} + C_v) - 2\omega^2 M_v C_v \\ B_v &= (L_{av} L_{gv} - M_v^2) \\ &\quad \times \{ \omega^4 C_v(C_{av} + C_{gv}) + \omega^4 C_{av} C_{gv} \} \end{aligned} \right\} \quad (24)$$

Using the additional relation that $C_{av} \ll C_v$, C_{gv} , we can determine the line constants L_{av} , C_{av} , L_{gv} , M_v , and C_v by relating the voltage and current of the line to the equivalent voltage and current of the helix:

$$E_{av} = E_2, \quad E_{gv} = E_1, \quad I_{av} = I_2, \quad I_g = I_1, \quad \Gamma_v = \beta.$$

Thus, we obtain the constants of the equivalent line of the passive double helix shown in Fig. 9 (d), which are as follows:

$$\left. \begin{aligned} L_{av} &= \frac{\mu_0 \beta^2}{2\beta_0^2 \zeta} (1 - \varepsilon^{2\xi - 2\zeta}) \\ C_{av} &= 0 \\ L_{gv} &= \frac{\mu_0 \beta^2}{2\beta_0^2} \sqrt{\frac{1}{\eta \zeta}} \varepsilon^{\eta - \zeta} (1 - \varepsilon^{2\xi - 2\eta}) \\ C_{gv} &= \frac{2\beta_0^2}{\mu_0 \omega^2} \sqrt{\eta \zeta} \frac{\varepsilon^{\xi - \eta}}{1 - \varepsilon^{2\xi - 2\eta}} \end{aligned} \right\}$$

$$\left. \begin{aligned} M_v &= \frac{\mu_0 \beta^2}{2\beta_0^2} \sqrt{\frac{1}{\eta \zeta}} \varepsilon^{\eta - \zeta} (1 - \varepsilon^{2\xi - 2\eta}) \\ C_v &= \frac{2\beta_0^2 \zeta^2}{\mu_0 \omega^2} \frac{1}{1 - \varepsilon^{2\xi - 2\zeta} - \sqrt{\frac{\zeta}{\eta}} \varepsilon^{\eta - \zeta} (1 - \varepsilon^{2\xi - 2\eta})} \end{aligned} \right\} \quad (26)$$

These values of inductance and capacitance vary with frequency. Frequency dependence is, however, practically negligible.

2.2.5. Constants of Equivalent Single-Helix Transmission Line

The method of computing the equivalent line constants of the single helix was described in the preceding paper, and the results calculated are as follows:

$$\left. \begin{aligned} L_c &= \frac{\beta_c}{\omega} Z_{0c} \\ C_c &= \frac{\beta_c}{\omega} \cdot \frac{1}{Z_{0c}} \end{aligned} \right\} \quad (27)$$

$$\begin{aligned} Z_{0c} &\approx \frac{\omega \mu_0 b'}{p \beta_c \tan \phi_c} \cdot \frac{K_1(\beta_c b')}{K_1(\beta_c a')} \\ &\quad \times \{ I_1(\beta_c b') K_1(\beta_c a') - I_1(\beta_c a') K_1(\beta_c b') \} \end{aligned} \quad (28)$$

where

L_c : series inductance of equivalent line
 C_c : shunt capacitance of equivalent line
 Z_{0c} : characteristic impedance of single helix
 a' : radius of inner conductor
 b' : radius of helix
 ϕ_c : pitch angle of helix.

The phase constant β_c is given by the following equation:

$$\frac{\omega^2 \varepsilon_0 \mu_0}{\beta_c^2 \tan^2 \phi_c} \approx \frac{I_0(\beta_c b') K_1(\beta_c a') + I_1(\beta_c a') K_0(\beta_c b')}{I_1(\beta_c a') K_1(\beta_c b') - I_1(\beta_c b') K_1(\beta_c a')} - \frac{K_0(\beta_c b')}{K_1(\beta_c b')} \quad (29)$$

$$\frac{\varepsilon^* I_1(\beta_c b') K_0(\beta_c a') + I_0(\beta_c a') K_1(\beta_c b')}{I_0(\beta_c a') K_0(\beta_c b') - I_0(\beta_c b') K_0(\beta_c a')} - \frac{K_1(\beta_c b')}{K_0(\beta_c b')}.$$

where ϵ^* : dielectric constant of ceramics.

Applying the above computing method to the helixes shown in Fig. 9 (c) 2 and 3, we can compute the equivalent line constants L_{ac} , C_{ac} , L_{gc} , and C_{gc} of Fig. 9 (d) 2 and 3.

2.2.6. Composite Line

The composite line constants of Fig. 9 (e) can be computed from Eqs. (6), substituting the calculated values of L_{ac} , C_{ac} , L_{gc} , C_{gc} , and the constants given in Eqs. (26).

3. Analysis of Experimental Results

In this section we analyze the measured characteristics of the experimental tubes, using the theory described in the preceding section.

3.1. Equivalent Line Constants

We compute first the equivalent line constants of the double helix shown in Fig. 9 (c) 1. The dimensions of the double helix are as follows;

$$a=4.3 \text{ mm}, \quad b=4.4 \text{ mm}, \quad c=5.5 \text{ mm}$$

$$\tan \phi = \tan \psi = 1.42 \times 10^{-2}$$

where a , b , and c have the meanings shown in Fig. 10. We calculate the line constants at 300 Mc and hereafter we shall neglect their frequency dependence.

$$L_{av} = 8.33 \times 10^{-4} \text{ H/m}$$

$$C_{av} = 0$$

$$L_{gv} = 6.72 \times 10^{-5} \text{ H/m}$$

$$C_{gv} = 8.2 \times 10^{-10} \text{ F/m}$$

$$M_v = 6.72 \times 10^{-5} \text{ H/m}$$

$$C_v = 7.2 \times 10^{-11} \text{ F/m.}$$

The equivalent line constants of helixes of the type shown in Fig. 9 (c) 2 and 3 with the following dimensions are computed.

The dimensions of the helixes are:

| | radius of inner conductor | radius of helix |
|-------|------------------------------|--------------------|
| anode | 4.67 mm | 5.5 mm |
| grid | 2.86 mm | 3.36 mm |

The constants are

$$L_{ac} = 8.93 \times 10^{-5} \text{ H/m}$$

$$C_{ac} = 1.44 \times 10^{-9} \text{ F/m}$$

$$L_{gc} = 1.08 \times 10^{-4} \text{ H/m}$$

$$C_{gc} = 1.27 \times 10^{-9} \text{ F/m.}$$

The composite line constants in Fig. 9 (e) or Fig. 7 are computed from Eqs. (6). The contour lengths of the helix of the experimental tubes are:

$$l_{av} = 27.3 \text{ mm}, \quad l_{ac} = 7.68 \text{ mm}$$

$$l_{gv} = 8.0 \text{ mm}, \quad l_{gc} = 13.1 \text{ mm.}$$

Therefore the line constants are as follows:

$$L_a = 6.7 \times 10^{-4} \text{ H/m}$$

$$C_a = 2.5 \times 10^{-9} \text{ F/m}$$

$$L_g = 8.7 \times 10^{-5} \text{ H/m}$$

$$C_g = 1.03 \times 10^{-9} \text{ F/m}$$

$$M = 5.25 \times 10^{-5} \text{ H/m}$$

$$C = 1.64 \times 10^{-11} \text{ F/m.}$$

The mutual conductance per unit axial length is computed from the static characteristics of the experimental tube.

$$g_m = 1.33 \text{ U/m.}$$

3.2. Propagation Constants

The propagation constants, which can be computed from Eq. (4), are presented in Fig. 12. The attenuation constants and the phase constants in the figure have the following relation with the propagation constants.

$$\left. \begin{aligned} \Gamma_1 &= \alpha_1 + j\beta_1 \\ \Gamma_2 &= \alpha_2 + j\beta_2. \end{aligned} \right\} \quad (30)$$

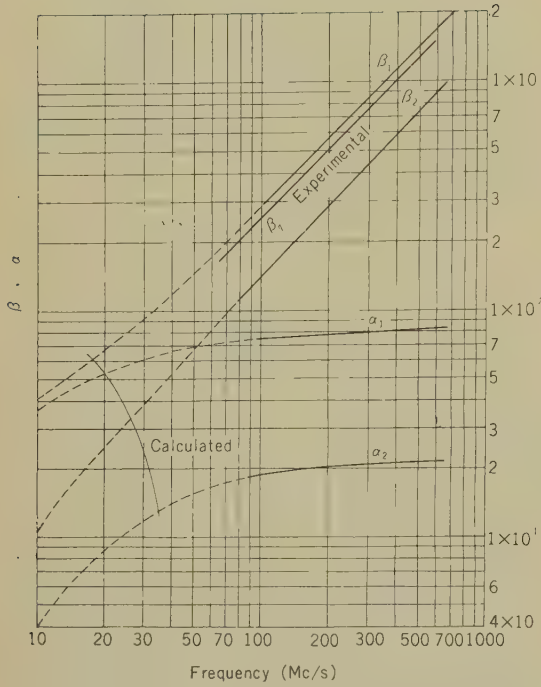


Fig. 12—Propagation constants.

In Fig. 12, Γ_2 represents the attenuation wave, while Γ_1 represents the amplification wave.

We suspect the calculated results in Fig. 12 contain some error in the low frequency region because we have adopted the approximation of Eq. (10). However the fit of the experimental data with the calculated curves seems to be quite good.

3.3. Impedance Matching

We have four modes of wave traveling on

the helical lines of the tube.

$$E = m_1 \varepsilon^{\Gamma_1 z} + m_2 \varepsilon^{-\Gamma_1 z} + m_3 \varepsilon^{\Gamma_2 z} + m_4 \varepsilon^{-\Gamma_2 z} \quad (31)$$

where E : voltage or current on the line
 m_1, m_2, m_3, m_4 : constants.

In order to obtain the correct solution of the voltage and current, we must solve the four equations of the voltage and current on the anode and grid lines under the following boundary conditions:

$$\left. \begin{array}{l} \text{at } z=0 \quad E_g = E_0 \\ \quad \quad -E_a = Z_a I_a \\ \text{at } z=l \quad E_g = Z_g I_g \\ \quad \quad E_a = Z_a I_a \end{array} \right\} \quad (32)$$

where

E_0 : input voltage of grid line

Z_g : grid line termination impedance

Z_a : anode line termination impedance.

After this calculation is performed, the optimum termination impedance can be determined. As the above calculation is, however, too complicated, we may neglect the attenuating wave for simplification.

We have for the forward amplifying wave on the grid line

$$E_g = \varepsilon^{-\Gamma_1 Z} \quad (33)$$

By employing this equation we can derive the other values of voltage and current from Eqs. (1).

$$\left. \begin{array}{l} E_a = \frac{\{\omega^2 L_g (C_g + C) - \omega^2 M C + j\omega M g_m + \Gamma_1^2\}}{\omega^2 \{L_g C - M(C_a + C)\}} E_g \\ I_a = \frac{\omega^2 \{M^2 (C_a + C) + L_a L_g (C_g + C) - M C (L_a + L_g)\} + j\omega M L_a g_m + \Gamma_1^2 L_a}{j\omega (L_a L_g - M^2) \{L_g C - M(C_a + C)\}} \Gamma_1 E_g \\ I_g = \frac{\omega^2 [M \{L_g (C_g + C) + L_a (C_a + C)\} - C (L_a L_g + M^2)] + j\omega M^2 g_m + \Gamma_1^2 M}{j\omega^3 (M^2 - L_a L_g) \{L_g C - M(C_a + C)\}} \Gamma_1 E_g \end{array} \right\} \quad (34)$$

The matching impedance of the anode and the grid lines is calculated as follows:

$$\left. \begin{aligned} Z_{0a} &= \frac{E_a}{I_a} = R_{0a} + jX_{0a} \\ Z_{0g} &= \frac{E_g}{I_g} = R_{0g} + jX_{0g} \end{aligned} \right\} \quad (35)$$

where $R_{0a} \dots X_{0g}$ are the real and imaginary parts of impedances Z_{0a} and Z_{0g} . Fig. 13 shows $R_{0a} \dots X_{0g}$. As the values of imaginary parts X_{0a} and X_{0g} diminish, those of Z_{0a} and Z_{0g} become real in the high frequency region. The experimentally determined values of the matching resistances are shown in the figure.

3.4. Gain

The voltage gain of this tube N can be computed from the following equation.

$$N = \frac{E_{g,z=l}}{E_{g,z=0}} \cdot \frac{E_a}{E_g} \quad (36)$$

where

$E_{g,z=0}$: grid line voltage at $z=0$ (input voltage)

$E_{g,z=l}$: grid line voltage at $z=l$

E_a : anode line voltage

E_g : grid line voltage.

The ratio of the anode line voltage to the grid line voltage E_a/E_g is kept constant throughout the line and it can be calculated from Eq. (34) as follows:

$$\begin{aligned} \frac{E_a}{E_g} &= \frac{\omega^2 L_g (C_g + C) - \omega^2 MC + j\omega M g_m + \Gamma_1^2}{\omega^2 \{L_g C - M(C_a + C)\}} \\ &= R_e \left(\frac{E_a}{E_g} \right) + jI_m \left(\frac{E_a}{E_g} \right) \end{aligned} \quad (37)$$

where

$R_e(E_a/E_g)$: real part of E_a/E_g

$I_m(E_a/E_g)$: imaginary part of E_a/E_g .

The calculated results of the above equation are shown in Fig. 14.

The value of $E_{g,z=l}/E_{g,z=0}$ can be easily computed from the following equation.

$$\frac{E_{g,z=l}}{E_{g,z=0}} = e^{\alpha_1 l} \quad (38)$$

By substituting the value of α_1 in Fig. 12 and the value $l=30$ mm, we have

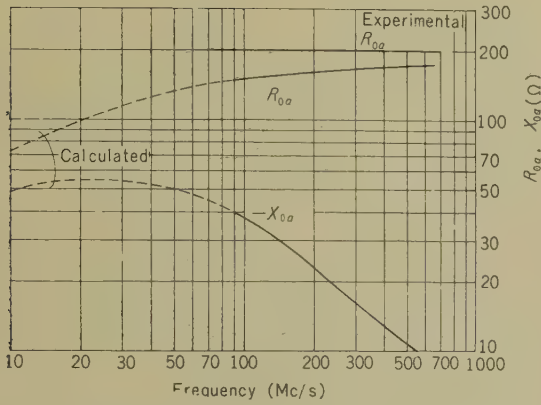


Fig. 13 (a)—Matching impedance of anode line, Z_{0a} .

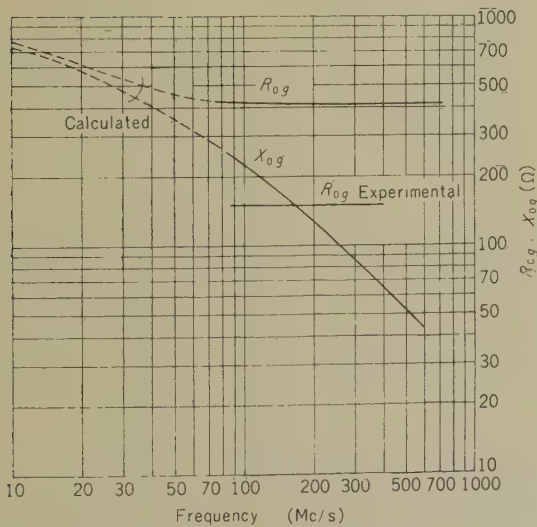


Fig. 13 (b)—Matching impedance of grid line, Z_{0g} .

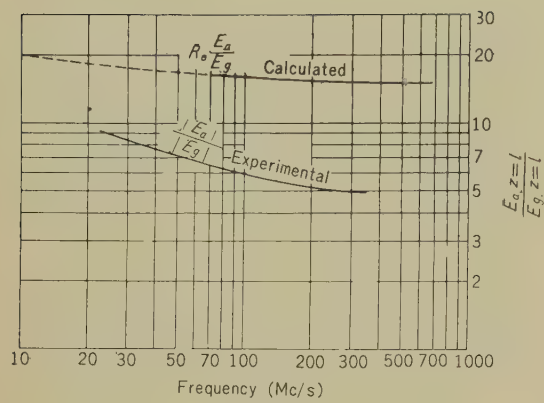


Fig. 14—Ratio of anode voltage to grid voltage.

$$\frac{E_{g,2-1}}{E_{g,2=0}} = 11.0$$

Now we can compute the theoretical value of the gain according to Eq. (36). For example, at 300 Mc/s

$$N=165.$$

On the other, the experimental value of gain is about 2.5. The difference may be due to the fact that we have neglected the line loss in the theoretical calculation.

Conclusion

The anode and the grid of our experimental

feedback-type distributed-amplifier tube composed a double helical line, and the measured value of its amplification band is from zero to 300 Mc/s. In this paper theoretical considerations on the operation of the tube and on the characteristics of the double helix have been carried out.

Therefore, it can be concluded that amplification frequency band of the present tube has been greatly extended in comparison to that of the former tube.⁽¹⁾

Here the author wishes to point out that the frequency limit of the amplification band of the experimental tube was due to the cutoff frequency of the output termination networks.

Acknowledgment

The author avails of this opportunity to express his gratitude to his associates in the Model Shop Section. Hearty thanks are extended to Mr. Z. Kiyasu and Dr. M. Kuwata for their beneficial discussions.

References

- (1) T. Kojima: Distributed Amplifier Tube, *Rev. Electr. Commun. Labor. NTT*, Jap. 8, 7-8, 1960.
- (2) I. A. D. Lewis: Analysis of a Transmission Line Type of Thermionic-Amplifier Valve P.I.E.E. 100, Part IV, 5, 1950.
- (3) J. R. Pierce: *Traveling-wave Tubes*, Van Nostrand, 1950.

* * * *

Recent Development of Quartz Crystal Units for Telecommunication*

Kiyoshi TAKAHARA†

A new method and equipments devised for manufacture of 1-1,000 kc crystal units, analytical studies on the effects of evaporated metal films on the characteristics of the crystal resonator vibrating in the contour modes, development of crystal units in the frequency range 10-100 Mc, a new device for adjusting the load capacitance of crystal oscillators to a specified value and its application to some kinds of crystal oscillators, and development of a small and precise constant temperature oven for crystal units are described in this paper.

1. Introduction

Quartz crystal units have widely been used for the generation of stable frequency. Today, no communication system can exist without a master oscillator, in which a quartz crystal unit is the key component.

In recognition of this vital importance of quartz crystal units in present and future long-distance multi-channel communication systems, the Electrical Communication Laboratory has carried out a large-scale program of research and development of quartz crystal units for the past ten years.

This paper, which presents some results of this work, covers:

(1) High-stability crystal units whose quality factor, Q , is larger than two million at room temperature.

(2) Development of overtone crystal units in the frequency range of 10~100 Mc.

(3) A new device for adjusting the load capacitance of crystal oscillators.

(4) Development of a small constant-temperature oven for crystal units.

2. Improvement of the Characteristics of Low-Frequency Crystal Units

2.1. General

In order to produce high-stability crystal units in the 1 kc~1,000 kc frequency range, it is very important that both stability and vibration loss be studied in order to determine the most favorable design procedures. This section treats the experimental studies carried out for this purpose.

2.2. Etching

Etching after the final lapping of the crystal plates was found to be very effective for reducing vibration loss and for improving the drive level characteristics of the crystal units. The etch consisted of a saturated water solution of ammonium bifluoride at 24°C.

Table 1 illustrates the effect of etching on some typical samples. The crystal plates are 200 kc, CT-cut square plates 1 mm thick.

* Ms in Japanese received by the Electrical Communication Laboratory on 8 January, 1959. Originally published in the *Kenkyū Zituyōka Hōkoku (Electrical Communication Laboratory Technical Journal)*, Vol. 8, No. 2, pp. 123-201, 1959.

† Circuit Components Research Section.

Table 1
IMPROVEMENT OF SERIES RESISTANCE R_1 BY ETCHING
(R_1 BEING MEASURED IN THE ATMOSPHERE)

| Etching Time Sample Number | Before Etching | 1 hr. | 2 hrs. | 3 hrs. | 4 hrs. | 5 hrs. | 7 hrs. |
|-------------------------------|----------------|--------------|--------------|--------------|--------------|--------------|--------------|
| 1 | 1050 Ω | 860 Ω | 850 Ω | 870 Ω | — | 850 Ω | — |
| 2 | 1050 Ω | 850 Ω | 840 Ω | 840 Ω | — | 830 Ω | — |
| 3 | 1050 Ω | 840 Ω | 835 Ω | — | 810 Ω | — | 820 Ω |

Before being etched, they were lapped with AO-emery No. 304, and after each etching period, all plates were mounted in the same manner. Series resistance R_1 and series resonance frequency were measured in the atmosphere.

As will be shown later, the effect of etching is more noticeable when the crystal units are sealed in a vacuum. Namely, in the case of evacuated crystal units, Q becomes ten or more times as large after etching.

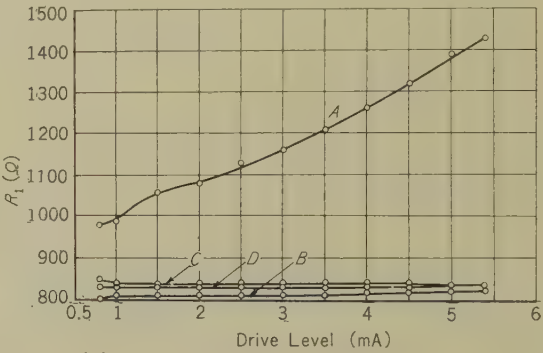
Fig. 1 illustrates the improvement of drive level characteristics of the crystal plates tabulated in Table 1. As may be seen from the figure, the frequency and resistance of crystal units which have been etched are substantially constant for drive levels up to 5 mA.

Therefore, all plates were etched for about one hour at 24°C.

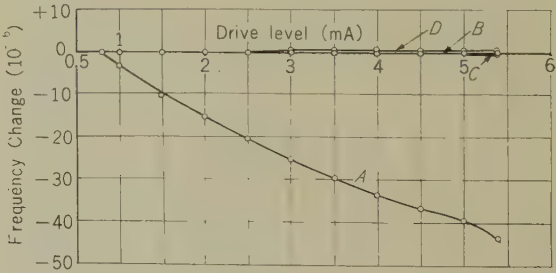
2.3. Mounting Processes and their Effects on the Characteristics of the Crystal Units

2.3.1. General

Among the several methods for the mounting of resonators vibrating in the contour modes, wire mounting¹⁾²⁾, as schematically shown in Fig. 2, was found to be the most suitable.³⁾ In the course of the manufacturing process, however, there are many factors which produce important effects on the characteristics of the crystal units. The following



(a) Change of series resistance R_1



(b) Frequency change

A : Before etching,
B : After etching for 1 hr.,
C : After etching for 5 hrs.,
D : After etching for 7 hrs.

Fig. 1—Improvement of drive level characteristics by etching (the crystal plates are 200 kc, CT-cut plates 1 mm thick).

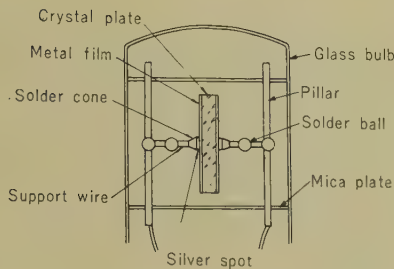
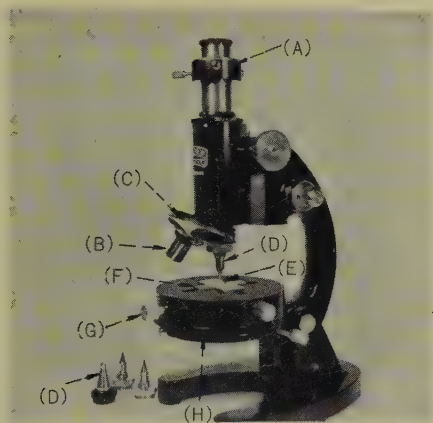


Fig. 2—Wire mounting.



(A): Eye piece with precise gauge attached,
(B): Objective, (C): Revolver,
(D): Spotting mandrel, (E): Crystal plate,
(F): Precise vice. (G): Knob for moving
the base precisely, (H): Base.

Fig. 3—Apparatus used for the application
of silver paste to the center of the
crystal plate.

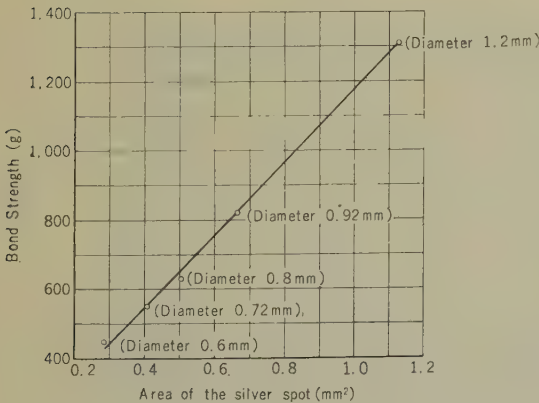


Fig. 4—Bond strength between silver spot
and crystal plate.

are among the most important.

2.3.2. Silver Spotting

In the author's device, silver paste is applied to the crystal plate so that the center of the silver spot coincides with the node of vibration as accurately as possible, in order to obtain an accurate attachment for the support wire in the soldering stage which follows.

The apparatus used for the application of the silver paste to the center of the crystal plate is shown in Fig. 3. This apparatus chiefly consists of a microscope, with a precise gauge and a vice attached to it. By using this apparatus, the silver paste can be applied with an accuracy of 5/100 mm or better.

Fig. 4 illustrates the bond strength between the silver spot and the crystal plate, while Fig. 5 shows the effects of an increase in the area of the silver spot on the drive level characteristics of the crystal units. These experiments suggest that the area of the silver spot should be made as small as possible, so long as the mechanical robustness of the crystal unit is not sacrificed.

2.3.3. Soldering

The equipment used for soldering the support wires to the center of the silver spot is shown in Fig. 6. Soldering is carried out with hot air whose temperature is 250~280°C and whose flow rate is about 5 l per minute.

Some experimental results, illustrative of the change of characteristics of the crystal units caused by change of the amount of solder (from 0.05 mg to 2.1 mg), are shown in Figs. 7 to 9. In these experiments, the amount of solder on the same crystal plate was changed.

Fig. 7 illustrates the temperature characteristics of series resistance R_1 , and Fig. 8 illustrates the drive level characteristics. In Fig. 9 (a), the frequency-temperature characteristics of the two crystal units are compared, and in Fig. 9 (b), the difference between the two curves is illustrated in order to represent the effect produced by the increase of solder.

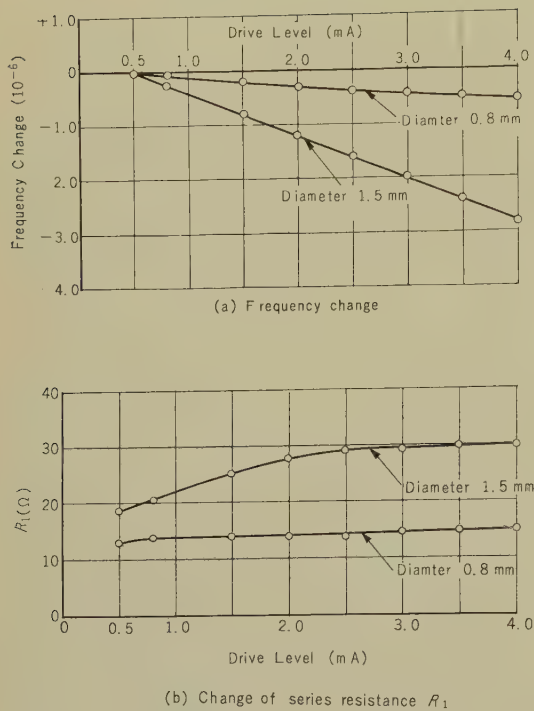
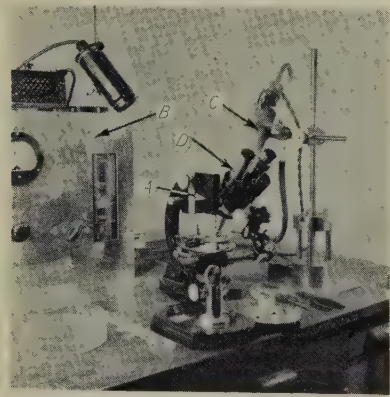


Fig. 5—Effects of an increase in the area of the silver spot on the drive level characteristics of the crystal units (crystal plate is 200 kc CT-cut plate 0.8 mm thick).



A: Soldering Machine,
B: Constant air flow generator,
C: Furnace for making hot air,
D: Microscope.

Fig. 6—Equipment used for soldering support wire to the silver spot.

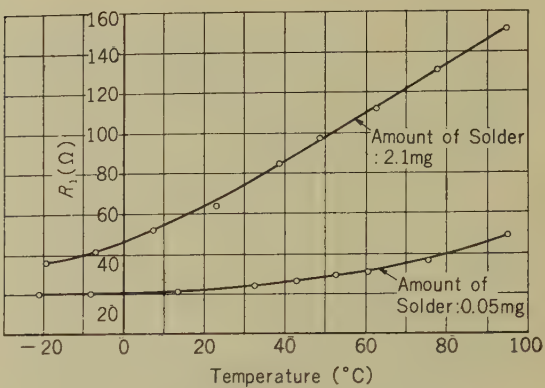


Fig. 7—Change of temperature characteristics of series resistance R_1 caused by change of the amount of solder for a 200 kc CT-cut crystal plate 0.75 mm thick.

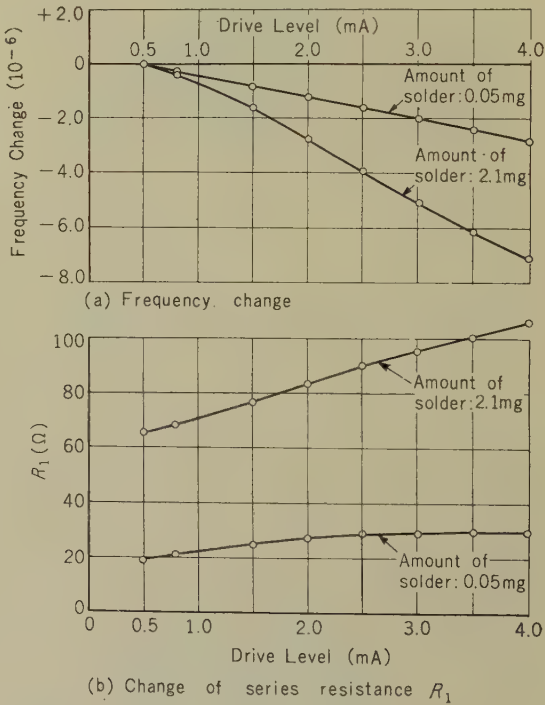


Fig. 8—Change of drive level characteristics of crystal units caused by the change of amount of solder (for a 200 kc CT-cut crystal plate 0.75 mm thick).

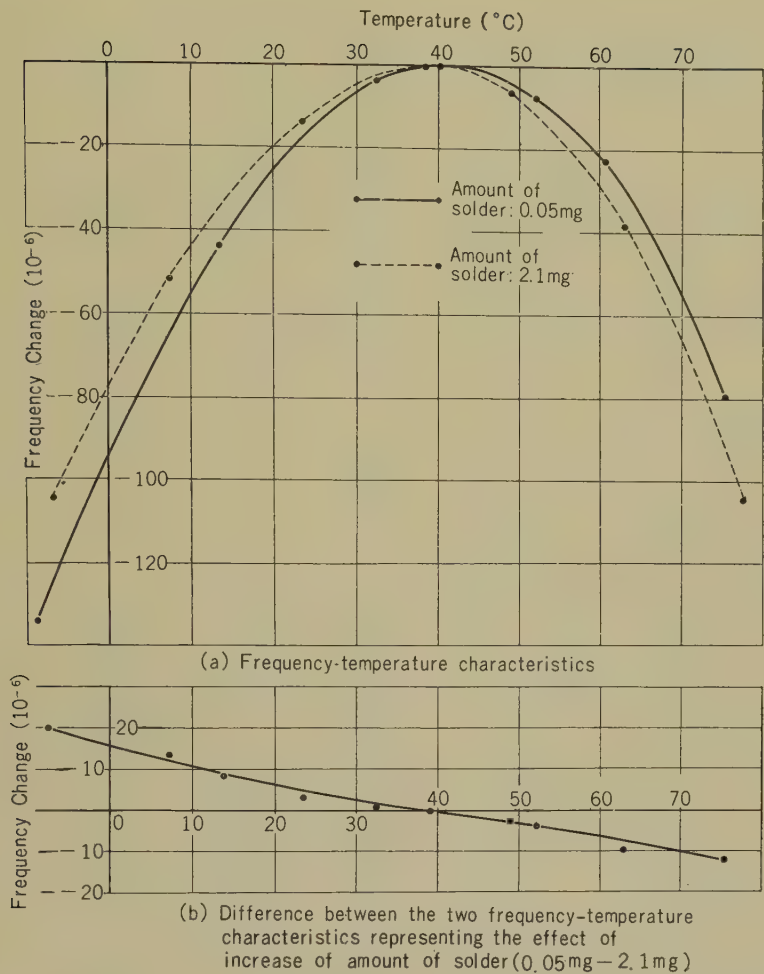
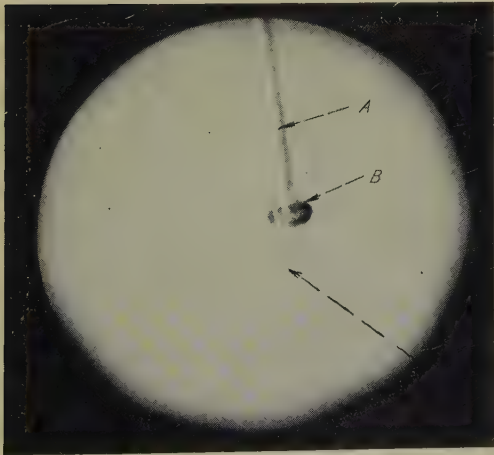


Fig. 9—Change of frequency-temperature characteristics caused by increase of amount of solder for a 200 kc CT-cut crystal plate 0.75 mm thick.



A : Support wire, B : Attachment point.
C : Crystal plate.

Fig. 10—A headed wire attached to crystal plate.

From these experiments, it is apparent that the amount of solder should be as small as possible so long as the bond strength between the support wire and the crystal plate is satisfactory.

As shown in Fig. 10, a wire with an upset head (called headed wire) enables us to attach the support wires to the crystal plate with the extremely small amount of solder of about 0.03~0.05 mg without sacrificing the strength of the bond between them.

2.3.4. Accuracy of Attachment of the Support Wire

Some examples representing the accuracy of attachment of the support wire in crystal units actually manufactured are shown in Fig. 11. In this figure, the deviation of the attached points from the desired points are plotted for nine crystal units. The figure shows that most of the support wires have been attached to the desired point with an error of less than 0.1 mm.

Some experimental results representing the

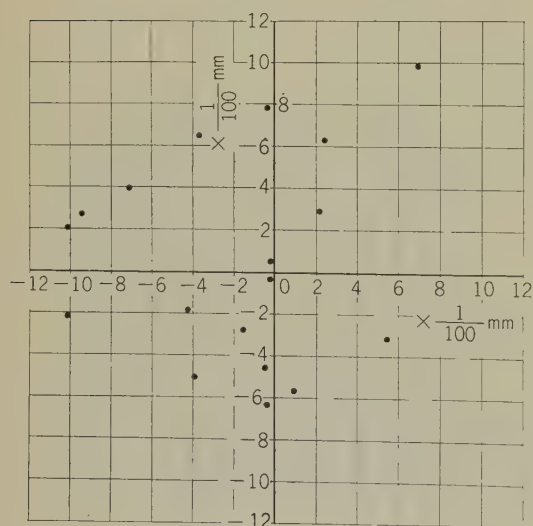


Fig. 11—Some examples representing the deviation of the attachment points from the desired points (0.15 mm phosphor-bronze support wires).

relations between the accuracy of attachment of support wires and the characteristics of the crystal units are shown in Fig. 12. In this experiment, a wire was attached to the center of the plate as accurately as possible on one of the major surfaces of each crystal, and on the other, the attachment point was either 0.5 mm, 0.25 mm, or less than 0.1 mm from the center of the plate. Then, the temperature characteristics of series resistance R_1 of these crystal units were measured in vacuum. Fig. 12 shows that when high quality crystal units must be made, support wires must be attached to the nodal point as accurately as possible.

2.3.5. Electrode Plating

The metal film electrodes were deposited by evaporation. In crystal resonators vibrating in the contour modes, the metal film produces considerable effects on both the frequency and vibration loss characteristics of the crystal units, which makes it necessary to evaluate these effects precisely. Some analytical studies on this subject will be explained in Section 3.

2.3.6. Effects of Vibration of the Support Wires

The experimental device used for detecting the effects of vibration of support wires on the characteristics of the crystal units is illustrated in Fig. 13. In this experiment, one of the support wires was fixed to the frame at the proper length, while on the other a V-shaped wire with one-gm weights attached to each end was hung in such manner that the length l shown in Fig. 13 could be accurately changed. The crystal unit was connected to a CI meter, and frequency and activity were measured in the atmosphere.

Fig. 14 (a) and (b) illustrate the relations between the characteristics of the crystal units and the length of the support wires: In Fig. 14 (a), the wires are attached to the nodes on both the major surfaces; in Fig. 14 (b) one of the wires is attached to the node and the other to the point 0.5 mm from the

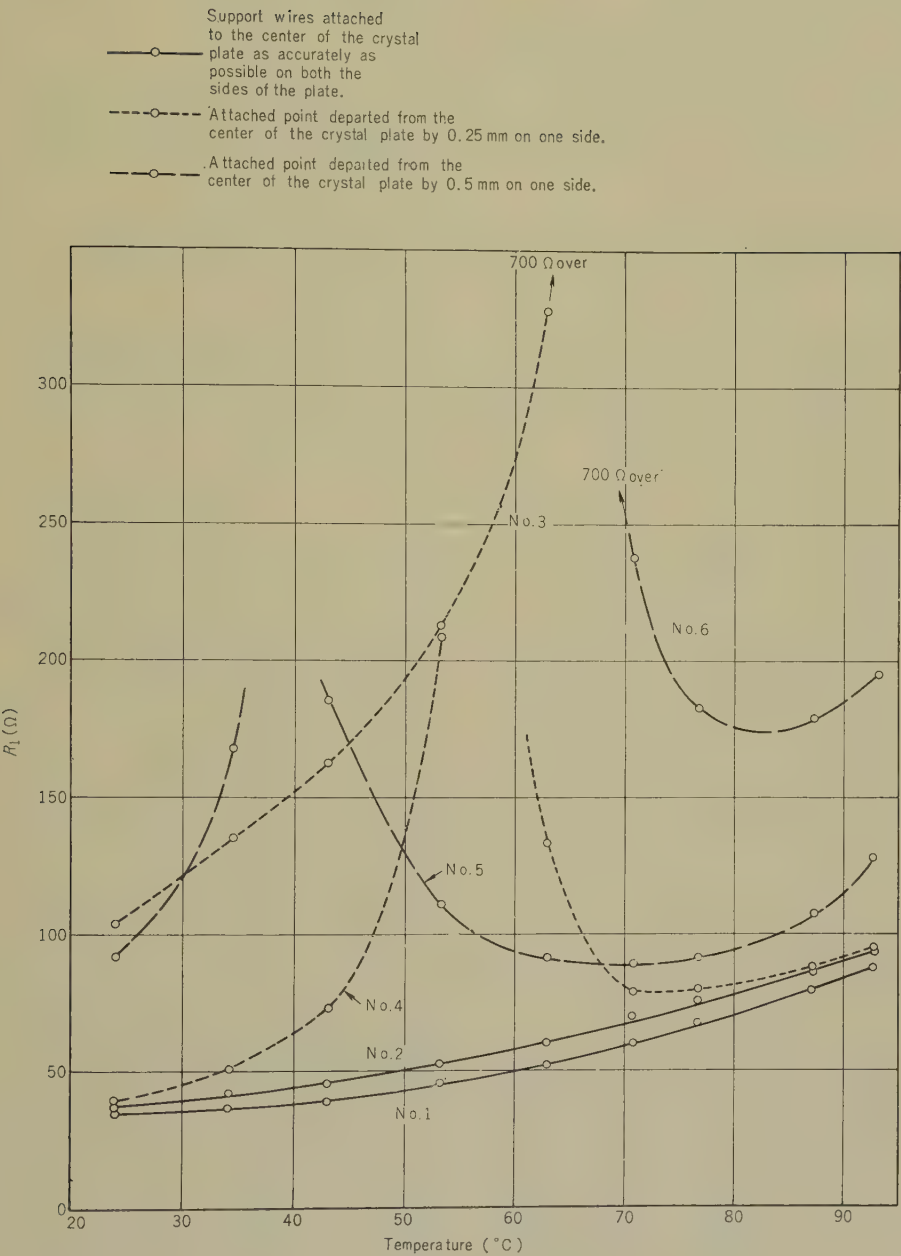


Fig. 12—Relations between the accuracy of attachment of support wires and the temperature characteristics of series resistance R_1 for 300 kc, crystal plates with 1.0 mm thick. The 0.15 mm phosphor-bronze support wires (headed wires) were used.

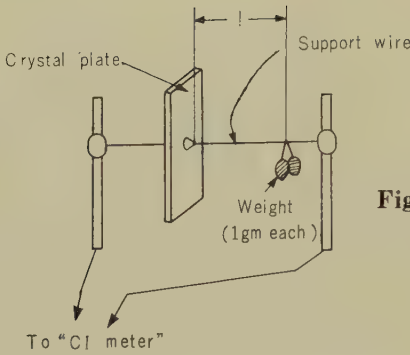
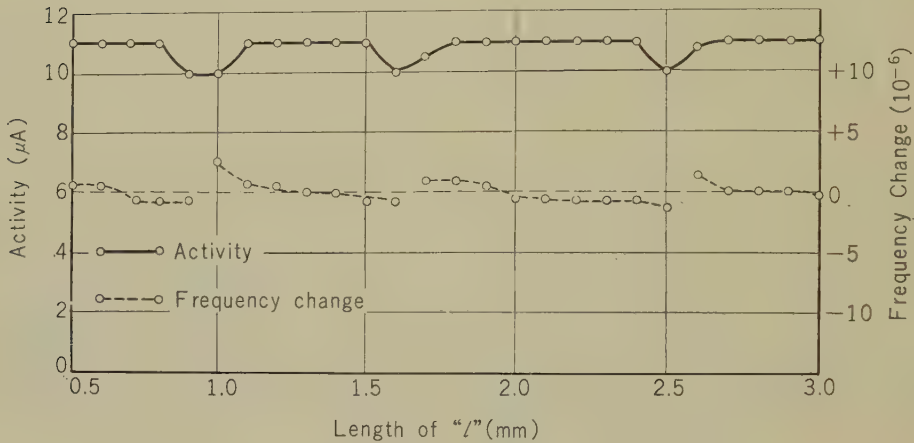
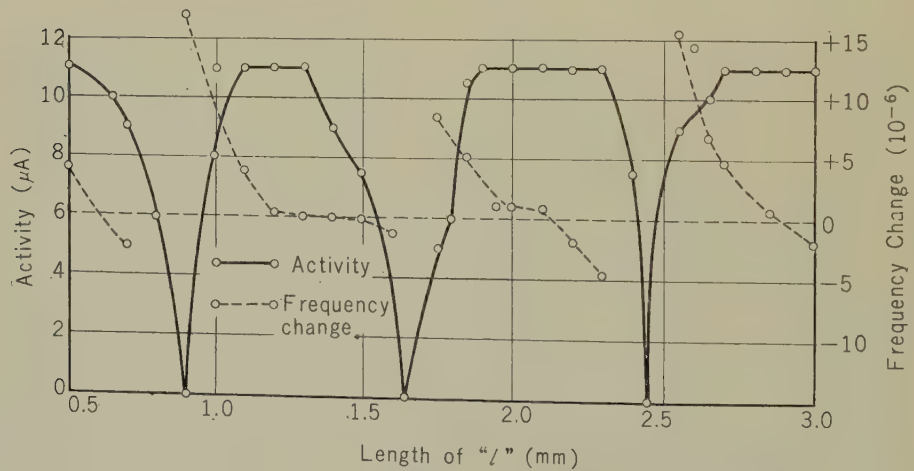


Fig. 13—Experimental device for detecting the effects of the vibration of support wires on the characteristics of the crystal units.



(a) Support wires were attached to the node on both the major surfaces.



(b) One of the support wires was attached to the node, while the other to the point departing from the node by 0.5 mm.

Fig. 14—Relation between the characteristics of the crystal units and the length of support wire for 300 kc, CT-cut, 1.0 mm thick crystal plate measured in the atmosphere.

node.

From these experiments and from some other experiments, the following are concluded:

(a) The effects of the vibration of support wires on the characteristics of the crystal units are closely related to the accuracy of attachment of the support wires and the diameters of the wires. This suggests that the wires should be attached to the nodes as accurately as possible, and the diameters of the wires should be made as small as possible; so long as the mechanical robustness of the crystal unit is satisfactory.

(b) The support wires should be fixed to the frame at the points where activity is maximum and frequency change is minimum.

2.3.7. Vacuum Sealing

Usually, when crystal resonators vibrating in the contour modes are sealed in a vacuum, their frequency increases slightly, while vibration loss decreases. As illustrated in Table 2, the decrease in vibration loss depends a great deal on the treatment of the crystal plate and the mounting features of the crystal units—amount of solder, thickness of the metal film, diameter of the support wire, etc.—and in a suitably manufactured crystal unit the improvement of Q due to sealing in a vacuum reaches thirty or more times.

As a result of experiments for examining the relations between the characteristics of the crystal units and the vacuum, it was clarified that when the vacuum exceeds 1×10^{-1} mm Hg, the frequency and the vibration loss are scarcely changed by increase of the vacuum; therefore we used a vacuum of about 1×10^{-2} mm Hg for all crystal units.

2.4. Some Features of the Crystal Units

The crystal units manufactured by the processes illustrated above proved to have very high Q and excellent reproducibility.

Fig. 15 illustrates Q and R_1 of three CT-cut crystal units manufactured under the same conditions. As shown in this figure, values of Q as large as two million or better

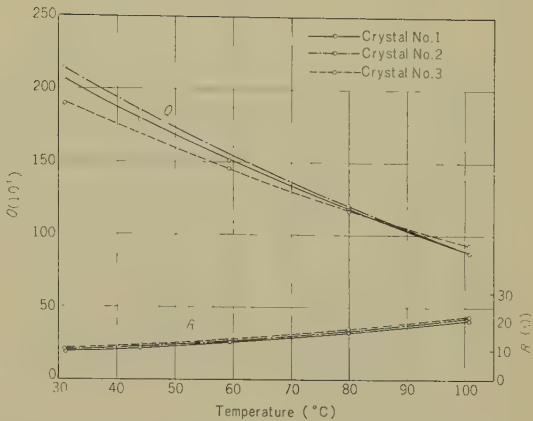


Fig. 15— Q and series resistance R_1 of 150 kc, CT-cut crystal units.

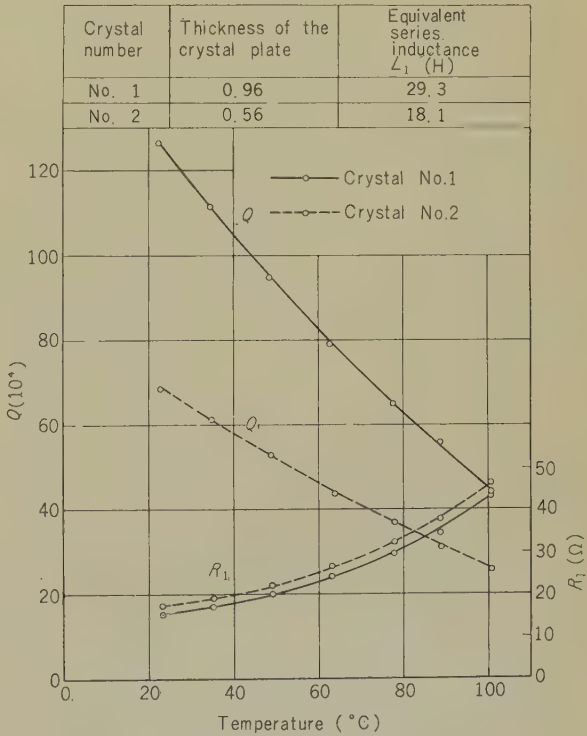


Fig. 16— Q and R_1 of two crystal units differing from each other in crystal plate thickness but the otherwise the same (crystal plates are -18.5°C X-cut, 25.0 mm long and 12.5 mm wide).

Table
EFFECTS OF VACUUM SEALING ON THE

| Frequency (kc) | Mode of Vibration | Orientation | Thickness of the Crystal Plate | Etching | Mounting Features | | |
|-------------------|----------------------|-------------|--------------------------------------|----------|---|--------------------------|-------------------|
| | | | | | Diameter of the Support Wire (mm) | Amount of Solder (mg) | Elec- Material |
| 8 | Flexural | X-cut | 1.0 | Not Done | 0.15 | * | Silver |
| 100 | Face Shear | DT-cut | 0.91 | Done | 0.15 | 0.05 | Silver |
| 200 | Face Shear | CT-cut | 0.8 | Done | 0.15 | 0.05 | Silver |
| 200 | Face Shear | CT-cut | 0.75 | Done | 0.15 | 2.1 | Silver |
| 200 | Face Shear | CT-cut | 0.8 | Done | 0.15 | 0.05 | Silver |
| 450 | Face Shear | CT-cut | 0.3 | Done | 0.15 | 0.35 | Silver |

1. Measurements were held at 20~30°. 2. * shows that no measurement was held.

are attainable at room temperature. Fig. 16 shows Q and R_1 of two crystal units manufactured under the same conditions and differing from each other only in the thickness of the crystal plate. In this figure, R_1 of the two crystal units coincide with each other at all temperatures, but since the equivalent inductance of the crystal unit is proportional to the thickness of the crystal plate, the Q of the units is proportional to the thickness.

These experiments suggest that the vibration loss of crystal units of the contour mode is chiefly determined by that of the materials attached to the crystal plate in the course of mounting, and that the vibration loss of the crystal plates themselves has little effect on the vibration loss of the crystal units.

Fig. 17 shows some experimental results representing the long-term frequency drift of crystal units. This figure suggests that after one-half year's operation of crystal units, their frequency drift becomes smaller than 5×10^{-8} per one-half year.

Fig. 18 illustrates the characteristics of a very narrow band crystal filter in which high stable crystal units with very high Q are

employed.

2.5. Summary

This section has treated some experimental work carried out for the improvement of the characteristics of crystal resonators vibrating in the contour modes.

The results can be summarized as follows:

- (1) Etching the crystal plate improves Q and drive level characteristics of the crystal units.
- (2) The equipments devised for mounting the crystal resonator are illustrated.
- (3) The effect of each mounting process on the characteristics of the crystal units is shown in detail.
- (4) The excellent characteristics of the crystal units obtained as the result of this work are briefly described.

3. Effects of Evaporated Metal Films on the Characteristics of Crystal Resonators Vibrating in the Contour Modes

3.1. General

In designing and fabricating low frequency

2

CHARACTERISTICS OF THE CRYSTAL UNITS

| trode Thickness (μ) | In Atmosphere | | In Vacuum (Vacuum Degree: about 1×10^{-2} mmHg) | | | |
|------------------------------|--------------------|-----------|--|-----------|-------------------------------------|--|
| | $R_i(\Omega)$ | $Q(10^3)$ | $R_o(\Omega)$ | $Q(10^3)$ | Frequency Change from in Atmosphere | Ratio of Q In-vacuum and in Atmosphere |
| * | 16.4×10^3 | 19.2 | 2.3×10^3 | 137 | +191 | 7.1 |
| 0.07 | 740 | 42.1 | 24 | 1,300 | +9.7 | 30.9 |
| 0.06 | 660 | 35.8 | 9 | 2,600 | +24.6 | 72.6 |
| 0.06 | 560 | 39.5 | 63 | 351 | * | 8.9 |
| 1.3 | 740 | 31.5 | 106 | 200 | * | 7.4 |
| 0.21 | 760 | 26.2 | 250 | 79.7 | * | 3.0 |

3. Dimension of 8 kc crystal plate : 60 mm in length and 50 mm in width.

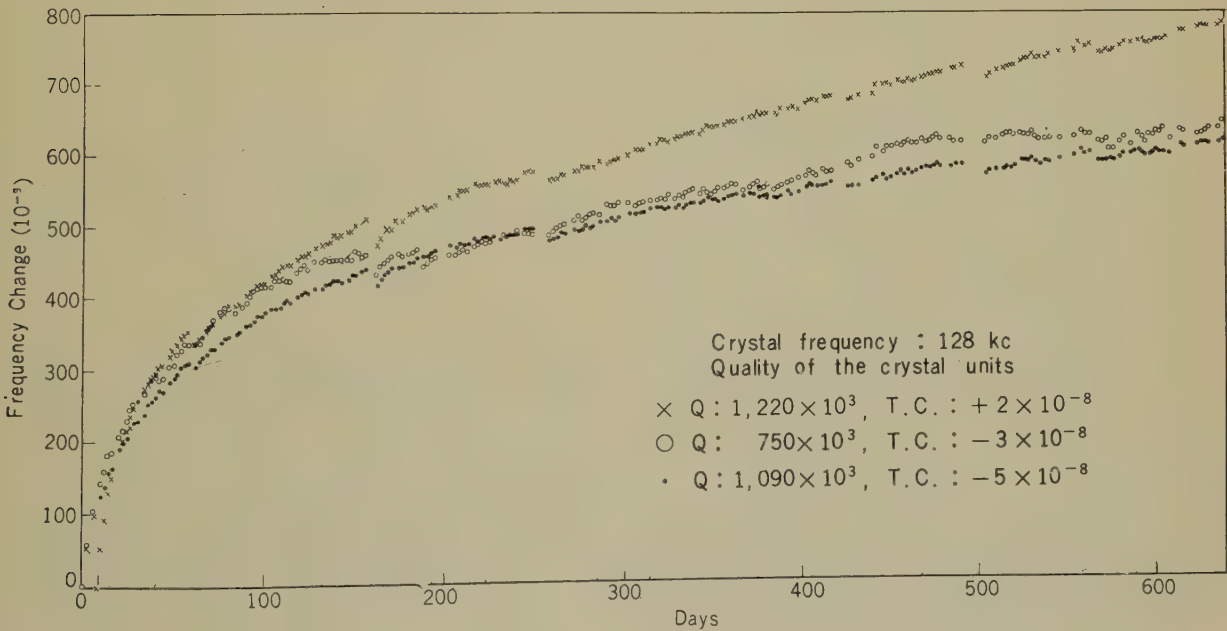


Fig. 17—Long-term frequency drift of crystal units.

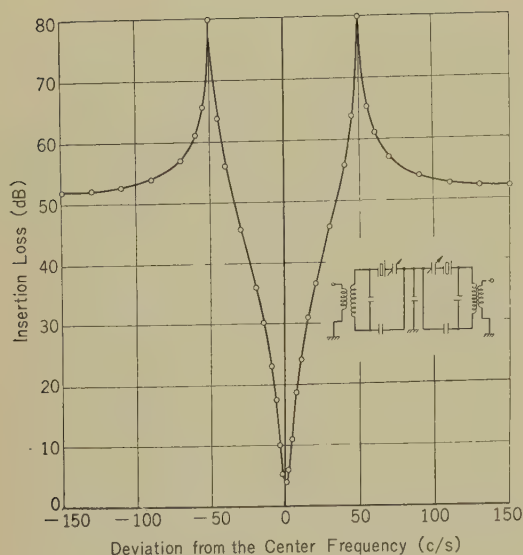


Fig. 18—Very narrow band crystal filter with crystal units of very high quality (center frequency: 200 kc).

crystal units, it is most important to evaluate the effects of the metal film deposited on the major surfaces of the crystal plates as electrodes on the characteristics of the crystal units; especially on the vibration loss and resonant frequency.

As already described in the preceding section, the author has succeeded in manufacturing very high Q crystal units with sufficient reproducibility. This enabled us to experimentally separate the vibration loss of the metal film from the loss of other parts of the crystal units.⁴⁾ Moreover, the experiment in which the metal films are partially deposited on various parts of the major surfaces of the crystal plates enabled the author to measure the effective elastic constants of the evaporated metal film. This enabled us to calculate theoretically the frequency change caused by the deposition of the metal film.

In this section, the frequency change and the increase of vibration loss of the crystal units caused by the deposition of the metal film are theoretically calculated on the crystal vibrator in fundamental longitudinal mode. And then it is shown that the results of all

the experiments on fundamental longitudinal crystals agree well with the theory. Furthermore, some experimental results on face shear crystals are given which show that the theoretical considerations described in this section are applicable to all the crystal resonators vibrating in the contour modes.

In these experiments, the thickness of the metal film was chosen in such a way that the electrical resistance of the film can be ignored.

3.2. Effects of the Evaporated Metal Film on the Characteristics of the Fundamental Longitudinal Crystals—Theory

3.2.1. General

We now consider the properties of the evaporated metal film in crystal units, such as those illustrated in Fig. 19, in which the crystal vibrates in the direction of Y' -axis in the fundamental longitudinal mode.

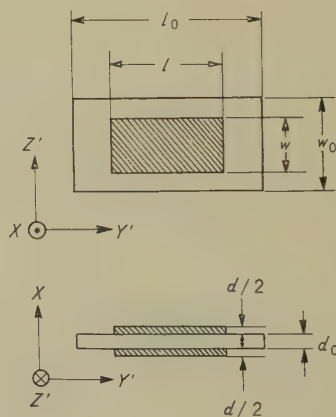


Fig. 19—Shape and dimensions of crystal plate vibrating in the fundamental longitudinal mode (the shaded area represents the metal-film electrode).

Before making the calculations, the following two assumptions are made:

(1) The distribution of strain throughout the crystal plate is not affected by the depo-

sition of the metal film. The distribution of strain of the metal film is the same as that of the crystal plate. Therefore, in the crystal resonator vibrating in the fundamental longitudinal mode, the distribution of strain S of both the crystal plate and the metal film is represented by the following equation.

$$S = A \sin\left(\frac{\pi}{l_0}\right) y' \cos \omega_0 t \quad (1)$$

where A = The amplitude of vibration

$\omega_0 = 2\pi$ times the resonant frequency.

(2) The property of the internal vibration loss of the metal film can be expressed by Voigt's model.⁵⁾ In other words, the relations between stress T and strain S are represented by the following equation.

$$T = \dot{E}S = E(1 + j\delta)S \quad (2)$$

where \dot{E} : Complex elastic modulus

E : Real part of \dot{E}

δ : Ratio of the imaginary part to the real part of the complex elastic modulus.

3.2.2. Frequency Change

From assumption (1), the change of resonant frequency $\Delta f/f$ caused by the deposition of the metal film is⁶⁾

$$\frac{\Delta f}{f} = -\frac{1}{2} \left(\frac{\Delta W_k}{W_k} - \frac{\Delta W_p}{W_p} \right) \quad (3)$$

where W_k = Kinetic energy of the crystal plate

ΔW_k = Kinetic energy of the metal film

W_p = Strain energy of the crystal plate

ΔW_p = Strain energy of the metal film.

In the crystal unit illustrated in Fig. 19,

$$\left. \begin{aligned} \frac{\Delta W_k}{W_k} &= \frac{\rho}{\rho_0} \frac{w}{w_0} \frac{d}{d_0} \frac{2}{\pi} \varphi_1(\alpha) \\ \frac{\Delta W_p}{W_p} &= \frac{M}{M_0} \frac{w}{w_0} \frac{d}{d_0} \frac{2}{\pi} \varphi_2(\alpha) \end{aligned} \right\} \quad (4)$$

where ρ_0 : Density of the crystal plate

ρ : Density of the metal film

M_0 : Young's modulus of the crystal plate along the Y'axis

M : Young's modulus of the metal film

$$\left. \begin{aligned} \varphi_1(\alpha) &= \int_{\alpha} \cos^2 \alpha d\alpha \\ \varphi_2(\alpha) &= \int_{\alpha} \sin^2 \alpha d\alpha \end{aligned} \right\} \quad \alpha = \frac{\pi}{l_0} y' \quad (5)$$

and \int_{α} means that integrations are to be carried out along the Y'axis over the range where the metal film is deposited. From equations (3) and (4), the frequency change becomes

$$\frac{\Delta f}{f} = -\frac{1}{\pi} \frac{w}{w_0} \frac{d}{d_0} \left\{ \frac{\rho}{\rho_0} \varphi_1(\alpha) - \frac{M}{M_0} \varphi_2(\alpha) \right\} \quad (6)$$

Therefore, at the angle α_0 at which the following relation is satisfied:

$$\frac{M}{M_0} = \frac{\rho}{\rho_0} \frac{\cos^2 \alpha_0}{\sin^2 \alpha_0} \quad (7)$$

the change of the resonant frequency caused by the deposition of the metal film becomes zero. Therefore, when α_0 is measured by experiment, Young's modulus of the metal film can be calculated from equation (7).

In the case of the fully plated electrode, $\Delta f/f$ is obtained by

$$\frac{\Delta f}{f} = -\frac{1}{2} \frac{d}{d_0} \frac{\rho}{\rho_0} \left\{ 1 - \frac{\cos^2 \alpha_0}{\sin^2 \alpha_0} \right\} \quad (8)$$

3.2.3. Vibration Loss

For the purpose of representing the effect of vibration loss of the metal film on the Q of the crystal unit, series resistance R_1 in the equivalent electrical circuit of the crystal unit is represented by the series circuit of R_{1p} and R_{1r} as illustrated in Fig. 20.

R_{1p} represents the resistance caused by the vibration loss of the metal film, and R_{1r} the resistance caused by other parts of the units.

The following equation is derived from

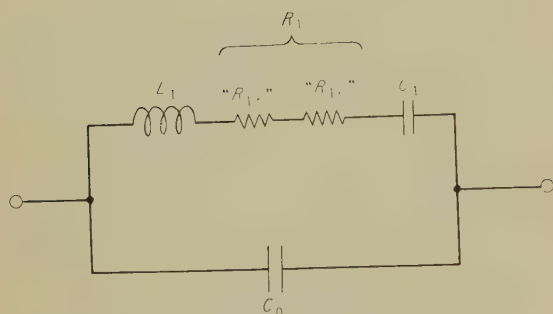


Fig. 20—Equivalent electrical circuit of the crystal unit.

assumption (2);

$$\Delta W' = \{(2\pi)/Q_t\} W \quad (9)$$

where $\Delta W'$ = Energy consumed in the metal film per cycle.

W = Maximum energy stored in the metal film.

$Q_t = 1/\delta$ of the metal film for longitudinal vibration.

From equation (9), the energy ΔW consumed in the metal film per unit time is shown by

$$\Delta W = \frac{M\omega_0}{2Q_t} A^2 \cdot w \cdot d \cdot \left(\frac{l_0}{\pi}\right) \varphi_2(\alpha). \quad (10)$$

On the other hand, the electrical energy ΔW_R consumed in R_{1p} during the same time is

$$\begin{aligned} \Delta W_R &= (1/T_0) \int_0^{T_0/2} l_0 \cdot R_{1p} dt \\ &= \frac{1}{2} R_{1p} A^2 \cdot \varepsilon^2 \cdot w^2 \cdot (l_0/\pi)^2 \cdot \omega_0^2 \left\{ \int_{\alpha} \sin \alpha d\alpha \right\}^2 \end{aligned} \quad (11)$$

where ε = Piezoelectric strain constant of the crystal.

i_0 = Piezoelectric current passing through the motional branch of the equivalent electrical circuit.

By equating ΔW and ΔW_R , the following relation is obtained:

$$R_{1p} = \frac{M}{Q_t \omega_0} \frac{d}{\varepsilon^2 \omega} \frac{\pi}{l_0} \frac{\varphi_2(\alpha)}{\left\{ \int_{\alpha} \sin \alpha d\alpha \right\}^2} \quad (12)$$

From the calculation of series inductance L_1 ,

$$R_{1p} = \frac{2}{Q_t \pi} \omega_0 L_k \frac{M}{M_0} \frac{w}{w_0} \varphi_2(\alpha) d \quad (13)$$

where $L_1 = L_k d_0$

In the case of fully plated electrodes,

$$R_{1p} = \frac{\omega_0 L_{k0}}{Q_t} \frac{M}{M_0} d \quad (14)$$

where $L_1 = L_{k0} d_0$.

By using the representation of Fig 20, the Q of the crystal unit can be expressed as

$$\frac{1}{Q} = \frac{1}{Q_p} + \frac{1}{Q_r} \quad (15)$$

where $Q_p = \frac{\omega_0 L_1}{R_{1p}}$, $Q_r = \frac{\omega_0 L_1}{R_{1r}}$

and Q_p represents the vibration loss of the crystal unit caused by the vibration loss of the metal film, and Q_r represents that caused by other parts of the crystal unit.

Equation (15) gives a quantitative representation of the effect of the metal film on the Q of the crystal units.

From equations (14) and (15),

$$\frac{1}{Q_p} = \frac{2}{Q_t \pi} \frac{M}{M_0} \frac{w}{w_0} \frac{d}{d_0} \varphi_2(\alpha) \quad (16)$$

In the case of fully plated electrodes,

$$\frac{1}{Q_p} = \frac{1}{Q_t} \frac{M}{M_0} \frac{d}{d_0} \quad (17)$$

Combining equations (7) and (16), we get

$$Q_t = \frac{2}{\pi} Q_p \frac{w}{w_0} \frac{d}{d_0} \frac{\rho}{\rho_0} \frac{\cos^2 \alpha_0}{\sin^2 \alpha_0} \varphi_2(\alpha) \quad (18)$$

3.3. Preparation of the Specimen and Method of Measurement

In preparing the crystal units, crystal plates were lapped precisely with AO-emery No. 304 and light oil. Then, they were etched in a saturated water solution of ammonium bifluoride at 24°C for one hour. In soldering the support wires (headed wire) to the crystal plates, 0.05 mg of solder was used at each junction point. After the deposition of the metal films in the determined shape and thickness, the crystal vibrators were sealed in a vacuum of about 1×10^{-2} mm Hg.

The metal film was deposited evenly by evaporation on both of the major surfaces of the crystal plate. The thickness of the evaporated metal film was determined by the following calculation:

thickness

$$= \frac{(\text{deposited mass})}{(\text{area of the metal film}) \times (\text{density})}$$

(19)

The difference between the thickness of the metal film determined by the above method and that determined by the interferometer method did not exceed 5%. The accuracy of measurement of R_1 was better than $\pm 0.5 \Omega$.

3.4. Vacuum Annealing

To obtain a metal film with low vibration loss and uniform characteristics, annealing the evaporated metal film in vacuum proved very effective. Fig. 21 illustrates an example of the change of R_1 in the course of vacuum annealing in a vacuum of about 1×10^{-2} mm Hg. The crystal plate used in this experiment was CT-cut and evaporated silver films about 0.4μ thick were deposited on the major surfaces. As shown in this figure, during the first cycle, the crystal unit was heated very gradually up to 160°C, was maintained at this temperature for about eight hours, and then cooled very gradually down to room

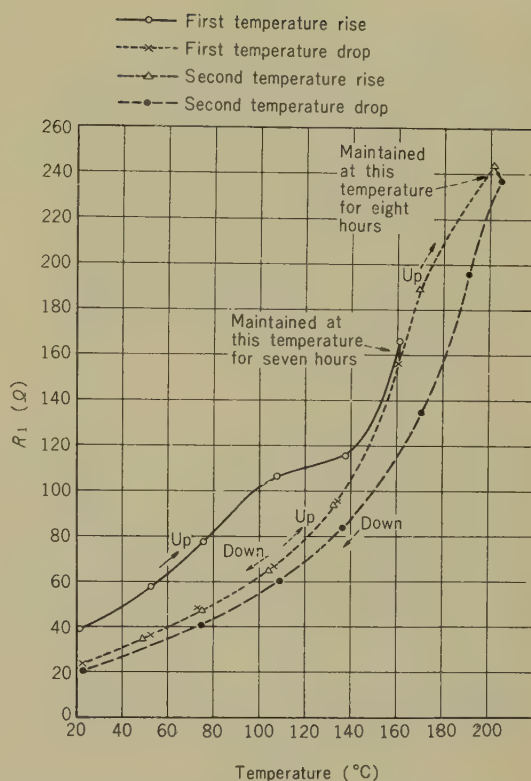


Fig. 21—Change of series resistance R_1 by vacuum annealing (the crystal is a 200 kc, CT-cut plate on whose major surfaces 0.4μ thick evaporated silver film has been deposited).

temperature. During second cycle, the crystal unit was heated up to 200°C and cooled down to the room temperature. During the two annealing cycles, R_1 of the unit was measured and plotted as shown in Fig. 21. The experiments showed precisely the same results whether evaporated gold films or evaporated silver films were used. From Fig. 21 and from other experiments, the following description of evaporated metal films of silver and gold can be made:

(a) Vibration loss of the metal film is decreased to a considerable extent by vacuum annealing. The magnitude of the decrease of vibration loss is determined by the annealing temperature.

(b) Below the annealing temperature, the

vibration loss may be considered to have inherent temperature characteristics.

From these results, all the crystal units used in the following experiments were annealed at 150–155°C for eight hours, since in these crystal units, the support wires are attached to the crystal plates with solder whose eutectic temperature is 183°C.

3.5. Experiments on Crystal Resonators Vibrating in the Fundamental Longitudinal Mode

3.5.1. General

The crystal plates used are -18.5° X-cut plates with a length of 25.0 mm, width of 12.5 mm and thickness of 1.0 mm. The dimensions of the evaporated metal film are $l=24.0$ mm and $w=11.5$ mm as shown in Fig. 19. In this paper, this electrode shape will be called the "standard shape".

3.5.2. Determination of Effective Young's Modulus of the Evaporated Metal Film

From equation (7), the effective Young's modulus of the evaporated metal film can be estimated only when α_0 is determined by experiment. From equations (6) and (7), the following equation is obtained:

$$\frac{\cos^2 \alpha_0}{\sin^2 \alpha_0} = \frac{\varphi_1(\alpha)}{\varphi_2(\alpha)} + \frac{1}{\varphi_2(\alpha)} \frac{\Delta f}{f} \frac{\pi}{2} \frac{w_0}{w} \frac{d}{d/2} \frac{\rho}{\rho_0} \quad (20)$$

Now, in the right hand of the equation (20), the first term can be determined very precisely by the measurement of dimensions of the deposited metal film. However, the second term involves values in which experimental errors are liable to occur. Therefore, if an experimental method is found that enables us to make the second term very small as compared with the first term, the value of α_0 can be determined very precisely.

Fig. 22 illustrates the experimental method devised to meet the above-mentioned purpose. As shown in the figure, evaporated 0.1μ thick metal films of the "standard shape" were deposited on both the major surfaces of six crystal plates, all of which have the same orientation and dimensions. Then, the area of the electrode was divided into twelve equal segments, and evaporated metal films $d/2$ in thickness were deposited on both the major surfaces in the following manner: On crystal (a), at both ends; on crystal (b), at the second segments from both ends;; on crystal (f), on the central part. By this experiment, the effects of the metal films deposited in the second deposition can be detected without changing the equivalent series

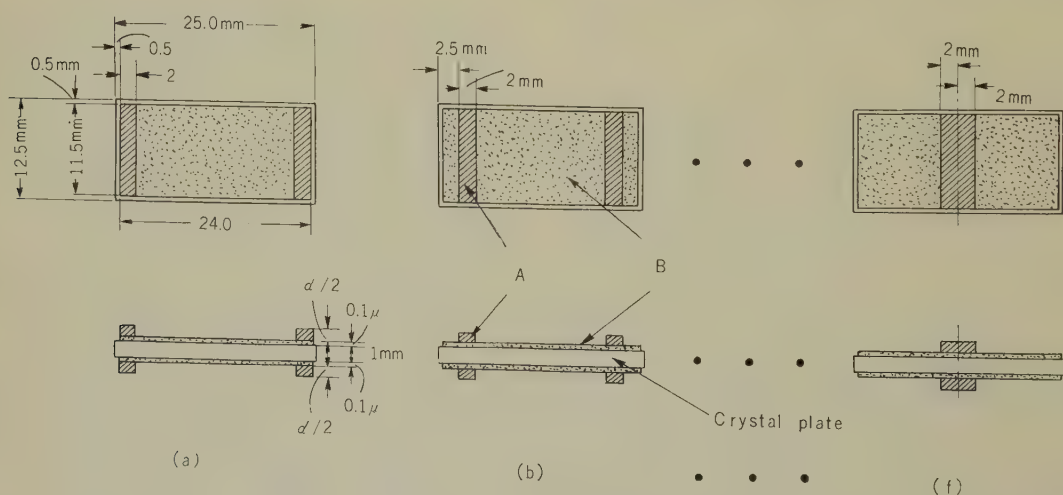


Fig. 22—Partial deposition of the metal films.

Table 3

FREQUENCY CHANGE CAUSED BY THE PARTIAL DEPOSITION OF EVAPORATED SILVER FILMS (THE METHODS OF PARTIAL DEPOSITION ARE ILLUSTRATED IN FIG. 22; THE THICKNESS $d/2$ IS 0.53μ).

| Code of the Crystal Units | Frequency Change (10^{-6}) | |
|---------------------------|--------------------------------|------------------|
| | Measured Value | Calculated Value |
| (a) | -581 | -588 |
| (b) | -543 | -487 |
| (c) | -287 | -333 |
| (d) | -130 | -163 |
| (e) | -22.0 | -20 |
| (f) | +90.5 | +63 |
| Total | -1,472.5 | -1,528 |

inductance of the units.

Next, frequency changes caused by the second deposition were measured and are shown in the second columns (measured value) of Table 3 (silver) and Table 4 (gold). From these tables, it can be seen that minimum frequency change occurs with crystal (e) in Table 3, and with crystal (f) in Table 4.

From the frequency changes of these crystals and from equation (20), the following values are obtained:

For silver,

$$\frac{\cos^2 \alpha_0}{\sin^2 \alpha_0} = 0.126 \quad \alpha_0 = 70^\circ 30'$$

For gold,

$$\frac{\cos^2 \alpha_0}{\sin^2 \alpha_0} = 0.043 \quad \alpha_0 = 78^\circ 40'$$

(21)

Table 4

FREQUENCY CHANGE CAUSED BY THE PARTIAL DEPOSITION OF EVAPORATED GOLD FILMS (THE METHODS OF PARTIAL DEPOSITION ARE ILLUSTRATED IN FIG. 22, THE THICKNESS $d/2$ IS 0.22μ).

| Code of the Crystal Units | Frequency Change (10^{-6}) | |
|---------------------------|--------------------------------|------------------|
| | Measured Value | Calculated Value |
| (a) | -442.4 | -449 |
| (b) | -423.5 | -377 |
| (c) | -267.6 | -270 |
| (d) | -145.0 | -151 |
| (e) | -56.3 | -49 |
| (f) | +9.8 | +9 |
| Total | -1,325.0 | -1,287 |

From equation (7) and the values in (21), the effective Young's modulus of the evaporated metal films are determined as follows:

For silver,

$$M = 3.43 \times 10^{11} \text{ dyne/cm}^2$$

For gold,

$$M = 2.01 \times 10^{11} \text{ dyne/cm}^2$$

(22)

It should be noticed that the effective elastic constants of the evaporated metal films are extremely small as compared with the elastic constants of the same metal in the bulk state. Namely, Young's moduli of silver and gold are 7.90×10^{11} dyne/cm² and 8.0×10^{11} dyne/cm² respectively.

3.5.3. The Effects of the Evaporated Metal Film on the Resonant Frequency of the Crystal Units

From equation (6) and the values in (22), it is possible to calculate theoretically the frequency change caused by the deposition of the evaporated metal film. In the case of fully plated electrodes,

for silver film,

Δf/f = -3.46 × d/2d0 (23)

for gold film,

Δf/f = -6.99 × d/2d0 (24)

Table 5 illustrates the comparison between the experimental results and the calculated values. As can be seen from the table, the calculated values coincide with the experimental results with an accuracy of 3 % or better.

The third columns of Table 3 and Table 4 represent the calculated values of frequency change caused by the partial deposition of evaporated metal films on the crystal units shown in Fig. 22 (a)-(f). Again, in these tables, calculated values are in good agreement with the experimental results.

Some precise examinations of equation (6) have brought the following to light:

(a) The frequency change caused by the deposition of the evaporated metal film is proportional to both the width and thickness of the metal film.

(b) The contribution of each point along the longitudinal axis to the frequency change is proportional to n, where n is represented by the following equation:

n = -ρ/ρ0 { cos² α - cos² α0 / sin² α0 sin² α } (25)

Fig. 23 illustrates the values of n for silver and gold films. The integration of the value of n over the deposited area is also proportional to the frequency change.

Table 5

FREQUENCY CHANGE CAUSED BY THE DEPOSITION OF 0.1 μ THICK EVAPORATED METAL FILMS ON BOTH THE MAJOR SURFACES OF A 1.0 MM THICK CRYSTAL PLATE (METAL FILMS ARE FULLY PLATED; CRYSTAL PLATE IS -18.5° X-CUT).

| | Measured Value (10 ⁻⁶) | Calculated Value (10 ⁻⁶) |
|------------------------|---------------------------------------|---|
| Evaporated Silver Film | -335 | -346 |
| Evaporated Gold Film | -720 | -699 |

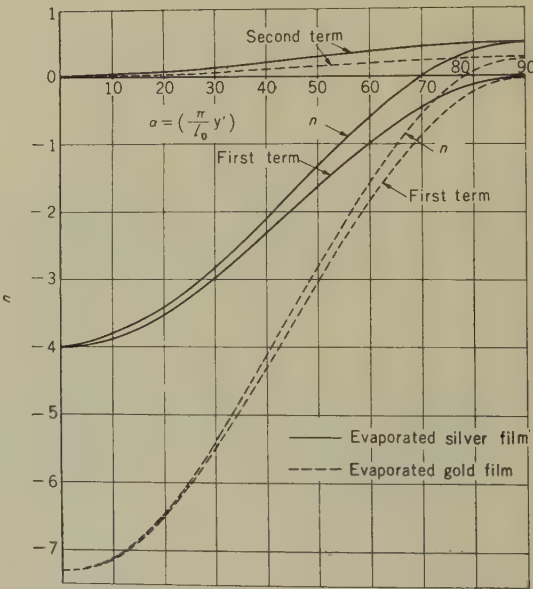


Fig. 23—Values of “n” represented in Eq. (25).

3.5.4. The Effects of the Evaporated Metal Film on the Q of the Crystal Units

(a) Uniformity of R_1

For the purpose of examining the uniformity of R_1 of the crystal units manufactured under the same conditions, four crystal units were made. On two of them evaporated $0.1\ \mu$ thick silver films were deposited once, and on the other two, $0.05\ \mu$ thick films were deposited twice. Then, the temperature characteristics of R_1 of these units were measured and plotted as shown in Fig. 24. From this figure, it can be said that the temperature characteristics of R_1 are sufficiently uniform, and they do not depend on the number of layers deposited.

(b) Relation between R_1 and the thickness of the metal film

The thickness of the evaporated silver film on the same plate was successively increased, and after each deposition the temperature characteristics of R_1 of the unit were measured and are illustrated in Fig. 25. In Fig. 26, the relation between R_1 and the thickness of the silver film is plotted at several temperatures from Fig. 25. From these figures it is apparent that R_1 increases proportionally to the thickness of the metal film in good agreement with equations (12)–(14).

If each straight curve in Fig. 26 is extrapolated to the axis of the ordinates, the intersection of the two lines will represent the value of R_1 of the crystal unit when the thickness of the metal film has become zero, and this value will be representative of R_{1r} .

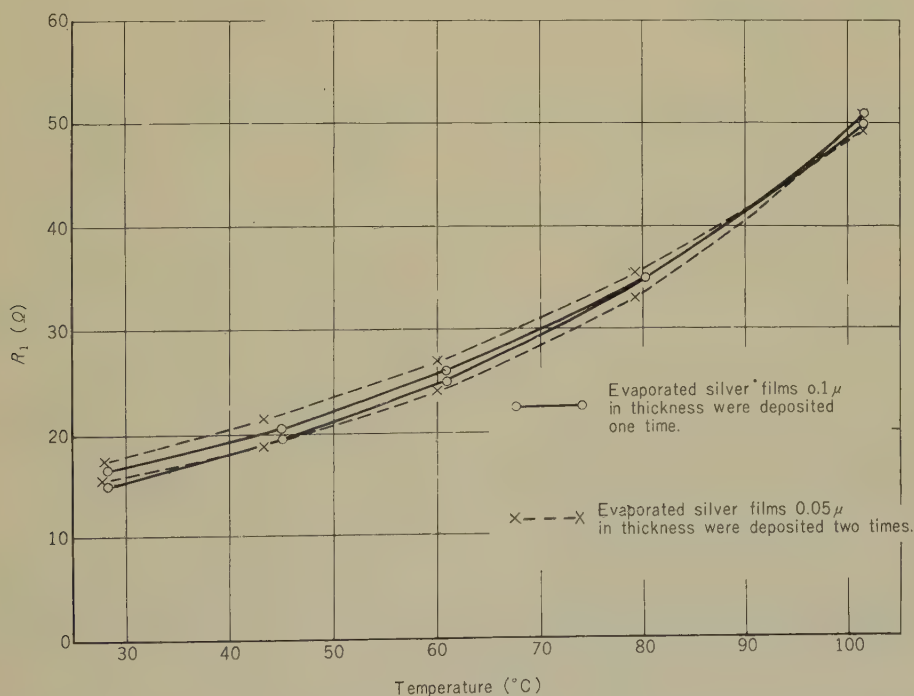
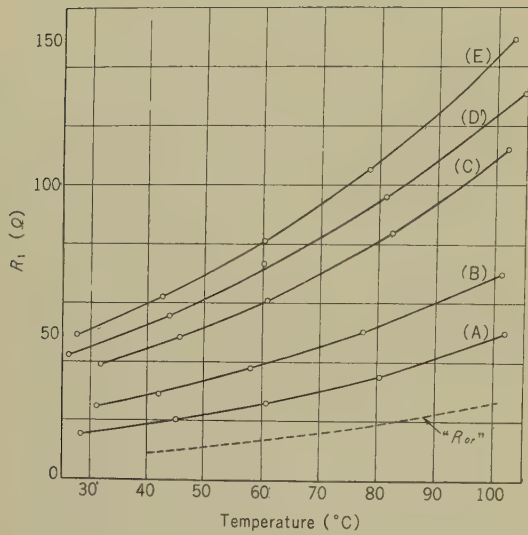


Fig. 24—Temperature characteristics of R_1 of four crystal units (crystal plates are -18.5°C , X-cut; 25.0 mm long, 12.5 mm wide, and 1 mm thick; the metal film is of “standard shape”; the crystal units were annealed in vacuum for eight hours at 150 – 153°C).



- (A): Silver film $0.11\ \mu$ thick was deposited at first.
- (B): Silver film $0.11\ \mu$ thick was added (total; $0.22\ \mu$).
- (C): $0.20\ \mu$ was added (total; $0.42\ \mu$).
- (D): $0.08\ \mu$ was added (total; $0.50\ \mu$).
- (E): $0.09\ \mu$ was added (total; $0.59\ \mu$).

Fig. 25—Temperature characteristics of R_1 of the crystal units (the thickness of the evaporated silver films are increased successively; the crystal plate is the same as that shown in Fig. 24).

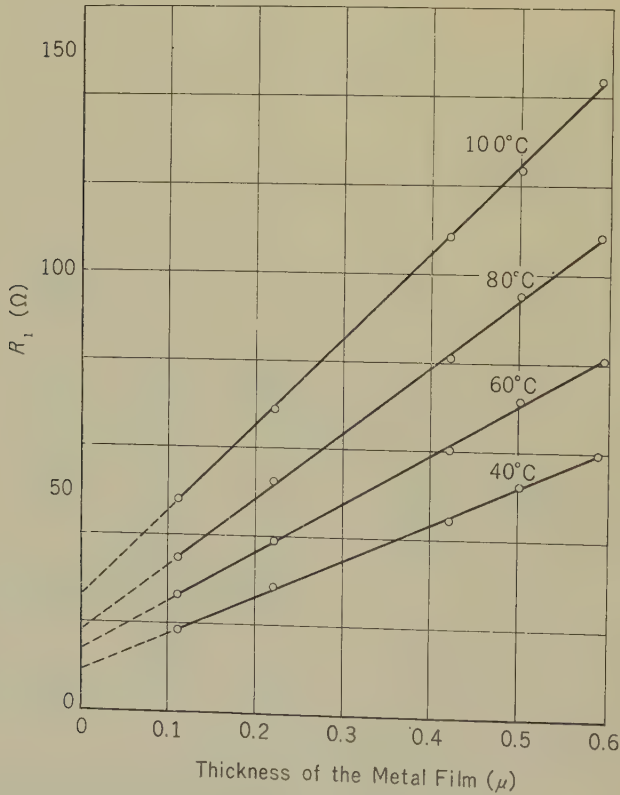


Fig. 26—Relation between R_1 and the thickness of the evaporated silver film, derived from Fig. 25.

in Fig. 20. The dashed curve in Fig. 25 represent the temperature characteristics of R_{17} plotted in this way.

(c) Q_p and R_{1p}

From the foregoing experiments, the value of R_{1p} per unit thickness can be determined for the evaporated silver film. From this value and from the inductance L_1 of the -18.5° X-cut plate, when $l_0=25.0$ mm, $w_0=12.5$ mm, and the electrode is of the "standard shape",

$$L_1=28.6\ d_0H.$$

The value of Q_p was determined for $d_0=1.0$ mm, $d/2=0.1\ \mu$, and $f=101.6$ kc; and is plotted in Fig. 27. In the same manner as before, Q_p of the evaporated gold film was also determined for the same crystal plate, and is plotted in the same figure.

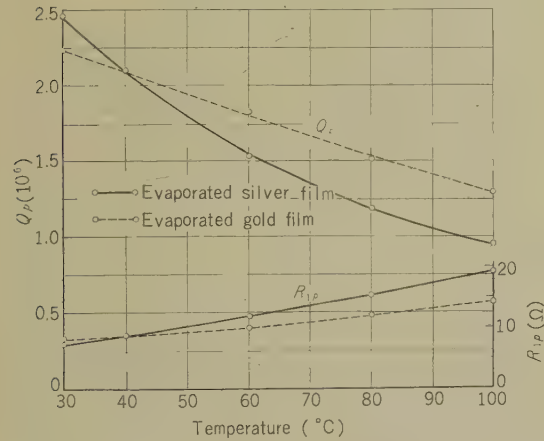


Fig. 27— Q_p and R_1 of the evaporated silver and gold films (the crystal plates are the same as those in Fig. 24; $d/2$ in Fig. 19 is $0.1\ \mu$).

(d) Q_l

By using the values of Q_p in Fig. 27 and the values of $\cos^2\alpha_0/\sin^2\alpha_0$ already determined, it is possible to estimate the values of Q_l

of the evaporated metal films from equation (18). These values are illustrated in Fig. 28, from which it should be noticed that the values of Q_l are extremely small as compared with those when metals are in the bulk state.

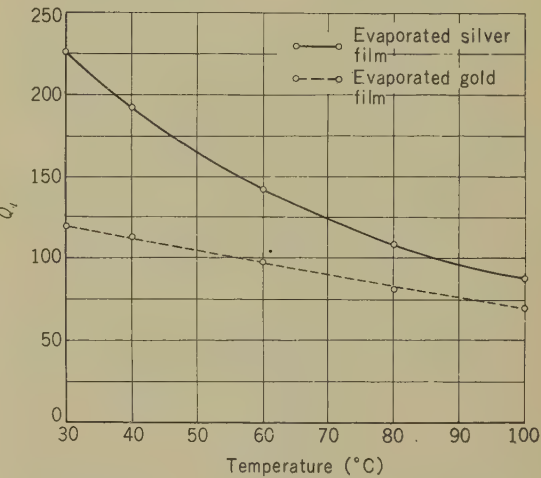


Fig. 28— Q of the evaporated silver and gold films in the longitudinal vibration (frequency is 101.6 kc; vacuum at the time of evaporation is $0.8-1.0 \times 10^{-4}$; the evaporated metal films are annealed in vacuum for eight hours at $150-153^\circ\text{C}$).

(e) Distribution of R_{1p} along the longitudinal axis

In the experiment of partial deposition of the evaporated metal films illustrated in Fig. 22, the increase of R_1 caused by the second deposition of the silver films was measured for six crystal units and is illustrated in Fig. 29. These values are calculated from equation (13) and from Fig. 28 for several temperatures and tabulated, together with the measured values, in Fig. 8. From Fig. 29 and Table 6, it is concluded that when evaporated metal films are deposited on the parts where displacement is large and strain is small, the increase of vibration loss of the crystal unit is very small, and vice versa.

Table 6

INCREASE OF R_1 CAUSED BY THE SECOND DEPOSITION OF THE EVAPORATED SILVER FILM WAS CALCULATED FROM EQ. (13) AND Q_i IN FIG. 28, AND COMPARED WITH THE MEASURED VALUES. ALL TH EXPLANATIONS IN FIG. 29 APPLY FOR THIS TABLE.

| Code of the Crystal Units | | | (a) | (b) | (c) | (d) | (e) | (f) |
|---------------------------|-------|------------------|-----|-----|------|------|------|------|
| Increase of $R_1(\Omega)$ | 35° C | Measured Value | 1.0 | 3.0 | 5.8 | 7.5 | 12.0 | 15.6 |
| | | Calculated Value | 0.6 | 2.5 | 5.6 | 8.9 | 11.8 | 13.4 |
| | 60° C | Measured Value | 1.0 | 4.9 | 8.8 | 12.5 | 18.9 | 23.3 |
| | | Calculated Value | 0.8 | 3.7 | 8.1 | 13.0 | 17.1 | 19.6 |
| | 95° C | Measured Value | 1.0 | 8.6 | 13.6 | 17.7 | 28.0 | 37.0 |
| | | Calculated Value | 1.3 | 5.7 | 12.5 | 20.2 | 26.6 | 30.3 |

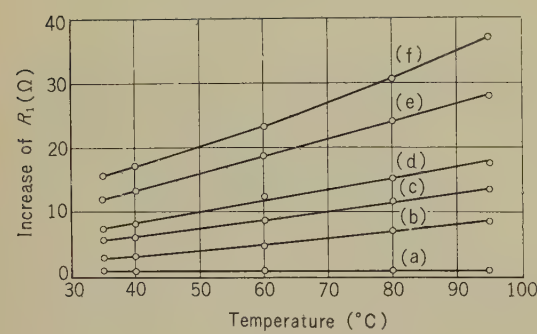


Fig. 29—Increase of R_1 caused by the second deposition of evaporated silver film in the experiment in Fig. 22 (the value of $d/2$ is 0.53μ ; (a)–(f) correspond to the units in Fig. 22).

3.6. Some Experiments with Crystal Units in Face Shear Mode

Some experiments with CT-cut 200 kc crystal units proved that the same considerations as in the case of longitudinal crystals are applicable to face shear crystals. The crystal plates used in the experiments were 1.0 mm thick, and on both the major

surfaces metal film electrodes with an area of 14 square mm were deposited.

Fig. 30 illustrates the relation between the thickness of the evaporated silver film and the frequency change. This figure shows that the resonant frequency changes proportionally to the thickness of the metal film.

Fig. 31 illustrates the temperature characteristics of R_1 of several crystal units, the metal films being different in thickness from one another. In Fig. 32, the relation between R_1 and the thickness of the metal film is plotted for several temperatures from Fig. 31. From these figures, it can be concluded that R_1 increases proportionally to the thickness of the metal film.

Fig. 33 illustrates the change of the frequency-temperature characteristics of the crystal unit caused by the increase of the thickness of the evaporated silver film. In this experiment, the thickness was increased from 0.08μ to 1.32μ on the same CT-cut crystal plate, and the frequency-temperature characteristics are plotted for each thickness in Fig. 33 (a). In Fig. 33 (b), the difference between the two curves is plotted in order to represent the effect of the metal film on

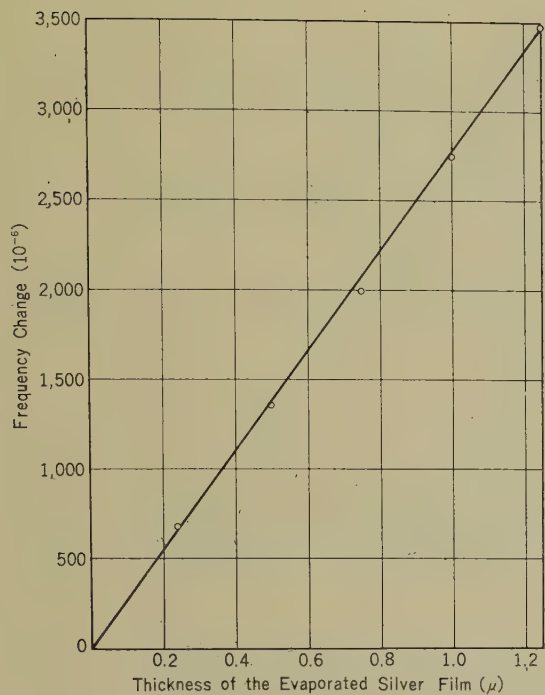


Fig. 30—Relation between the thickness of the evaporated silver film and frequency change (the crystal is a 200 kc CT-cut plate 1.0 mm thick; the dimensions of the metal film are 14.0 mm \times 14.0 mm; the unit is vacuum annealed in the manner described in Fig. 24).

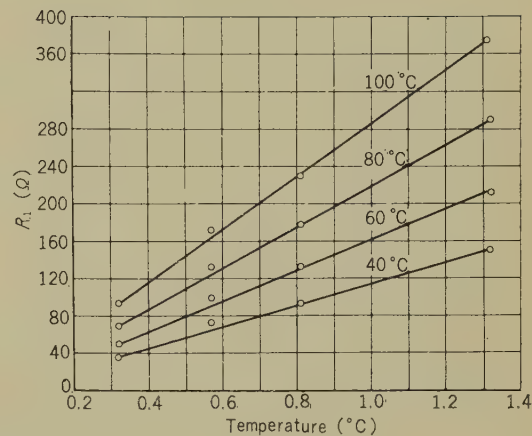
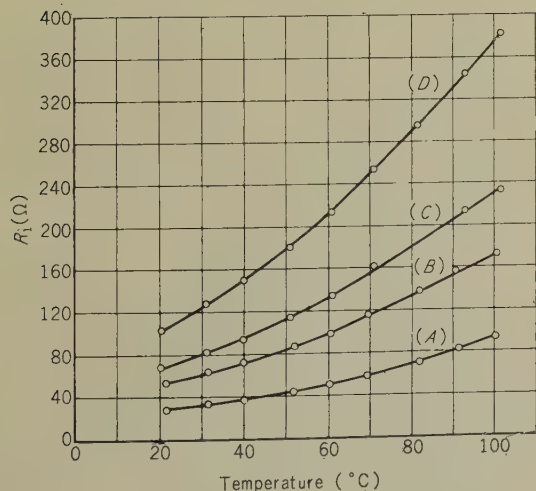


Fig. 32—Relation between R_1 and the thickness of the evaporated silver film; derived from Fig. 21.



- (A): Metal film thickness=0.32 μ .
- (B): Metal film thickness=0.57 μ .
- (C): Metal film thickness=0.81 μ .
- (D): Metal film thickness=1.3 μ .

Fig. 31—Temperature characteristics of R_1 of several crystal units (the thickness of the metal films are different from one another; the crystal plates are identical to those shown in Fig. 30).

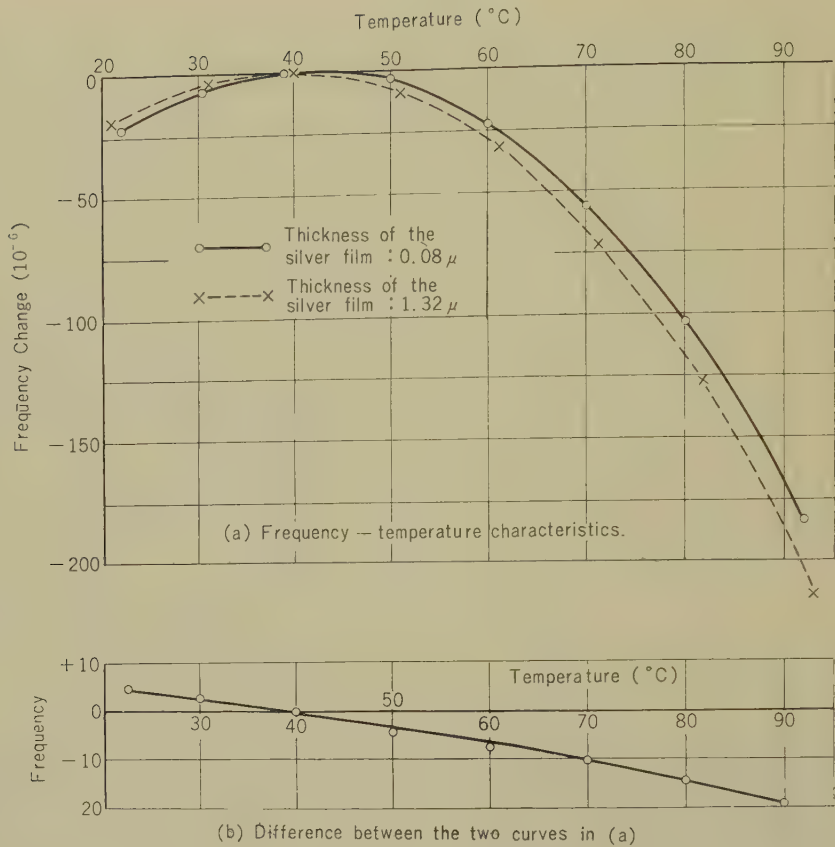


Fig. 33—Change of the frequency-temperature characteristics of the face shear crystal units caused by increase of thickness of the evaporated silver film.

the frequency-temperature characteristics of the crystal unit. Fig. 33 (b) shows that an increase of the thickness of the silver film from 0.08 μ to 1.32 μ corresponds to the addition of a temperature coefficient of -3.6×10^{-7} to the original crystal unit temperature characteristics.

3.7. Summary

The results obtained in this section are summarized as follows:

(a) Vacuum annealing

The vibration loss of the evaporated metal film is markedly decreased by vacuum an-

nealing. The magnitude of the decrease of vibration loss is determined by the annealing temperature. Below the annealing temperature, the vibration loss of the evaporated metal film can be considered to have inherent temperature characteristics.

(b) Frequency change

Frequency change caused by depositing the evaporated metal film can be determined from the Eq. (3). Generally speaking, when the metal film is deposited where strain is large, the frequency increases only slightly; on the other hand, when the metal film is deposited where displacement is large the frequency decrease is larger.

(c) Vibration loss

The properties of the internal vibration loss of the evaporated metal film are illustrated by Voigt's model. Therefore, the increase of the series resistance R_1 of the crystal unit is proportional to the thickness of the metal film. The magnitude of the increase of vibration loss of the crystal unit is very large when the evaporated metal film is deposited where strain is large, and vice versa.

(d) Elastic properties of the evaporated metal film

The effective Young's modulus of evaporated silver and gold films are shown in (22). The temperature characteristics of Q_t of these films are illustrated in Fig. 28.

(e) Other properties

The effect of evaporated metal film on the frequency-temperature characteristics of the crystal units cannot be ignored.

4. Fabrication of 10-100 Mc Crystal Units

4.1. General

Studies of lapping very thin crystal plates with sufficient parallelism and flatness, and of mounting the vibrators suitably, have enabled the author to manufacture crystal units with uniform quality in the frequency range from 10 to 75 Mc.⁸⁾ By polishing the crystal plates precisely, the author has succeeded in manufacturing crystal units with excellent quality up to 100 Mc.

In this section, experimental results of these crystal units are described together with the oscillator circuit used with these crystals.

4.2. Representation of the Quality of the Crystal Units

The quality of the crystal units is represented by Figure of Merit $= 1/\omega_0 C_0 R_1$ hereafter abbreviated " M ", R_1 , and $Q (= \omega_0 L_1 / R_1)$ in this section with the help of the parameters illustrated in Fig. 34. R_1 and L_1 were

measured on an appropriately modified CI meter whose accuracy of measurement was better than 5%.

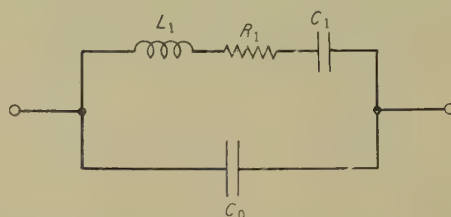


Fig. 34—Equivalent electrical circuit of the crystal unit.

Furthermore, in order to simplify the representations, M , R_1 , and Q at the n -th overtone will be denoted by M_n , R_{1n} , and Q_n respectively.

4.3. Specimens and Method of Mounting

The crystal plates used in the experiments were mostly AT-cut round plates with a diameter of 14 mm. Round metal film electrodes of appropriate diameter are deposited on both major surfaces. The metal film electrodes are connected to the wire leads as shown in Fig. 35.

The area of the electrode was chosen such that M of the crystal units would be maxi-

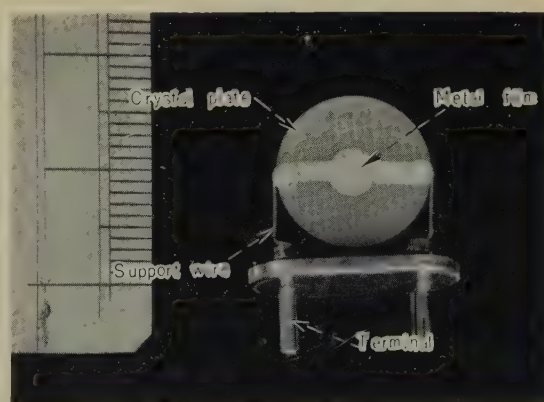


Fig. 35—Mounting of the crystal unit.

mum. Fig. 36 illustrates an example of the experimental results showing the relation between M and the diameter of the electrodes, for a typical crystal unit. Some other experiments similar to those illustrated in Fig. 36 showed that a parallel capacitance of 6–8 pF gave the maximum value of M .

4.4. Lapping

4.4.1. General

As is well-known, the qualities of very high frequency crystal units are principally determined by the parallelism, the roughness, and the flatness of the crystal plates.

“Plane parallel lapping” or “both side lapping,” in which all crystal plates are lapped simultaneously and tend to become equal to one another in thickness, and the parallelism of each crystal plate is improved automatically in the course of lapping, is adapted to the production of very high frequency crystal units. With the conventional lapping machine, however, when the crystal plates become very thin (thinner than 0.15 mm), the corresponding thickness of the workholder becomes too small to withstand the mechanical forces applied during the lapping procedure, which prevents lapping from proceeding.

Studies led the author to use the following two suitable methods of lapping.

4.4.2. Thwaite's Method⁹⁾

Thwaite's method was found to be most suitable for lapping crystal plates thicker than 0.1 mm. In making use of this method, however, attention should be paid to maintain the flatness of the planes of both the upper lap and the lower lap, because this method is a modification of the “drill press lap” in which both the laps tend to lose their flatness during the course of the lapping procedure.

Table 7 represents the quality of eight crystal units manufactured simultaneously by this method.

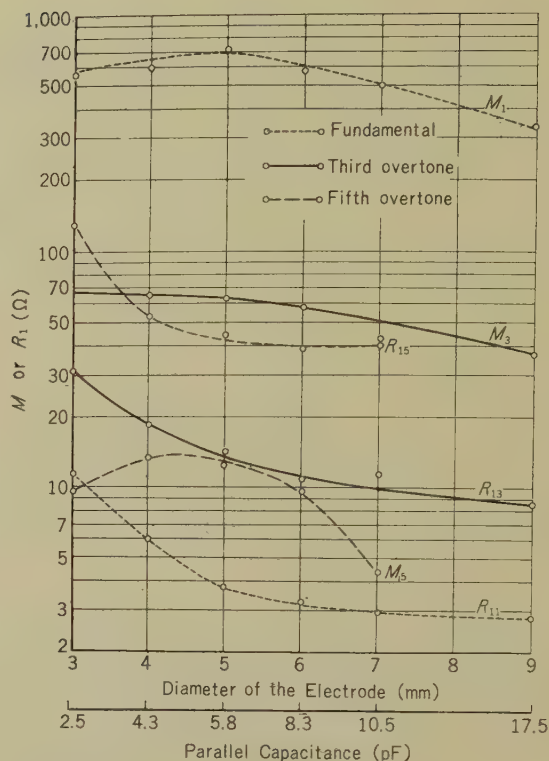


Fig. 36—The relations between M or R_1 and the diameter of the electrodes or parallel capacitance (the crystal plate is AT-cut; its fundamental frequency is 10.1 Mc).

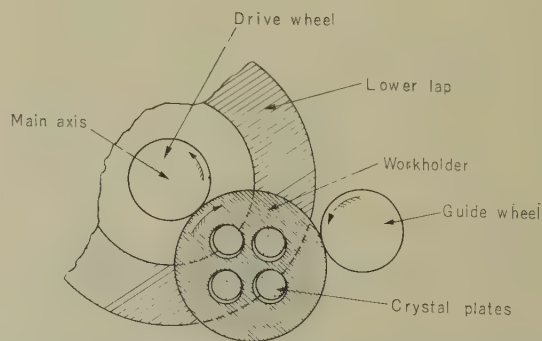


Fig. 37—Schematic illustration of Ida's method of lapping thin plates.

Table 7

QUALITY OF EIGHT CRYSTAL UNITS MANUFACTURED SIMULTANEOUSLY BY THWAITE'S METHOD ($C_0=6.0$ pF; Δt REPRESENTS THE PARALLELISM OF THE CRYSTAL PLATES).

| Thickness (mm) | Orientation | Δt (μ) | f_1 (Mc) | M_1 | R_{01} (Ω) | f_3 (Mc) | M_3 | R_{03} (Ω) | f_5 (Mc) | M_5 | R_{05} (Ω) |
|--------------------|-------------|-------------------------|---------------|-------|--------------------------|---------------|-------|--------------------------|---------------|-------|--------------------------|
| 0.112 ₉ | AT | 0 | 14.7 | 360 | 5 | 44.1 | 40 | 15 | 73.5 | 5.5 | 65 |
| 0.112 ₈ | // | 0 | // | 450 | 4 | // | 40 | 15 | // | 5.5 | 65 |
| 0.112 ₅ | // | 0 | // | 450 | 4 | // | 35 | 17 | // | 6.3 | 57 |
| 0.112 ₇ | // | 0 | // | 400 | 4.5 | // | 38 | 16 | // | 5.8 | 62 |
| 0.112 ₇ | BT | 0.1 | 22.6 | 230 | 5 | 67.8 | 6.2 | 63 | — | — | — |
| 0.112 ₆ | // | 0 | // | 210 | 5.5 | // | 6.0 | 65 | — | — | — |
| 0.113 ₀ | // | 0 | // | 200 | 6 | // | 5.6 | 70 | — | — | — |
| 0.112 ₇ | // | 0 | // | 210 | 5.5 | // | 5.6 | 70 | — | — | — |

4.4.3. Ida's Method⁸⁾

Fig.37 gives a schematic illustration of Ida's method. In this method, workholders were made small and the range of motion of workholders was localized by separating the revolution of workholders from the rotation of them so that the very thin workholders do not break or fracture during the lapping procedure. In addition, all the crystal plates are lapped together with the workholder, which are almost equal in thickness, therefore each crystal plate is lapped as a part of the group of a workholder and crystal plates.

Ida's method was found to be suitable for lapping very thin crystal plates (from 0.07mm to 0.15mm). Table 8 represents an example of the results obtained by this method.

4.5. Quality of the Lapped Crystals

Several kinds of crystal units were manufactured in the frequency range from 7.5 to

Table 8

AN EXAMPLE OF RESULTS OBTAINED BY IDA'S METHOD ($C_0=6.2$ pF)

| f_1 (Mc) | M_1 | R_{01} (Ω) | f_3 (Mc) | M_3 | R_{03} (Ω) |
|------------|-------|-----------------------|------------|-------|-----------------------|
| 20.0 | 370 | 3.5 | 60.0 | 15 | 28 |
| // | 370 | 3.5 | // | 14 | 30 |
| // | 320 | 4 | // | 17 | 25 |

24 Mc (expressed in their fundamental frequencies), by the above two methods.

Their M , R_1 , and Q at the fundamental, third, and fifth overtones are plotted in Figs. 38~40. In Figs. 38 and 39, the 90% two side tolerance limits (fiducial probability: 90%) are shown for M and R_1 at each overtone order.

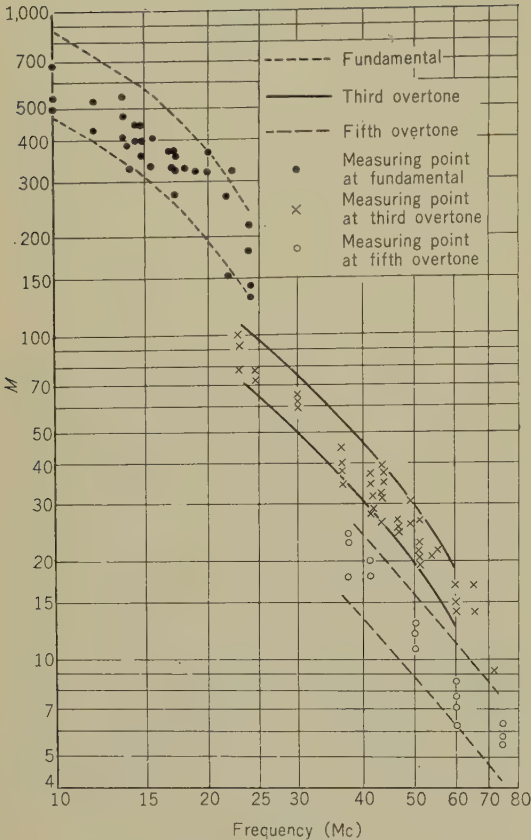


Fig. 38—Frequency characteristics of M ($C_0 = 5.8 \text{ pF} \sim 7.2 \text{ pF}$; dotted solid, and dashed curves represent 90% two side tolerance limits—fiducial probability = 90%—respectively).

From these figures the following conclusions are obtained:

- (1) At the same frequency, as the overtone order becomes higher, M becomes smaller and R_1 becomes larger.
- (2) On the contrary, as the overtone order becomes higher, Q becomes larger.
- (3) When the mean value of M_n is expressed as a function of frequency by the following equation

$$M_n = M_{mn} f^{-an} \tag{27}$$

where f is frequency expressed in Mc, the

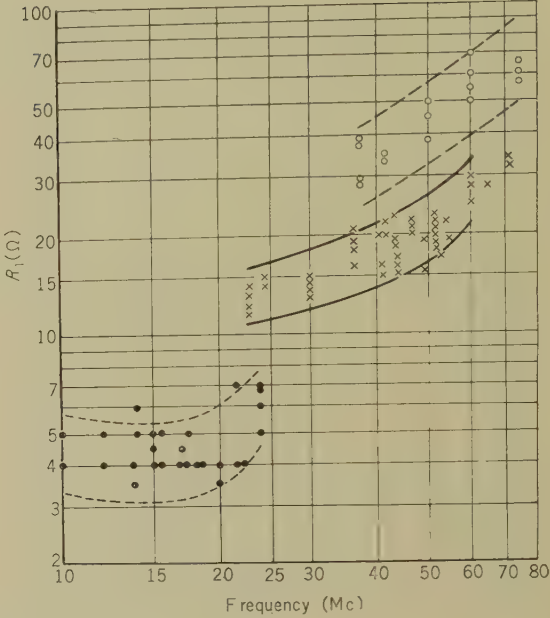


Fig. 39—Frequency characteristics of R_1 (the explanations in Fig. 38 are also applicable to this figure).

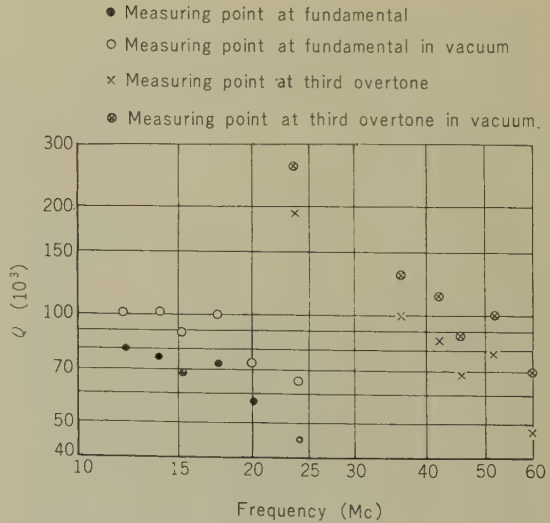


Fig. 40—Frequency characteristics of M ($C_0 = 5.8 \text{ pF} \sim 7.2 \text{ pF}$; vacuum is about $1 \times 10^{-2} \text{ mmHg}$).

values M_{mn} and α_n are as given in Table 9.

4.6. Polished Crystals

4.6.1. General

As already described in the preceding paragraph, lapping the crystal plates with suitable machines is suitable for the production of very high frequency crystal units with excellent quality and good reproducibility. However, lapping leaves extremely small scratches and cracks on the surfaces of the crystal plates, which seem to have unfavorable effects on the characteristics of the crystal units when the frequency of the crystal units becomes very high and these scratches and cracks become appreciable compared with the elastic waves in the crystal plate.

The author has succeeded in improving the qualities of VHF crystal units by polishing the crystal plates precisely, and this enabled him to manufacture excellent quality crystal units for frequencies up to 100 Mc. Fig. 41 (a) and (b) illustrate the observed roughness of a lapped surface and a polished surface respectively. As seen from the figures, the lapped surface shows a roughness of about 0.4μ , while the polished surface may be considered to be substantially smooth.

The parallelism of all of the crystal plates used in the experiment was measured by the use of a multiple beam interferometer, and it was observed to be better than 0.4μ .

4.6.2. Quality of the Polished Crystals

Figs. 42 and 43 illustrate M and R_1 of the polished crystals compared with those of the lapped ones. In these figures, dotted (fundamental), solid (third overtone) and dashed (fifth overtone) curves represent the 90 % two side tolerance limits of M and R_1 of lapped crystals reproduced from Figs. 38 and 39, and measured data represent M and R_1 of the polished crystals. From these figures the following conclusions are obtained.

(1) At the fundamental frequency, the difference between M and R_1 of polished crystals and lapped ones cannot be observed.

Table 9

THE VALUES M_{mn} AND α_n , WHEN THE MEAN VALUE OF M_n IS EXPRESSED AS $M_{mn}f^{-\alpha_n}$ (FIDUCIAL PROBABILITY OF α_n BEING 90%; f BEING THE FREQUENCY EXPRESSED IN MC).

| Overtone Order | Frequency Range (Mc) | $M_{mn} (10^3)$ | α_n |
|----------------|----------------------|-----------------|-----------------|
| Fundamental | 10 ~24 | 10.2 | 1.25 ± 0.15 |
| 3 | 22.5~60 | 22.6 | 1.74 ± 0.07 |
| 5 | 37.5~75 | 19.7 | 1.90 ± 0.19 |

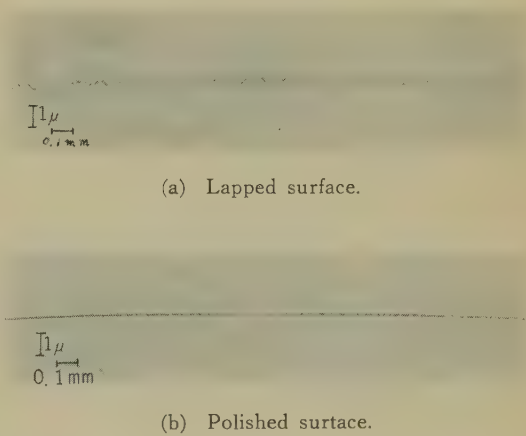


Fig. 41—Observed roughness of lapped surface and polished surface (lapping was done with AO-emery No.304 and light oil; polishing was done with cerium oxide powder and water on the pitch plate).

(2) At the third overtone, the quality is improved by a factor of about 1.5 if polished crystals are used.

(3) Polishing results in a remarkable improvement of the crystal units used at the fifth overtone, and even the use of the seventh overtone of polished crystals can be recommended.

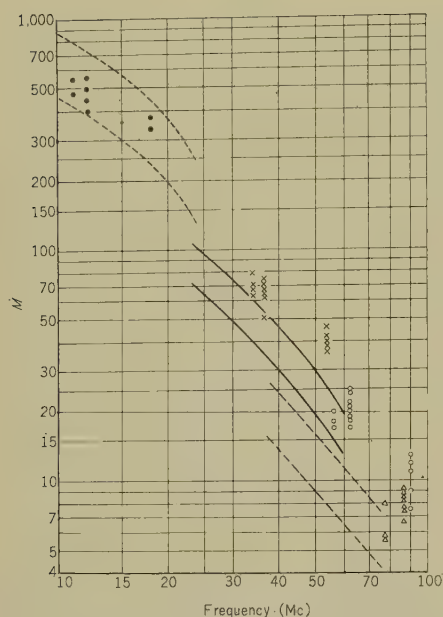


Fig. 42— M of the polished crystals compared with that of the lapped crystals ($C_0 = 5.8 \sim 7.2$ pF; dotted, solid and dashed curves represent 90% two side tolerance limits of M of the lapped crystals at fundamental, third overtone, and fifth overtone respectively; points ●, ○, ×, and Δ represent measured data for M of the polished crystals at fundamental, third overtone, fifth overtone, and seventh overtone respectively).

4.7. Oscillator Circuits

The oscillator circuit used for VHF crystal units is illustrated in Fig. 44. In this circuit, the crystal unit operates at its series resonance frequency. Fig. 45 illustrates the effects of detuning the plate tank circuit on the frequency and activity of the crystal oscillator. The experimental results shown in Fig. 45 and other similar data proved that the oscillator circuit shown in Fig. 44 provides satisfactory results as a crystal oscillator up to 100 Mc.

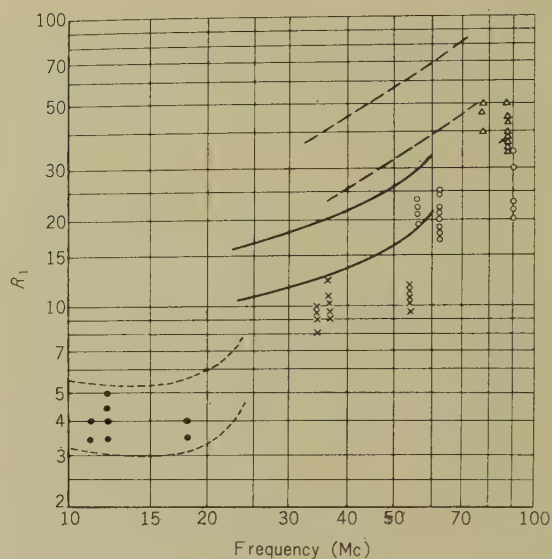


Fig. 43— R_1 of the polished crystals compared with that of lapped crystals (the explanations in Fig. 42 are also applicable to this figure).

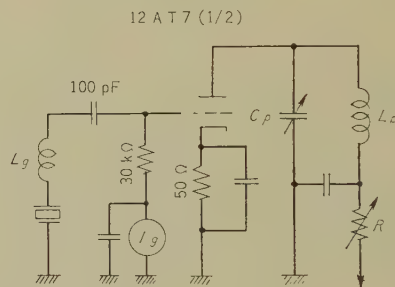


Fig. 44—Oscillator circuit used for VHF crystal units.

4.8. Summary

In this section, a brief description has been given on the development of 10~100 Mc crystal units. It is summarized as follows:

(1) Thwaite's method and Ida's method were employed in order to lap VHF crystal plates.

(2) The crystal units manufactured by a suitable lapping machine have excellent and uniform qualities.

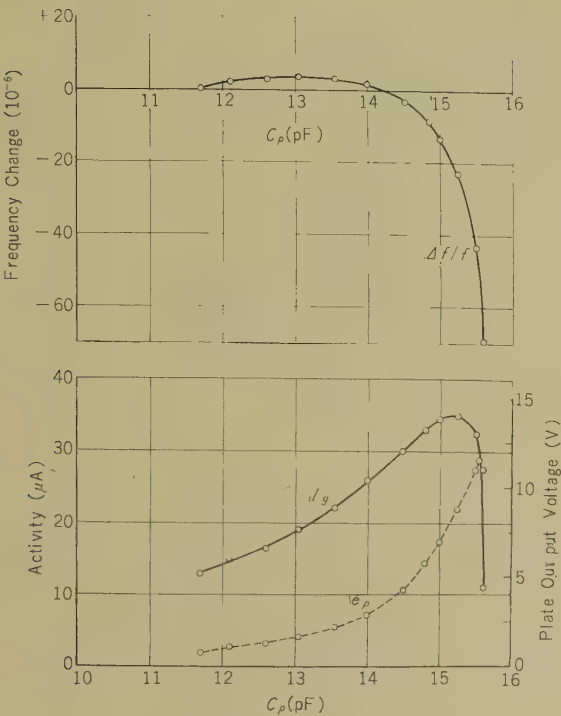


Fig. 45—Effect of detuning of the plate tank circuit of the oscillator shown in Fig. 44 on the frequency and activity of the crystal oscillator (this experiment was carried out at 40 Mc using third overtone crystal units).

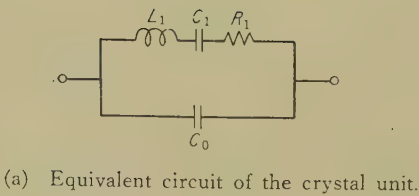
(3) The author has succeeded in obtaining crystal units of excellent qualities up to 100 Mc by polishing the crystal plates precisely.

(4) The oscillator circuit illustrated in Fig. 44 provides satisfactory results as a crystal oscillator up to 100 Mc.

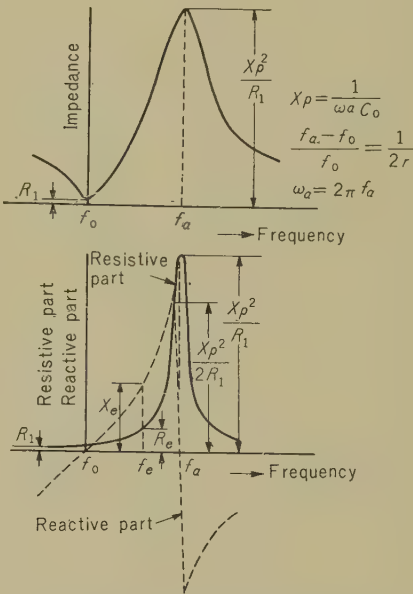
5. Adjustment of Load Capacitance of Crystal Oscillators

5.1. General

When a crystal unit is designed to operate as an inductive impedance in a crystal oscillator, it is general practice to specify the load capacitance of the oscillator for the representation of the nominal operating point of the crystal unit. Therefore it is necessary to ad-



(a) Equivalent circuit of the crystal unit.



(b) Impedance-frequency characteristics of the crystal unit (when $x_p/R_1 \gg 1$).

Fig. 46—Equivalent circuit and impedance-frequency characteristics of the crystal unit.

just not only the load capacitance of the test circuit but also that of crystal oscillators actually used to the specified value.

This section presents a new method devised for adjustment of the load capacitance of the crystal oscillators to the specified value accurately and easily.

5.2. Adjustment of Load Capacitance

5.2.1. Load Capacitance

In the vicinity of the resonance frequency, the electrical characteristics of the crystal

unit are generally represented by the equivalent circuit shown in Fig. 46 (a), and the frequency characteristics of its impedance, reactive part and resistive part are schematically illustrated by Fig. 46 (b).

In crystal oscillators in which the crystal unit is designed to operate as an inductive impedance, the relation between the oscillator circuit and the crystal unit can be expressed by the simple equivalent circuit shown in Fig. 47, where C_L represents an equivalent capacitance looking from the crystal terminals into the oscillator circuit at the crystal unit frequency. In such a crystal oscillator, the reactance X_e of the crystal unit amounts to $1/2\pi f_e C_L$, and oscillation frequency f_e is equal to the frequency corresponding to X_e on the reactance curve, as shown in Fig. 46 (b).

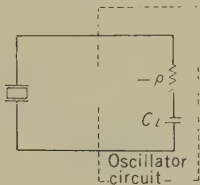


Fig. 47—Relation between the oscillator circuit and the crystal unit.

Therefore, when the value of C_L is given, the oscillation frequency of the crystal unit is simply determined by C_L , and this value is called the “load capacitance.”

5.2.2. Difference between the Crystal Oscillator and Self-excited-oscillator

For example, in the crystal oscillator shown in Fig. 48, if a coil is inserted in place of the crystal unit, this circuit is reduced to a Colpitts circuit and its self-excited oscillation frequency is also determined by the load capacitance of the oscillator just in the same way as in the case of the crystal unit. However, the change of the self-excited oscillation

frequency $\Delta f_e'$ caused by a small change of load capacitance ΔC_L is far greater than that of the crystal oscillator Δf_e , and the frequency change ratio of Δf_e to $\Delta f_e'$ can be represented by the following equation:

$$\frac{\Delta f_e}{\Delta f_e'} = \frac{1}{r} \frac{1}{\left(1 + \frac{C_L}{C_0}\right)\left(1 + \frac{C_0}{C_L}\right)}, \tag{28}$$

where r is the capacitance ratio of the crystal unit, which amounts to about 200 in the case of AT-cut plates and about 400 in the case of BT-cut plates.

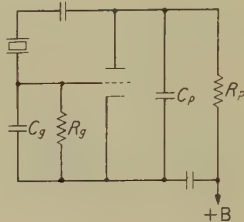


Fig. 48—C-R type pierce oscillator.

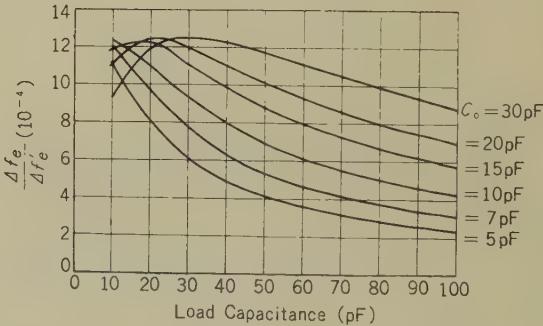


Fig. 49—Calculated value of equation (28), where r is estimated to be 200.

Fig. 49 illustrates the calculated value of equation (28), and Fig. 50 shows some experimental results representing the frequency change caused by change of load capacitance for a coil and for crystal units.

As may be easily seen from these figures, the change of frequency in the case of the

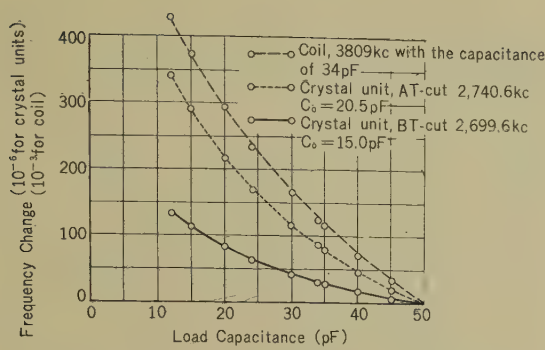


Fig. 50—Frequency change caused by the change of load capacitance.

coil is many thousands of times as large as that in the case of the crystal unit, and this is the very property which is utilized here for the adjustment of load capacitance.

5.2.3. General Method

The general method of adjusting the load capacitance of a crystal oscillator to a specified value C_{L0} is as follows:

- (1) A variable-inductance coil mounted on the same type of base as that of the crystal unit is prepared; then, the series resonance frequency of the coil and C_{L0} are adjusted to f_0 by the adjustment of the coil, where f_0 is the frequency of the crystal unit to be used.
- (2) Next, the coil is inserted in the crystal socket of the oscillator to be used, and the oscillation frequency is adjusted to f_0 by adjustment of the variable parts of the oscillator.
- (3) As the result of the above operations, the load capacitance is now adjusted to C_{L0} at the frequency f_0 .

5.2.4. Explanation of the Principle

5.2.4.1. Theory

This paragraph explains the above-mentioned principle. Here the C-I meter shown in Fig. 51 is used in obtaining the series resonance frequency of the coil and the specified load capacitance C_{L0} .

(1) Coil adjustment

As described in the paragraph 5.2.3. (1), when a coil is inserted in the crystal socket of the CI meter in place of the crystal unit, and the inductance of the coil and the variable parts of the CI meter are so adjusted that both in the crystal side and the resistance side of switch S_1 the oscillation frequencies become nearly equal to f_0 , the inductance L_0 of the coil is expressed as follows:

$$L_0 \cong \frac{1}{(2\pi f_m)^2 C_{L0} \left(1 + \frac{\Delta C_n}{C_{L0}}\right)} \left(1 - 4 \frac{C_{L0}}{C_m} \frac{\Delta f_{m,n}}{f_m}\right) \tag{29}$$

$$\Delta f_{m,n} = f_m - f_n,$$

where f_m and f_n denote the oscillation frequencies of the CI meter when switch S_1 is thrown to the coil side and the resistance side respectively; ΔC_n is the error in the value of C_{L0} , as compared with the true value, and C_m is the capacitance determined by the following equation:

$$f_0 = \frac{1}{2\pi \sqrt{LC_m}} \tag{30}$$

where L is the inductance of the coils in the plate and grid circuits of the CI meter shown in Fig. 51.

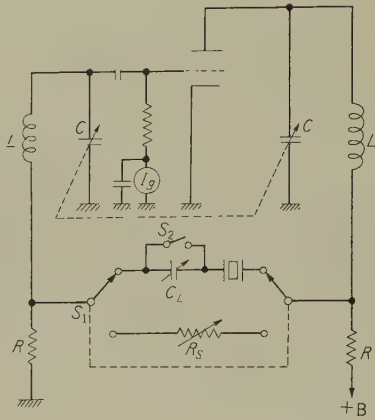


Fig. 51—C-I meter.

(2) Adjustment of the oscillator

When this coil is inserted in the crystal oscillator, and the oscillation frequency is adjusted to f_c (nearly equal to f_0), then the frequency f_c is expressed as follows:

$$\frac{1}{2\pi f_c L_0} = 2\pi f_c C_L \quad (31)$$

In equation (31), C_L denotes the effective capacitance of the crystal oscillator looking from the crystal socket into the oscillator; this means the load capacitance of the crystal oscillator at the frequency of f_c as defined in paragraph 5.2.1.

From the equations (29) and (31), C_L becomes

$$C_L \cong C_{L0} \left[1 - 2 \frac{\Delta f_c}{f_m} + 4 \frac{C_{L0}}{C_m} \frac{\Delta f_{mn}}{f_m} + \frac{\Delta C_n}{C_{L0}} \right] \quad (32)$$

where $f_c = f_0 - f_m$

In the right-hand side of equation (32), the terms except the first term represent the error of adjustment of load capacitance and from this equation it is expected that the error can be made very small.

5.2.4.2. Experimental Results

Figs. 52 and 53 illustrate some experimental results concerning the error of adjustment of the load capacitance in terms of deviations of crystal frequency. In these figures, Δf_0 is represented by

$$\Delta f_0 = f_0' - f_0 \quad (33)$$

where f_0' is the oscillation frequency of the crystal unit in an oscillator whose load capacitance has been adjusted to C_{L0} , and f_0 is the series resonance frequency of the crystal unit and the specified load capacitance C_{L0} .

In Fig. 52, the relations between $\Delta f_0/f_0$ and $\Delta f_{mn}/f_m$ are illustrated. In this figure the solid curve represents the experimental results and the dotted curve shows the value calculated

from equation (32). The relations between $\Delta f_0/f_0$ and $\Delta f_c/f_m$ are illustrated in the same way in Fig. 53.

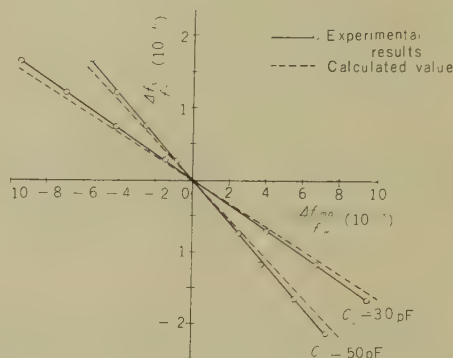


Fig. 52—Relation between $\Delta f_{mn}/f_m$ and $\Delta f_0/f_0$ (the crystal unit is 4,000 kc BT-cut; C_m is 69.2 pF).

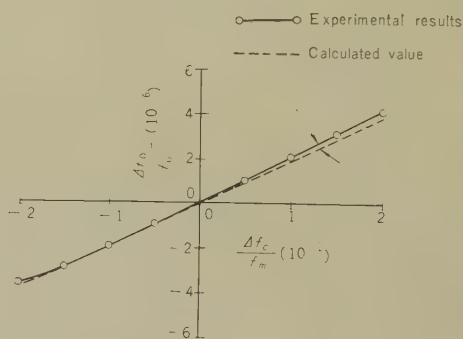


Fig. 53—Relation between $\Delta f_c/f_m$ and $\Delta f_0/f_0$ ($C_{L0} = 40$ pF; the crystal unit is 4,000 kc, BT-cut).

From these figures it can be concluded that when an adjustment accuracy of $\pm 1 \times 10^{-6}$ is required for crystal frequency, an accuracy of adjustment of $\pm 2 \times 10^{-3}$ of the self-excited oscillator frequency is sufficient. Such an accuracy is obtainable by the use of a simple beat tone in almost all the applications.

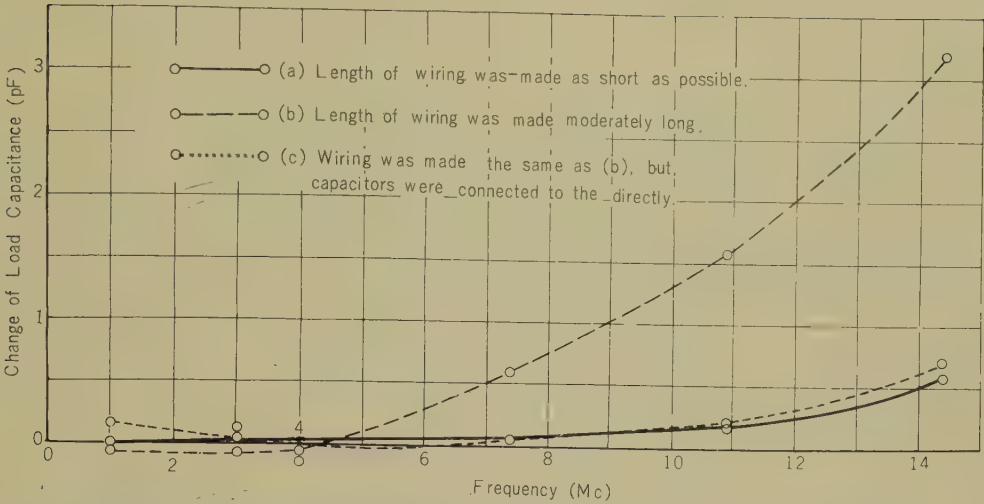


Fig. 54—Frequency characteristics of the load capacitance of a C-R type Pierce oscillator (load capacitance is adjusted to 40 pF at 4.15 Mc).

5.3. C_L Meter

5.3.1. Frequency Characteristics of the Load Capacitance in Some Crystal Oscillators

In crystal oscillators in which the load capacitance consists chiefly of capacitors, load capacitance can be kept substantially the same value over an extremely wide frequency range.

For example, Fig. 54 illustrates the frequency characteristics of the load capacitance of the C-R type Pierce oscillator shown in Fig. 48. In this figure, the solid curve (a) represents the characteristic when the wiring was made as short as possible, while the dashed curve (b) represents the characteristic when the wiring was made moderately long. Dotted curve (c) represents the characteristic when the wiring was made as long as that in the case of curve (b), but the capacitors which principally determine the load capacitance were connected directly to the crystal socket. The equivalent circuits corresponding to the three cases are shown in Fig. 55, where dotted lines represent the distributed inductance and capacitances caused by the wiring and interelectrodes capacitances of the tubes.

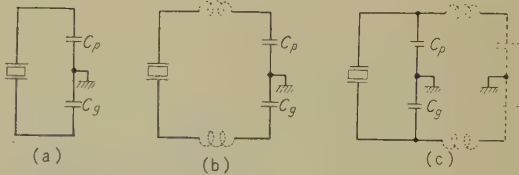


Fig. 55—Equivalent circuits of the three circuits described in Fig. 54.

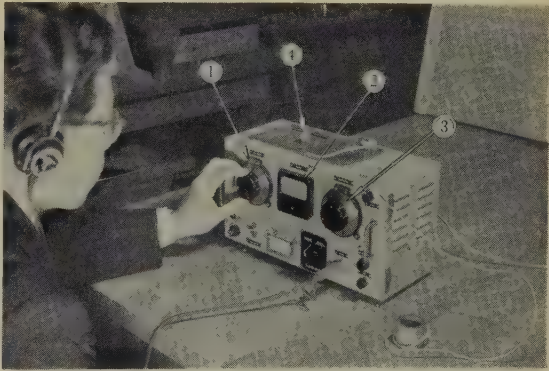


Fig. 56— C_L meter.

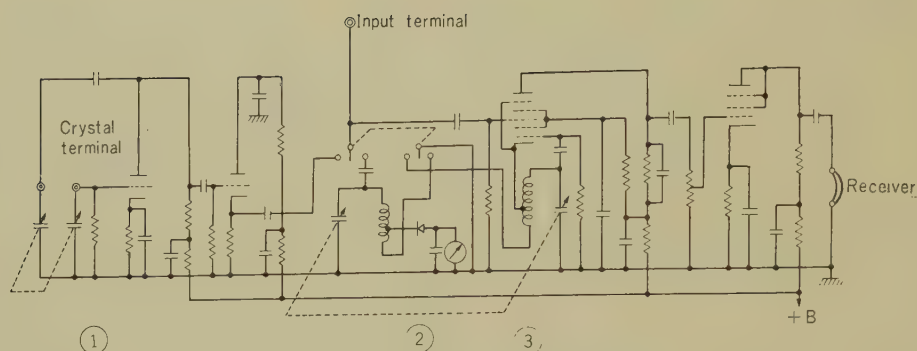


Fig. 57—Circuit diagram of C_L meter.

From Fig. 54 it can be said that when appropriate attention is paid to the wiring of the actual oscillator circuits, the load capacitance of these oscillators can be kept substantially constant over the frequency range from 1 Mc to 10 Mc, and this is one of the most advantageous properties of these oscillators.

5.3.2. C_L Meter

A simple instrument devised for the adjustment of load capacitances of the C-R type Pierce oscillator (Fig. 48) is shown in Figs. 56 and 57. In these figures, (1) shows a crystal oscillator whose load capacitance is variable and which maintains the same load capacitance over a wide frequency range; (2) shows an absorption type frequency meter equipped so that only 1:1 beat tones may be caught when the frequencies of two oscillators are compared; and (3) shows a variable frequency oscillator equipped in order to hold a frequency temporarily for transfer purposes, and (4) in Fig. 56 shows a coil sealed in a metal case (the case is connected to ground) and mounted on the same base as the crystal unit. Furthermore, this instrument is so constructed that the frequencies of (1), (2), and (3) are almost equal to one another at the same dial reading when coil (4) is inserted in the socket of oscillator (1).

In using this instrument, the following procedures are taken: Coil (4) is inserted in the crystal oscillator (1), and its load capaci-

tance is adjusted to a specified value by using a calibration chart. Then, the frequency of oscillator (3) is made equal to that of oscillator (1). Next, coil (4) is inserted in the crystal oscillator to be used, and its frequency is made equal to that of oscillator (3). Now the load capacitance of the crystal oscillator has been adjusted to the specified value. In these operations, the adjustment of oscillation frequencies are carried out with beat tones.

The measurement of load capacitances of the crystal oscillators can be carried out by the reverse of the operations mentioned above. The change of inductance of coil (4) due to long-time drift or temperature change is not very serious, because in this instrument coil (4) is used only for the transformation of a load capacitance into frequency.

In order to maintain the accuracy of this instrument, it is necessary to calibrate the load capacitance of oscillator (1) at intervals, comparing it with standard capacitors by the means mentioned in paragraph 5.2.3.

C_L meter is very suitable for the adjustment and measurement of load capacitance within the range from 10 pF to 100 pF, with an accuracy of $\pm 1 \times 10^{-6}$, expressed in terms of AT-cut crystal unit frequency.

5.4. Summary

A new method devised for the adjustment of load capacitance of crystal oscillators to a specified value, and its application to some kinds of oscillators have been described in

this section. By this method, adjustment and measurement can be carried out with an accuracy of $\pm 1 \times 10^{-6}$ expressed in terms of AT-cut crystal unit frequency. Frequency characteristics of load capacitance of a C-R type crystal oscillator are illustrated, and some wiring methods are suggested for keeping the same load capacitance over a wide frequency range.

6. Development of a Small Constant-Temperature oven for Crystal Units¹⁰⁾

6.1. General

When a crystal oscillator is required to have highly precise frequency stability, it is sometimes necessary to keep the crystal unit within a limited temperature range independent of ambient temperature changes. A small, accurate, stable constant-temperature oven is suitable for this purpose. Although constant-temperature ovens have been used for crystal units for a long time, their temperature stability and reliability are not sufficient for telecommunication services.

Improvements in the construction of the thermostat and studies on the interior arrangement of the constant-temperature oven have enabled the author to obtain small, accurate, stable constant-temperature ovens capable of maintaining their initial characteristics for at least five years.

This section describes the construction and the design features of the constant-temperature oven.



Fig. 58—An example of the constant temperature oven.

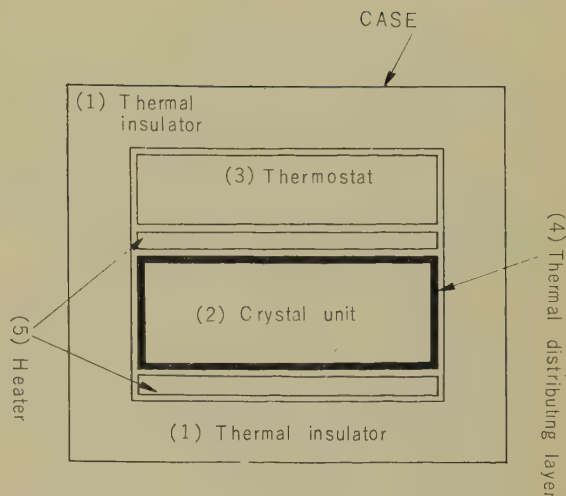


Fig. 59—Internal arrangement of the constant temperature oven shown in Fig. 58.

6.2. Outline

Fig. 58 illustrates an example of the constant-temperature oven, and Fig. 59 shows its internal arrangement. According to Fig. 59, the parts of the constant temperature oven is as follows:

(1) Paulownia, a kind of wood growing in Japan which has excellent thermal insulating properties (thermal conductivity: 0.21×10^{-3} cal per cm, sec, $^{\circ}\text{C}$) is used for the thermal insulating layer. The function of this layer is to keep the thermal power in the constant temperature oven and to obtain a uniform thermal distribution within the crystal part.

(2) In the crystal part, crystal units are inserted. Thermal characteristics of this part are as follows:

- (a) The temperature of this part is within $\pm 1.5^{\circ}\text{C}$ of a specified temperature. The allowance is due to the tolerances in manufacturing the thermostat.
- (b) The temperature change caused by a change in ambient temperature from $0 \sim 40^{\circ}\text{C}$ is smaller than $\pm 0.5^{\circ}\text{C}$.
- (c) Temperature fluctuations are smaller than 0.2°C .
- (d) The temperature change caused by a

supply voltage change of $\pm 10\%$ is smaller than 0.2°C .

(3) A spherical shell-type bimetallic thermostat with quick on-off motions is used.

(4) A copper plate whose function is to attenuate the thermal fluctuation of the crystal unit and to obtain a uniform thermal distribution within the crystal part is used as the thermal distributing layer.

(5) Heaters are operated in the state of black heat. Two heaters are arranged so that the ratio of the power dissipation of one to that of the other is closely related to the thermal stabilities of the crystal part as will be explained in paragraph 6.3.2.

6.3. Design Features

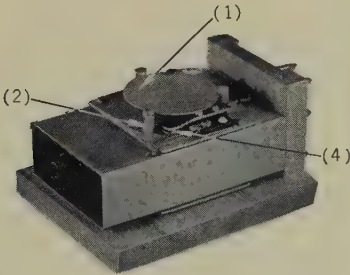
6.3.1. Thermostat

Figs. 60 (a) and (b) illustrate the external appearance and the construction respectively of the thermostat. In these figures, (1) shows the spherical shell type bimetallic thermostat; the three pillars indicated by (2) are the

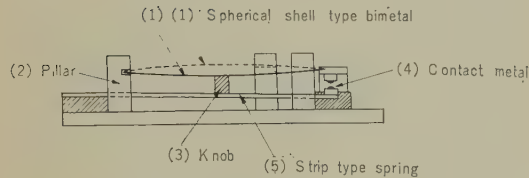
supports of the bimetallic disk. The knob which pushes the bimetallic disk slightly when the contact is open is shown at (3). The contacts made of an alloy of 10 % osmium and 90 % platinum are shown at (4); and (5) shows the strip type spring which holds the knob (3) and one of the contacts.

In Fig. 61, the relation between the displacement of the central part of the bimetallic disk (denoted by δ) and the temperature is shown. In this figure, when the temperature rises to θ_1 , δ comes to the point C, where δ jumps to point B and the contact opens. As the result the temperature falls, when it reaches θ_2 , next jump occurs from the point D to A, causing the contact to close and the temperature to rise. This is repeated successively.

Therefore, in Fig. 60, when the top of the



(a) External appearance



(b) Construction

Fig. 60—Spherical-shell type thermostat.

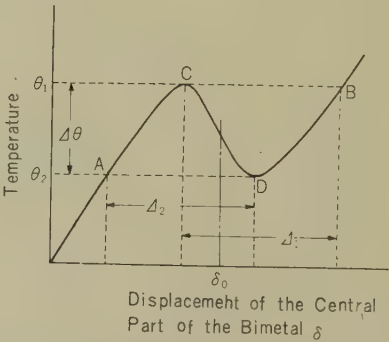


Fig. 61—Relation between the displacement of the central part of the bimetallic disc and the temperature.

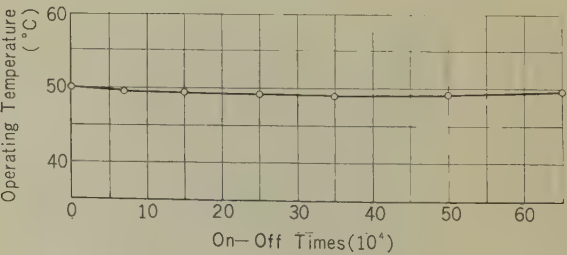


Fig. 62—Long-time thermal stability of the thermostat measured by an accelerated test.

knob (3) is situated at point δ_0 in Fig. 61 when the contact is closed, quick on-off motion of the contact always takes place, and long life of thermostat is assured.

Fig. 62 illustrates an example of the long-time thermal stability of the thermostat measured by an accelerated test. From these results, satisfactory thermal stabilities are expected for at least five years.

6.3.2. Stabilization of Crystal Temperature against Ambient Temperature Changes

(a) General principle

Notation

θ_{r0} : Temperature rise of the thermostat when the contact of the regulator is short-circuited and electric power is supplied to the heater even when the contact is open.

θ_{l0} : Temperature rise of the crystal unit for the same conditions as above.

θ_r : Mean value of the on-off temperature of the thermostat.

θ_l : Crystal temperature.

θ_a : Ambient temperature.

T_0 : On-off period of the thermostat.

T_1 : The period when the contact is closed.

n : T_0/T_1 ($n > 1$)

Since the temperature rise is proportional to the mean power supplied, the value of n can be expressed by

$$n = \frac{\theta_{r0}}{\theta_r - \theta_a} \quad (34)$$

In the same way

$$\theta_l = \theta_a + \frac{\theta_{l0}}{n} \quad (35)$$

From equations (34) and (35), θ_l becomes

$$\theta_l = \frac{\theta_{l0}}{\theta_{r0}} \theta_r + \theta_a \left(1 - \frac{\theta_{l0}}{\theta_{r0}} \right) \quad (36)$$

Therefore, when the following condition is satisfied,

$$\theta_{r0} = \theta_{l0} \quad (37)$$

θ_l is always equal to θ_r and is independent of the ambient temperature changes.

Furthermore, when

$$\theta_{r0} > \theta_{l0} \quad (38)$$

θ_l changes in the same direction as the ambient temperature change, while, when

$$\theta_{r0} < \theta_{l0} \quad (39)$$

θ_l changes in the opposite direction from the ambient temperature change. So, if we find a method of satisfying equation (37), we will be able to design a constant temperature oven in which crystal temperature is independent of ambient temperature change.

(b) Compensating heater method

In the arrangement of the constant temperature oven shown in Fig. 63, when the ratio of the power dissipation (this ratio is denoted by p) of heaters A and B (both heaters are regulated by the same regulator) is varied and the ambient temperature is changed, then the crystal temperature changes as illustrated in Fig. 64. When 6.5 is chosen as the value of p , this constant temperature

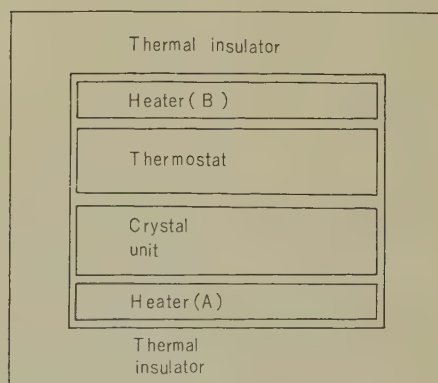


Fig. 63—Construction of the constant temperature oven used in the experiment in Fig. 64.

oven satisfies equation (37). In this way, when at least two heaters are arranged in a constant temperature oven, and the appropriate ratio of power dissipation of these heaters is chosen, then a constant temperature oven in which the crystal temperature is independent of the ambient temperature changes will be obtained.

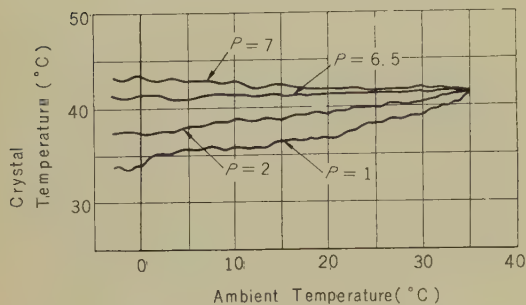


Fig. 64—Relation between crystal temperature and ambient temperature (p denotes the ratio of power dissipation of heater (A) to that of heater (B) in Fig. 63).

The heater which mainly supplies the power to the crystal, is called the “main heater,” and the heater which is equipped in order to improve the stability of crystal temperature is called the “compensating heater.” The constant temperature oven shown in Figs. 58 and 59 is obtained by modification of that shown in Fig. 63.

6.3.3. Reduction of Thermal Fluctuation

When on-off type thermostats—such as bi-metallic thermostats or mercury relays—are used, it is sometimes necessary to reduce the thermal fluctuation of the crystal unit by the use of appropriate thermal filters. For example, the combination of the metal plate and thin air gap shown in Fig. 65 is effective for this purpose.

By using a simple analogy to C-R type electrical filter circuits, the reduction factor of thermal fluctuation A is expressed as

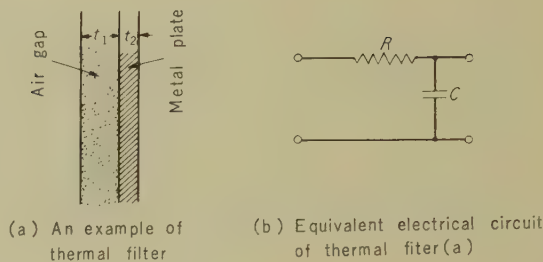


Fig. 65—Thermal filter.

follows:

$$A = \frac{1}{\sqrt{1 + (\omega_0^2 C^2 R^2)}} \tag{40}$$

where R = Thermal resistance of the air gap (mm min °C/cal)

C = Thermal capacity of the metal plate (cal/°C)

$$\omega_0 = 2\pi / T_0$$

T_0 = On-off period of the thermal regulator expressed in minutes

In the case of the combination of a copper plate and an air gap,

$$A = \frac{1}{\sqrt{1 + \left(15.2 \frac{t_1 t_2}{T_0} \right)^2}} \tag{41}$$

where t_1 and t_2 are the thickness of the copper plate and air gap, respectively, in mm.

6.4. Overall Characteristics

Overall characteristics of the small constant temperature ovens designed and manufactured under the above mentioned principles are illustrated in Fig. 66. As shown in this figure, the constant temperature oven was switched on at an ambient temperature of 40°C. After 4.5 hours, the ambient temperature was gradually cooled down to 0°C and maintained at that temperature for 2.5 hours. During this period, the crystal temperature was measured and is illustrated in this figure.

In measuring the crystal temperature, a

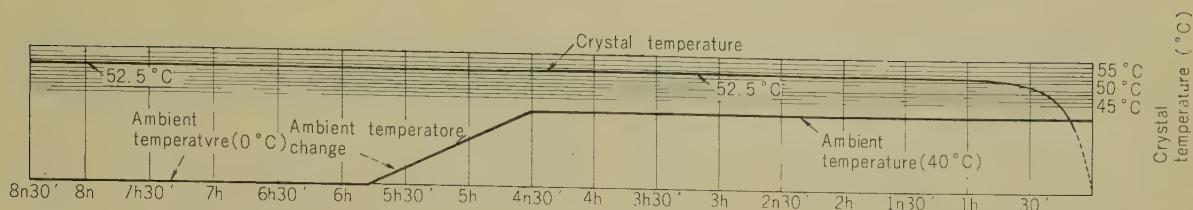


Fig. 66—Temperature stability of the constant temperature oven shown in Fig. 58.

50 Ω platinum wire was inserted in place of the crystal unit, and the change of resistance of this wire was indicated on a recorder in terms of temperature changes. Even very small temperature changes were detected in spite of the wide ambient temperature changes.

6.5. Summary

In this section, brief descriptions have been made on the development of small, accurate, stable, constant temperature ovens. These descriptions are summarized as follows:

(1) The outline of the constant temperature oven is described.

(2) A spherical-shell type bimetallic thermostat was used. Some notes are given about the construction of a thermostat with a long useful life.

(3) General principle of crystal temperature stabilization against ambient temperature changes is described. A practical application of this principle, the "compensating heater method" is shown.

(4) In order to reduce the thermal fluctuation of the crystal unit, the use of thermal filters consisting of a thin air gap and a metal plate is recommended.

(5) Overall characteristics of the constant temperature oven designed and manufactured under the above principles are shown.

7. Conclusion

For the past ten years, the author has devoted himself to the research and development of quartz crystal units. The results obtained are summarized as follows:

(1) New methods and equipments devised

for the manufacture of 1~1,000 kc crystal units have enabled the author to obtain high Q and highly stable crystal units with favorable reproducibility.

(2) Effects of the evaporated metal film on the characteristics of the crystal resonator vibrating in the contour mode were analytically studied. Q and Young's moduli of the evaporated metal films were also measured.

(3) Studies of lapping and polishing very thin crystal plates have enabled the author to obtain 10~100 Mc crystal units with excellent qualities.

(4) A new device for adjusting the load capacitance of the crystal oscillators to a specified value and its application to some kinds of crystal oscillators were presented.

(5) A small, accurate, stable, constant-temperature oven was developed for the stabilization of crystal oscillator frequencies.

Acknowledgment

The author wishes to express his sincere thanks to Dr. Noboru Takagi, Professor of Tokyo University, to Dr. Toshio Hayasaka, Associate Director of the Laboratory, and to Mr. Tokio Muto, Chief of the Circuit Components Research Section of the Laboratory, for their valuable guidances and suggestions given during the course of this work.

The author also wishes to thank Dr. Morio Onoe, Assistant Professor of Tokyo University, and to Dr. Ichiro Ida in the Laboratory, for their kind suggestions during this work.

Furthermore, the author wishes to acknowledge the valuable assistance of Mr. Hiroshi Kojima and Mr. Minoru Kobayashi of the Laboratory, who supplied him with lots of technical details included in this paper.

References

- (1) L. Rohde: Neuartige Steuer- und Filter-Quartze, *Zeitschr. F. Techn. Physik*, Nr. 3, s. 75, 1939.
- (2) R. A. Heising: Quartz Crystals for Electrical Circuits, p. 276, p. 333, p. 356, p. 493, *Van Nostrand*, 1946.
- (3) T. Nijo, K. Takahara and H. Kojima: Fabrication of Wire Mounted Crystal Units, *Electr. Commun. Labor. Techn. J. NTT*, Jap., Vol. 3, No. 2, p. 209, 1954.
- (4) K. Takahara and H. Kojima: The effects of the Evaporated Metal Film on the Q of the Contour Vibration Crystal Units, *J. Inst. Electr. Commun. Eng. Jap.* Vol. 40, No. 6, p. 690, 1957-6.
- (5) W. Voigt: *Lehrbuch der Kristallphysik*, S. 792, Teubner, Berlin, 1910.
- (6) M. Onoe: Effects of Evaporated Electrodes on Quartz Resonator Vibrating in a Contour Mode, *IRE*, Vol. 45, No. 5, p. 694, 1957-5.
- (7) C. Zener: Elasticity and Anelasticity of Metals, p. 41, the Univ. of Chicago press, 1948.
- (8) K. Takahara, I. Ida, M. Kobayashi and Y. Arai: 10-75 Mc Crystal Units, *J. Inst. Electr. Commun. Eng. Jap.* Vol. 39, No. 12, p. 1018, 1956-12.
- (9) J. E. Thwaites and C. F. Sayers: The Production of Very Thin Quartz Oscillator Plates, *P.O.E.E.*, Vol. 46, part 3, p. 105, 1953-10.
- (10) H. Tanaka and K. Takahara: Studies of Small Constant Temperature Oven for Crystal Units, *Monthly Report of Electr. Commun. Labor. NTT*, Jap., Vol. 3, No. 8, p. 5, 1950-8.

* * * *

Studies of Magnetization Processes of Magnetic Cores by Supersonic Methods*

Katsumi NISHIGUCHI† and Hiroshi SAWABE‡

When a supersonic vibration is applied to a magnetic core, the voltage output induced in a winding on the core is approximately proportional to the remanent flux. Measurements of remanent induction were made on various magnetic cores with rectangular B-H characteristics used in memory devices. Although the method is somewhat complicated, it is useful to non-destructively investigate the inner structure of magnetic cores.

1. Introduction

Various methods are used for testing the properties of magnetic materials, but methods using ballistic galvanometers or current pulses have the disadvantages that the internal states of the specimen are different after measurement. The so-called nondestructive methods which do not change the internal states of the specimen included the following:

- (a) Crossed magnetic field method
- (b) Secondary distortion method
- (c) Supersonic magnetostriction method

These methods all depend on the fact that there is difference of π in the output signal phase according to whether the residual induction is positive or negative. Furthermore, the theoretical output voltage of all of these methods is small.

However, the use in method (c), of supersonic magnetostriction, which is a mechanical method, allows a greater degree of freedom in the measurements than obtainable with the all-electrical methods. The results of

measurements of the various properties of magnetic cores through the application of supersonic vibration are reported in this paper. This measurement method, which was developed in our laboratory several years ago for the measurement of ferroelectric samples, ⁽¹⁾ has recently been applied to the measurements of ferromagnetic materials and very attractive results have been obtained.

2. Relation between Magnetic Field and Magnetostriction Output

Investigations were made first of the relation between the dc magnetic field and magnetostriction output; measurements which could be made with ease. Since magnetostriction is small in the irreversible boundary displacement and mainly occurs in the reversible rotation, ⁽²⁾ the magnetostriction output is small in magnetic cores which show square hysteresis-loop characteristics. Comparative studies, therefore, were made in an experiment between magnetic cores showing square hysteresis loop characteristics and those with a hysteresis loop which was more gradual. The characteristics of the magnetic core materials used are shown in Table 1.

Fig. 1 represents the cross section of the transducer used in the experiments. Here a duralumin diaphragm of 0.035 mm thickness was fixed inside a brass cylinder. A 500 kc

* MS in Japanese received by the Electrical Communication Laboratory on June 6, 1960. Originally published in the *Kenkyū Zitūyōka Hōkoku (Electrical Communication Laboratory Technical Journal)*, N.T.T., Vol. 9, N. 10, pp. 1149-1162, 1960.

† Switching Apparatus Research Section.

‡ Electronics Research Section.

barium-titanate crystal was cemented on one side of the diaphragm and a ferrite core of 4 mm outer diameter, 2 mm inner diameter and 1 mm thickness with a uniform winding was cemented on the other. With the crystal made to resonate with the driving sine wave signal, measurement was made of the relative value of magnetostriction voltage output induced in the winding. Figs. 2 and 3 show

the relation between magnetic field current and magnetostriction signal output with respect to materials A and B respectively. This characteristic represents the irreversible boundary displacement performed from inside the magnetic core, with the valley shown in these figures corresponding to the mutual cancellation of the inside and outside magnetostriction. Beyond the valley point, therefore,

Table 1

CHARACTERISTICS OF THE MAGNETIC CORES

| | A | B |
|---------|--|----------------------------|
| | Square hysteresis loop characteristics | Hysteresis loop was gentle |
| μ_0 | | 800 |
| μ_m | | 3,500 |
| B_s | 2,900 | 2,500 gauss |
| B_r | 2,600 | 1,200 gauss |
| H_c | 1.0 | 0.6 |

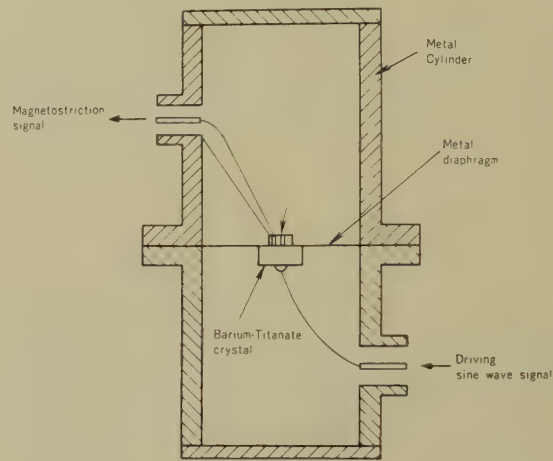


Fig. 1—Transducer.

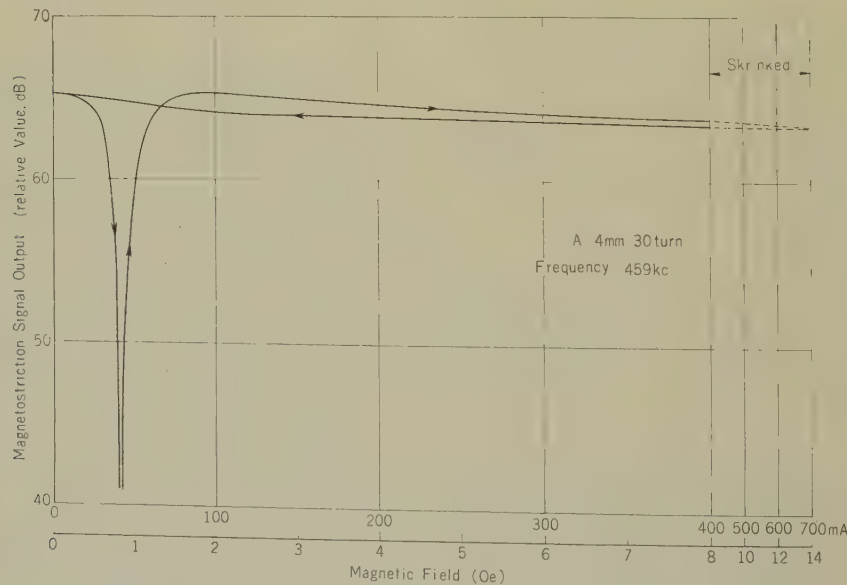


Fig. 2—D.C. magnetic field vs. magnetostriction signal output.

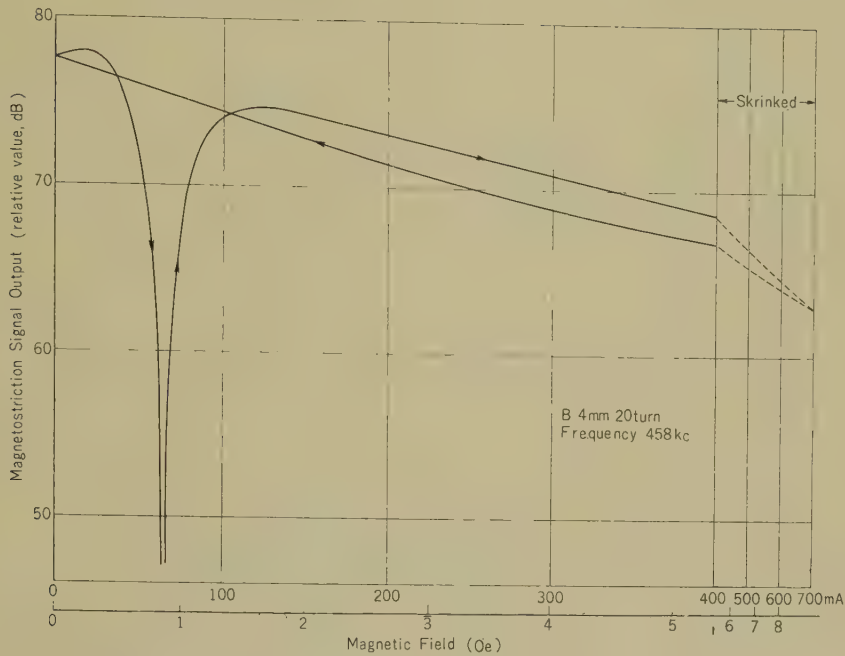


Fig. 3—D.C. magnetic field vs. magnetostriction signal output.

the phase of the magnetostriction signal output differs by π ; however in the graphs, only absolute values are shown. Also, only the positive side of the dc magnetic field current is plotted here; the negative side is symmetrical.

It may be seen from Figs. 2 and 3 that as already mentioned before, in a magnetic core which shows a square hysteresis loop characteristic like material A, the magnetostriction signal output is small, but it will not decrease very much even when the dc magnetic field current becomes great.

Next, the magnetostriction signal characteristic after demagnetization is shown in Fig. 4, and those for materials A and B in the case where the dc magnetic field current is reduced to 0 in the midst of hysteresis loop are shown in Figs. 5 and 6 respectively. Here, also it may be seen that in material A which shows a square hysteresis loop characteristic, the magnetostriction signal does not depend much upon the intensity of magnetic field current.

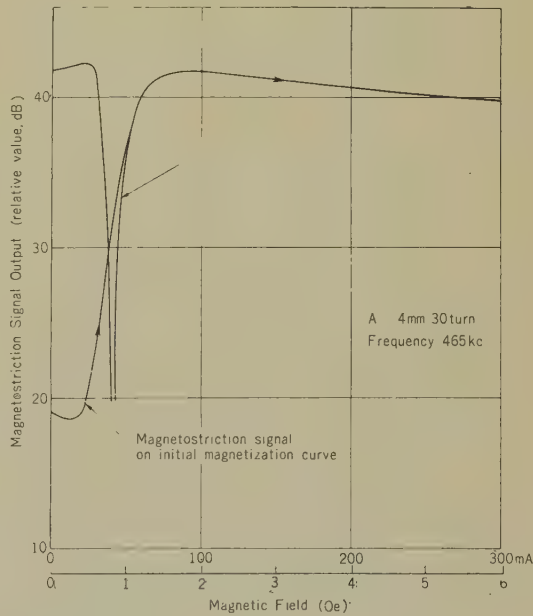


Fig. 4—Magnetostriction signal on initial magnetization curve.

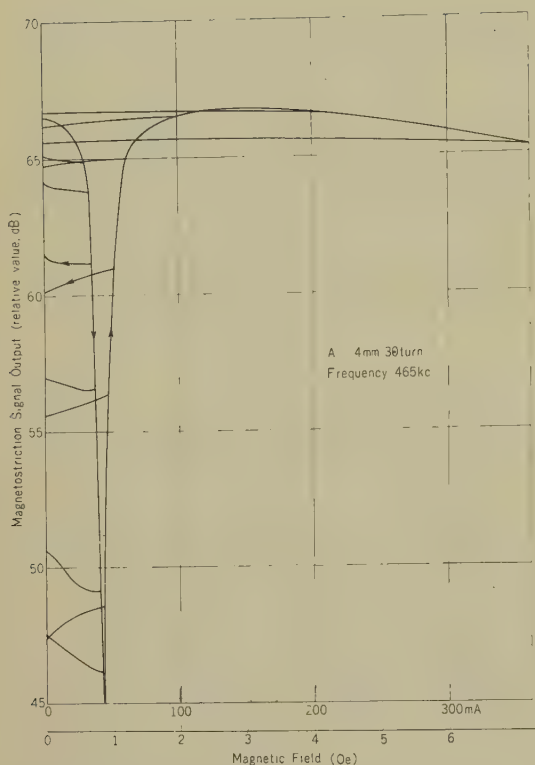


Fig. 5—Magnetostriction signal where d.c. magnetic field is reduced halfway in hysteresis loop.

3. Relation between Magnetic Induction and Magnetostriction Signal

In order to apply the Villari effect to the measurement of the magnetization process of a magnetic core, the relation between the magnetostriction signal and remanent induction must be obtained first. Fig. 7 shows a block diagram for measuring this relation. The magnetic core is reversed, through polarity reversing pulses, to positive and negative remanent induction alternately. Change of magnetic induction is measured by integrating and amplifying the differentiated waveform of remanent induction which appears in the other winding. Supersonic vibration is applied at the same time, and then, by measuring the magnetostriction signal, the relation between magnetostriction signal and

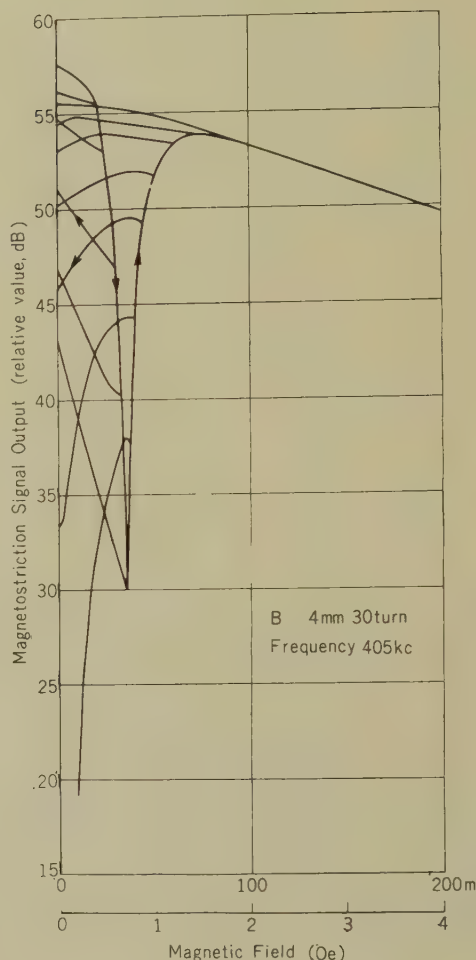


Fig. 6—Magnetostriction signal where d.c. magnetic field is reduced halfway in hysteresis loop.

remanent induction can be obtained.

Fig. 8 represents the relation thus obtained between magnetostriction signal and remanent induction for the square hysteresis loop core, in which it may be seen that the two are proportional to each other except in the vicinity of the saturation point.

Next, measurement was made of the magnetization characteristic due to current pulses. With the magnetic core set at the negative saturation point first, remanent induction was measured by the supersonic method, applying signal pulses successively.

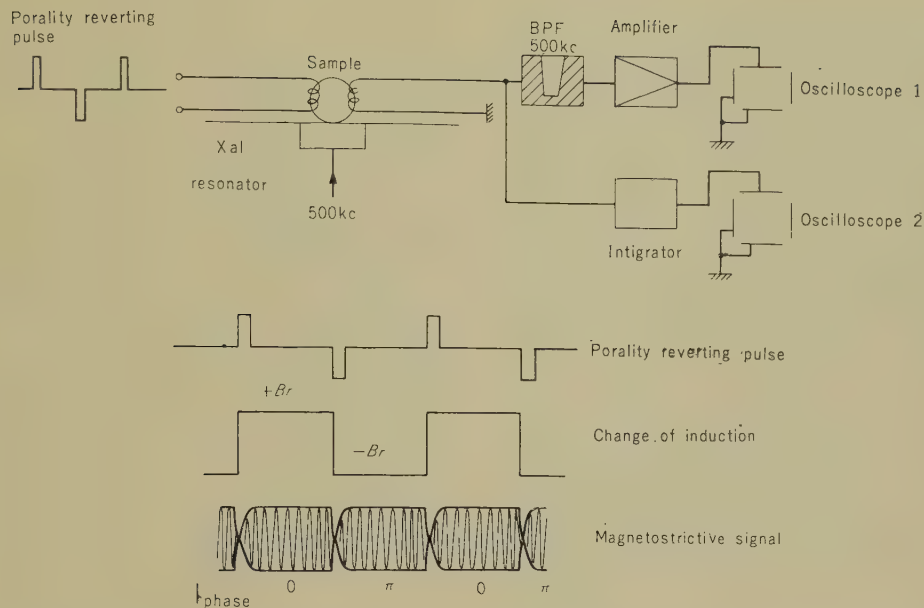


Fig. 7—Measurement of relation between remanent induction and magnetostriction signal.

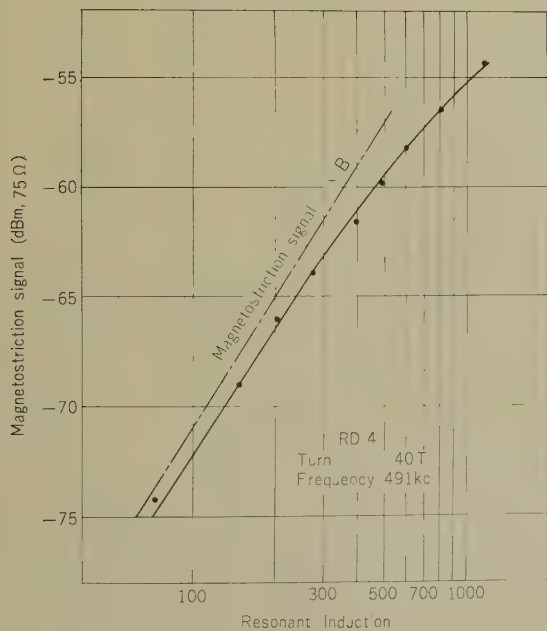
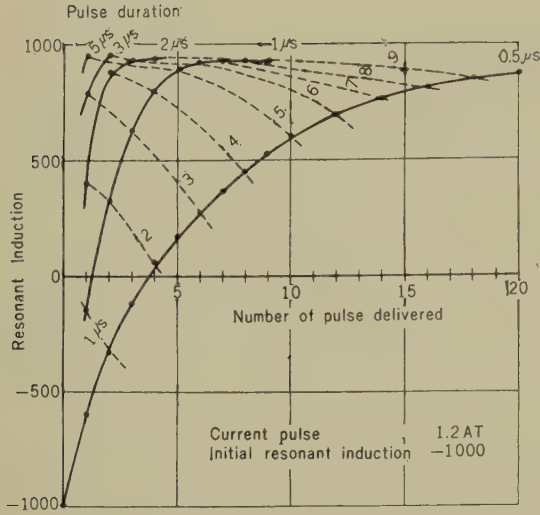


Fig. 8—Relation between remanent induction and magnetostriction signal in the ferrite core having square hysteresis characteristic.

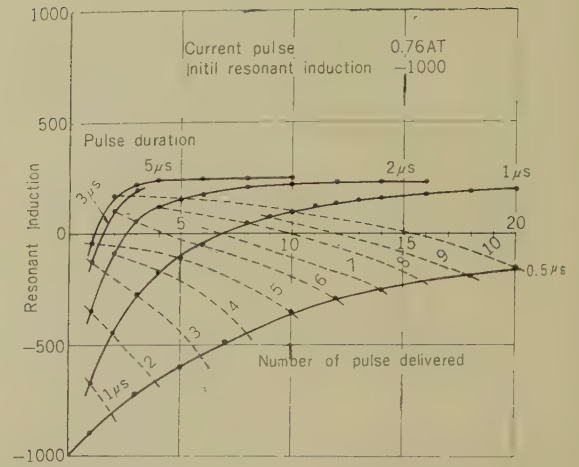
Five pulse durations were used: 5, 3, 2, 1, and 0.5 ms. Fig. 9 (a)–(d) show the measurement results for core RD₄ having square hysteresis, and the solid curves indicate the relation between the number of applied pulses and the remanent induction. Total time duration of applied pulses is given as the parameter.

As seen clearly from Fig. 9, the change of the remanent induction caused by applying an infinite number of pulses is small when the current pulses are small. The dotted curves in the figure represent the combination of the points where the total duration of applied pulses (pulse duration \times number of pulses) is constant. When pulse duration becomes smaller, change of magnetic induction will also be smaller, even though the total duration remains constant.

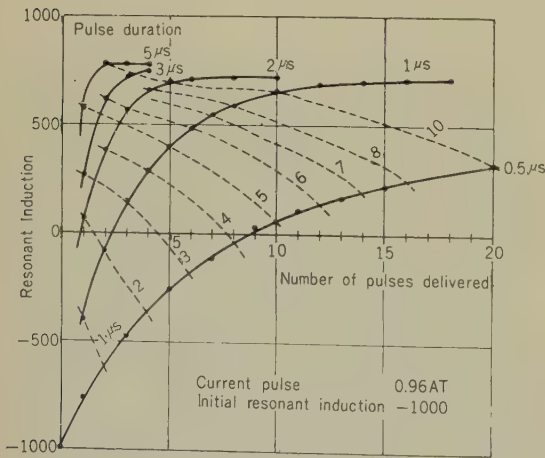
While it is possible to measure the properties of magnetic cores by means of the above method, it is important in a memory element that the magnetic core be fully reversed by a single pulse, but not be reversed even if many pulses of half the amplitude are applied. Fig. 10 shows the result of mea-



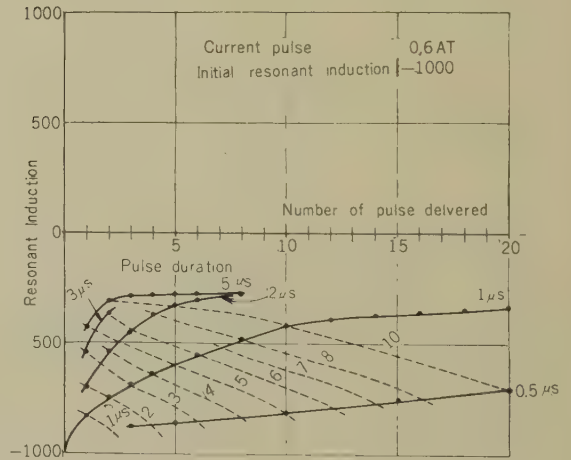
(a)



(c)



(b)



(d)

Fig. 9 (a)—Magnetization process by pulse current (Specimen RD₄).

measurements made for such evaluation, where the solid curve indicates the relation between magnetic field and the pulse duration required to magnetize the magnetic core by a single pulse, from $-B_s$ to $+0.8B_s$, while the chain line indicates the relation between pulse duration and $H_R/2$ and the dotted curve the relation between magnetic field (H_{NR}) and

the pulse duration required to magnetize magnetic core from $-B_s$ to $-0.8B_s$. In this case, the value of τ_s indicated by the crossing point of curves $H_{NR}-1/\tau_s$ and $(H_R/2)-(1/\tau_s)$ will be the switching time of the magnetic core.

By measuring the switching time for magnetic cores with different ratios of inner and

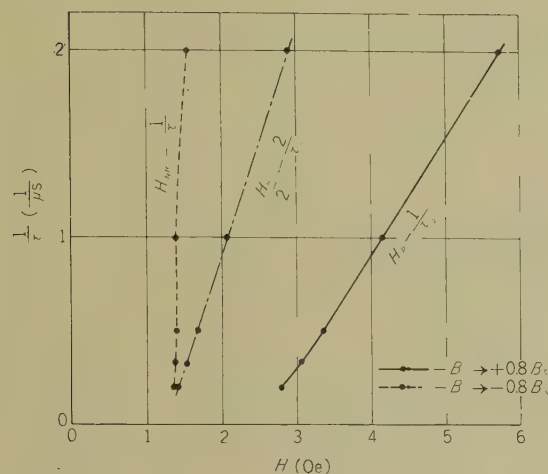


Fig. 10—Switching characteristic of square hysteresis loop magnetic core.

outer diameters, it was confirmed that, as regards magnetic cores of the same material, the nearer to 1 the ratio of inner and outer diameters is, the shorter the switching time will be.

4. Conclusion

In the method of measuring various pro-

perties of magnetic cores by the supersonic method, the measurement process is extremely complicated, as it is necessary to determine the relation between the magnetostriction signal and remanent induction. Moreover, the better the quality of the square hysteresis loop core is, the less the magnetostriction signal will be, so that the measurement will be all the more difficult. Nevertheless, this method is considered to be of considerable use for measuring the physical properties of magnetic substance, since nondestructive reading is made available.

5. Acknowledgement

We would like to express our heartfelt thanks to Mr. Kiyasu, Zen'iti Mr. Itiro Endo, and Mr. Fushimi, for their kind help and guidance.

References

(1) K. Fushimi and K. Kataoka: Ultrasonic Measurement of Polarization Switching Processes in Barium-Titanate Single Crystal, *Journal of Applied Physics*, **29**, 8, (1958.08), 1947/1251.
(2) R. M. Bozorth: Ferromagnetism, D. Van Nostrand Comp. Inc., 1951, Chap. 13.

* * * *

A High-Speed Facsimile System with Electronic Scanning^{*}

Keijiro KUBOTA,[†] Kazuo KOBAYASHI,[†] Yoshitaro OKAJIMA,[†]
and Shogo NANBO[†]

This paper describes an experimental high-speed facsimile system with electronic horizontal scanning and mechanical vertical scanning. A Vidicon is used at the transmitting terminal while a flying-spot cathode-ray tube is used at the receiving terminal where the signal is recorded on electrophotographic paper. The transmitting speed of a facsimile system of this type is limited by the recording speed, which is dependent on the light sensitivity of the electrophotographic paper, the brightness of the flying-spot cathode-ray tube, etc. At present, the maximum transmitting speed is a horizontal repetition rate of 100 c/s with a vertical paper speed of 10 mm per second. In general, facsimile systems with electronic scanning are suitable for the high speed transmission of small-size copy, and have the additional advantage that the pictures can be enlarged or contracted during reception.

1. Introduction

Various high-speed facsimile systems have been reported. Among the most well known are Ultrafax, which uses photographic film and flying spot kinescopes at both the transmitting and receiving terminals, and a high-speed facsimile system which uses a thin-window cathode-ray tube and Electrofax paper at the receiving terminal; both were developed by RCA.

The high-speed facsimile system described in this paper features the use of a Vidicon in the transmitter, a flying-spot cathode-ray tube in the receiver, and electrophotographic paper for recording. The original copy can be transmitted from a well lighted room, and a permanent record is obtained directly as

the received picture. Developing and washing of photographic film are unnecessary at both the transmitter and receiver; therefore the operation of the apparatus is extremely simple.

2. Design Fundamentals

A one-inch Vidicon and a five-inch flying-spot cathode-ray tube were used. There are the same type of Vidicon and flying-spot cathode-ray tube that are used in television, and have a resolution of several hundred lines. Unlike television, facsimile requires that the received picture have uniform quality not only in the center but also near the margin. Furthermore, the tubes are used with single line sweeps. Therefore, it is not desirable to design facsimile on the same resolution capability basis that is used for television.

Suppose that the resolution capability is 500 lines, and that a line density of 4 to 5 lines per mm are necessary to obtain a received picture whose quality is the same as

^{*} MS in Japanese received by the Electrical Communication Laboratory on 25 July, 1960. Originally published in the *Kenkyū Zituyōka Hōkoku (Electrical Communication Laboratory Technical Journal)*, N.T.T., Vol. 9, No. 10, Oct. pp. 1193-1200, 1960.

[†] Telegraph Section.

that received by a facsimile with all-mechanical scanning. Then the original picture should have a width of 100 to 125 mm, but it became smaller as the resolution capability near the margin was below 500 lines.

The horizontal repetition rate is limited by the frequency bandwidth of the transmission line, the persistence of the Vidicon, the recording speed of the electrophotographic paper, etc. For example, if the horizontal repetition rate is 100 c/s and the horizontal retrace ratio is 5%, then the maximum keying frequency becomes 26.4 kc. The blanking signal is used as the synchronizing signal. To perform continuous recording with electrophotographic paper, charging, exposing, developing, and fixing must be carried out continuously. The recording speed is determined by the sensitivity of the electrophotographic paper, the brightness of the flying-spot cathode-ray tube, and the loss of light flux of the lens system. Also, it is important that the spectral responses of the electrophotographic paper, the flying-spot cathode-ray tube, and the lens system be compatible.

Rose-bengal sensitized zinc-oxide electrophotographic paper is used in this system.

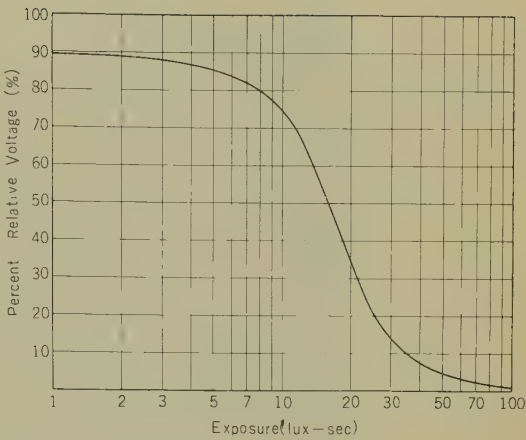
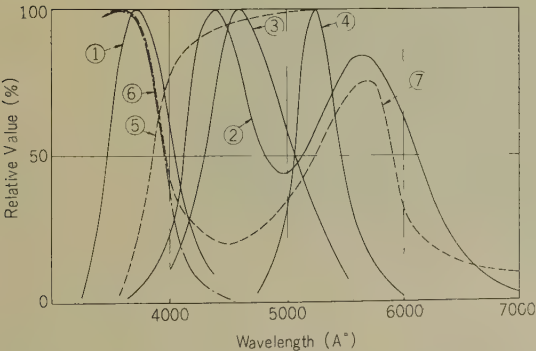


Fig. 2—Light-voltage decay on charged rose bengal sensitized electro-photographic paper.

The spectral response characteristics of the flying-spot cathode-ray tube phosphor, the transmission lens, and the rose-bengal sensitized zinc-oxide electrophotographic paper are shown in Fig. 1; while the voltage-exposure characteristics which represent the sensitivity of the rose-bengal sensitized zinc-oxide electrophotographic paper are shown in Fig. 2.

3. Apparatus

A photograph of the apparatus is shown in Fig. 3, and the outline of the system is illustrated by the block diagram in Fig. 4. At the transmitting terminal, the Vidicon output signal passes through the CR-coupled amplifier and then dc restoration is carried out by the keyed-clamp circuit. This clamped signal is amplitude modulated in the modulator and at the same time synchronizing signal is inserted. The time constants of the coupling circuits and the negative feedback circuits were decided with great care so that the amplifier would have excellent low-frequency characteristics. In order to improve the linearity of the sawtooth current used for horizontal scanning, the principles of the bootstrap circuit were used. A shading correction circuit and an aperture correction



Radiant energy from cathode-ray tube phosphor :
①-P16, ②-P4, ③-P11, ④-P1
Transmission of lens :
⑤-F1.5, 100 mm
Sensitivity of electrophotographic paper :
⑥-Zinc oxide paper, ⑦-Rose bengal sensitized zinc oxide paper.

Fig. 1—Spectral response characteristics.

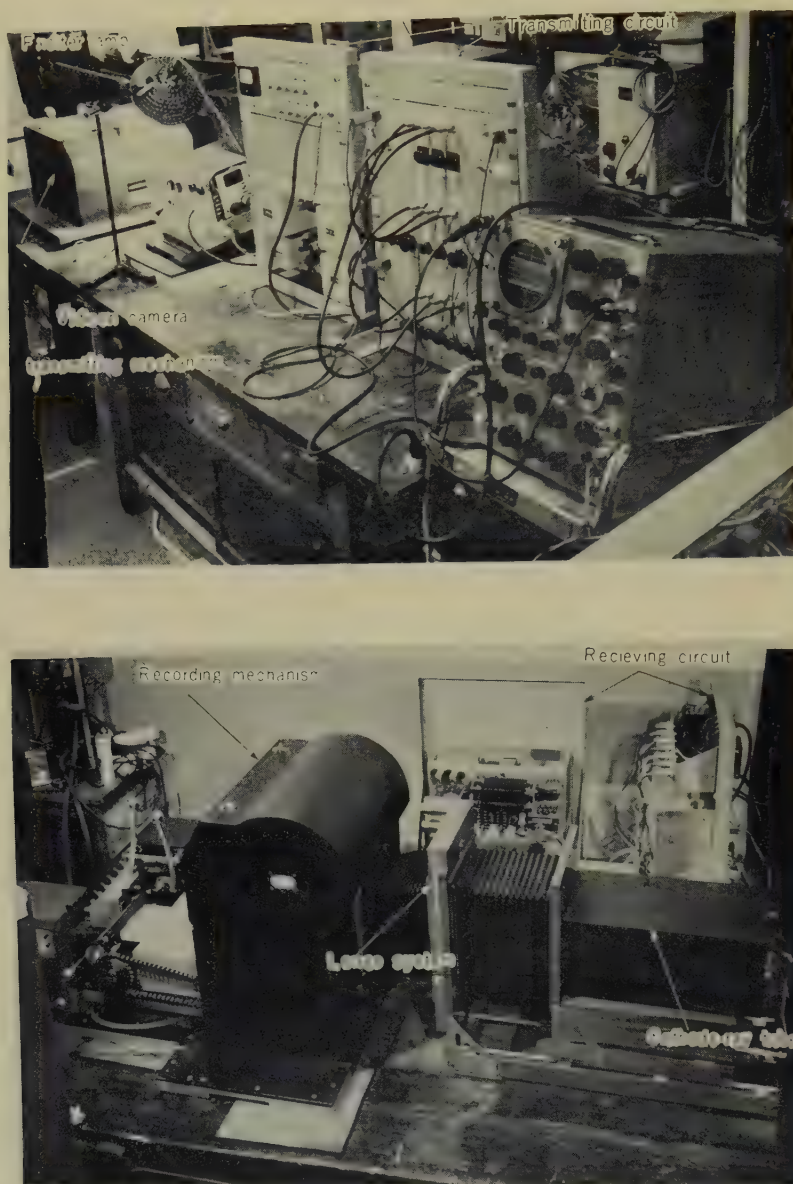


Fig. 3—Apparatus.

circuit are also provided.

At the receiving terminal the incoming signal is amplified and detected, and the output signal is used to intensity-modulate a flying-spot cathode-ray tube. The synchronizing signal is separated at the output of the detector, and this signal is used to sweep the flying-spot cathode-ray tube. The moving

electrophotographic paper records the focussed cathode-ray tube image. The continuous recording apparatus is shown in Fig. 3. At first, the rolled electrophotographic paper is uniformly charged by corona discharge in the charging unit. After it moves to the position of exposure, the paper is exposed to the image on the flying-spot cathode-ray tube,

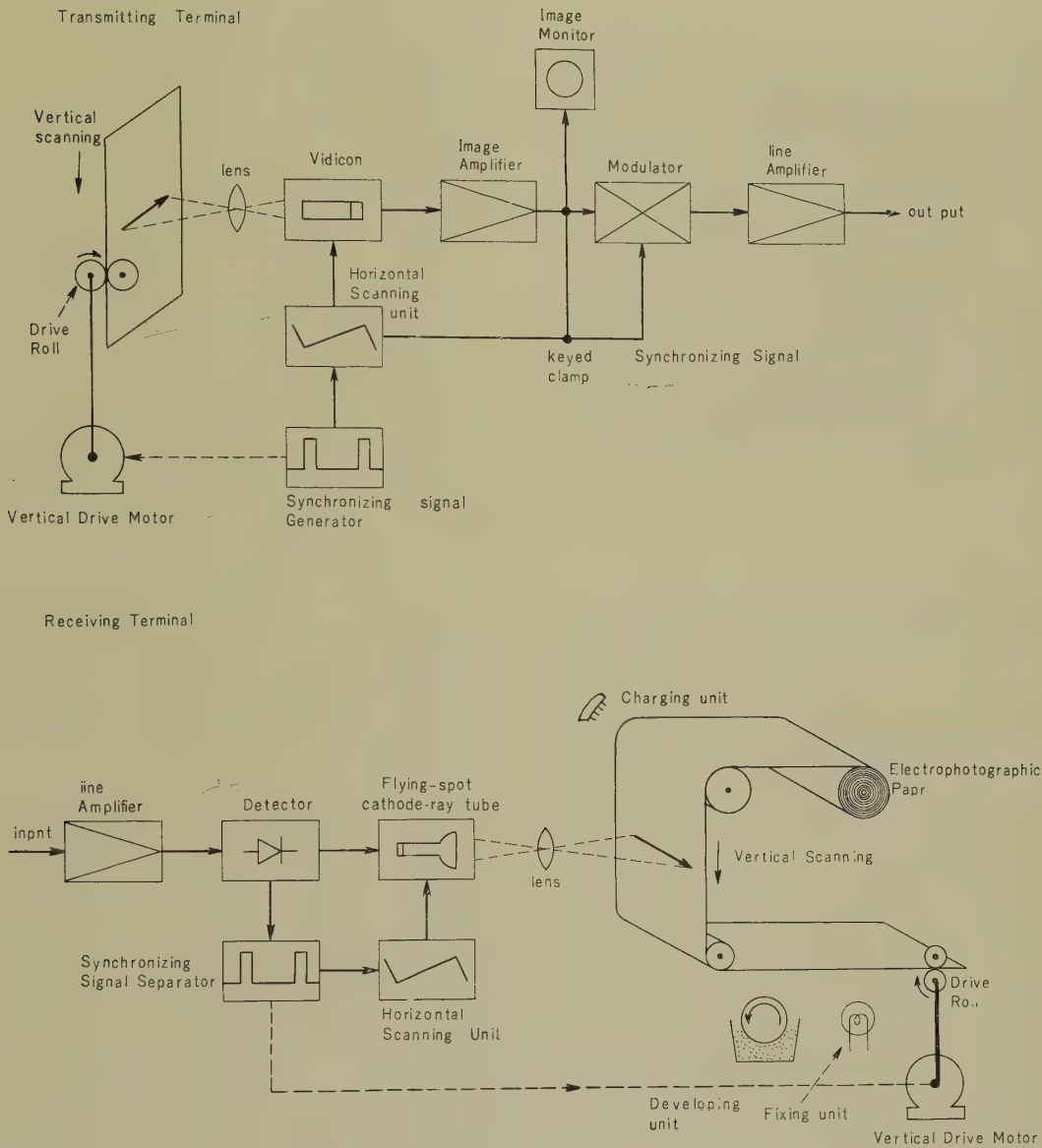


Fig. 4—Blockdiagram of high-speed facsimile.

which performs horizontal scanning only. Next the paper passes through the developing unit and the fixing unit, and a direct permanent picture is obtained.

The developing unit consists of rotating 4-pole electromagnetic brushes whose direction of rotation is opposite to that of the paper feed. The developing powder, which is in a box, is attracted by the magnetic poles. The attracted developing powder is carried up-

ward by the rotation of the poles and develops the electrophotographic paper. Fixing is accomplished by heating the paper with an infrared lamp.

4. Experimental Results and Considerations

The quality of the received picture depends mainly upon the resolution capabilities of the

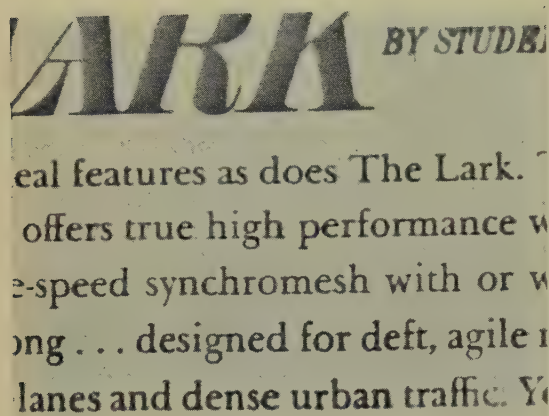


Fig. 5—Samples of the received picture.

Vidicon and the flying-spot cathode-ray tube. For fixed resolution capabilities the resolution per unit area is dependent on the length of the horizontal scanning line. To receive pictures with the same quality as those received by all mechanical facsimile systems with 4 to 5 lines per mm not only in the central part of the picture but also near the margins the length of the horizontal scanning line must not exceed several centimeters. The intrinsic resolution capability of the electrophotographic paper is above 10 lines per mm which is sufficiently high.

Since the Vidicon is used with a single line sweep the storage time is short and the signal output is small. Therefore it cannot be said that the S/N ratio is extremely good, but the system is usable for the transmission of black and white pictures. Unlike television, facsimile is used for the transmission of still pictures; therefore special attention must be paid to sweep linearity and jitter.

As the recording speed is dependent on the phosphor of the flying-spot cathode-ray tube, tubes with P-16, P-11, and P-4 phosphors were tried and the results compared. It was found that the P-4 phosphor is most suitable for use with rose-bengal sensitized zinc-oxide paper. When an f:1.5 lens with a focal length of 10 mm is used the maximum horizontal repetition rate is 100 c/s and the maximum paper speed is 10 mm per second.

This high-speed facsimile was given a field trial using a 60–108 kc group band of a 12 Mc. coaxial cable system. It was found that the circuit characteristics were good and that passage through the transmission line had not caused any deterioration of this picture. Samples of the pictures received are shown in Fig. 5. The pictures shown in Fig. 5 were received with a horizontal repetition rate of 50 c/s, a vertical paper feed of 5 mm per sec, and a horizontal scanning line length of about 60 mm.

As mentioned above, the quality of the pictures received depends on the resolution capabilities of the Vidicon and the flying-spot cathode-ray tube, while the speed of transmission depends on the recording speed. Therefore the development of a Vidicon with high resolution, a flying-spot cathode-ray tube with high resolution and high brightness, and electrophotographic paper with high sensitivity is desirable. Another method of increasing the recording speed would be to record using a thin-window cathode-ray tube without using a lens system.

5. Conclusion

This trial has shown that this electronic scanning system is suitable for high-speed facsimile with small-size copy. The operation of this apparatus is simple because a Vidicon is used for transmitting and electrophotographic paper is used for recording.

At present transmission is limited to a horizontal repetition rate of 100 c/s and a vertical paper feed of 10 mm per second. In addition, if good quality is to be expected of the received picture the length of the horizontal scanning line is limited to several centimeters. In general engineering problems relating to sweep linearity and jitter occur with electronic scanning, but there is the advantage that the picture may be enlarged or contracted as it is received.

Acknowledgement

The authors wish to express their heartfelt thanks to Dr. H. Okuno and Dr. M. Kaji for

their guidance during the course of this project.

References

- (1) D. S. Bond and V. J. Duke, "Ultrafax," *R.C.A. Rev.*, **10**, 1, p. 99, 1949.
- (2) Olden R., "A Thin-Window Cathode-Ray Tube for High-Speed Printing with 'Electrofax,'" *R.C.A. Rev.*, **18**, 3, p. 343, 1957.

* * * *

The Dimensional Accuracy of Molded Spur Gears of 610-Nylon*

Tetsuo KUDO† and Takashi YAMANARI†

This paper describes the effects of the number of gates (single and multiple) and their shapes on the accuracy of molded spur gears of 610-Nylon, for light load use, whose pitch diameter ranges from 5 to 40 mm with module of 0.6 and a 20 degree pressure angle.

In general, injection molded spur gears made through multiple gates are expected to have circles with good roundness, and accuracy better than those made through a single gate. Adequate gate position, proper injecting direction, and uniformity of conditions at each gate for resin flow are also required. In addition, if a hole or projection (e.g. cam. etc.) is located near the circumference of the disk, it causes warpage of the addendum circle. The errors and variations of pitch circle and normal pitch, and the "displacement over a given number of teeth" increase when the addendum circle has warpage. The accuracy of molded spur gears of 610-Nylon which we have prepared for study show no difference for those made through single gates and those made through multiple gates. The accuracy limits of these gears ranges from Japan Gear Manufacturers Association standard class 6 to 7.

1. Introduction

The dimensional accuracy of injection molded spur gears made of thermoplastics is often decreased by warpage of the disk.

Usually, the die for injection molding has only one gate to inject the resin into the cavity. If the moldings are manufactured in a die with an unsatisfactory gate, warpage is liable to occur.

If a disk-type molding is made through a gate in the circumference as shown in Fig. 1 (a), the circumference of the molding will not have perfect roundness. In order to prevent this deformation, a ring gate as shown in Fig. 1 (b) can be used. But this procedure

is not always be suitable, since the structure of the die becomes complicated. It would, therefore, be better to use a die having multi-gates as shown in Fig. 1 (c).

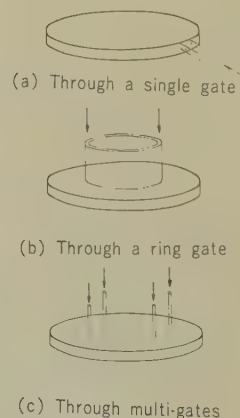


Fig. 1—Disk type moldings made through various kinds of gate.

* MS in Japanese received by the Electrical Communication Laboratory, on June 4, 1960. Originally published in the *Kenkyū Zituyōka Hōkoku (Electrical Communication Laboratory Technical Journal)*, N.T.T., Vol. 9, No. 9, pp. 1085-1116, 1960.

† Switching Apparatus Research Section.

It is necessary for the addendum circle of a molded spur gear, where the teeth exist, to have no warpage.

It is shown in the paper of K. W. Hall and H. H. Alvord⁽¹⁾ that the accuracy limits of injection molded spur gears of 66-Nylon manufactured through a ring gate ranged from commercial class 1 to 2 of AGMA* standard (these are equivalent to class 6 to 7 of JGMA** standard in Japan). These gears, had a pitch diameter of 2.5 in. and the diametral pitches were 20 and 32 (i.e. about 1.25 and 0.8 in module). In their

paper, however, the tendencies and values of the errors were not described.

In this paper, the results of a study on the effects of the forms and number of gates, single and multiple, on the accuracy of molded spur gears of 610-Nylon for light-load use are described.

2. Samples

Five kinds of injection molded spur gears of 610-Nylon were prepared as shown in Fig. 2, i.e., 200 pieces of Samples I and II

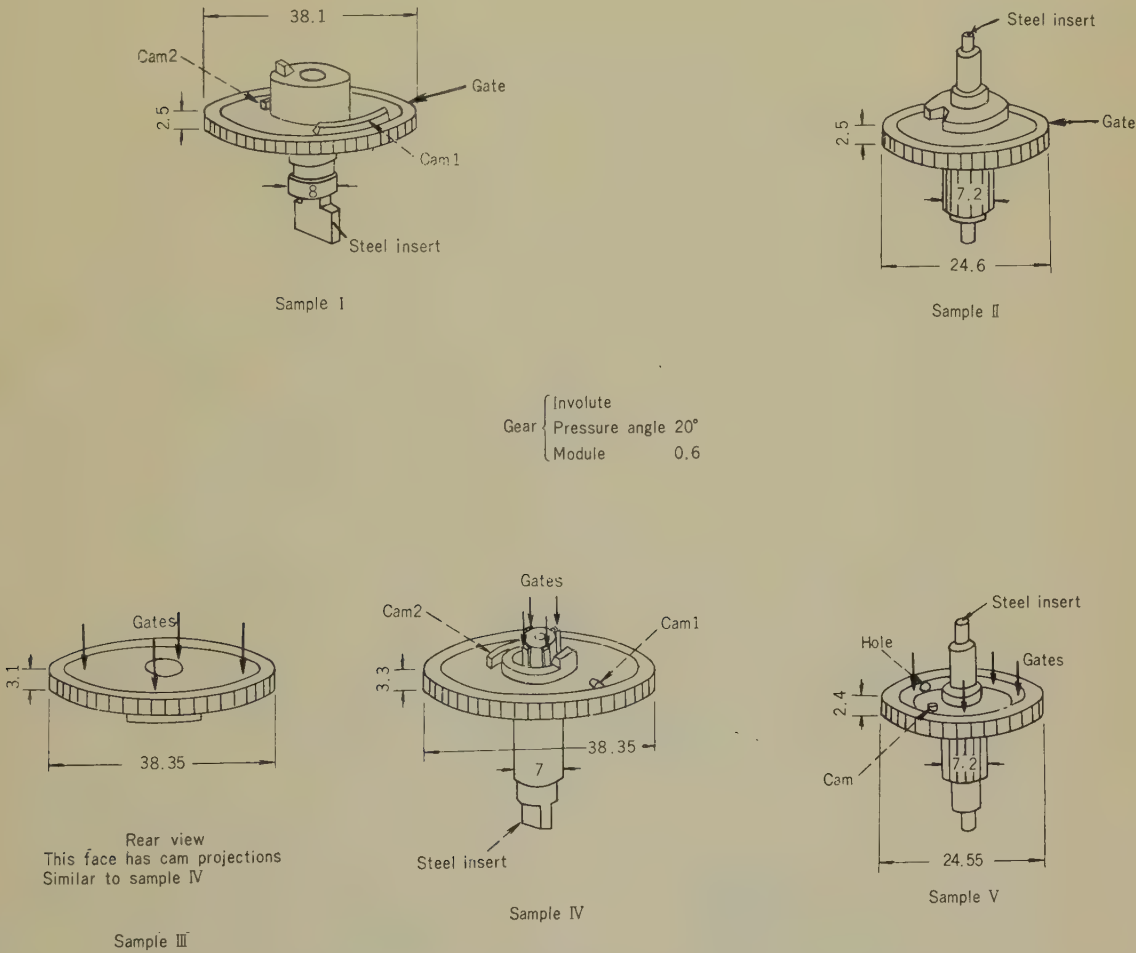


Fig. 2—Forms and gate styles of samples. (All dimensions in mm.)

* American Gear Manufacturers Association.
** Japan Gear Manufacturers Association.

were made through a single gate and 100 pieces of Samples III to V were made through multi-gates (4-gates); and 10 pieces of Samples I and II and 5 pieces of Samples III to V were extracted for measurement.

3. Roundness of addendum circle (Warpage of disk)

In general, when a molding having a gear and shaft is rotated, with its shaft supported

vertically and the addendum circle of the gear not having roundness or the molding having an eccentricity of center between the shaft and the gear disk, wavy motion of the addendum circle and pitch circle of the gear will occur in the horizontal plane.

In this paper, only the warpage of addendum circle is described, but the eccentricity of center is not considered, because the latter is caused mostly by the manufacturing error of the die.

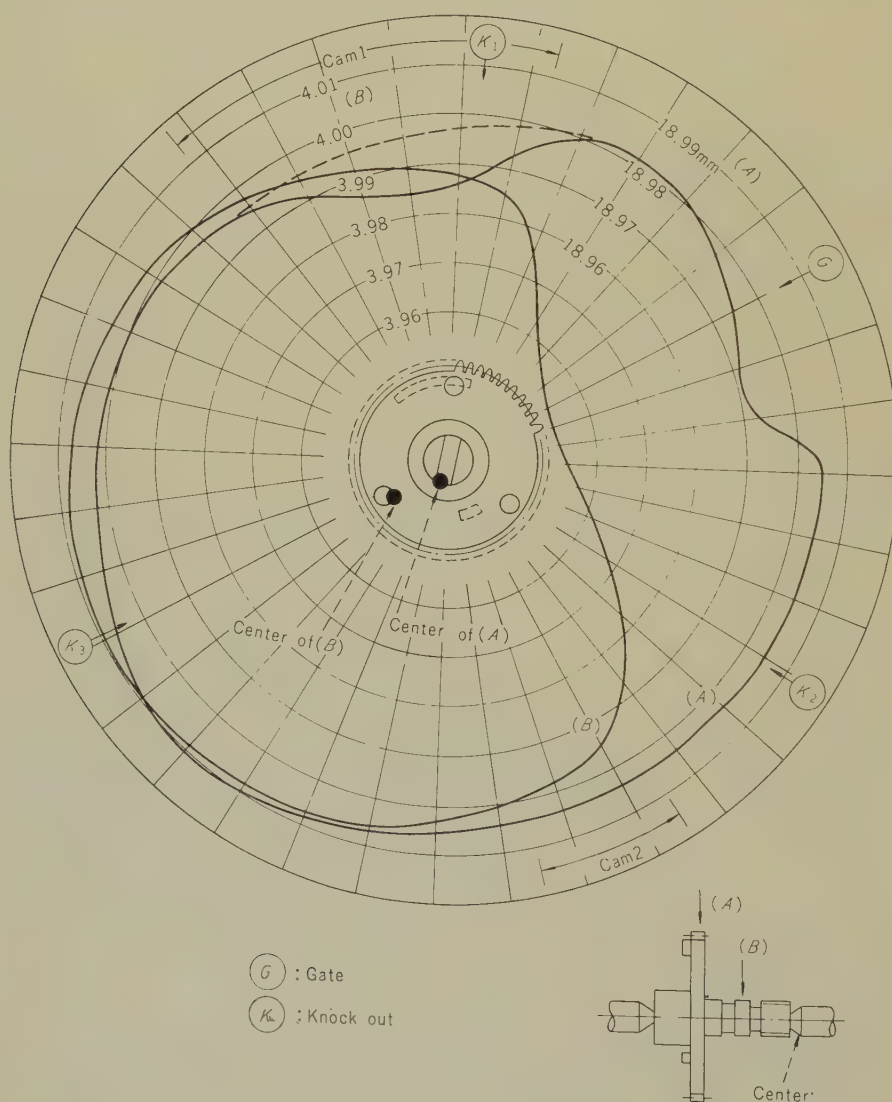


Fig. 3—"Runout" and warpage of sample I.

Figs. 3-6 indicate some typical samples of mean values measured for the “runout” of the addendum circle, shaft, and insert. The centers and deviations from the real circle of circumferences for each part can be assumed by drawing the inscribed or outscribed circle of each figure.

3.1. Influence of Form

Samples I, III, and IV have a projecting

cam near the circumference of the disk, and these circumferences have a partial warpage of about 0.005–0.02 mm, as shown in Figs. 3-5.

Especially, the partial indented warpage (shrinkage) of Sample I is larger than that of the other samples, since the length of its cam is greater than in the cases of the other 2 samples, although in all cases, the cam is located at the same distance from the circumference of the disk.

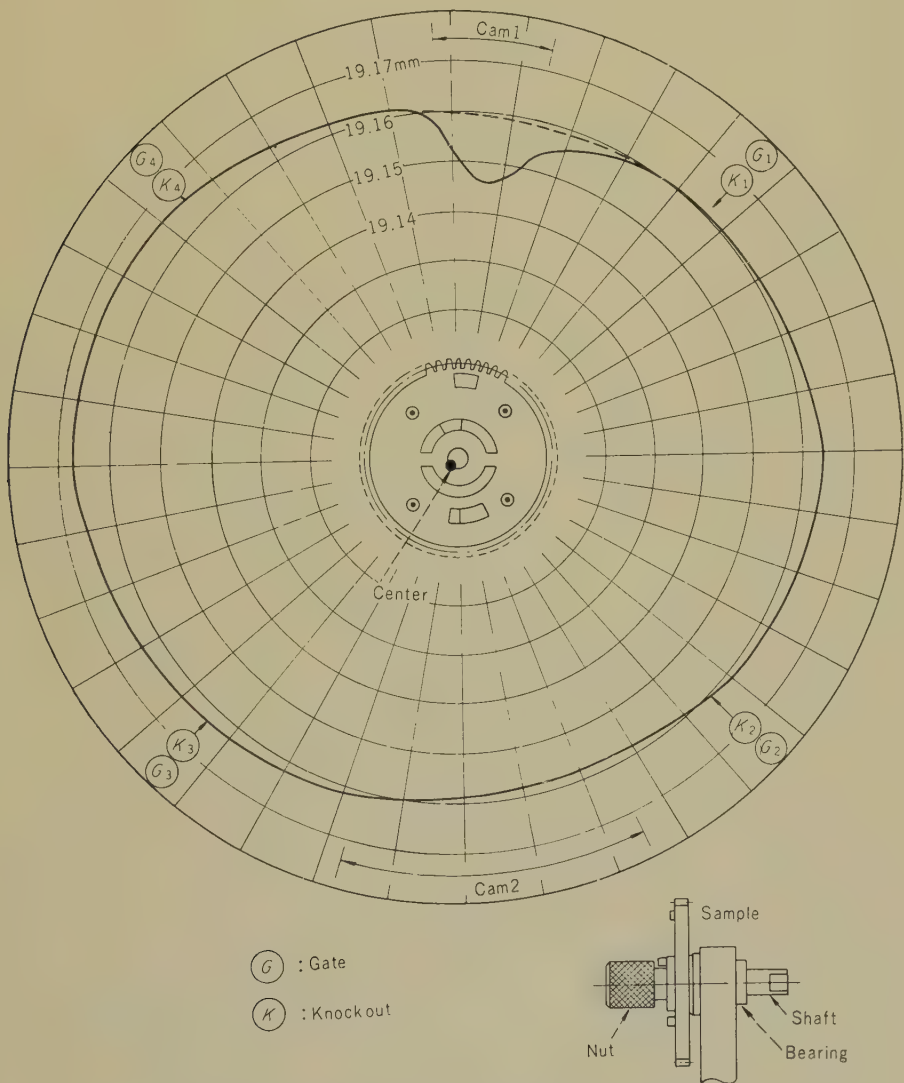


Fig. 4—“Runont” and warpage of sample III.

On the other hand, Sample V has a hole near the circumference of the disk, so that it has partial swollen warpage (less shrinkage) of about 0.04 mm.

If the projection, hole etc. are far from the circumference, no influence is observed.

3.2. Effect of Gates

The maximum values of warpage of the circumference of the disk and shaft assumed

by the previous measurement are shown in Table 1. This table gives the values for two cases where the partial warpgges which are caused by projections and hole are and are not taken into account.

In order to give information on the affects of the gate type and injecting direction of the resin on the warpage, the latter case is considered in this section.

Values measured on the circumference of the disk and shaft of Sample I made

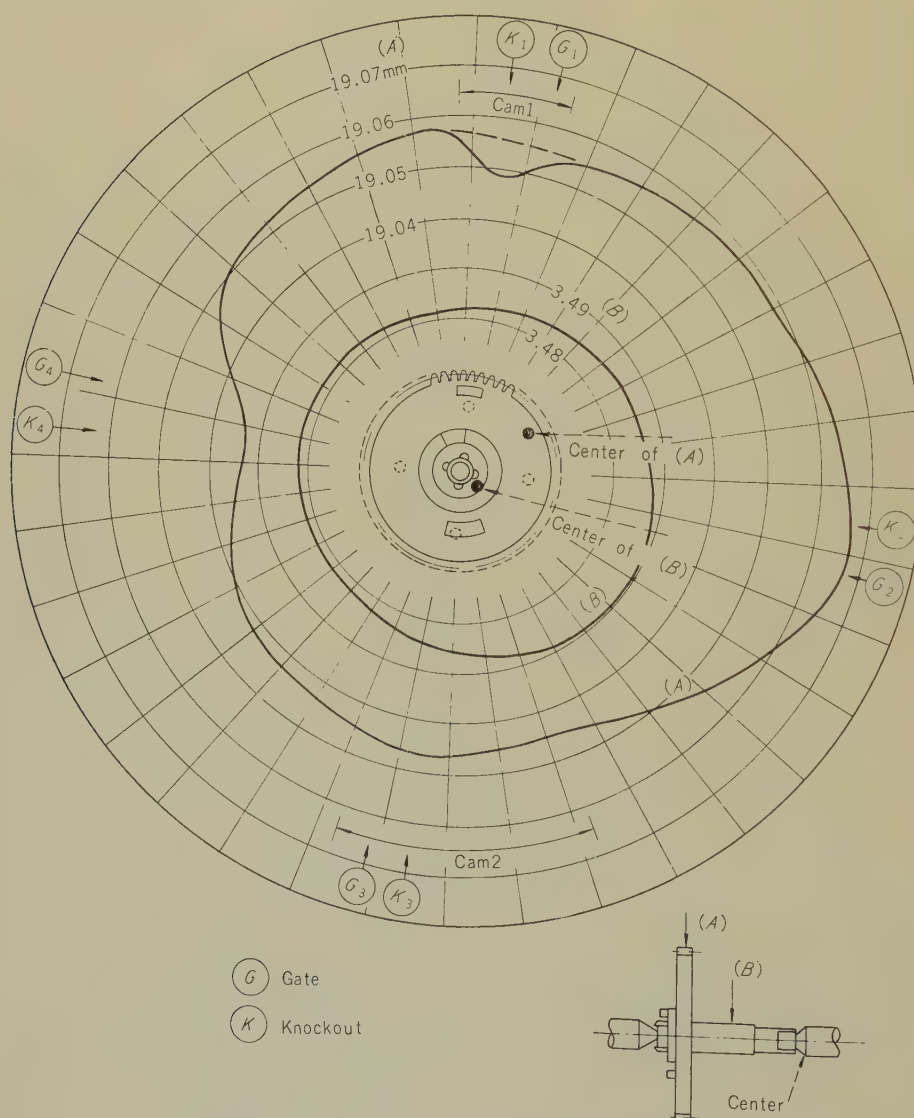


Fig. 5—"Runout" and warpage of sample IV.

through a single gate and on Sample IV made through multi-gates, both having similar form, are shown in Figs. 3-5. The shaft of Sample V made through multi-gates has good roundness, as compared with Sample I made through a single gate.

This result is supposed to be caused more by the difference in gate position and injecting direction of the resin flow rather than by the number of gates.

There is no difference in the values of

warpage of disk between Samples I (by single gate) and IV (by multi-gates), because these gears have a partial warpage corresponding to the gate position.

Sample III, as shown in Fig. 4 has good roundness, because it is made through gates suitably positioned. Sample V is made through multi-gates having a location similar to those used for Sample III; but the warpage of the former is larger than that of the latter, as shown in Figs. 4 and 6. This war-

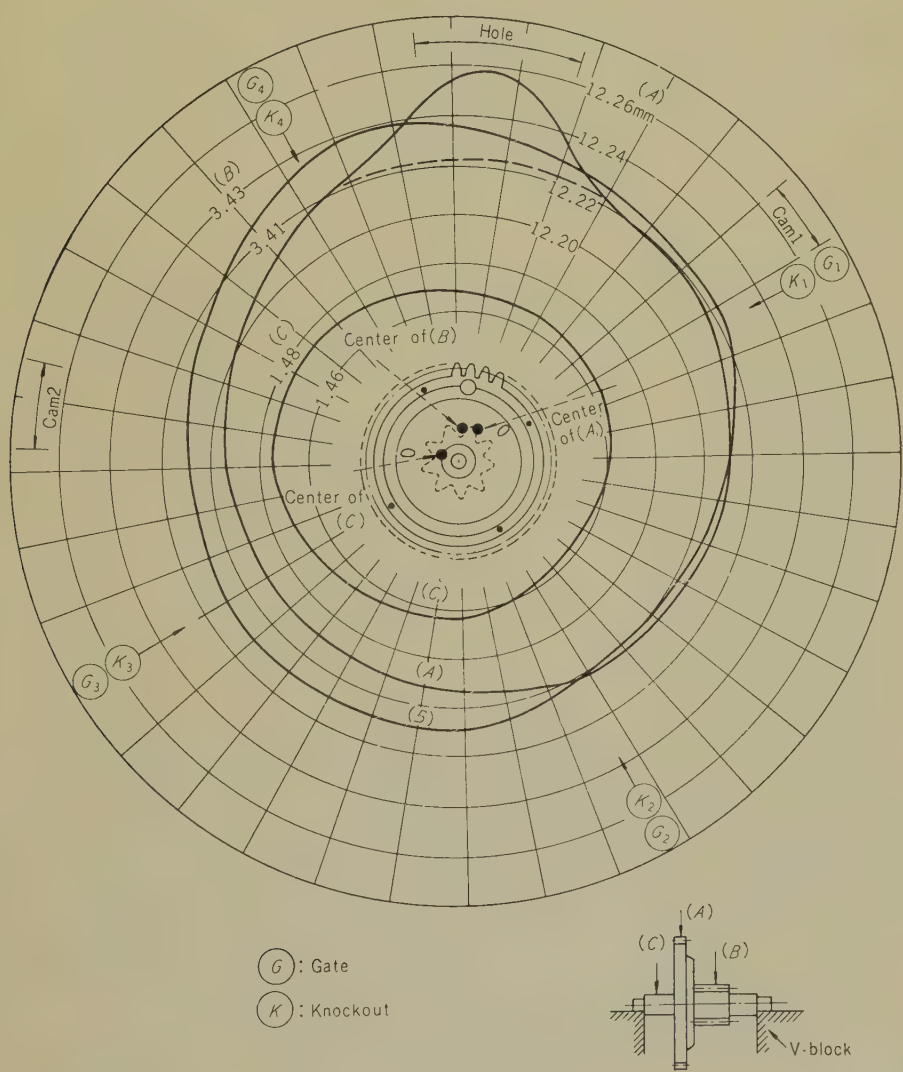


Fig. 6—"Runout" and warpage of sample V.

Table 1
MAXIMUM DEVIATION OF CIRCUMFERENCE FROM ASSUMED REAL CIRCLE

| Classification | Sample | Part | Gate | Partial deviation* from assumed real circle | |
|----------------|--------|--------|--|---|-----------------|
| | | | | Not considered | Considered |
| Disk | I | Gear | Single | less than 0.015 | less than 0.020 |
| | II | // | // | // 0.015 | same as left |
| | | Pinion | // | // 0.015 | // |
| | III | Gear | Multiple (4 gates) Near the circumference | // 0.005 | less than 0.020 |
| | IV | // | Multiple (4 gates) Near the shaft | // 0.015 | same as left |
| | V | // | Multiple (4 gates) Near the circumference | // 0.010 | less than 0.045 |
| | | Pinion | // | // 0.020 | same as left |
| | Shaft | I | Shaft | Single | // 0.035 |
| II | | // | // | // 0.005 | — |
| IV | | // | Multiple (4 gates) | // 0.005 | — |
| V | | // | // | // 0.005 | — |

(mm)

* Not by effect of gates, but hole and projection as considered in Section 3.1.

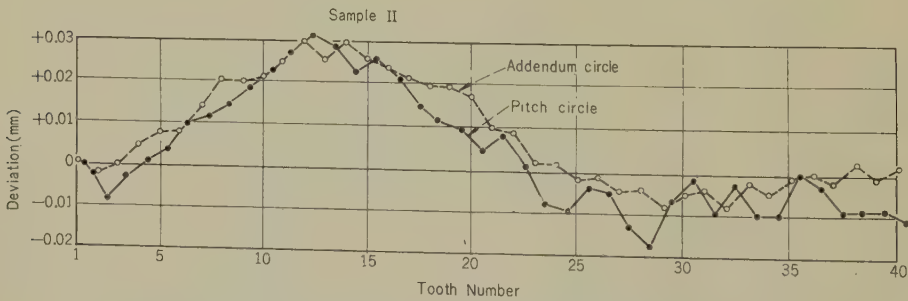


Fig. 7—Deviation of pitch circle and addendum circle.

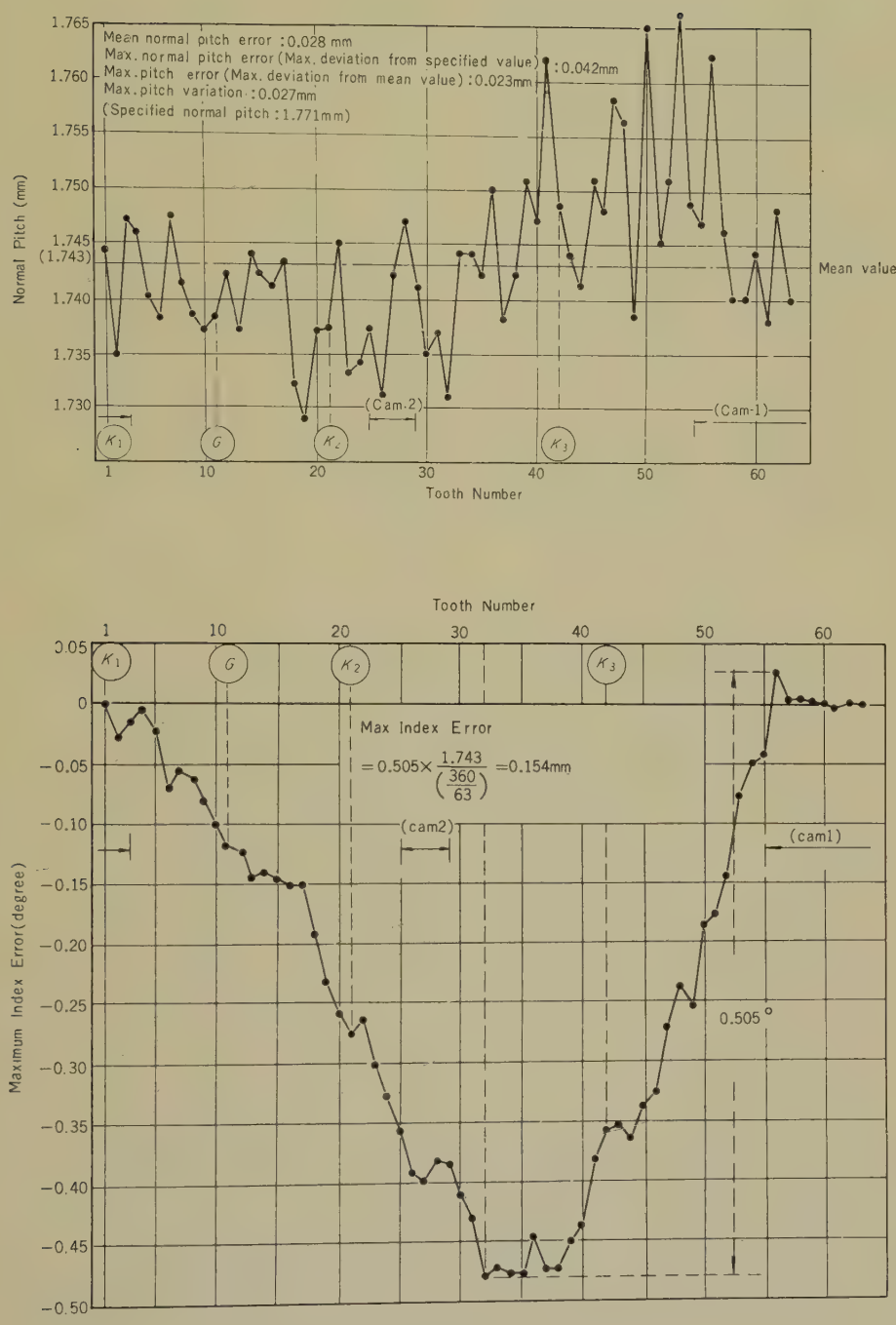


Fig. 8—Normal pitch of sample I.

page may occur because of the inequality of each gate condition. It may be concluded from the results obtained above that it can hardly be expected that the addendum circle of molded gears made through multi-gates will always have good roundness.

3.3. Conclusions of This Section

In general, injection molded gears made through multi-gates are expected to have addendum circles with good roundness. Proper gate position, injecting direction, and uniformity of each gate condition for resin flow are also required.

If a hole or projection (e.g. cam, etc.) is located near the circumference of the disk, it will cause warpage of the addendum circle. For instance, in the case of Sample III, good

roundness is supposed to be obtained without any partial warpage affected by the cam projection.

Each maximum value of the warpage of a molded gear given in this paper shows no difference whether it is made through a single gate or multi-gates.

4. Pitch Circle

Fig. 7 shows the variation of pitch circle measured by means of an over pin method and the addendum circle with shaft supported for Sample II. These curves roughly coincide with each other, but are different in detail, since the measured values by the over pin method include not only circular errors but also the errors of tooth profiles and pitches.

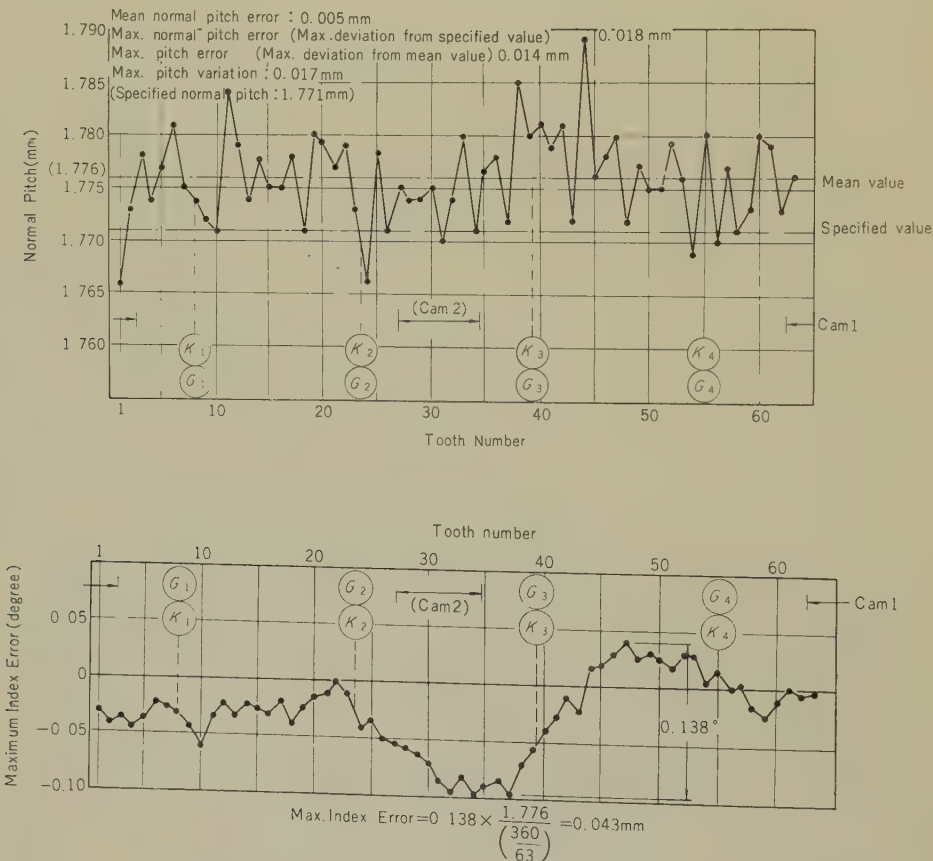


Fig. 9—Normal pitch of sample III.

The amplitude of variation of the pitch circle for each sample is about 0.06 mm in all cases. This value ranges from JGMA standard class 6 to 7.

5. Normal Pitch of Teeth

The mean values of the normal pitch of teeth for some samples measured by a micro-meter-microscope are shown in Figs. 8-10.

The pitch values of Sample I shown in Fig. 8 tend to be relatively small near the

cam projection and gate, while those of Sample V (see Fig. 10) tend to be relatively large at the hole. This tendency corresponds to warpage of the addendum circle. The pitch variations of Sample III showing good roundness are smaller than those in other cases as shown in Fig. 9.

The conclusion is that, if the addendum circle shows good roundness, the variation of the pitch of the gear teeth will be small. Furthermore, the normal pitch errors of a gear include the errors of angle dividing and

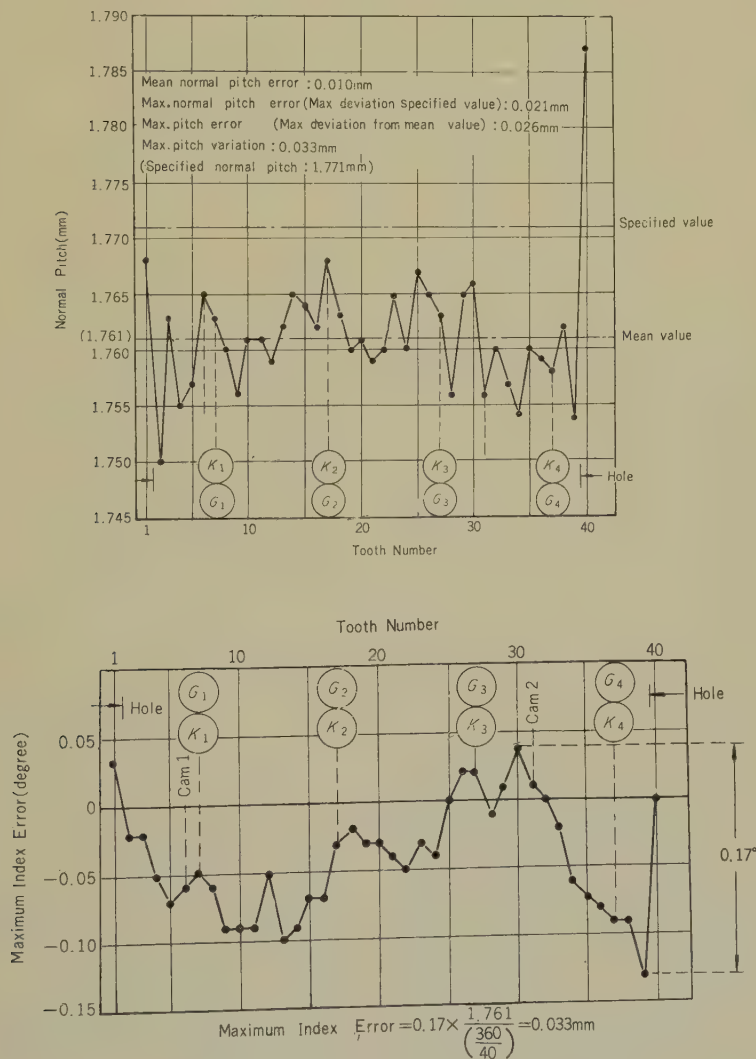


Fig. 10—Normal pitch of sample V.

Table 2
NORMAL PITCH ERRORS

| Error | Sample I | | II | | III | | IV | | V | |
|----------------------|--------------------|------------|-----------|------------|-----------|------------|-----------|------------|-----------|------------|
| | Pitch dia. 37.8 mm | | 24 mm | | 37.8 mm | | 37.8 mm | | 24 mm | |
| | Value (μ) | JGMA class | Value (μ) | JGMA class | Value (μ) | JGMA class | Value (μ) | JGMA class | Value (μ) | JGMA class |
| Mean Normal Pitch | -28 | — | -18 | — | 5 | — | -9 | — | -10 | — |
| Max. Normal Pitch | -42 | 7 | -28 | 7 | 18 | 5 | -26 | 6 | -21 | 6 |
| Max. Pitch Error | 23 | 6 | 14 | 5 | 14 | 5 | 17 | 5 | 26 | 7 |
| Max. Pitch Variation | 27 | 6 | 18 | 5 | 17 | 5 | 25 | 6 | 33 | 7 |
| Max. Index Error | 154 | 7 | 39 | 4 | 43 | 4 | 71 | 6 | 33 | 4 |
| Total | — | 7 | — | 7 | — | 5 | — | 6 | — | 7 |

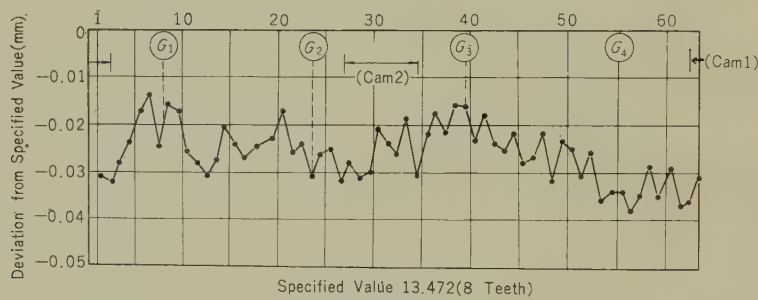


Fig. 11—"Displacement over a given number of teeth" of sample III.

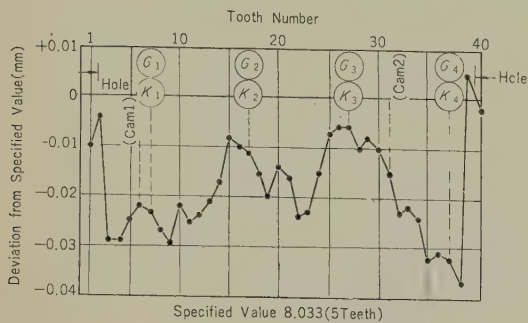


Fig. 12—"Displacement over a given number of teeth" of sample V.

Table 3
"DISPLACEMENT OVER A GIVEN NUMBER OF TEETH"

| Sample | Specified Value | \bar{x} | σ | R | Max. Error | JGMA class | Note |
|-------------|---------------------|-----------|----------|-------|------------|------------|--|
| * I | | | 0.009 | 0.040 | | | Measured for any 10 points per 10 samples. |
| II (Gear) | 8.10 (5 teeth) | 8.085 | 0.013 | 0.060 | -0.040 | 6 | // |
| II (Pinion) | 2.94 (2 teeth) | 2.897 | 0.006 | 0.020 | -0.050 | 7 | Measured for any 6 points per 10 samples. |
| III | 13.472 (8 teeth) | 13.457 | 0.005 | 0.024 | -0.038 | 6 | Measured for all points per 5 samples. |
| IV | 13.472 (8 teeth) | 13.427 | 0.007 | 0.030 | -0.061 | 7 | // |
| V | 8.033 (5 teeth) | 8.015 | 0.010 | 0.042 | -0.037 | 6 | // |

(in mm)

* The standard number of teeth over which this measurement is to be made is teeth, but these measurements were made over 6 teeth.

tooth profile of the die at the time of manufacture, and these errors should be little.

The pitch errors of each sample are within the accuracy limits of JGMA standard shown in Table 2. Here, Sample III belongs in class 5, because its roundness is better than that of others which belong in classes 6 and 7.

The pitch error, pitch variation and maximum index error except the partial warpages caused by projections and holes should be within the accuracy limits of JGMA standard classes 5 and 6.

6. "Displacement over a Given Number of Teeth"

Some examples of the measured results on the "displacement over a given number of teeth" are shown in Figs.11 and 12. The number of teeth in these figures represents the number of centers of the teeth measured. The variation of Sample III (see Fig.11) having good roundness of the disk is small as in the case of normal pitch variation. On Sample V, the influence of hole near the circumference of disk appears clearly, as

shown in Fig. 12.

The accuracy limits of these samples are shown in Table 3, and as a whole, these gears are within the accuracy limits of JGMA standard classes 6 and 7.

If the mean values measured for each sample are correct, the variations (i.e. 3σ) will be within 0.04 mm, and this value corresponds to JGMA standard class 6.

7. Conclusions

In general, injection molded gears made through multi-gates are expected to have good roundness of addendum circle and accuracy better than similar gears made through a single gate, and suitable gate position and injecting direction as well as the uniformity of each gate condition for resin flow are also required.

In addition, if a hole or projection (e.g. cam etc.) is located near the circumference of the disk, it will cause warpage of addendum circle.

In general, the errors and variations of pitch circle, normal pitch and "displacement over a given number of teeth" increase with

the warpage of the addendum circle.

The accuracy of molded spur gears of 610-Nylon, which the authors have prepared and whose pitch diameter ranges from 5 to 40 mm with module of 0.6 and 20 degree pressure angle, show no difference according to whether they are made through a single gate or multi-gates, because these gears have holes or projections near the addendum circle and have not been made by suitable gate design.

The accuracy limits of these gears range from JGMA standard class 6 to 7.

The accuracies of molded gears of 6 and 66-Nylons are expected to be the same as in the case of 610-Nylon, and these results may

be applicable to other similar moldings.

Acknowledgement

The authors wish to express their sincere thanks to Dr. T. Hayasaka and Dr. G. Ito of the Electrical Communication Laboratory for their advice and instructions, and to Dr. S. Senba of the Mechanical Laboratory for his kind assistance and instructions.

Reference

- (1) K. W. Hall, H. H. Alvord: ZYTEL Spur Gears, *Mech. Engng*, **81**, 5, 1959, p. 50.

* * * *

Triple Balanced Modulator using Binocular Type Cores*

Takashi ITO†

Research on the Triple Balanced Modulator (T.B.M.) has been carried out to simplify parametron control systems and to obtain higher control rates.

The T.B.M., which consists of several nonlinear elements and a suitable power supply circuit, is a control circuit with three input terminals and one output terminal which functions as an amplitude gate or as a phase product circuit.

In these experiments, binocular-type magnetic cores were utilized as the nonlinear elements of the T.B.M. As a result the basic characteristics of the T.B.M. were obtained and the problems to be considered when the T.B.M. is applied to parametron control systems have been determined.

Introduction

The Triple Balanced Modulator is a control element with three input terminals and one output terminal which serves as an amplitude gate or a phase switch which produces the triple product of binary codes which represent phases. If utilized as a phase switch, it is effective in simplifying circuit arrangements and increasing control rates.

With the view to applying the T.B.M. to the switch-selection code circuit of a fully-electronic switching system, the author employed binocular-type ferrite cores as the nonlinear elements, and conducted some basic experiments on the relation between the non-uniformity of the magnetic characteristics and operation of the T.B.M.; especially on the phase switching characteristics for the case when the T.B.M. is applied to a parametron control system. He also performed some

tests of a system in which the selection code circuits utilize both the T.B.M.'s and parametrons. The present paper describes the results of the experiments and interprets their meaning.

1. Principle of the T.B.M.

Fig. 1 shows the basic circuit of the T.B.M. The symbol \square in the figure signifies a nonlinear element, which is a circuit element with three pairs of input and one pair of output terminals that is equipped with a voltage or current supply circuit so as to satisfy the orthogonal condition. The circuit arrangement may be more or less changed according to the kind of drive, voltage or currents, of the nonlinear element, but the circuit function is the same in principle.

Fig. 2 shows an actual circuit of the T.B.M., in which toroidal magnetic cores are employed as the 4 nonlinear elements. The dotted lines illustrate the configuration when the toroidal magnetic cores are replaced by binocular-type cores.

If the input ampere turns of each magnetic core in Fig. 3 is assumed to be $\sqrt{2} A \cos \omega t$, the output voltage e of the magnetic core is

* Ms received by the Electrical Communication Laboratory on May 2, 1960. Originally published in the *Kenkyū Zituyōka Hōkoku (Electrical Communication Laboratory Technical Journal)*, Vol. 9, No. 7, pp. 739-752, 1960.

† Transmission Research Section.

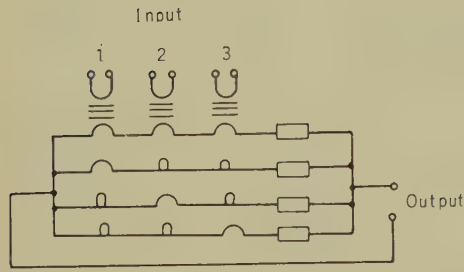


Fig. 1—Basic circuit of the T.B.M. input, output.

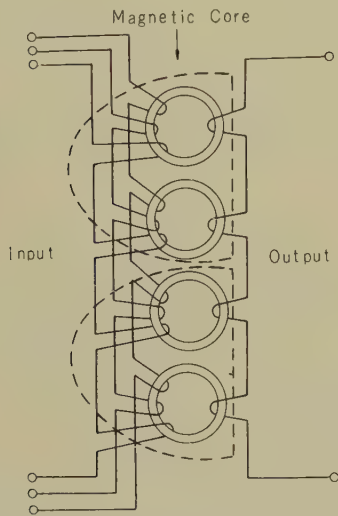


Fig. 2—Current shape T.B.M. circuit with ring magnetic cores and binocular magnetic cores (dotted line).

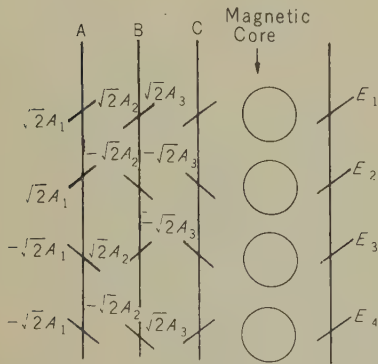


Fig. 3—Input ampere turns of each magnetic core.

generally given by the following formula:

$$e = n \sqrt{2} (\beta_1 A + \beta_2 A^2 + \beta_3 A^3 + \dots) \sin (\omega t - \varphi). \tag{1}$$

Therefore, if the effective value of e/n is assumed to be E , $\beta_2 \ll \beta_1$, and $\beta_3 \ll \beta_1$, the following approximate formula will be obtained:

$$E = \beta_1 A + \beta_3 A^3. \tag{2}$$

If the 4 magnetic cores of the T.B.M. have identical characteristics of the type given in formula (2), and if the input ampere turns of the magnetic cores are $\sqrt{2} A_1$, $\sqrt{2} A_2$, $\sqrt{2} A_3$ respectively for the three inputs A, B, and C, the output voltages per turn in magnetic cores E_1 , E_2 , E_3 , and E_4 :

$$\begin{aligned} E_1 &= \beta_1 (A_1 + A_2 + A_3) + \beta_3 (A_1 + A_2 + A_3)^3 \\ E_2 &= \beta_1 (A_1 - A_2 - A_3) + \beta_3 (A_1 - A_2 - A_3)^3 \\ E_3 &= \beta_1 (-A_1 + A_2 - A_3) + \beta_3 (-A_1 + A_2 - A_3)^3 \\ E_4 &= \beta_1 (-A_1 - A_2 + A_3) + \beta_3 (-A_1 - A_2 + A_3)^3. \end{aligned}$$

Therefore

$$E_0 = E_1 + E_2 + E_3 + E_4 = 24 \beta_3 A_1 A_2 A_3. \tag{3}$$

This equation means that output voltage of the T.B.M. is proportional to the product of the three input ampere turns A_1 , A_2 , A_3 and the coefficient β_3 based on the nonlinearity of the magnetic core. Eq. (2) represents the function of the T.B.M., and is generally effective without restriction on the magnetic core, provided that the nonlinear element has the form of nonlinear characteristic given by Eq. (2). This means, as E. Gotô has expressed, that the T.B.M. functions as the following analog circuits:

- (1) triple coincidence circuit
 - (2) triple balanced modulator
- and as the following digital circuits
- (3) triple and double coincidence circuit
 - (4) triple product circuit (i.e. triple phase switching circuit) if phase binary code is taken into consideration.

Table 1
FUNCTION OF T.B.M. ON BINARY CODE

| Signal | | Amplitude Binary Code 1 or 0 | | | | | | | | Phase Binary Code + (phase 0) or - (Phase π) | | | | | | | |
|----------|---|------------------------------|---|---|---|---|---|---|---|--|---|---|---|---|---|---|---|
| Input | A | 1 | 1 | 0 | 0 | 1 | 0 | 1 | 0 | + | + | - | - | + | - | + | - |
| | B | 1 | 0 | 1 | 0 | 1 | 1 | 0 | 0 | + | - | + | - | + | + | - | - |
| | C | 1 | 0 | 0 | 0 | 0 | 1 | 1 | 0 | + | - | - | + | - | + | - | - |
| Output | E | 1 | 0 | 0 | 0 | 0 | 0 | 0 | 0 | + | + | + | + | - | - | - | - |
| Function | | Triple Coincidence | | | | | | | | Triple Product | | | | | | | |

The amplitude function of the triple coincidence and the phase function of the triple product are tabulated in Table 1.

2. Chief Aim of Experiment

The function of the T.B.M. is, as may be seen in the above from its operation principle, decidedly determined by the following factors.

- (1) nonlinearity of magnetic core as given by Eq. (2)
- (2) orthogonal condition of circuit as shown in Fig. 3.

In other words, a magnetic core with nonlinearity of which the second coefficient β_2 is as small as possible while the third coefficient β_3 is as great as possible, is desirable.

However, even if the nonlinearity of the magnetic core cannot be expressed by Eq. (2), the consequence is nothing more than ineffectuality of Eq. (3), and the function of the triple product is still preserved. So it may be concluded that factor (1) is not so important compared with factor (2), i.e. the orthogonal condition of the circuit that contains four magnetic cores.

Moreover the nonlinearity of the magnetic core (See Table 2) varies greatly with the type of magnetic core used, and even for cores of the same type variations are large, and selection for cores with a low value of β_2 causes

Table 2
DIFFERENCE IN NON-LINEARITY BETWEEN
MAGNETIC CORES

| Magnetic Core | Coefficient | | |
|---------------------------------------|-------------|-----------|-----------|
| | β_1 | β_2 | β_3 |
| L_1D_4 | 0.33 | 0.21 | 2.29 |
| L_2D_4 | 0.36 | 0.71 | 1.04 |
| L_2D_4 (High Temperature Treatment) | 0.36 | 0.75 | 0.53 |
| // | 0.32 | -0.003 | 2.67 |
| L_3D_4 | 0.26 | 0.13 | 0.36 |

a low yield. From these considerations, the present experiment has been carried out with greater stress on the orthogonal condition, especially on the effects of the degradation caused by the nonuniformity of magnetic core characteristics on the function of the T.B.M., and much consideration was given to phase characteristics for the case when the T.B.M. is applied to parametron control systems.

3. Magnetic Core

In the experiment MnZn Ferrite binocular-type parametron magnetic cores produced by the Tohoku metal Co. were chiefly employed

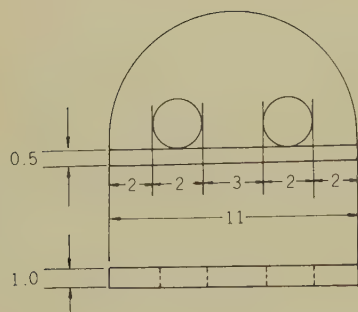


Fig. 4—Shape and size of binocular magnetic core (mm).

Their size is given in Fig. 4.

The use of a binocular-type magnetic core is more favorable because

- (1) it enables better uniformity of magnetic characteristics to be obtained than 4 with toroidal magnetic cores.
- (2) it unifies the kind of magnetic core, for the binocular type magnetic core is the standard type for parametrons.
- (3) it facilitates winding operation and detection of errors more than the toroidal type does.

In practical use, however, economy is an important factor, so it would be rash to say only for the above reasons that binocular-type magnetic cores are preferable to toroidal cores.

Fig. 5 is an example of the μ -H characteristics at 1 Mc/s of the binocular-type magnetic core used in this experiment.

4. T.B.M. as Amplitude Gate

This experiment was carried out, as mentioned above, with greater stress on the function of the T.B.M. utilized as a phase switch. But, the T.B.M. also functions as an amplitude gate; an example of this characteristic is shown in Fig. 6.

Fig. 6 shows the relation between the input ampere turns, within the range of 5–50 mAT at a frequency 2 Mc/s, and output level when three input signals are ON (ON in the figure), and the relation of the input ampere turns to output level when one or two input signals

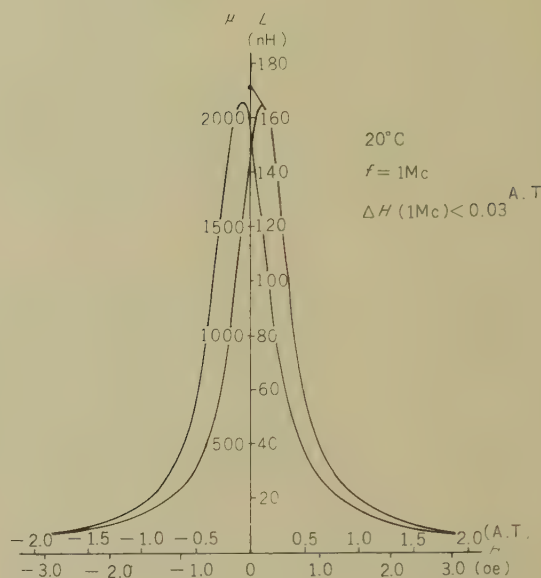


Fig. 5—Typical μ -H characteristic of binocular magnetic core.

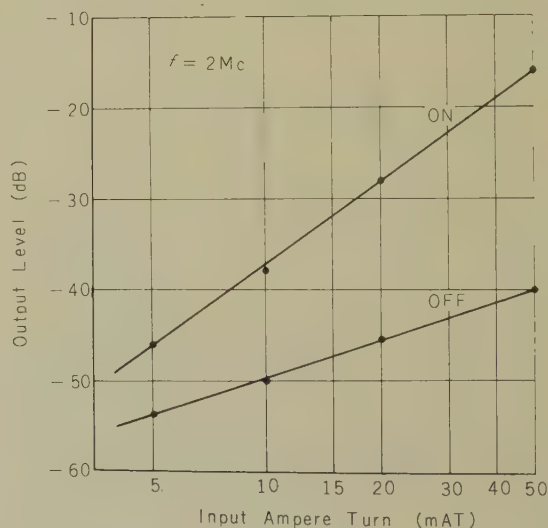


Fig. 6—Amplitude gate characteristic of the T.B.M.

ON=Output level when 3 inputs are supplied.
OFF=Output level when 1 or 2 input are OFF.

are OFF (OFF in the figure). The difference between the two levels gives the switching ratio per input ampere turn. Though the switching ratio is determined by the orthogonal condition, and especially by the degree of balance of the magnetic characteristics among the four holes of the magnetic cores, values of switching ratio of about 20 dB at 25 mAT and about 30 dB at 50 mAT are obtainable by keeping the nonuniformity of inductance per turn of each hole ($\Delta L_0/L_0$) within the limit of $\pm 3\%$.

5. T.B.M. as Phase Switch

The problems to be considered concerning the phase switching function of the T.B.M. are itemized into the following three:

- 1) phase nonuniformity of switched output signals
- 2) phase shift in signal current caused in the circuit including magnetic core
- 3) input signal ampere turns, output signal amplitude and phase.

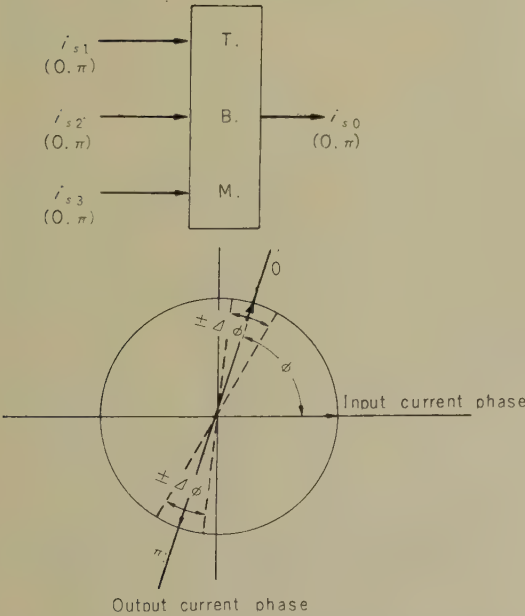
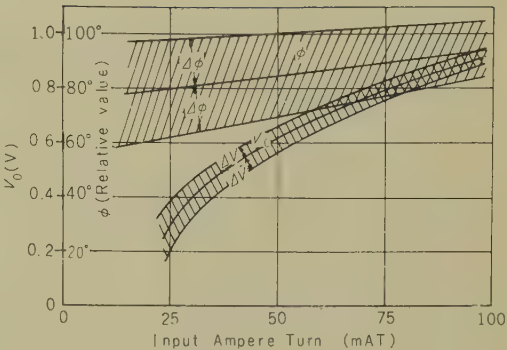
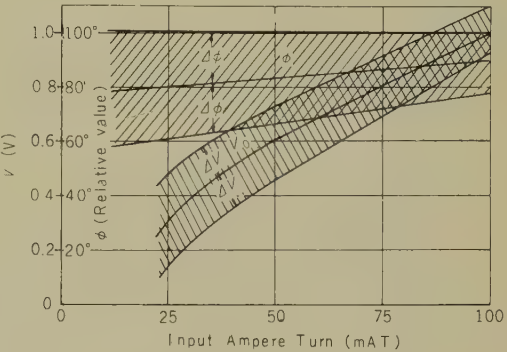


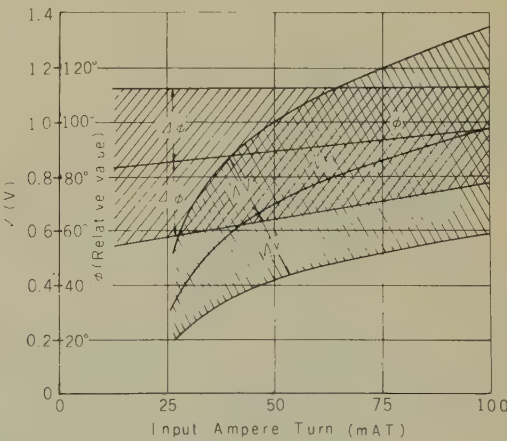
Fig. 7—Shift and nonuniformity input current phase.



(a) $\Delta L_0/L_0 < \pm 3\%$



(b) $\pm 3\% < \Delta L_0/L_0 \leq \pm 9\%$



(c) $\pm 6\% < L_0/L_0 \leq \pm 10\%$

Fig. 8—Phase and voltage of output vs. input ampere turns input ampere turn, relative value.

These three problems discussed in detail in the following sections.

5.1. Phase Nonuniformity of Output Signal

When three input currents i_{s1} , i_{s2} , and i_{s3} are applied to the T.B.M., as in Fig. 7, the output current i_{s0} has a phase difference of ϕ or $\phi + \pi$ with respect to the input circuit. This phase difference of ϕ will be called the phase shift, and that output signal phase distributed within the range of $\pm \Delta\phi$ will be called the phase nonuniformity.

This phase nonuniformity is caused by the unbalance of the magnetic characteristics of the magnetic cores and is determined by input ampere turns, as is seen in Fig. 8.

Fig. 8 show the results of measurement of the phase shift of the resonant output current (ϕ in relative value), nonuniformity of the switched phase ($\Delta\phi$), output voltage (V_0), and nonuniformity of output voltage concerning three kinds of T.B.M.'s, each of which is constructed with one of the three different kinds of binocular magnetic cores. These core are chosen as their $\Delta L_0/L_0$ are within 3%, 3%~6%, and 6%~10% respectively. Phase shift and phase nonuniformity are measured with Lissajous figure on a cathode-ray tube, so the accuracy may not be very high, but the general tendencies are recognizable.

For instance, nonuniformity of the output voltage tends to become greater in proportion to non-uniformity of L_0 in magnetic cores. The same tendency as above is also observed for switching phase though it is not so evident as in the case of output voltage. Phase shift scarcely tends to change so far as the tuning capacitance and the center value of L_0 do not vary largely. Nonuniformity of switching phase decreases in general in proportion to increase of current value, while that of the absolute value of voltage decreases at smaller range of $\Delta L_0/L_0$ and increases at greater range of it. The value of $\Delta V_0/V_0$ tends to decrease in general as in Fig. 9.

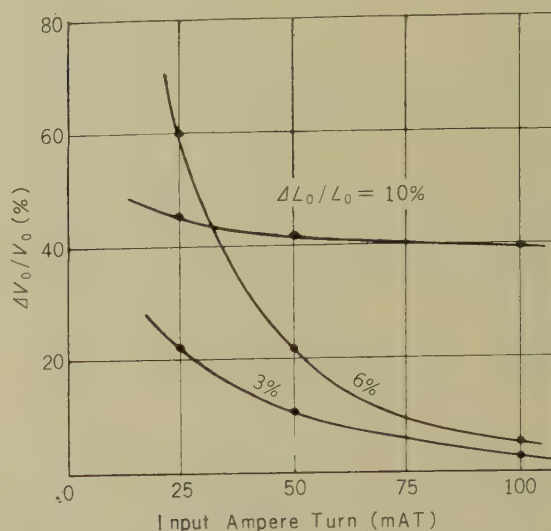


Fig. 9—Relation between input ampere turns and $\Delta V/V_0$.

5.2. Phase Shift

In case the T.B.M. is coupled to the stages of a parametron, it is presumed that phase difference between input and output either diminishes to the same phase (0) or grows to the opposite phase (π), and that hysteresis of the magnetic core produces phase shift ϕ_1 as is seen in Fig. 10; furthermore, that when the output circuit is at resonance it causes phase shift ϕ_2 . If the phase difference of $\phi_1 + \phi_2$ grows too large, the phase of the output signal of the T.B.M. may fall into the non-sensitive region of the parametron where the control of parametron becomes unstable, or if worse, impossible.

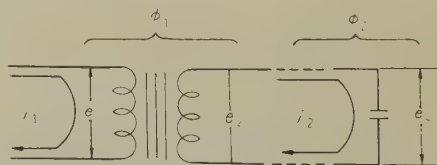


Fig. 10—Phase shift in magnetic core and output circuit.

Phase shift ϕ_1 of a single magnetic core is given by the following equation:

$$\phi_1 = \tan^{-1} \frac{8\gamma}{\alpha_1 + \alpha_2 H_m + \alpha_3 H_m^2 + \dots} \tag{4}$$

where $\alpha_1, \alpha_2, \alpha_3, \dots$ and γ are the constants dependent on the materials used in the magnetic core, and H_m is the maximum value of magnetic field.

If H_m is sufficiently small, ϕ_1 may be negligible, but when the T.B.M. with binocular-type magnetic core is driven by the output signal of a parametron, ϕ_1 is nearly equal to 10° .

If ϕ_1 is assumed to be the phase difference between primary current i_1 and secondary current i_2 before the T.B.M. is at resonance, it may be that $\phi_2 \doteq \pi/2$ at resonance; the resistance component of the secondary circuit being neglected.

And when a T.B.M. with a binocular-type magnetic core having four 5-turn input windings through each hole is coupled with a parametron and the output circuit tuned with a capacitor of 1400–1600 pF, $\Phi_2 = (\phi_1 + \phi_2)$ becomes 74° – 75° ; the reactance component being neglected.

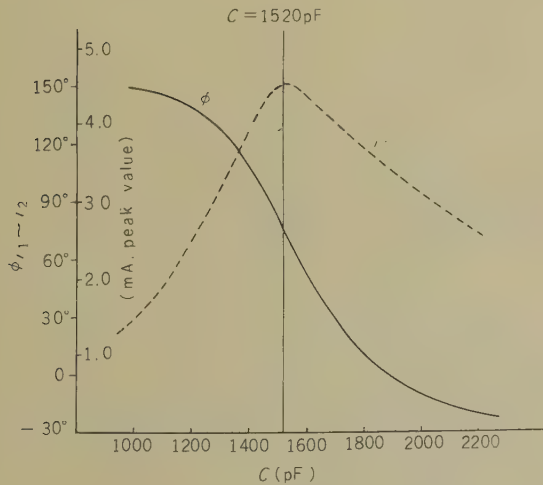


Fig. 11—Measured value of phase shift in the T.B.M.

Fig. 11 is an example of an experimental value which is in good agreement with the value predicted above, although this characteristic changes in accordance with the current value and the combination of three input phases.

5.3. Input Signal Ampere Turns and Output Signal Amplitude

In the T.B.M. circuit of Fig. 12, we assume that input currents are applied in the direction which arrows point, (assuming that the current and winding of each coil remain the same). Therefore the direction and the magnitude of magnetic force acting on each core are given in the figure, one output voltage of the 4 magnetic cores being $E_{(3A)}$, while those of the other three cores are all $-E_{(A)}$.

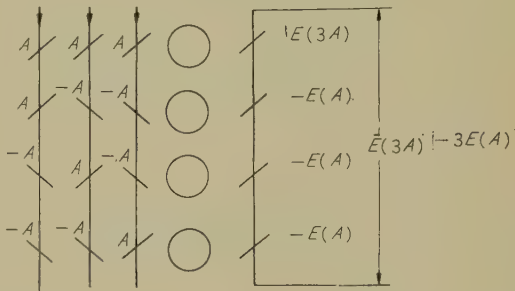


Fig. 12—Relation between input ampere turns and output voltage in each magnetic core.

As is seen in Fig. 13, the sum of output voltages produced in three magnetic cores magnetized in the negative direction with the magnitudes of $3E_{(A)}$ is smaller than that of one core magnetized $E_{(3A)}$ in the positive direction, if compared in absolute value. This difference may be due to nonuniformity of magnetic cores. As a result, the voltage $E_{(3A)} - 3E_{(A)}$ is generated as the output of the T.B.M.

From the typical nonlinearity of the magnetic cores used in the experiment, an output

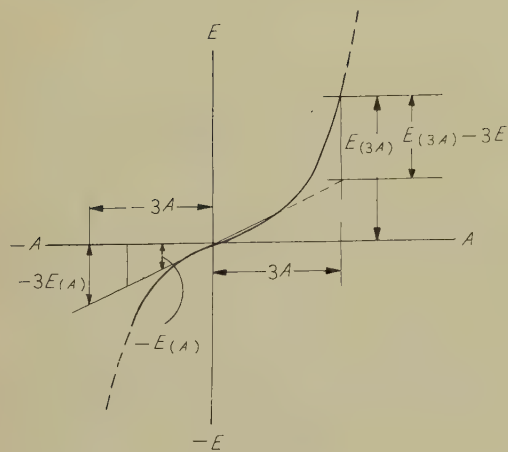


Fig. 13—Nonlinearity characteristic of magnetic core and output voltage.

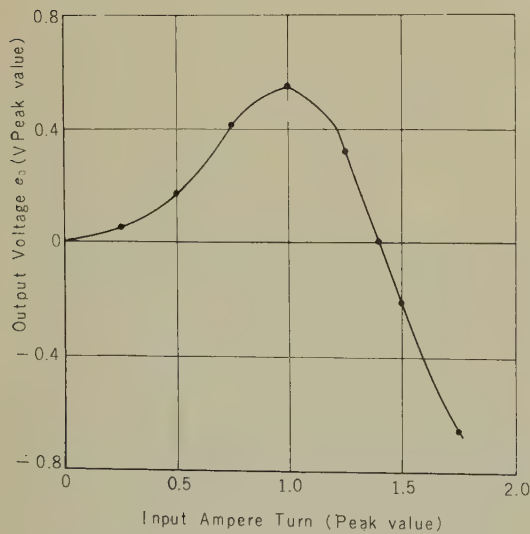


Fig. 14—Measured value of output voltage, output voltage, peak value.

voltage of $e_0(=E_{(3A)}-3E_{(A)})$ is calculated vs. input ampere turns within the range of $0\sim 2$ AT (peak value). The result is shown in Fig. 14.

The fact that this characteristic has a peak and goes below the range of $e_0<0$ may be due to the influence of the change in non-linearity of the core, i.e., as the ampere turns increase, the magnetic state of the core reaches to the upper saturation region of the hysteresis curve.

Data concerning a standard 5-turn winding the T.B.M. driven by parametrons are in the following. The ampere turn is in the range of $0.2\sim 0.3$ AT (peak value) and the open circuit output voltage e_0 is below 10 mV. Therefore, it is difficult to drive a parametron by the direct output voltage of the T.B.M. without tuning the output circuit. At present, as the standard parametron is of the current coupled type, the T.B.M. output must be tuned. Owing to this connection, unstability due to phase shift described in the section 5.2 appears, but, as the output current is obtained by about 4 mA as in Fig. 11, the amplitude of which can be determined nearly to that of a coupling current got in logical circuits composed only of parametrons, and the form of current wave can also be improved.

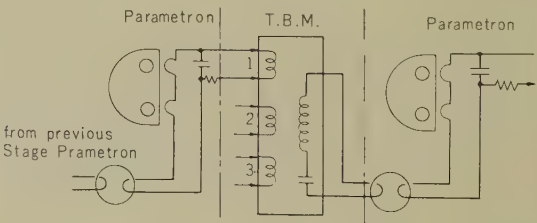


Fig. 15—Connection of the T.B.M. with parametron.

5.4. Input Ampere Turn and Output Signal Phase

The relation between the input ampere turns and the output signal phase has briefly been described in Fig. 8, i.e.;

- (1) Phase shift does not vary much with increase in the input ampere turns.
- (2) Nonuniformity of phase generally diminishes in proportion to increase in the input ampere turns.

Phase shift shows slight lag in proportion to increase in the input ampere turns, but in this case it is due to the fact that detuning is caused by decrease of inductance through decrease of effective permeability, and it is clearly seen in Fig. 11 that phase lag appears in accordance with increase in input ampere turns.

On the other hand, as the operation is almost linear within the limit of small input ampere turns, the difference of the subtraction $E_{(3A)}-3E_{(A)}$ shown in Fig. 13 becomes so small that it becomes difficult to discriminate phase and moreover nonuniformity develops. Fig. 16 is given in order to make these problems clear, though it is not from the data of the magnetic cores employed in the experiment. The abscissa values represent phase difference of the output current from the input current, and the ordinate values output

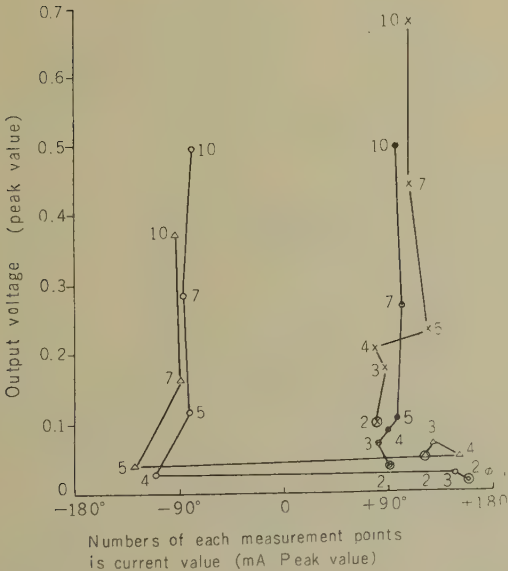


Fig. 16—Decrease of phase switching ability in the range of small input ampere turns.

voltage (peak voltage at the terminal of the tuning capacitor). The figures at each measured point show values of input signal current.

There appear two groups around $\pm 90^\circ$ according to the combination of the three input signal phases, which are the switched phases corresponding to 0 and π .

It will be noticed here that phase discrimination is impossible in case the value of current is below some particular point, and that phase nonuniformity diminishes inversely proportional to increase in current value. In this case, each winding of one input circuit has five turns, and the measuring frequency is 1 Mc/s.

The reason why the phase switched to 0 or π hardly shows any shift in spite of increase in input ampere turns is that the data were after the circuit was retuned for each measurement. Consequently input ampere turns of about 50~100 mA/T may be appropriate in one winding of one input circuit from considerations of the current and winding supplied by the parametron.

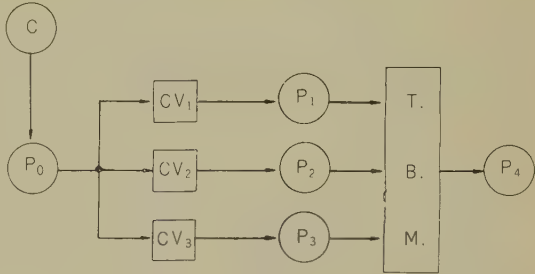


Fig. 17—Measuring circuit for control test of parametron by the T.B.M.

6. Drive of Parametron

Fig. 18 illustrates the limit within which output signal phase of a parametron can be controlled by input drive. This result was obtained with the measuring circuit shown in Fig. 17 by changing phase converter CV of each input, and shifting the output signal phase by varying the T.B.M. output tuning

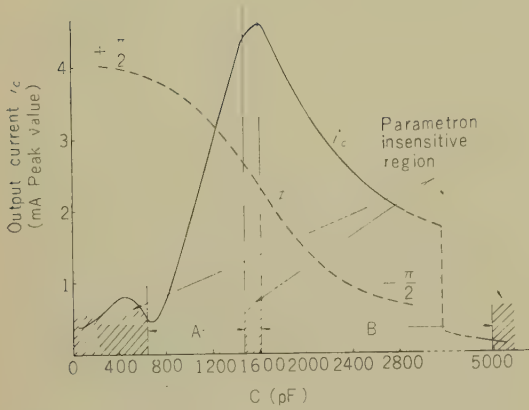


Fig. 18—Control region of the T.B.M. connected to parametron.

capacitor.

The shaded portions of the figure are the uncontrollable regions of parametron phase. The left uncontrollable region is perhaps caused by tuning to 2 Mc/s, as the small peak of the output current i_c curve suggests, and the right one by decrease of the output current below the magnitude of critical coupling attenuation. The latter region generally appears above 3,000 pF capacitance, though there is a great difference between individual the T.B.M.

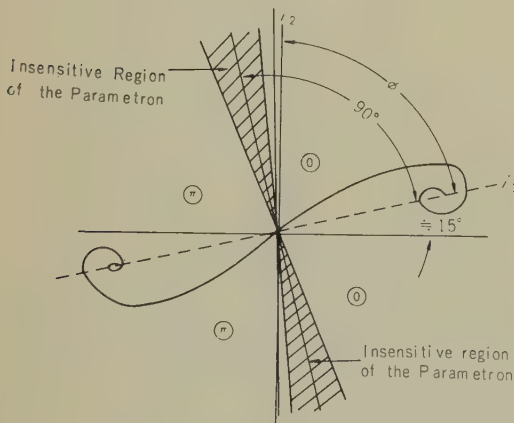


Fig. 19—Insensitve regions of parametron.

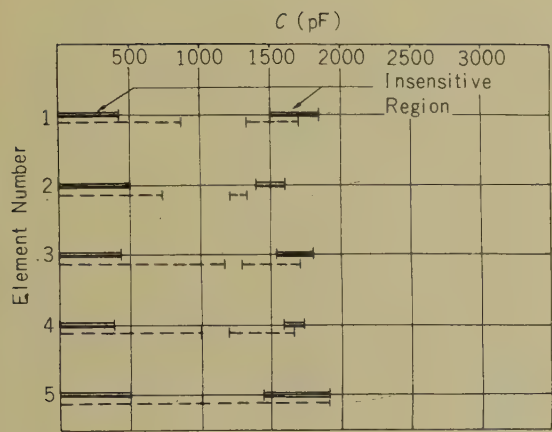
The middle shaded region appears around the 1 Mc/s tuning point, and its width is narrow in comparison with the former ones. It is easy to see that there is an insensitive portion of parametron response at $90^\circ \pm \Delta\phi$ as shown in Fig. 19 and that the phase of the output current i_2 of a T.B.M. leads that of the input current i_1 by $70^\circ \sim 80^\circ$ when tuuing is arranged in the output circuit.

Thus if we adjust the tuning of a T.B.M. output circuit correctly, the output signal of the T.B.M. is theoretically very critical to parametrons and may not be practically sensible by parametrons in next stage. By these reasons, this insensitive region of T.B.M. occurs.

From the above result, it may be said that region A or B should be preferred to obtain the optimum value of T.B.M. output circuit tuning capacitance, but with a little more consideration, it will be concluded that region B, especially at about C of 2000 pF, is the most appropriate, for;

- (1) region B is by far wider than region A
- (2) if C is arranged in region B, especially at the value of 2000 pF, phase shift of the T.B.M. output signal current is so small as to diminish the danger of approaching the insensitive region of the parametron, and besides, nonuniformity of phase shift is kept rather small.
- (3) current decrease by detuning does not matter if the magnitude of critical coupling attenuation is taken into consideration.
- (4) when T.B.M. input circuits are connected in series, or when the output circuit is branched off, region A gets narrower, while region B remains almost unchanged (This will be described in detail later).
- (5) a component of 2 Mc/s enters region A in some measure.

Fig. 20 shows the measured limit of controllable phase of the parametron to the change of C when the parametron is driven. This test was conducted with 5 T.B.M.'s using a magnetic core whose value of $\Delta L_0/L_0$



Dotted lines show the regions in the case of the series connection of an input circuit with the input circuits of six other T.B.M.s.

Fig. 20—Difference of controllable regions between elements.

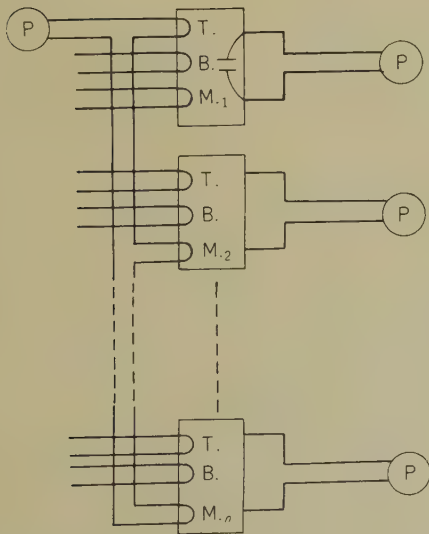


Fig. 21—Series connection of input circuits.

is within $\pm 5\%$ ($\Delta L_0/L_0 < \pm 5\%$). The results enable us to know the difference of width between the upper and lower regions, and nonuniformity in the uncontrollable regions.

The characteristics of the parametrons and T.B.M.'s employed in the experiment are;

Parametron

- magnetic core: binocular-type manufactured by Tōhoku Metal Co.
- primary windings: 1 turn \times 2
- secondary windings: 9 turns \times 2
- exciting current: 0.35 A ($f = 2$ Mc/s)
- bias current: 0.55 A
- capacitor: $\div 4000$ pF
- resistor: 400 Ω
- oscillation voltage: about 2V measured at terminals of 400 Ω

T.B.M.

- magnetic core: same as parametron
- input windings: 5 turns \times 4 for each input
- output windings: 5 turns \times 4
- capacitor: 1000~2000 pF
- input current: 5 mA
- output current: 2~4.5 mA (at resonance).

7. Series Connection of T.B.M. Input Circuits and Branch Connection of Output Circuits

7.1. Series Connection of Input Circuits

When a parametron supplies many T.B.M.'s with current as shown in Fig. 21; that is, when T.B.M. input circuits are connected in series, the controllable region of the parametron generally becomes narrower. The dotted lines in Fig. 20 are examples of this tendency.

The following two reasons may be given as causes:

- (1) inconstancy of input current due to series connection
- (2) lag of input signal phase due to series connection.

The results of the test show that the affect of cause (1) is almost negligible; and that for cause (2), only inputs connected in series pro-

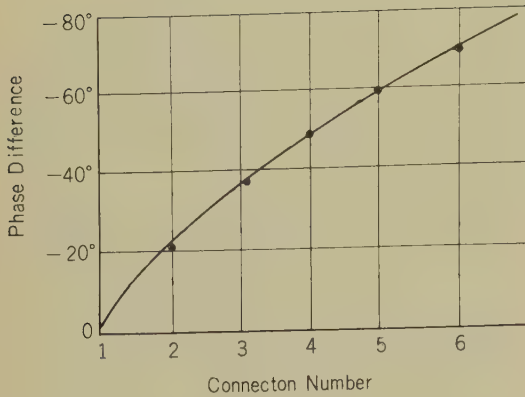


Fig. 22—Change of input current phase due to series connection of input circuits.

duce the phase lag shown in Fig. 22.

However cause (2) can be removed. The phase of the current in the circuit composed of 3 inputs or circuits connected in series in common is different compared with those of 2 input circuits connected or single input circuit only.

Therefore adequate coils for phase compensation are added in series in the latter two cases respectively so that in all cases we get nearly equal phases of input currents, and then compensating phase shift of output signal due to the application through adjustment of tuning condenser. In this case, non-uniformity of L_0 of the magnetic core exerts a great influence, and so much attention should be paid to this for a system requiring many series connections.

7.2. Branch Connection of Output Circuit

The following considerations must be taken when the T.B.M. output is branched into several parametrons (See Fig. 23).

- (1) decrease of output current due to increase of load impedance
- (2) phase shift of output signal

As the T.B.M. output and the parametron are coupled together by a winding of one turn on a 8 mm diameter magnetic coil, the impedance is so small that decrease of output current (1) matters little. But as turning point

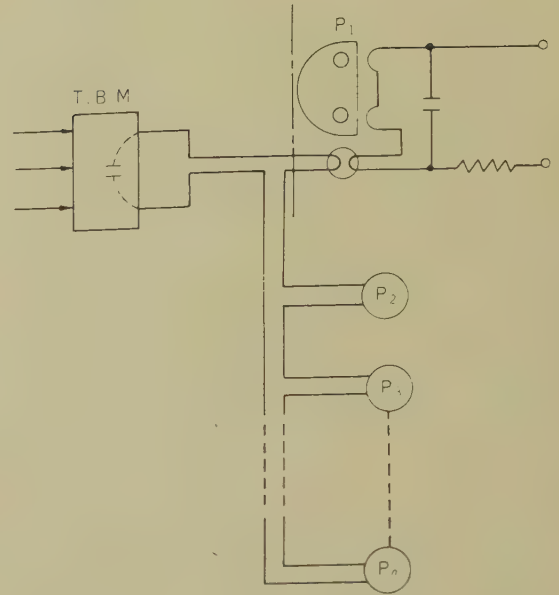


Fig. 23—Branch of output.

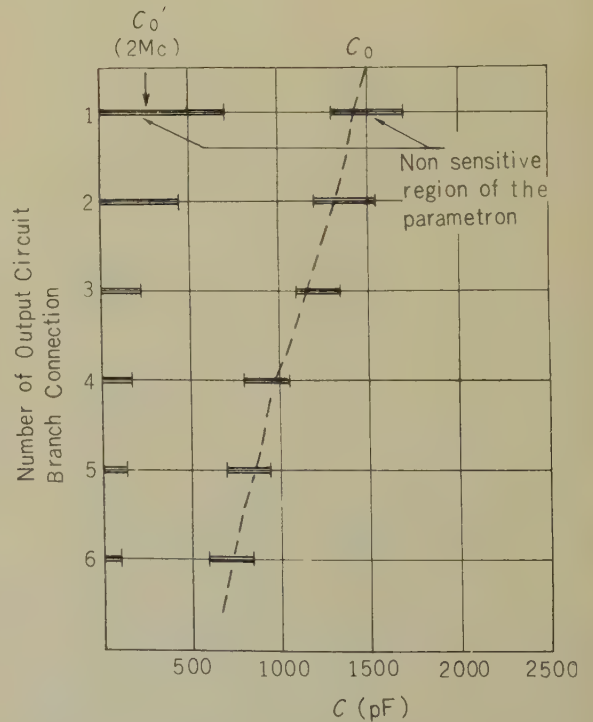


Fig. 24—Change of controllable region due to branch of output.

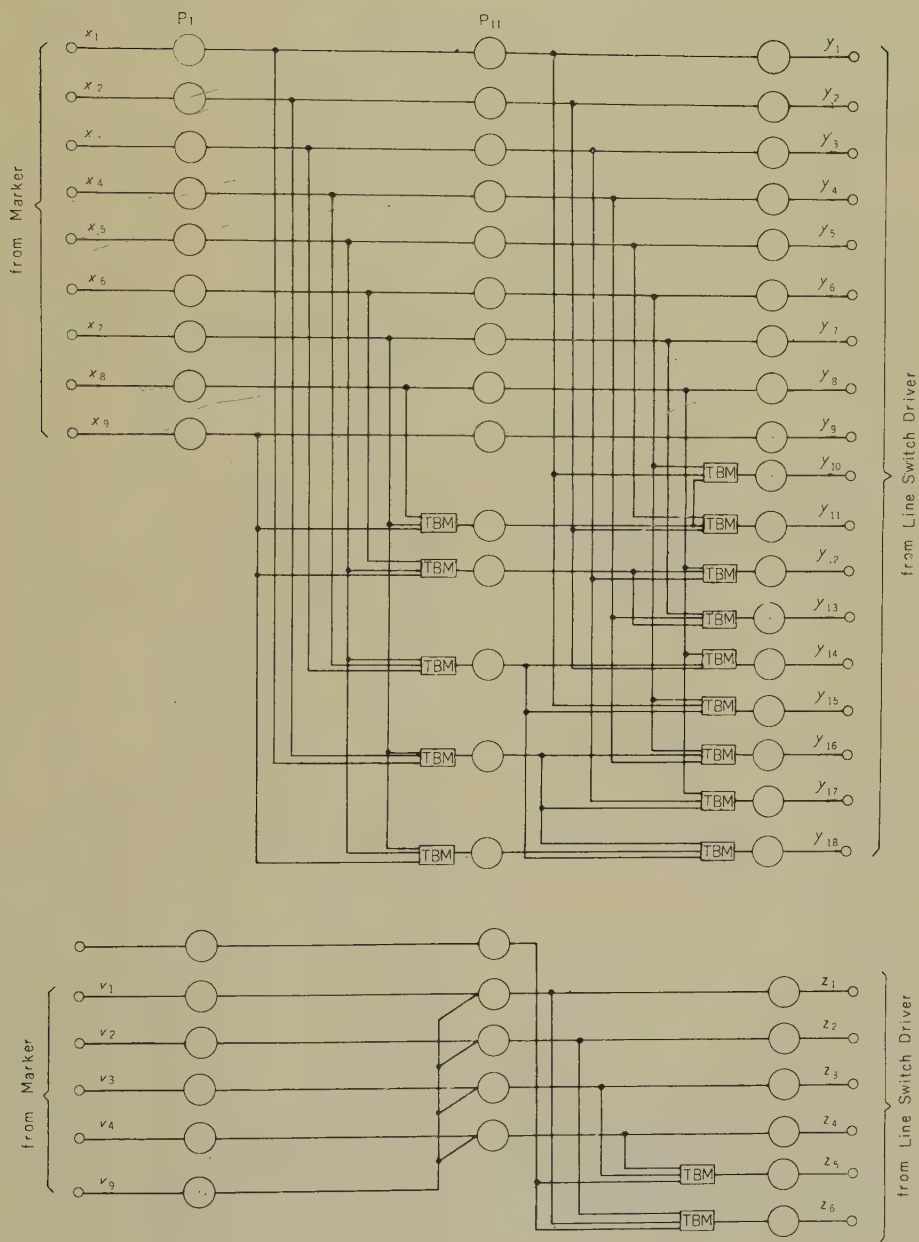


Fig. 25—Switch selection coding circuit.

of output circuit varies a great deal even with slight change of such small impedance, consequently output signal phase shifts as a matter of course, and the controllable region of the T.B.M. moves to the left. (See Fig. 24)

8. Experiment of Coding Circuit

In the ω -switching system, binary signals of 18 or 6 bits are applied for the selection of a line switch of 256 points or for the selection of a trunk switch of 16 points.

In order to improve the reliability of selection redundant codes of 10 and 2 bits are added to the binary signals. The circuit-producing switch selection signal with the added redundant codes is called the coding circuit, and is shown in Fig. 25. Addition of three variables is carried by the T.B.M. and one parametron at its output; but if one wants to add only with parametrons, four parametrons in two stages are required.

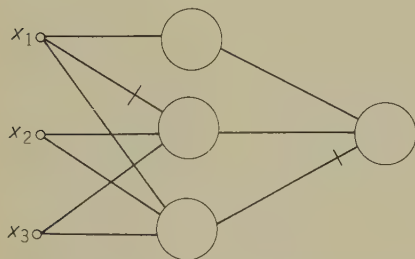


Fig. 26—Three variables adding circuit using parametrons.

Therefore the number of parametrons needed is cut in half by employing 14 T.B.M.'s, the number of stages reduced from 5 to 3, the circuit is simplified, and the control rate is improved.

8.1. Driving Test

The test was conducted with the view to ascertaining whether the phase of the 18 output signals appears in a fixed pattern or not when the phase of the 8-input parametron

signal is driven according to the predetermined code table. The stability of the appearance was also tested.

The kinds and rating of the T.B.M.'s and parametrons adopted here are the same as the ones described in section 6. In this circuit branch connection of the T.B.M. outputs is not used, while number of series connections in each input circuit can be more than five. In order to obtain the optimum condition, the tuning capacitance of each T.B.M. is adjusted.

Phase control of the input signal is done with an 8 phase converter (CV), and observation of output phase was carried out with 18 2-bit discharge tubes.

Observation was taken several times for all the 256 patterns, but no mispattern was found. The stability of the pattern depends chiefly on the stability of the parametron system and therefore, there is no problem in this respect concerning the T.B.M. on the condition that temperature never varies to an extreme.

8.2. Selection Test

The next test was carried to ascertain whether signals are produced at the fixed output terminal of the selecting circuit at the fixed selection ratio by input parametron signals. The test circuit is illustrated in Fig. 27. The coding circuit is composed only of circuits with 4 inputs and 6 outputs for trunk switch selection. The selector is a circuit with a winding corresponding to 6 inputs at its 16 magnetic cores, and produces 16 outputs. Full equipment was not utilized in this test.

Signals with three times as much amplitude as those at the nonselected terminal outputs appears corresponding of the phase pattern of 4 inputs at the fixed output terminal of the selector, and therefore selecting action of the circuit with the selection ratio of 3:1 was found to be normal.

9. Selection of Magnetic Cores

In order to select the magnetic cores, the inductance bridge for parametron magnetic

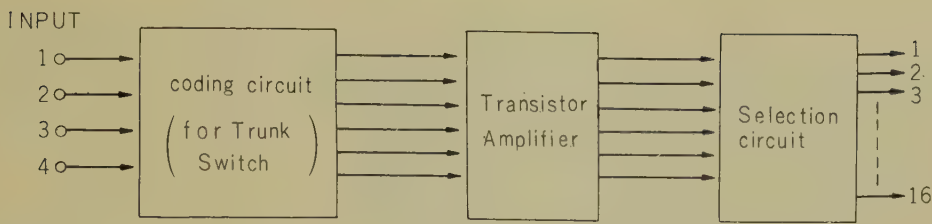


Fig. 27—Selection testing circuit.

core selection was employed, and small amplitude inductance L_0 of a 1 turn winding at the frequency of 0.95 Mc/s was measured. The measuring current was 1 mA, and demagnetization was of course conducted beforehand. Room temperature during measuring was $22^{\circ}\sim 27^{\circ}\text{C}$. If strict selection is wanted, constant temperature is required, because L_0 varies by about 4% at $20^{\circ}\text{C}\pm 10^{\circ}\text{C}$.

10. T.B.M. Unit

A diagram of the T.B.M. unit adopted for the ω -switching system, and its wiring are shown in Fig. 28. Each unit has 10 T.B.M.'s, and each terminal board has ten terminals (G, C and terminals numbered from 1 to 8), Terminals 1-2, 3-4, 5-6 are for three inputs, and 7-8 are for output. C is so designed as to enable measurement of capacitor terminal voltage between terminals 8 and C; phase can also be observed here. C is also utilized in adjusting the capacitance of the capacitor. Terminal G is placed outside the circuit, but it can be used as an ground terminal as occasion demands.

The dimensions of the unit are the same as those of the parametron unit; this enables one to equip the units side by side.

The rating of the magnetic core and the number of turns are mentioned in Section 6. Polyurethane wire of 0.2 mm diameter was used, and styrol capacitors whose capacitance is within $\pm 2.5\%$, was employed. Photographs of individual T.B.M. elements and the completed unit are shown in Fig. 29.

Conclusion

In the application of the T.B.M. composed

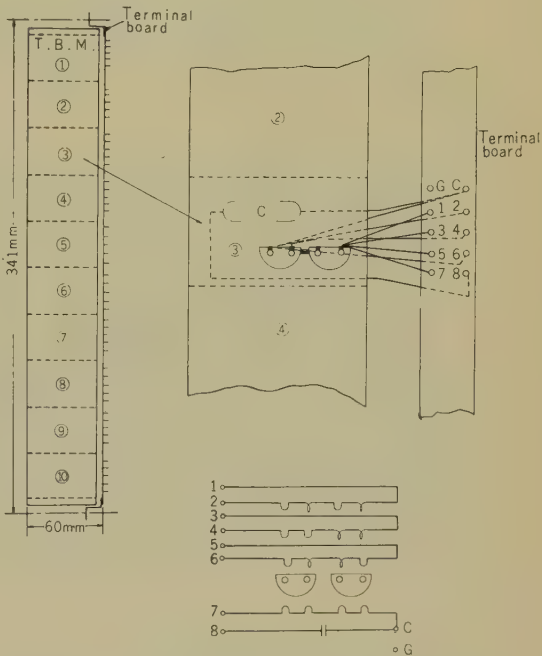


Fig. 28—Construction of unit and its windings.

of binocular type ferrite magnetic cores to parametron control systems, the problems concerning magnetic core, phase shift, input ampere turns, output tuning circuit, and abnormal operation due to series connection of the input circuit or branch connection of the output circuit must be considered. This paper has reported the results of the tests conducted about these problems which can be summed up as follows.

- (1) When binocular type magnetic cores used in parametrons at present are applied to nonlinear element of the T.B.M., the T.B.M. is of good practi-

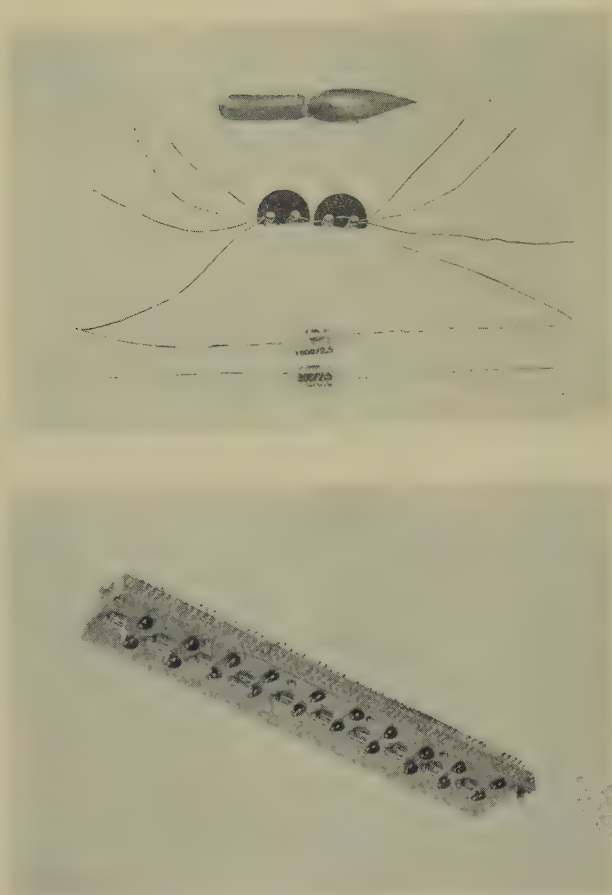


Fig. 29—T.B.M. Element (upper) and T.B.M. Unit (bottom).

- cal use for parametron control systems.
- (2) The value of $\Delta L_0/L_0$ of the magnetic cores must be uniform to within $\pm 3\%$.
 - (3) Input ampere turns of $50 \sim 100$ mAT are appropriate at one winding of one input circuit.
 - (4) Stability is improved if the output tuning circuit is detuned a little and a larger value of capacitance is used.
 - (5) When $\Delta L_0/L_0$ of the magnetic core is within $\pm 3\%$, more than 5 series connections to the input circuits of other T.B.M.'s, or branch connection from an output circuit may be made.

The author expresses his gratitude to Dr. Kiyasu, Vice-Director, and to Dr. Endo, Chief of the Electronics Research Section, who guided him in this study.

References

- (1) E. Gotô: Triple Balance Modulator and its Application to Computing Circuit. (Abstract Conference of I.E.C.E. Japan) No. 213, Apr. 1957.
- (2) Endô and Kusunoki: Gate Circuit by H.F. Signal. (Electrical Communication Laboratory Technical Journal), N.T.T., Vol. 8, No. 7, pp. 1,079-1,085, 1959.

Papers Contributed to Scientific and Technical Journals by the Members of the Laboratory

Papers Published in Other Publications of the Electrical Communication Laboratory

U.D.C. 546.39'185 : 548.55 : 66.065.58 : 621.395.614

Growing of A.D.P. Plate-Type Crystals

Yasuo TOMITA and Tsuyoshi YAMAGUCHI

Kenkyû Zituyôka Hôkoku (Electr. Comm. Labor. Techn. Journ.), NTT, **10**, 1, pp. 71-84, Jan., 1961

Large-scale plate-type Z crystals were grown to investigate the relationship between humidity and the resistivity of A.D.P.

U.D.C. 621.371 : 551.510.52 : 621.391.81 : 538.566

The Results of Radio Wave Propagation Tests on Over Small Clearance Paths

Takeo OMORI and Rihachi SATO

Kenkyû Zituyôka Hôkoku (Electr. Comm. Labor. Techn. Journ.), NTT, **10**, 1, pp. 1-34, Jan., 1960

The results of propagation tests conducted on over small clearance paths at frequencies of 6 Gc/s, 11 Gc/s, and, 24 Gc/s are described in this paper.

U.D.C. 621.372.81

Reflections and Mode Conversions at Imperfect Junctions of TE_{01} Wave Transmission Line

Ken-ichi NODA

Kenkyô Zituyôka Hôkoku (Electr. Comm. Labor. Techn. Journ.), NTT, **10**, 1, pp. 85-94, Jan., 1961

Imperfect junctions cause attenuation increase and delay distortion TE_{01} wave transmission lines. Reflection at slight tilt and offset, and mode conversion at elliptically distorted junctions have been calculated.

U.D.C. 621.385.632.12 : 621.375.13

Feedback Type Distributed Amplifier Tube

Takuya KOJIMA

Kenkyû Zituyôka Hôkoku (Electr. Comm. Labor. Techn. Journ.), NTT, **10**, 2, pp. 209-226, Feb., 1961

A positive-feedback type distributed-amplifier tube has been developed. The anode and grid form a double coaxial helix. Flat gain from low frequency to 300 Mc was obtained.

Translations of many of these papers will appear in a future addition of the Review of Electrical Communication Laboratory.

Please address requests for copies of these papers, which are in Japanese, directly to the authors to whom credited at: The Electrical Communication Laboratory, 1551 Kitizyôzi, Musasino-si, Tokyo.

U.D.C. 621.385.832.032.24.001.2

New Manufacturing Method of Fine Mesh Electrode for Storage Tube

Saburo ISIKAWA

Kenkyû Zituyôka Hôkoku (Electr. Comm. Labor. Techn. Journ.), NTT, **10**, 2, pp.193-208, Feb., 1961

New methods of manufacturing fine nickel and copper mesh which are coated on one side with a thin layer of calcium fluoride for use as the storage grid of storage tubes are described.

U.D.C. 621.395.61.001.2 : 534.6] : 621.391.88

Transmission Performance of the 600 Type Telephone Set

Zenji YAMAGUCHI

Kenkyû Zituyôka Hôkoku (Electr. Comm. Labor. Techn. Journ.), NTT, **10**, 1, pp.95-110, Jan., 1960

Transmission performance of the 600-type telephone set is discussed with regard to articulation, loudness and naturalness. It is found that the telephone set satisfies the design objects.

U.D.C. 621.397.12 : 621.397.331.2

Electronic Scanning High-Speed Facsimile

Keijiro KUBOTA, Kazuo KOBAYASHI, Yoshitaro OKAZIMA, and Shogo NANBO

Kenkyû Zituyôka Hôkoku (Electr. Comm. Labor. Techn. Journ.), NTT, **10**, 2, pp.115-153, Feb., 1961

A vidicon is used at each transmitting terminal and a flying-spot cathode-ray tube is used to write in electro-photographic paper at each receiving terminal. This system was tested over a coaxial-cable system with a bandwidth of 48 kc.

U.D.C. 621.397.232.6 : 621.397.12

A New Type of Vestigial-Sideband Facsimile System

Keijiro KUBOTA and Kazuo KOBAYASHI

Kenkyû Zituyôka Hôkoku (Electr. Comm. Labor. Techn. Journ.), NTT, **10**, 1, pp.53-70, Jan., 1961

This paper presents the principle and describes the experimental results of a simplified synchronous detection method for facsimile systems.

U.D.C. 661.882.095.048.5 : 539.232 : 667

Application of Organic Titanium Compounds

Tunezo NARABA

Kenkyû Zituyôka Hôkoku (Electr. Comm. Labor. Techn. Journ.), NTT, **10**, 1, pp.35-51, Jan., 1960

The application of organic titanium compounds to heat-resisting paints, crosslinkage agents, surface protecting films, and thin films of Barium titanate is described.

These organic titanium compounds were developed as basic materials for use in various electrical communications applications.

Papers Published in Publications of Scientific and Technical Societies

U.D.C. 541.13

Regularities in the Activity Coefficients of Strong Electrolytic Solutions
Zeit. Physik. Chem. Folge **27**, pp. 34-41, 1961

Two regularities were obtained while investigating the concentration dependence of the mean ionic molal activity coefficient of many electrolytes. It was calculated that they are attributable to the hydration effect.

U.D.C. 541.13

The Semi-empirical Treatment of the Regularities in the Activity Coefficients
of Strong Electrolytic Solutions

*Makoto MORIYAMA**Zeit. Physik. Chem. Neue Folge* **25**, pp. 310-300, 1960

Two regularities are treated quantitatively using Glueckauf's equation for the activity coefficient. It has become clear that they are closely connected with the interaction between the hydrated atoms.

U.D.C. 534.121.1:534.64

A New Method of Measurement of Diaphragm Constants

*Minji SUZUKI and Akira SUZUKI**Journ. Electr. Comm. Engin. Japan*, **44**, 3, 442, pp. 55-59

A new method for the measurement of diaphragm constants is reported. In this method, first the volume displacement of pressure is calculated using the ratio of pressure to volume displacement. Next the displacement at the center of diaphragm is measured, and the effective area of the diaphragm is calculated from the value of displacement and acoustic stiffness of the diaphragm. This method is convenient for the measurement of large quantities diaphragms. Accuracy is about 2-4%.

U.D.C. 537.311.4:621.317.331

On Equipment for Measuring Contact Resistance

*Takuya TANII and Kozo TOMA**Journ. Soc. Precision Mechanics of Japan*, **27**, 3, pp. 12-17, 1960

The performance and construction of an equipment to study the relation between contact resistance and contact load are described. The equipment is designed to work free from sliding motion between contact members and with little disturbance from external vibration. Accurate measurements, in which the time variation of the contact resistance are shown.

* * * *

CONTENTS

| | |
|---|-----|
| Chatter Vibration of Switching Relay | 99 |
| <i>Masao TAKAMURA, Yuiti SHIMIZU,</i> <i>and Yuji OTUKA</i> | |
| Feedback Type Distributed Amplifier Tube | 150 |
| <i>Takuya KOJIMA</i> | |
| Recent Development of Quartz Crystal Units for Telecommunication | 165 |
| <i>Kiyoshi TAKAHARA</i> | |
| Studies of Magnetization Processes of Magnetic Cores by Supersonic Methods | 207 |
| <i>Katumi NISHIGUCHI and Hiroshi SAWABE</i> | |
| A High-Speed Facsimile System with Electronic Scanning | 214 |
| <i>Keijiro KUBOTA, Kazuo KOBAYASHI,</i> <i>Yoshitaro OKAJIMA, and Shogo NANBO</i> | |
| The Dimensional Accuracy of Molded Spur Gears of 610-Nylon | 220 |
| <i>Tetsuo KUDO and Takashi YAMANARI</i> | |
| Triple Balanced Modulator Using Binocular Type Cores | 233 |
| <i>Takashi ITO</i> | |
| Papers Contributed to Scientific and Technical Journals by the Members of the Laboratory | 248 |